

2012

Evaluation of harmonic motion elastography and acousto-optic imaging for monitoring lesion formation by high intensity focused ultrasound

<https://hdl.handle.net/2144/1490>

Boston University

BOSTON UNIVERSITY
COLLEGE OF ENGINEERING

Dissertation

**EVALUATION OF HARMONIC MOTION ELASTOGRAPHY AND ACOUSTO-OPTIC
IMAGING FOR MONITORING LESION FORMATION BY HIGH INTENSITY
FOCUSED ULTRASOUND**

by

ANDREW BRUCE DRAUDT

B.S. Cornell University, 1985

M.S. Boston University, 2007

Submitted in partial fulfillment of the
requirements for the degree of
Doctor of Philosophy

2012

Acknowledgments

I am grateful to my advisor, Prof. Robin Cleveland, for invaluable direction and guidance, investment in my work, and for giving me freedom to define the research. I'm also grateful for the expert and congenial collaboration of my committee members; in particular, Prof. Ron Roy, who always encouraged exploration and gave me a sense of possibility, Prof. Paul Barbone, on whom I could depend for accurate, precise, and thorough analysis of problems, and Prof. Gregory Clement, who gave me a sense of the relevancy of the work. I'm also grateful to Prof. Glynn Holt, for quick and dependable insight into problems, experimental skill and experience, scientific enthusiasm, and levity.

I'm thankful to have been funded for my work, which was provided by the Bernard M. Gordon Center for Subsurface and Imaging Systems (GenSSIS) via the NSF ERC award number EEC-9986821.

I'm grateful to have collaborated in the acousto-optics lab with my colleague Puxiang Lai; together we solved problems on our way to the first optical observation of HIFU lesion growth in real time. For their tutelage, insight, and assistance, I thank Prof. Greg McDaniel, Prof. Ray Nagem, Jon Kracht, Bruno During, Caleb Farney, Ashwin Kumar, and David Campbell.

I am especially grateful to Mark Hessler for his friendship, encouragement, intellect and humor during these years of graduate school.

**EVALUATION OF HARMONIC MOTION ELASTOGRAPHY AND ACOUSTO-OPTIC
IMAGING FOR MONITORING LESION FORMATION BY HIGH INTENSITY
FOCUSED ULTRASOUND**

(Order No.)

ANDREW BRUCE DRAUDT

Boston University, College of Engineering, 2012

Major Professor: Robin O. Cleveland, Associate Professor of Mechanical Engineering

ABSTRACT

Malignant or benign tumors may be ablated with high-intensity focused ultrasound (HIFU). This technique, known as focused ultrasound surgery (FUS), has been actively investigated for decades, but slow to be implemented and difficult to control due to lack of real-time feedback during ablation. Two methods of imaging and monitoring HIFU lesions during formation were implemented simultaneously, in order to investigate the efficacy of each and to increase confidence in the detection of the lesion. The first, Acousto-Optic Imaging (AOI) detects the increasing optical absorption and scattering in the lesion. The intensity of a diffuse optical field in illuminated tissue is mapped at the spatial resolution of an ultrasound focal spot, using the acousto-optic effect. The second, Harmonic Motion Imaging (HMI), detects the changing stiffness in the lesion. The HIFU beam is modulated to force oscillatory motion in the tissue, and the amplitude of this motion, measured by ultrasound pulse-echo techniques, is influenced by the stiffness. Experiments were performed on store-bought chicken breast and freshly slaughtered bovine liver. The AOI

results correlated with the onset and relative size of forming lesions much better than prior knowledge of the HIFU power and duration. For HMI, a significant artifact was discovered due to acoustic nonlinearity. The artifact was mitigated by adjusting the phase of the HIFU and imaging pulses. A more detailed model of the HMI process than previously published was made using finite element analysis. The model showed that the amplitude of harmonic motion was primarily affected by increases in acoustic attenuation and stiffness as the lesion formed and the interaction of these effects was complex and often counteracted each other. Further biological variability in tissue properties meant that changes in motion were masked by sample-to-sample variation. The HMI experiments predicted lesion formation in only about a quarter of the lesions made. In simultaneous AOI/HMI experiments it appeared that AOI was a more robust method for lesion detection.

CONTENTS

1	Introduction: HIFU Lesion Monitoring	1
1.1	Focused ultrasound surgery	1
1.2	Monitoring lesion development	2
2	Background: Physical Mechanisms	9
2.1	Heating in tissue	9
2.2	Acoustic forcing	17
3	Methods and Preliminary Measurements	20
3.1	Measuring displacement in tissue	20
3.2	Basic methods and setup	24
3.3	Design of system for combined forcing and tracking	26
3.4	Acoustic fields: measurements and modeling	33
3.5	Temperature measurements and comparison with models	45
3.6	Tissue Properties	53
3.7	Validation and preliminary results	71
4	Bubbles	79
4.1	Background and theory	79
4.2	Modeling scattering from cavitation bubbles	85
4.3	Observations	90
4.4	Conclusions:	97
5	The Finite Element Model	99
5.1	Introduction	99

5.2	The general model	102
5.3	Validation and exploration of the model	109
5.4	The combined model of HMI during lesion formation	124
5.5	Combined model results	126
6	HMI Results and Comparison with FEM	135
6.1	Lesions produced in chicken	135
6.2	Bulk motion, thermal apparent displacement, and bubbles	145
6.3	Conclusions	149
7	Combined Acousto-Optic Imaging and HMI	150
7.1	Background	150
7.2	Detection of lesions with pulsed ultrasound	154
7.3	Detection of lesions with CW ultrasound	159
7.4	AOI and tissue motion	164
7.5	Combined Harmonic Motion Imaging and Acousto-Optic Imaging	168
7.6	Conclusion	177
8	Conclusions and Future Work	178
8.1	Suggestions for future work	180
Appendix A	Equipment list	182
Appendix B	Timing Circuit Diagram	183
Appendix C	Design of Magnetostrictive Shaker	185
Appendix D	Code	187
Appendix E	Nonlinear effects on HMI	192

Appendix F Additional Bubble Results	216
References	223
Curriculum Vitae	236

List of Tables

Table 3-1 Properties of thermocouples used in study. All were obtained from Omega Inc., Stamford, CT. Response times provided by Omega.	47
Table 3-2 Values of attenuation and lesion increase, from the literature	58
Table 3-3 Values from literature for increase in shear modulus caused by lesion	69
Table 3-4 Material properties used for chicken breast	70
Table 5-1 Material properties used for chicken breast	109
Table 7-1 Position and size of three lesions measured with pulsed AOI method, compared with post-dissection manual measurements.	159

List of Figures

Figure 1.1 Speed of sound in water and porcine liver, from Kaczkowski and Anand (2004).	5
Figure 2.1 Dose vs. temp for the case where temp rises from 25 to 70 in 10 sec., a conservative rate for actual lesion conditions. The red line at 240 indicates the threshold for cellular necrosis for muscle (Meshorer 1983).....	11
Figure 2.2 Plot from Sapin-de Brosses et al. (2010). Shear moduli of bovine muscle samples, along with representative phases of protein denaturation (from Tornberg 2005). The rate of temperature rise for this study was 0.5 deg.C. per minute.....	13
Figure 2.3 Temperature vs. time at focal zone, actual and measured by thermocouple. Viscous heating contribution is often thought to become constant at time t'	15
Figure 2.4 Cartoon of interface between two materials, showing incident, transmitted, and reflected acoustic waves, and the area of integration for the surface force calculation	18
Figure 3.1 Left: a portion of two A-lines taken before and after a static compression of aprx. $67\mu\text{m}$ applied to an agar-graphite phantom molded to the shape of a 35mm film canister. Right: Displacement vs. depth from the gradient speckle-tracking routine.	22
Figure 3.2 (a) Backscatter A-line from chicken. (b) test lined synthesized from spectrum of A-line above. (c) representative curve of artificially applied displacement, and response of cross-correlation speckle tracker routine. (d) error in cross-correlation speckle tracker for an applied displacement of 15 AD units applied gradually over a length 5% of total line length. 1% random noise was applied as described in text. The X and Y parameters are number of depth elements and fractional overlap between elements.....	23
Figure 3.3 Basic schematic of experimental setup for HMI.....	24
Figure 3.4 Timing diagram of the HIFU voltage and interrogation pulses.....	25
Figure 3.5 Steady state tissue displacement calculated from Green's function solution	28
Figure 3.6 H02 HIFU transducer plus polycarbonate mount with	29
Figure 3.7 Diagram of electrical connections.....	31

Figure 3.8 Depiction of coincident interrogation pulse and HIFU field, for the case where the pulse propagates (Left) on a HIFU crest, or (Right) on a HIFU trough.....	32
Figure 3.9 Calibration of h102 HIFU transducer with membrane and fiber	34
Figure 3.10 Comparison of measured pressure for h102 HIFU transducer to results from the angular spectrum method and O'Neil's solution to the Rayleigh integral. Peak pressure was 1.23MPa.....	37
Figure 3.11 h102 focal plane measurements taken in first null, with fine spatial grid.	37
Figure 3.12 Contour plot of acoustic fields of h102 and interrogation transducers,	38
Figure 3.13 Axial pressure for 2-layer angular spectrum model with various parameters.....	39
Figure 3.14 Measured fields through chicken tissue at depth=63mm(the focus in water). Thick lines are measured pressure without tissue, and predicted curve from angular spectrum model ("asprop"). All samples are 18mm thick, except for "thin", which is 14mm. The asprop curve is for 18mm thick sample.....	40
Figure 3.15 On-axis intensity for the h102 transducer without central hole, for a source pressure of 41	
Figure 3.16 Left: pressure waveform at focus, taken by fiber-optic hydrophone. Right: plots of "Ifac" for various measured waveforms and waveforms calculated by the KZK equation, along with the polynomial function that will be used to yield $Ifac(f)$	44
Figure 3.17 Data from four thermocouple types, placed at focus of 0.74MPa.....	46
Figure 3.18 Photo of thermocouples used in the lab. Left to right: closed needle, wire, exposed needle.....	46
Figure 3.20 Lumped-element model for thermal mass of thermocouple. T_{in} is outside temperature, T is measured temperature, $R1$ is the thermal conduction resistance between the tissue and thermocouple, $C1$ is the thermal mass of the sheath, $R2$ is the resistance between the sheath and the junction weld, and $C2$ is the mass of the weld.	48
Figure 3.21 Left: Measured temperature at focus in chicken for 4MPa HIFU, along with best-fit curve for artifact and its bulk and artifact components. Right: Measured temp in chicken for	

5MPa HIFU taken 1.5 and 3mm from axis, which had durations of 2 and 4 seconds respectively.....	49
Figure 3.22 Thermocouple curve for a 2MPa HIFU exposure in chicken. The blue curve shows viscous heating at the focal spot. The thermocouple was then backed up 1.47mm and the HIFU run again (cyan). The magenta curve shows the “push-in” data, in which the thermocouple was quickly moved from $r=1.47\text{mm}$ to $r=0$ at the end of HIFU. The black curve is the model, with absorption= 3.4Np/m/MHz	51
Figure 3.23 Thermocouple “push-in” data for various length 5MPa exposures.	52
Figure 3.24 Typical output of attenuation analysis of a tissue sample in the parallel plate apparatus. Green and blue waveforms are received pulses with and without sample. Rather than using the slope, the value of attenuation is taken as 5.25 Np/m/MHz , which is the value at 2MHz (spectral peak).	54
Figure 3.25 Attenuation (Np/m/MHz) vs temperature for chicken sample.	55
Figure 3.26 Attenuation for chicken sample in controlled water bath. Error bars represent 3 measurement locations at each temperature.....	55
Figure 3.27 clock time vs temperature, for the data in Figure 3.26.	56
Figure 3.28 Attenuation vs. surface position over a cross-section of chicken tissue with a HIFU lesion.	58
Figure 3.29 Scale drawing of scattering cross-section setup.....	60
Figure 3.30 Time waveforms from the pzt needle hydrophone vs scattering angle.	60
Figure 3.31 “Focus” simulation of 2 cycles from h102. Left: $\log(\text{Hilbert transform})$ of pressure when p_{max} reaches focus at $z=0$ ($t=43\mu\text{s}$). Right: $\text{abs}(\text{Hilbert})$ of pressure as a function of time and angle for points on an arc 6cm around focus, to match Figure 3.30. The calculation stopped at $80\mu\text{s}$, but would have shown no further energy than shown, for $\text{angle}>60^\circ$	61

Figure 3.32 RMS voltage of the hydrophone signal vs. angle, during the time window of the arrival of the scattered burst. Red curve is the difference between waveforms with and without sample. Right: zoom in of left plot.....	62
Figure 3.33 Sound speed of chicken breast as a function of temperature in hot water	64
Figure 3.34 Shear modulus of four chicken samples Left: magnitude, Right: tan(phase) i.e. “loss factor”	66
Figure 3.35 Stiffness of chicken samples showing effect of cycling temperature 20°C to 50°C to 20°C. Left and Right: two different samples.....	67
Figure 3.36 Shear modulus vs. temperature for two samples, taken on different days. Rheometer oscillation frequency was 10Hz. Sample #1 had 10 min. wait time between points, sample #2 had 5min wait time. The curve for sample#1 reached 88kPa upon returning to 20 degrees. Left: magnitude, Right: tan(phase) “loss factor”	67
Figure 3.37 Values for $G(T)$ and $\alpha(T)$ used for FEM models, normalized to the value at 20°C. The measured curves were simplified into linear segments that could be easily incorporated into the FEM model. Also shown are the alternate hypothetical curves for the high heat rates found in HIFU.	70
Figure 3.38 Scale drawing of magneto-strictive vibration exciter. Pin with 2mm head translates horizontally within a gel phantom, and the motion is measured using speckle tracking with the 7.5MHz interrogation transducer.	71
Figure 3.39 Displacement vs. time as measured by the LDV and the ultrasound pulse/echo speckle-tracker. Left: at the pin head. Right: at the surface of the phantom.....	72
Figure 3.40 Displacement amplitude at 40Hz vs depth measured by speckle-tracking. The interrogation	72
Figure 3.41 Displacement vs. time vs. depth during a 10 cycle “push run”. The sample was chicken, and forcing wave was 3MPa peak pressure 1.1MHz HIFU, modulated at 40 Hz.....	74
Figure 3.42 Fourier amplitude of the oscillations in Figure 3.41, vs depth into tissue.....	75

Figure 3.43 Typical results of HMI interrogations during lesion formation. Each vertical line is the Forrier amplitude of the HMI displacement vs. depth, for one interrogation. Interrogations occur every 4 to 5 seconds, and are interspersed with HIFU heating. One interrogation was always taken before the start of heating, and usually many were taken after heating stopped. The black line on top indicates the entire duration of the heating.	76
Figure 3.44 Displacement amplitude at 40 Hz at peak depth, for 4 separate	76
Figure 3.45 SNR vs. depth for 8 pairs of A-lines from a typical push run in chicken.....	77
Figure 4.1 Plot of bubble size thresholds as a function of equilibrium radius and fluid viscosity, from Yang et al. (2004), for an ultrasound excitation of 2.5MPa peak pressure at 1MHz. "SI" is the shape instability threshold. "IC" is the limit beyond which inertial cavitation can no longer occur, and "RDxx" are the maximum growth levels for rectified diffusion, for various percent gas concentration xx in the fluid.....	82
Figure 4.2 Bubble dissolution time vs. gas concentration and initial bubble size, for bubble	85
Figure 4.3 Calculated response of a bubble to a 1.2MPa pulse from the interrogation transducer. Viscosity =.....	86
Figure 4.4 Normalized spectrum from measured backscattered interrogation pulse from chicken, along with calculated spectrum from nonlinear bubble scatterers. Viscosity=0.02 Pa s87	
Figure 4.5 Modeled values of R(t) for various initial bubble sizes in response to a 7MPa HIFU.....	88
Figure 4.6 Oscillations in bubble radius R(t) caused by a 7MPa 1.1MHz HIFU wave,.....	88
Figure 4.7 Calculated voltage after the hipass filter for the same model as Figure 4.5. This is intended to show relative voltage levels for various size bubbles. The magnitude is inaccurate due to the uncertainty of the size of each pressure pulse created during inertial implosions.	89
Figure 4.8 Spectra of the voltage signals from the scattering of 7MPa, 1.1MHz	90

Figure 4.9	Data from a 7MPa, 36s HIFU exposure. (a) A-lines from interrogation transducer, showing growth of region of increased echogenicity, possibly caused by scattering from bubbles. (b) zoom-in. (c) spectrogram of.....	92
Figure 4.10	HMI results for the data shown in Figure 4.9.....	93
Figure 4.11	8MPa 36s HIFU exposure in chicken. (a)A-lines showing the only region of increased echogenicity. (b) spectrogram of line #1457. (c) time trace of a portion of line #1457, showing periodic spikes. (d) HMI displacement. Black bar over top indicates HIFU on-time.....	95
Figure 4.12	Harmonic content, relative to fundamental, of 33 cycle bursts backscattered from chicken at various pressure levels.....	96
Figure 5.1	Mesh for the basic 3d model Units are meters.....	102
Figure 5.2	Mesh for 2-d axisymmetric models, with imported acoustic field.....	103
Figure 5.3	Generalized Maxwell model, consisting of a number of spring-dashpot elements.....	108
Figure 5.4	Temperature response to 4MPa, 5 sec exposure at 1.1MHz for absorption=5 Np/m/MHz. Results are shown from the Parker model, the FEM thermal model using the acoustic filed calculated from the angular spectrum method, and the FEM thermal model for the same Gaussian beam used in the Parker model.....	110
Figure 5.5	Comparison of Green's function solution and FEM solution for the case.....	111
Figure 5.6	Effect of mesh size on axisym static solution. The labels "normal" etc. are.....	112
Figure 5.7	The various axisymmetric grids used in the grid size study. Units are in meters. From upper left to lower left, the designated sizes, along with the length of the tightest mesh in each, were: fine(0.25mm), normal(0.5mm), coarse (1mm), extra coarse(2mm).....	113
Figure 5.8	FEM model output for axial displacement at a depth of 13mm, which is the location of maximum displacement. Top: force applied as square wave from 0 to F_0 . Bottom: force applied as a sinusoid. blue: general Maxwell model, green: 3d model with $E=18\text{kPa}$, red: 3d model with $E=36\text{kPa}$	115

Figure 5.9 Fourier amplitude vs depth for time-harmonic solutions of the	116
Figure 5.10 Four waveforms selected at random from 27 push-runs. Top two are from breast#1, bottom two from breast #2. These are from the segments of the A-lines representing a depth of 13mm into the tissue.....	118
Figure 5.11 Fourier amplitude of displacement vs depth into tissue, along with standard deviation, for breasts #1, 2, and 3. The first two each contain data from 8 runs spaced >10mm apart. The third plot is for 11 runs spaced 1mm apart.....	119
Figure 5.12 Measured waveform compared to model output. Left: time waveform at focal depth. Right: Fourier amplitude vs. depth into tissue. Model output is shown for nominal values (absorption=4 Np/m/MHz, Young's modulus = 36kPa, Rayleigh damping factor = 1.35e-3), and for modified parameters (absorption=9 Np/m/MHz, Young's modulus = 18kPa, Rayleigh damping factor = 4e-3).....	120
Figure 5.13 Push runs amplitude vs water bath temp. Left: measured. Right: FEM model.....	121
Figure 5.14 Simplified curves for measured values of $G(T)$ and $\alpha(T)$ used for FEM models, normalized to the value at 20 degrees C.....	121
Figure 5.15 Effects of changing stiffness and absorption inside a "small" and "large" lesion. (a): initial softening, in which G drops 30%. (b): final stiffening, in which G changes either 2x or 4x. (c): increasing attenuation, either 2x or 5x. (d): both increased attenuation and stiffness.	123
Figure 5.16 Schematic of the combined FEM model.....	124
Figure 5.17 Axial pressure field with simulated lesion. Method 1 is modified.....	125
Figure 5.18 Amplitude after 28 sec exposure, with and without extra.....	127
Figure 5.19 Temperature at focus for 28 sec 7MPa exposure. Final lesion absorption = 2x or 5x healthy tissue. "Feedback" refers to whether the increased acoustic absorption of the lesion is included in the heat source.	127

Figure 5.20 Temperature at end of 7MPa 28s exposure. a) no feedback, b) feedback included from increase in lesion absorption (5x healthy), c) feedback plus heat absorption from boiling, d) feedback with final $\alpha=2x$ healthy, with boiling. Note that the color scale saturates at 100°C.....128

Figure 5.21 Lesion size, defined by when temperature is over 57°C. Left: radius at center, Right: length, for the four cases in Figure 5.20. “Base” refers to un-modified tissue parameters, and no special treatment of boiling.....129

Figure 5.22 Amplitude vs. depth at times during lesion sequence $t=0, 2, 3, 6, 12, 18, 28$ sec. Shear modulus $G=12kPa$, absorption= $4Np/m/MHz$, Rayleigh damping parameter $\beta=1.35e-3$. Final lesion absorption $\alpha_F=5x\alpha$, final stiffness $G_F=4xG$130

Figure 5.23 Amplitude vs. depth at times during lesion sequence $t=0, 2, 3, 6, 12, 18, 28$ sec. Shear modulus= $12kPa$, absorption= $4Np/m/MHz$, Rayleigh damping parameter $\beta=1.35e-3$. Use “modified” parameters for slower protein denaturation (Figure 3.37) $\alpha_F = 2x\alpha$, $G_F = 2xG$130

Figure 5.24 Amplitude vs. depth at times during lesion sequence $t=0, 2, 3, 6, 12, 18, 28$ sec. Alternate tissue parameters to match measured values (Figure 5.12). Shear modulus changed from= $12kPa$ to $6kPa$, Healthy absorption from $4Np/m/MHz$ to $9Np/m/MHz$. Rayleigh damping parameter from $\beta=1.35e-3$ to $4e-3$. Also use the “modified” parameters for slower protein denaturation (Figure 3.37): $\alpha(T)$ final = $2x$ healthy, $G(T)$ final = $2x$ healthy.131

Figure 5.25 Modeled displacement amplitude for various values of final attenuation and stiffness. The three rows represent final values of attenuation of 5x, 2x, and 1x initial attenuation, from top to bottom. Color scale ranges are 0-2 μm , 0-1.3 μm , and 0-1 μm , respectively. Final stiffness values are 1x, 2x, and 4x for the columns, from left to right.....133

Figure 6.1 Cross-section of a typical lesion made by the H102 transducer, with focus placed 15mm below surface. The lesion was made in a larger sample, then cut into a cube for photograph.....	136
Figure 6.2 Diameters of lesions made in chicken as a function of duration and.....	137
Figure 6.3 HMI results for 6 lesions made on the same chicken breast with HIFU peak pressure of 7MPa, lasting 28 sec. The sizes of the lesions were (a)3.5mm x 10mm @ 7mm, (b) 4mm x 13mm @ 5mm, (c)4.5mm x 11mm @ 7mm, (d) 3.5mm x 11mm @ 7mm, (e)4mm x 13.5mm @ 7.5mm, (f)5mm x 13mm @ 7mm. Black lines on top indicate the heating phase.	139
Figure 6.4 Data from 6 runs, all taken on the same chicken breast, at a peak pressure of 5MPa. (e) and (f) did not produce lesions. The lesion sizes of the others were (a) 2.5mm x 9mm @ 10mm, (b) 1.5mm x 7mm @ 12mm, (c) 1mm x 1mm @ 9mm, (d)5mm x 12mm @ 18mm	142
Figure 6.5 HMI data for fresh liver. All 5MPa, 70s, Lesion sizes were (a)no lesion, (b) no lesion, (c) 2mm x 10mm x 7mm, (d) 1mm x 2mm x 9mm, (e) 5mm x 10mm x 6mm, (f) 3.5mm x 7mm x 9mm	144
Figure 6.6 All A-lines from a data run in which a lesion of size 5x13x6 was produced in chicken with a 7MPa,	146
Figure 6.7 Data from same run as in Figure 6.6. Upper left: HMI data. The rest are spectrograms taken of the A-lines during the heating periods. The HIFU focus is at 20 μ s.	148
Figure 7.1 Schematic of the acousto-optic experiments.....	152
Figure 7.2 Schematic of the action of the PRC. A grating is made by the interference of the two beams which diffracts each in the direction of the other.....	152
Figure 7.3 Left: increase in absorption in a thin, back-lit cross-section of a lesion in chicken, which appears darker than the surrounding tissue. Right: Lesion appears white as a result of the increase in scattering.....	154

Figure 7.4 Experimental setup. The light passes through transparent.....	156
Figure 7.5 Photo of tissue sample mount, plus HIFU and imaging transducer.....	156
Figure 7.6 Cartoon depicting the approximate size of the acoustic and light fields.	157
Figure 7.7 Photodetector waveforms for acoustic pulses directed though the center of HIFU lesion in chicken. (a) pre-lesion, (b) post-lesion, (c) difference.	158
Figure 7.8 Left: AOI image of HIFU lesion in chicken breast. The HIFU focal zone is shown by the dashed oval. The tissue was scanned in increments of 1/3 mm in the horizontal dimension. Right: A standard B-mode ultrasound image of the same tissue where the dashed rectangle represents the area of the AOI image shown at left. The lesion was not visible in the B-mode image. Lesion was 4mm thick, 14mm long.....	159
Figure 7.9 Left: Photodetector(APD) voltage for 1.1MHz, 1MPa acoustic excitations lasting 5, 10, 50, and 100 cycles. Right: Output for 10,000 cycles, at both 1% and 50% duty cycle.	161
Figure 7.10 Schematic of addition of the lock-in amplifier to the AOI experimental setup.	162
Figure 7.11 Lock-in output during 8MPa HIFU exposure in chicken.....	163
Figure 7.12 Per-cent drop in LI signal for indicated HIFU exposure peak pressures and durations, in chicken breast. (from Lai 2011).....	163
Figure 7.13 APD output for a 2MPa, 500 cycle HIFU burst in bovine liver.	165
Figure 7.14 Response to 400 cycle HIFU burst. Left: AO interaction, Right: displacement measured by ultrasound speckle tracking.	167
Figure 7.15 Response to 1980 cycle HIFU burst.	167
Figure 7.16 Response to 14,000 cycle HIFU burst.....	167
Figure 7.17 Percent drop of LI signal as a function of lesion volume for the combined AOI-HMI experiment.	169
Figure 7.18 Data for a lesion measuring 3mm wide by 8mm long, made with a 8MPa, 60s HIFU exposure at 50% duty cycle. (a) HMI data showing tissue displacement Fourier amplitude at the modulation frequency of 40Hz. (b) Normalized curves for 1: Average	

displacement amplitude over 10mm focal zone, 2: total light level*-1, 3: lock-in output*-1, 4: RMS of backscattered interrogation pulse over 10mm focal zone. (c) Hilbert transform of backscatter. All time scales are aligned.....	171
Figure 7.19 Data for a lesion measuring 3mm wide by 11mm long, made with a 6MPa, 70s HIFU exposure at 50% duty cycle.....	172
Figure 7.20 Data for a lesion measuring 4.5mm wide by 10mm long, made with a 7MPa, 70s HIFU exposure at 50% duty cycle.....	173
Figure 7.21 Data for a lesion measuring 5mm wide by 15mm long, made with a 9MPa, 56s HIFU exposure at 50% duty cycle.....	174
Figure 7.22 No lesion found. 6MPa, 70s HIFU exposure at 50% duty cycle.	175
Figure C-1 Diagram of circuit built to synchronize the HIFU wave and interrogation pulses. Note: the plotting process erased the bar above the lower “Q” in each output pair.....	183
Figure D-1 Scale drawing of magnetostrictive vibration exciter. Pin.....	185
Figure D-2 Magnetostrictive performance specification for Terfenol alloy.	186
Figure F-1 Experimental setup for measuring scattering from bubbles in tissue samples or phantoms.	216
Figure F-2 Data from agar-graphite phantom exposed to 1.1MHz CW HIFU. (a), (c), and (e) were from one exposure in which the pressure was changed from 0.9MPa to 1.7MPa. (c) and (e) are time traces of the data in the spectra in(a). (b) and (d): same spot in phantom, exposed to constant 3.2MPa HIFU, 5 minutes after the previous exposure.	218
Figure F-3 Time and frequency data from central interrogation transducer, for the save experiment as shown in Figure F-2. (a): backscatter from the graphite particles, no HIFU. (b), (c): spectrum and time trace of data taken during the 0.9MPa portion of the HIFU exposure. (d): c-a.....	220
Figure F-4 A-lines from a 28s, 7MPa HIFU/HMI exposure in chicken.....	221

Figure F-5 Left: spectrogram of A-line #1 (pre-HIFU). Right: Last A-line taken with HIFU on.....221

Figure F-6 FFT of each A-line during HIFU. HMI interrogation lines were omitted.222

1

Introduction: HIFU Lesion Monitoring

1.1 Focused ultrasound surgery

Viscous heating by high-intensity focused ultrasound (HIFU) can generate high heat concentrations at target points within the body. It has been used for the sealing of blood vessels (haemostasis) (Vaezy et al. 1997); clot disruption (thrombolysis) (Trubestein et al. 1976, Tiukinhoy-Laing 2007); various ophthalmological procedures such as reduction of intra-ocular pressure (Silverman et al. 1991), retinal re-attachment (Rosescan et al. 1985), and treatment of intra-ocular tumors (Burgess et al. 1987). HIFU has been used to destroy tumor tissue in many organs of the body, including the kidney, breast, and bladder (Kennedy et al. 2003). It has been widely used for the treatment of uterine fibroids (McDannold et al. 2006) and tumors of the prostate (Chaussy and Thuroff 2003). In the latter application, cell necrosis is typically achieved by raising the temperature above 56°C for >1s (Hill et al. 2004). The necrosed region, usually called a lesion, takes the form of the ultrasound focal zone, which is typically a cigar shape of 1 to 5mm diameter and >10mm length. Many such lesions need to be overlapped in order to destroy a larger volume like a tumor. In order to avoid heating surrounding tissue, a cooling period must occur between exposures, making a complete HIFU treatment a lengthy procedure.

1.2 Monitoring lesion development

Imaging the placement and development of the lesion is important for tumor treatment, where it is desired to minimize exposure time and damage to healthy tissue while ensuring that every cancer cell is destroyed within tumors of complex shape. MRI is an effective and widely used modality for monitoring HIFU lesion formation clinically. It uses high magnetic fields to align the spin of protons in hydrogen nuclei, which scatter probing RF electric field pulses. Various tissue properties can be imaged, including temperature to a precision better than 0.4°C (Vykhodtseva et al. 2001). MRI guided focused ultrasound surgery is a very active research field and has been used clinically with success (Hindley et al. 2004). However, ultrasonic technology can be made cheaper and more portable than MRI. The temporal resolution for ultrasound is at present better than MRI, but MRI technology is quickly catching up. Other ultrasound-based methods of lesion monitoring have been researched, involving the measurement of changes in tissue properties such as stiffness and acoustic attenuation. Temperature may also be measured using ultrasound techniques, and lesion growth may be inferred. Some of the ultrasound-based methods relevant to this thesis are described below.

1.2.1 Conventional Ultrasound Imaging

Conventional ultrasound forms images based on the backscatter signal from the tissue. While HIFU heating produces an increase in speed of sound and attenuation in tissue, the change in backscattering coefficient is too small to enable detection via ultrasound imaging (Bush et al. 1993). Little or no correlation between the degree of backscattering and the degree of tissue damage has been found (Sibille et al. 1993, Bailey et al. 2001). Conventional B-mode imaging is thus ineffective at detecting HIFU-induced lesions. It can, however, detect cavitation during HIFU exposure (Veazy et al. 2001). Cavitation activity was shown to be temporally well correlated with the appearance of hyperechoic areas (Rabkin 2005). However, the presence and nature of these bubbles does not indicate the presence or extent of cell damage. Ultrasound Clinical HIFU systems designed to be used without MRI, such as the HAIFU jc200 (Chongqing Technology Co., Ltd., Chongqing China) are

equipped with standard ultrasound imaging systems to aid in visualization, but can only detect lesion formation if cavitation bubbles are present. Indeed, in a recent paper on clinical use of this machine on human breast cancer patients, Niu et al. (2010) monitored lesion growth using a thermocouple inserted into each lesion site.

Hyperechogenicity from cavitation has been proposed for use in guiding the HIFU focal spot to the desired location, however the short exposures (30-60ms) used may still cause unintended damage (Rabkin et al. 2006). Yao et al. [2002] used 2nd harmonic imaging on HIFU lesion formation, hypothesizing that the observed increase in echogenicity was due to stable microbubbles that can occur even at low insonation levels.

1.2.2 Spectral Techniques

The acoustic attenuation of thermally necrosed tissue is more than twice that of healthy tissue (Robinson and Lele 1972, Bush et al. 1993, Damianou et al. 1997, Tyreus et al. 2004), and this may be used to image lesion formation. A straightforward method was proposed to observe the development of a shadow in the B-mode image created by the increased attenuation of a HIFU lesion (Green and Arditi 1985, Baker and Bamber 2001). The technique involves integrating the backscattered signal over the region beyond the point of interest (e.g. lesion zone), and comparing to some baseline reference value. An increase in attenuation in the region in front of the integration zone will reduce the integrated backscatter coefficient, analogous to a shadow.

Spectral analysis of ultrasound backscatter has extended the usefulness of B-mode ultrasonic imaging (Kuc and Schwartz, 1979, Ophir et al. 1984). Attenuation in tissue is approximately linear with frequency. A common expression for attenuation in the neighborhood of some center frequency f_0 is $\alpha(f) = \alpha_0 + \beta(f - f_0)$ where α_0 is the attenuation at f_0 , and β is the local slope. Commonly mapped indicators of attenuation include the local slope in the spectrum of the backscatter, called “midband fit”, and the shift in the spectral peak. Acoustic attenuation mapping has been used successfully in vivo to determine the pathological state of liver tissue (Garra et al. 1984). Ribault et

al. [1998] applied the technique to HIFU lesions in prostate cancer, to map the difference in α or β before and after HIFU treatment. They reported that this method, called “differential attenuation mapping”, was able to achieve a resolution of 1cm in porcine liver.

Because Gaussian ultrasound pulses and their echoes are amenable to Gaussian statistics (Lizzi et al. 1997), the spectral peak of the backscatter will shift as a predictable function of depth and attenuation. Girault et al. (1998) showed that the attenuation slope is proportional to the time derivative of the peak frequency. The shift in peak was used by Bevan and Sherar (2001) to map attenuation in phantoms, but they found that the signal-to-noise ratio of the signal envelope limited the ability to localize the change in attenuation associated with thermal coagulation in the tissue.

If spectral techniques are to be useful as feedback during HIFU treatment, information indicating the tissue state will need to be presented in real time. To this end, Anand and Kaczkowski (2004) made movies of the region of interest, assigning color according to the spectral content of the backscattered energy from each region, compared to the spectral content at the start of HIFU. They also displayed the temperature at each point, as revealed by the local “apparent displacement” caused by the change in acoustic velocity with increasing temperature (see section 0). A similar approach was recently taken by Zhong et al. (2007), who used faster autoregressive techniques (Girault et al. 1998) rather than fast Fourier transforms to map the local attenuation vs. time. They simultaneously displayed changes of local integrated backscatter (IBS) (O’Donnell et al. 1979) in time, which revealed bubble activity.

1.2.3 Measuring temperature with apparent displacement thermometry

The speed of sound in tissue is a function of temperature (Figure 1.1). Therefore the heating from HIFU will change the time-of-flight of the elastographic interrogation pulses, producing an apparent displacement. This has been used to estimate temperature during lesion formation (Seip and Ebbini 1995, Simon et al. 1998, Maass-Moreno et al. 1996, Miller et al. 2002, Pernot et al. 2004, Anand and Kaczkowski 2008, Curiel et al. 2009). One problem is that velocity peaks and then decreases after a

certain temperature and the peak varies from 35°C to 60°C, depending on tissue fat content (Miller et al. 2002).

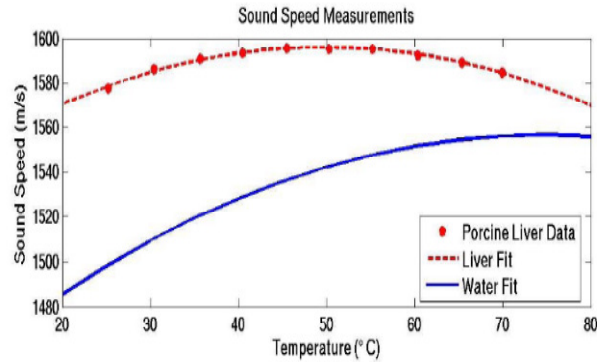


Figure 1.1 Speed of sound in water and porcine liver, from Kaczkowski and Anand (2004).

Kaczkowski and Anand [2004] addressed the problem of a non-monotonic change in velocity with temperature by fitting their displacement to a model. They modeled the velocity curve as a quadratic, and developed a method to estimate the local values of thermal diffusivity and heating source by fitting a solution to the heat equation to their velocity vs. temperature data. The accuracy of this method thus depends on the accuracy of a number of estimates and assumptions.

Because the velocity changes so little as a function of temperature in the temperature range where lesioning occurs, Miller et al. (2002) determined that the apparent displacement technique required such high SNR that to visualize a heated region of liver tissue with 95% certainty would be impossible, unless the liver were fat free, and the system could produce a 26dB SNR. Another possible drawback to this type of temperature monitoring is that the focused heating will also maximize the thermal lensing effect [Simon et. al. 1998, Alaniza et. al. 2002] in which the sharp temperature gradient across the focal region refracts the diagnostic beam, leading to diminished correlation between pre and post heating RF echo segments. This results in noisier apparent strain/temperature rise estimates at and beyond the focus.

1.2.4 Elastography and ARFI/HMI

In-vivo imaging the elastic properties of tissue (elastography) can be used to monitor lesion formation by virtue of the fact that stiffness in thermally necrosed tissue is 1.5 to 7 times that of healthy tissue (Robinson and Lele 1972, Bush et al. 1993, Damianou et al. 1997, Tyreus et al. 2004). In general, an internal stress or external strain is applied to the tissue, and the resulting displacement or motion is measured. The applied stress or strain may be static or cyclic. With static elastography, a constant external pushing force is applied, and the resulting deformation is measured, usually by measuring the location of scatterers within the tissue before and after compression (Ophir et al. 1991, O'Donnell 1994). A freehand method of applying compression was investigated by Doyley et al. (2001), but a more controlled compression is desirable. This was achieved for breast tissue with the use of x-ray mammogram plates by Ophir et al. (1991) and Garra et al. (1997). Tissue displacement was measured using ultrasound speckle tracking (Ophir et al. 1991). A resolution of 1mm in the axial and lateral directions was achieved by Srinivasan et al. (2004) using a 5 MHz imaging probe.

With dynamic elastography, a low frequency (1Hz – 10kHz) cyclic or transient force is applied, and resulting tissue motion measured. Early feasibility studies used a mechanical piston source (Parker et al. 1990, 1998), but acoustic radiation force from focused beams was later adopted, allowing a highly localized force to be applied deep inside tissue non-invasively. The radiation force from acoustic waves due to absorptive momentum transfer is given by $\mathbf{F}(r, t) = 2\alpha\mathbf{I}(r, t)/c$ where α and c are the acoustic attenuation and sound speed of the medium and \mathbf{I} is the acoustic intensity. Fatemi and Greenleaf (1998) use two focused beams of slightly different frequencies (3 MHz, 3.007 MHz), to produce a radiation force at the difference (beat) frequency of 7kHz. The forcing beam was scanned throughout the region, and the acoustic emissions from the resulting tissue motion were recorded with a remote hydrophone. The frequency of the forcing was varied in order to detect any frequency dependency of the tissue mechanical properties. Nightingale et al. (2001) used a short burst (<5ms) of focused ultrasound to provide the localized forcing, and measured the

tissue response using ultrasonic speckle tracking. Calling this method “Acoustic Radiation Force Impulse” imaging (ARFI), they used the same linear array transducer for both the forcing bursts and tracking pulses. Clinical success with imaging relative tissue stiffness was achieved (Nightingale et al. 2006), and the method is currently available on commercial ultrasound imaging machines, as a supplemental, qualitative mode.

Lizzi et al. (2003) examined the use of ARFI for HIFU lesion monitoring. A finite-difference model was made which treated the lesion as an ellipsoid of increased stiffness (5x), but the increase in acoustic attenuation was not considered. The modeled tissue motion was less in the region of the lesion, and preliminary experiments in liver tissue showed a similar result. This thesis will reveal an opposite relationship, that the diminished motion caused by increased stiffness is secondary to the enhanced motion from the increased attenuation. Also showing this opposite relationship, Haw (2008) employed ARFI to monitor HIFU lesion formation in store-bought chicken tissue. A finite-element model was also made which took into account both increased absorption and stiffness. The results showed an increase in tissue amplitude due to increased absorption, followed by a smaller decrease in motion when the lesion grew outside the acoustic focal region. It was suggested that this was due to the increase in stiffness in the lesion just outside the acoustic field, since it is in that region that shearing forces bear upon the forced region.

Konofagou and Hynynen (2003) used separate transducers to provide the forcing and tracking functions, and imparted oscillatory tissue motion by modulating a constant forcing wave. Many interrogation pulses were fired for each cycle of the forcing oscillation, and the displacement of the tissue motion was thus measured. The technique is referred to as “Localized Harmonic Motion” (LHM) imaging, or “Harmonic Motion Imaging” (HMI). A major advantage is the immunity to ambient tissue motion and apparent displacement caused by the temperature dependence of the speed of sound. Curiel et al. (2009) employed HMI in-vivo in rabbit thigh tissue and reported a decrease in amplitude during lesion formation.

In this chapter, focused ultrasound surgery was introduced. It was seen that monitoring lesion formation was critical for clinical success. Thermally induced coagulative necrosis results in changes in acoustic attenuation, tissue stiffness and optical absorption and scattering. Methods abound for the detection of these changes, using both ultrasound and laser light, but none have clearly emerged as a robust solution to the lesion detection problem. This motivated the goal of this thesis; to developing a strategy to detect two or more of these changes simultaneously, to gain insight into the lesion formation process and to gain certainty of lesion formation.

2

Background: Physical Mechanisms

2.1 Heating in tissue

In a medium which absorbs acoustic energy such as tissue, the rate of heating per volume is given by

$$q = \frac{2\alpha}{\rho c \omega^2} \left(\frac{\partial p}{\partial t} \right)^2 \quad (2.1)$$

for a time-harmonic acoustic wave Pierce (1989). p is the pressure, α the acoustic absorption, ρ the material density, c the acoustic velocity, and ω the angular frequency. For plane waves this reduces to

$$q = 2\alpha I \quad (2.2)$$

It is emphasized that the absorption α is here distinct from attenuation, which is the degree to which the energy in an ultrasound beam is diminished due to both absorption *and* scattering. Estimates in the literature for the ratio of absorption to attenuation in tissue vary widely, from 70% to 99% (Hill et al. 2004), with the majority being 80% to 90%. Measuring acoustic absorption is not straightforward. In classic works by Fry and Fry (1957), and Parker (1983, 1985), absorption is

measured by analysis of the temperature vs. time curve measured by thermocouple inserted at the HIFU focus. The initial slope, before thermal diffusion takes place, is proportional to the heat rate, which in turn is proportional to absorption. As will be seen, however, there are problems associated with measuring temperature with thermocouples. Two alternative methods of measuring absorption will be described in chapter 3 .

2.1.1 Effect of heating on tissue properties

As tissue temperature rises between the freezing and boiling points of water, many physiological changes occur which affect physical properties. Properties that may enable thermal lesion detection include stiffness, viscosity, sound speed, acoustic absorption and scattering, optical index, and optical absorption and scattering. The physiological processes that affect these properties during thermal necrosis are principally protein denaturation. The main proteins involved are myosin, actin, and collagen, and each undergo chemical processes of unfolding, aggregation, gelation, and longitudinal shrinkage (Tornberg 2005). There are numerous studies in the literature on the mechanical and more specifically acoustical properties of in-vivo or in-vitro tissue, somewhat less on thermally necrosed tissue, and still less on changes in properties *during* temperature increase. A concept known as *thermal dose* has been adopted to relate thermally-induced tissue changes with a temperature-time integral (Sapareto and Dewey 1984), which has been shown to correlate with degree of protein denaturation better than temperature alone. Their equation is

$$D(t) = \int_0^t R^{(43^\circ\text{C}-T(\tau))} d\tau \quad (2.3)$$

Where t is time, T is temperature in degrees C, and D is the dose, which is sometimes written T_{43} , and is measured in “equivalent minutes at 43 deg C”. A commonly accepted value for T_{43} for the occurrence of cell death is 240 min, although it is a function of tissue type and lower values have been reported (Damianou and Hynynen 1994, ter Haar 2001, Bailey et al. 2003). This equation is widely used in experimental and clinical applications of thermal ablation and hyperthermia. In Figure 2.1 this equation is plotted vs. temperature for the case of a rate of temperature increase that might

be found in a lesion-making HIFU exposure (25 to 60 degrees in 10 seconds). The value defined for tissue necrosis, 240 equivalent minutes, is crossed at 58 degrees, with a slope of about 30 equivalent minutes per degree C. Thus at HIFU heating rates, evaluation of the time at which the thermal dose reaches 240 minutes could practically be achieved by defining the lesions in regions where $T > 58^{\circ}\text{C}$. Only at much slower heating rates does the thermal history matter. According to TerHaar (2004b), a number of authors have concluded that the required temperature-time combination at the boundary of a HIFU lesion is 56 degrees C. for 1 to 2 seconds.

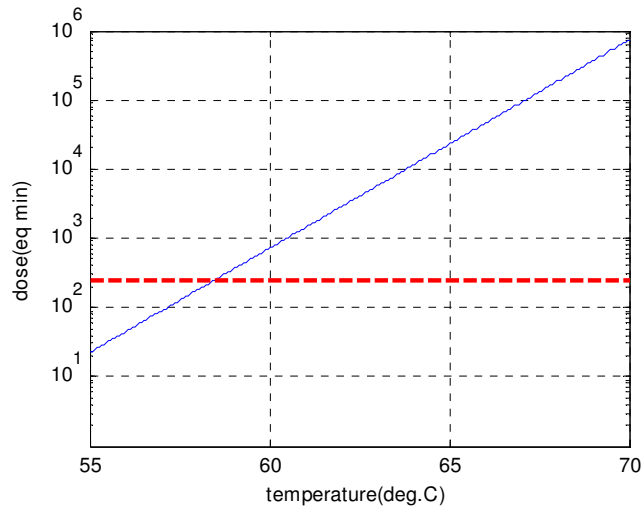


Figure 2.1 Dose vs. temp for the case where temp rises from 25 to 70 in 10 sec., a conservative rate for actual lesion conditions. The red line at 240 indicates the threshold for cellular necrosis for muscle (Meshorer 1983).

It is common in the literature to use the thermal dose to calculate when thermally-induced changes to absorption and shear modulus occur (Mast et al. 2005, Heikkila et al. 2010). However, in order for the dose equation(2.3) to be useful in the modeling of HMI during lesion formation, a relationship between shear modulus and dose level would be required that was valid at heating rates more typical of HIFU. As previously noted, at these rates the thermal dose covers many orders of magnitude in a few seconds. Because measuring stiffness and attenuation vs temperature or thermal dose takes time, there is little or no published research on attaining this relationship for the case of HIFU heating rates. It is conceivable that the stiffness changes from the various phases of protein denaturation occur on a timescale of seconds or even minutes, rather than milliseconds. This

discussion is equally pertinent to acoustic absorption as a function of thermal dose. Damianou et al. (1997) investigated the relationship between attenuation and thermal dose, for different *rates* of dose per time. They immersed canine muscle in constant temperature baths at various temperatures. The amount of time the tissue was left in the bath at each temperature was calculated to give the same thermal dose of $T_{43}=1000$. At a bath temperature of 46°C., the increase in acoustic attenuation was 30% over the unheated value. At a bath temperature of 54°C., the increase in attenuation was 70%. This indicates that attenuation does not increase as much if higher heating rates are used. The fact that the dependence of stiffness or attenuation on thermal dose varies with heating rate will be further investigated in chapter 3 .

In one of the most thorough studies to date on the temperature and dose dependence of tissue stiffness, Sapin-de Brosses et al. (2010) used a shear wave velocity technique to measure the shear modulus of bovine muscle and liver. Figure 2.2 shows measured shear modulus as a function of temperature, along with indications of where the various stages and types of protein denaturation occur. The collagen shrinkage occurs at the highest temperature and causes stiffness to increase to eventually many times the initial value (which occurs off to the right of this plot). Most of the denaturation phases are actually accompanied by a softening of the tissue, and it is only at the last stage that the familiar increase in stiffness occurs. (The reader may recall the increase in stiffness from the last steak they cooked, especially if it was “well done”). They found that the first stages of protein denaturation produced reversible changes in stiffness. The stiffness curves became irreversible with temperatures above about 60°C. This suggests that it is the last stage outlined here, the collagen shrinkage, that is associated with cell necrosis.

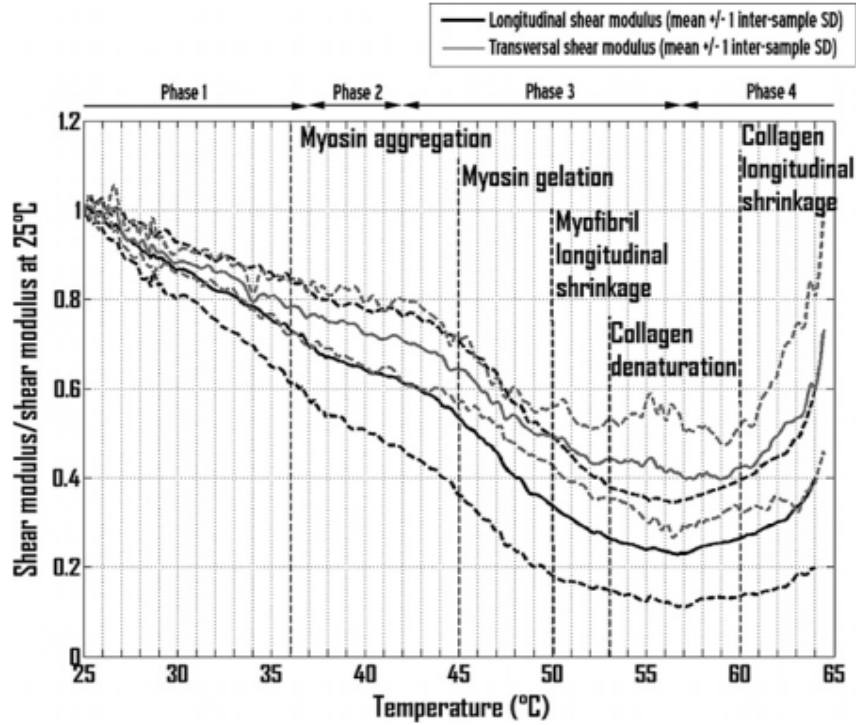


Figure 2.2 Plot from Sapin-de Brosset et al. (2010). Shear moduli of bovine muscle samples, along with representative phases of protein denaturation (from Tornberg 2005). The rate of temperature rise for this study was 0.5 deg.C. per minute.

2.1.2 Thermal modeling

The temperature of the tissue during lesion formation will be modeled using an FEM software package, as described in chapter 4. However, a simpler model was presented by Parker (1983, 1985), which is useful because it gives an analytical expression for the thermal field which can be quickly evaluated for benchmarking and incorporating into larger models that require temperature as input. In this approach, the heat equation in cylindrical coordinates is solved for the case of a heat source extending along the $r=0$ axis and having a Gaussian profile in the radial direction:

$q = 2\alpha I_0 \exp(-r^2/a^2)$, where α is the acoustic absorption, I_0 the peak intensity, and a the Gaussian radius of the beam. The heat equation is expressed as

$$\rho C \frac{\partial T}{\partial t} - K \frac{1}{r} \frac{\partial}{\partial r} \left(r \frac{\partial T}{\partial r} \right) = q \quad (2.4)$$

where ρ is density, C specific heat, and K thermal conductivity. Note that if the tissue studied were in-vivo tissue, blood vasculature carries heat, which is usually treated as a sink term in the heat equation (Pennes, 1948). The solution was made by taking advantage of the fact that both the acoustic field and the temperature field have a Gaussian radial distribution. The response of the temperature to a delta function in time was given as

$$T_{IR}(r,t) = \frac{2\alpha I_0}{\rho C \left[1 + \left(\frac{4\kappa t}{a^2} \right) \right]} \exp\left(\frac{-r^2}{4\kappa t + a^2} \right) \quad (2.5)$$

where κ is the thermal diffusivity (not to be confused with K , the thermal conductivity). Finding the temperature response to a time varying acoustic excitation is done by convolving $q(t)$ with (2.5). For continuous wave HIFU the convolution can be carried out analytically for $r=0$, yielding

$$T(t) = \frac{2\alpha I_0}{\rho C} \left(\frac{a^2}{4\kappa} \right) \ln \left(1 + \frac{4\kappa t}{a^2} \right) \quad (2.6)$$

For locations off axis or heat sources of arbitrary time dependence the convolution needs to be carried out numerically. Finally, the profile of the main lobe of the h102 HIFU transducer field used in this research was approximately Gaussian-shaped, and the thermal FEM showed that the temperature at the focus was nearly identical for a Gaussian beam and the actual beam. Deviations occurred off axis, however, when the contribution of the side lobes became significant.

2.1.3 Measuring temperature with thermocouples: viscous heating

It was important to measure temperature in order to check thermal models, and also as a means to measure acoustic absorption. The most direct method of temperature measurement from HIFU is to implant a fine wire thermocouple at or near the HIFU focal region. However, the difference in density between tissue and the metal of the thermocouples gives rise to relative motion and hence viscous heating due to friction. Fry and Fry (1954) modeled viscous heating for 13 μ m thermocouples in a castor oil medium. According to their model, an initial phase is dominated by viscous heating and a second phase is dominated by absorptive “bulk” heating from the acoustic beam. In the second

phase, temperature increase due to viscous heating was assumed to be constant. Thus the temperature at the end of the initial phase was simply subtracted in order to correct for the thermocouple viscous heating effect. This approach has been followed widely since then.

A number of authors (Fry and Fry 1954, Goss 1977, Parker 1985) were interested in measuring the acoustic absorption of a material by looking at the initial slope of the temperature vs. time due to acoustic heating. From equation (2.5) and the heat equation it is evident that at small time, $t \ll a^2/4\kappa$ the slope of $T(t)$ is proportional to absorption α . Thus if the initial slope could be measured, the material absorption coefficient could be found. Figure 2.3 shows a cartoon of the temperature near the acoustic focal zone and that measured by thermocouple. If viscous heating created at the thermocouple adds a constant temperature at some point in time t' within the linear region of the bulk heating, then the slope of the thermocouple output at this time will be the same as the slope of the actual bulk temperature. If one wanted to know the actual temperature at any time after this point, the value of the viscous contribution (assumed to be constant) could be subtracted off the thermocouple measurement. The viscous contribution was determined by taking the slope at t' and tracing a line back to the y axis and reading the intercept.

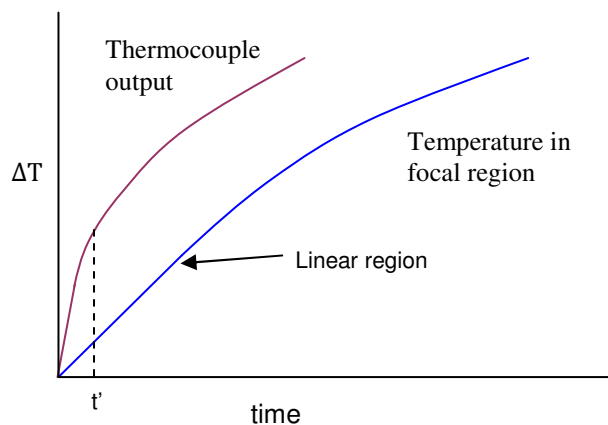


Figure 2.3 Temperature vs. time at focal zone, actual and measured by thermocouple. Viscous heating contribution is often thought to become constant at time t' .

There are two problems with this. One is that there may not be a window of time in which both the viscous heating levels off and the bulk diffusion has not started. For tissue or tissue phantoms, $\kappa \sim 1.6 \times 10^7$ (m²/s) and $a = 0.8$ mm, so $t' \ll 1$ s; the viscous heating “leveling” time, plus any thermocouple response time would have to be even less. Secondly, there is no reason to believe that the viscous heating contribution will *ever* level off. After all, if it is modeled in the same fashion as the main heating beam (as a heat source proportional to acoustic intensity), then diffusion will always result in a nonzero term for dT/dt .

In an effort to eliminate the effects of viscous heating, Clarke and ter Haar (1997) performed a multi-dimensional fit of their thermocouple data to separate models for HIFU beam heating derived by Parker (1985), and for the viscous heating itself, derived by Drewniak et al. (1990). The fit parameters reveal the relative amounts of heating caused by each source. This will be further developed in chapter 3. Huang et al. (2004) measured temperature rise in two different materials under the same conditions. One was a tissue-mimicking agar-graphite gel, and the other an identical gel without the graphite. The non-graphite gel had very low attenuation, and the temperature rise was thus assumed to arise from viscous heating only. The viscous-only curve could then be subtracted from the graphite gel curve to yield the true temperature. It was assumed that the viscous heating at and around the surface of the thermocouple is the same, with or without the presence of graphite particles. This may be problematic, since graphite is a lubricant and may reduce friction. Another approach was proposed by Yang (2003), who modeled the spatial temperature field numerically, treating the thermocouple as a region in space with greater heating. The amount of viscous heating could be adjusted to give results that agreed with data, (assuming accurate temperature data was available). This is essentially the same as the above method of Clarke and ter Haar, since their model employed a separate smaller heat source for the viscous heating.

While all of the above methods have produced data sets that appear to be internally consistent, none have been checked against other trusted temperature measurement methods, nor for varying conditions, thermocouples, or materials. The viscous heating around a thermocouple has been

introduced as an additional heating term in the heat equation, but a physical model does not appear to have been put forward that relates the magnitude of the term to *a-priori* properties of the thermocouple-tissue interface, such as surface roughness or chemical adhesion. Viscous heating, and friction in general, are not easily modeled. It is reasonable to expect that the viscous heating will not only depend on macroscopic physical surface roughness, but also on microscopic surface chemistry and on chemical properties of the surrounding material. For example, it is easy to qualitatively feel that there is far more “tug” on a needle thermocouple inserted in chicken tissue than in agar-graphite phantoms of similar mechanical properties. While it *may* be possible to make repeatable measurements in phantoms, if care is taken to control the surface chemistry of the thermocouple, it is probably not possible to account for viscous artifacts in tissue due to sample variability.

2.2 Acoustic forcing

2.2.1 Force due to absorption and scattering

Acoustic waves carry a net momentum, and when energy in the wave is lost to tissue by absorption there is a reduction in the momentum of the wave. The time rate of change in this momentum must result in a force on the tissue. The same is true for energy lost due to scattering. If the tissue scatterers are much smaller than the HIFU wavelength (i.e. Rayleigh scattering conditions), the force per volume imparted by the acoustic wave is given by

$$\mathbf{F} = 2\alpha\mathbf{I}/c \quad (2.7)$$

where α is the total attenuation coefficient, comprising components from absorption and from scattering (Westervelt 1951, Nightingale 2001).

2.2.2 Surface force

When an acoustic wave encounters an interface of two materials with different acoustic impedance, the wave will be partially reflected and will thus impart a force at the interface. In this thesis the two materials are water and either gelatin phantoms or chicken or liver tissue. For a plane wave, the momentum per time per area, also known as radiation pressure, is given by $\rho u^2 = p^2/\rho c^2 = I/c$ (Morse and Ingaard 1968)

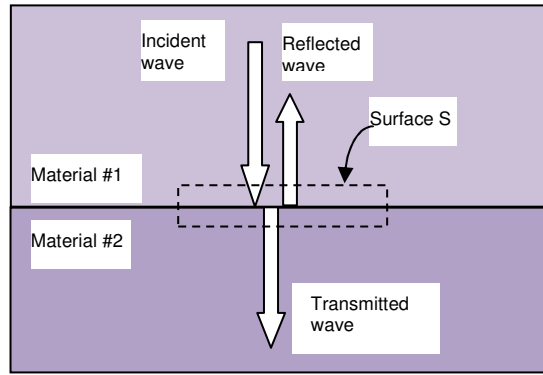


Figure 2.4 Cartoon of interface between two materials, showing incident, transmitted, and reflected acoustic waves, and the area of integration for the surface force calculation

Consider a volume that straddles the boundary and has a cross-sectional area S . The force on the volume is the sum of the momentum flow across the boundaries. The incoming wave has momentum flow through S of $S p^2/\rho_1 c_1^2$. Similarly, that of the transmitted wave is $S (Tp)^2/\rho_2 c_2^2$, and the reflected wave $-S (Rp)^2/\rho_1 c_1^2$ where R and T are the usual reflection and transmission coefficients; $R = (z_2 - z_1)/(z_2 + z_1)$, and $T = 2z_2/(z_2 + z_1)$. The minus sign is because momentum flow has directionality, and the reflected wave is traveling in the opposite direction as the incident wave. The force is the sum of the incoming flow (incident) minus the outgoing flows (transmitted and reflected). Dividing by S we have:

$$F/S = p^2/\rho_1 c_1^2 - [Rp]^2/\rho_1 c_1^2 - [Tp]^2/\rho_2 c_2^2 = (1+R^2)p^2/\rho_1 c_1^2 - T^2 p^2/\rho_2 c_2^2 \quad (2.8)$$

Using typical values for water and tissue, $\rho=1e3$, $c_1=1480$, $c_2=1585$, $F/S = 2.64e-11 * p^2$. For a lesion-producing peak pressure of 7MPa, the on-axis pressure at the tissue surface 15mm away is about 0.7MPa, resulting in a surface pressure of $F/S = 13 \text{ N/m}^2$.

Another mechanism by which a force could arise at the interface is known as “acoustic streaming” (Lighthill 1978), which arises from a net fluid flow caused by acoustic absorption of the HIFU beam in the water. The streaming was observed by placing dye in the water in front of the HIFU transducer as it was operated at a peak pressure of 7MPa. Between the transducer and the focus the dye was observed to move with a velocity $< 5\text{mm/s}$. Using elementary incompressible flow theory, the force at the surface of the tissue from this flow rate can be approximated by $F/S = \rho V^2 = 2.5e-2 \text{ N/m}^2$, which is negligible compared to the result shown above for the force due to the impedance mismatch.

3

Methods and Preliminary Measurements

This chapter describes the experimental setup, methods, calibration, and measurements of system properties for the HIFU and HMI systems. The acousto-optic technique and apparatus will be described in chapter 7

3.1 Measuring displacement in tissue

Ultrasound pulse-echo signals can be used to estimate strain in tissue (Wilson et al. 1982 and Dickinson et al. 1982). This is done by recording a pulse-echo “A-line” before and after a deformation. The second A-line is divided into overlapping segments, and each segment is cross-correlated to the same segment in the first line. The point of maximum correlation is a measure of how much the tissue represented by the segment has displaced from its position in the first line. The application of this technique for the present studies was similar to that typically applied in the literature (Ophir et al. 1991). In the HMI experiments the pulse-echo data from the interrogation transducer was obtained at a prf of 1.25kHz, and digitized at 100MHz. One A-line had 4096 samples, and represented a portion of tissue ranging from the water-tissue surface to a depth of 30mm. The lines were divided into 80 segments, with 85% overlap (for smoothing).

If $a_1(x)$ is the initial A-line and $a_2(x)$ the A-line after displacement, the cross-correlation method finds the displacement $u(x)$ which maximizes the integral

$$\int_0^L a_2(x + u(x)) \cdot a_1(x) dx \quad (3.1)$$

Cross-correlation produces a value for a shift in x which yields the best match between the two lines. The shift is an integer value of samples, each representing $7.5\mu\text{m}$. To achieve finer resolution, the 3 points around the peak from the cross-correlation was fit to a parabola, yielding an accuracy of $0.1\mu\text{m}$. A gradient based, iterative optimization technique was given as an alternative method to cross-correlation (Richards et al. 2009). In contrast to cross-correlation, the gradient-based method finds $u(x)$ to minimize

$$\int_0^L \left\{ [a_2(x + u(x)) - a_1(x)]^2 + k \left(\frac{du}{dx} \right)^2 \right\} dx \quad (3.2)$$

where k is called the *regularization constant*. Rather than overlapping elements, which is not compatible with this method, smoothing is provided by adding the cost function $k \left(\frac{du}{dx} \right)^2$ for high displacement gradients typically caused by noise, and is set to provide the amount of smoothing desired. This algorithm provides a maximum likelihood estimate of the displacement field under the assumption that the noise in the signal is Gaussian. It reduces strain decorrelation that results from piecewise constant interpolation of the displacement field. It also couples neighboring displacement estimates to give a consistent estimate of the displacement.

The gradient-based routine was re-written as a C “mex file” for Matlab (see 8.1.2Appendix D , which provided faster execution times than a speckle tracking routine based on Matlab’s cross-correlation function. Figure 3.1 shows the results of the gradient routine applied to two A-lines taken before and after a static compression of an agar-graphite phantom. The line is linear, as expected, except for small curvature at the ends caused by the holding device.

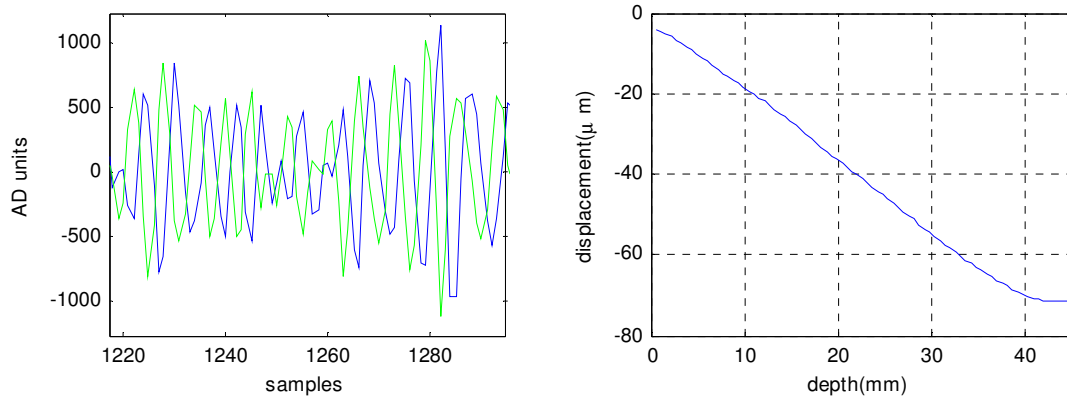


Figure 3.1 Left: a portion of two A-lines taken before and after a static compression of aprx. $67\mu\text{m}$ applied to an agar-graphite phantom molded to the shape of a 35mm film canister. Right: Displacement vs. depth from the gradient speckle-tracking routine.

3.1.1.1 Comparing the two methods: parametric studies

The two speckle-tracking routines described above were compared using an artificial known displacement applied to a custom A-line. The line (Figure 3.2(b)) comprised a random number sequence with the same spectral density as a typical measured A-line from a chicken sample (Figure 3.2(a)). To make the displaced A-line, the data was shifted by a pre-defined curve of displacement vs. depth. This was a “gradual” step function (hyperbolic tangent) with variable width from 0.1 to 5mm, and variable total step height from $0.7\mu\text{m}$ to $140\mu\text{m}$ (Figure 3.2(c)). The rms error between the applied displacement and the curve produced by the speckle-trackers was plotted on 3-d graphs with different combinations of independent variables as parameters: applied displacement step width, height, number of depth elements, and degree of smoothing (%overlap for the cross-correlation routine, regularization constant for the gradient routine). Sensitivity to random noise on each A-line was also studied. Figure 3.2(d) shows an example plot. The displacement applied was large in this case, at 15 AD-units, corresponding to $100\mu\text{m}$. The displacement was applied over 1.5mm. A different random noise sequence was added to each line, of amplitude 1% of the rms value of the A-line. This particular plot shows there is an optimal combination of number of elements and element overlap. The values for smoothing and element size were chosen for the displacements and noise

levels usually seen in the HMI data.

Based on a thorough exploration of the parameter space, the conclusion was that the routines were fairly comparable, but the gradient method in general had less error. One drawback of the gradient routine was that it was designed to give the optimum curve for any degree of correlation, so could produce misleading results if the input data was noisy and poorly correlated. As a rule, both routines were employed on the HMI data. The cross-correlation results served as a check on the smoother, more precise gradient results. Both routines could produce a separate output for degree of correlation, which was also used in determining the validity of the results.

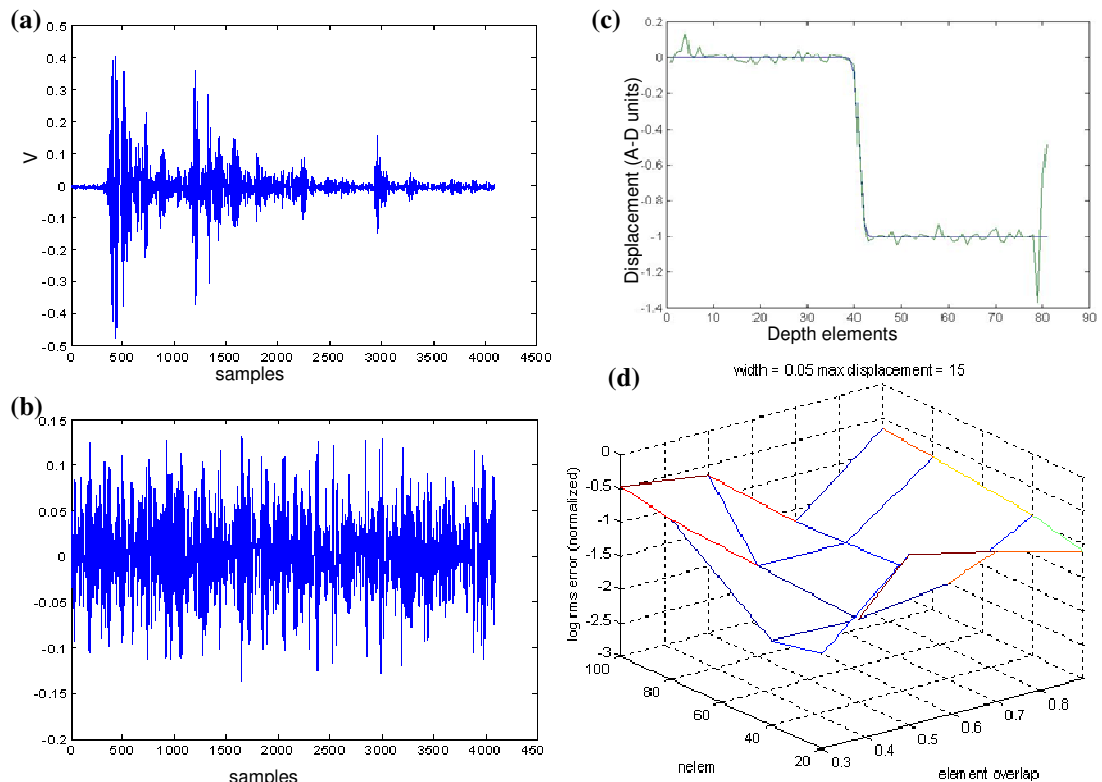


Figure 3.2 (a) Backscatter A-line from chicken. (b) test lined synthesized from spectrum of A-line above. (c) representative curve of artificially applied displacement, and response of cross-correlation speckle tracker routine. (d) error in cross-correlation speckle tracker for an applied displacement of 15 AD units applied gradually over a length 5% of total line length. 1% random noise was applied as described in text. The X and Y parameters are number of depth elements and fractional overlap between elements.

3.2 Basic methods and setup

Figure 3.3 is a basic schematic of the experimental setup used in the HMI measurements, showing the placement of the hardware and sample, and a simplified schematic of the electronics and connections. For a list of specific equipment used, see Appendix A.

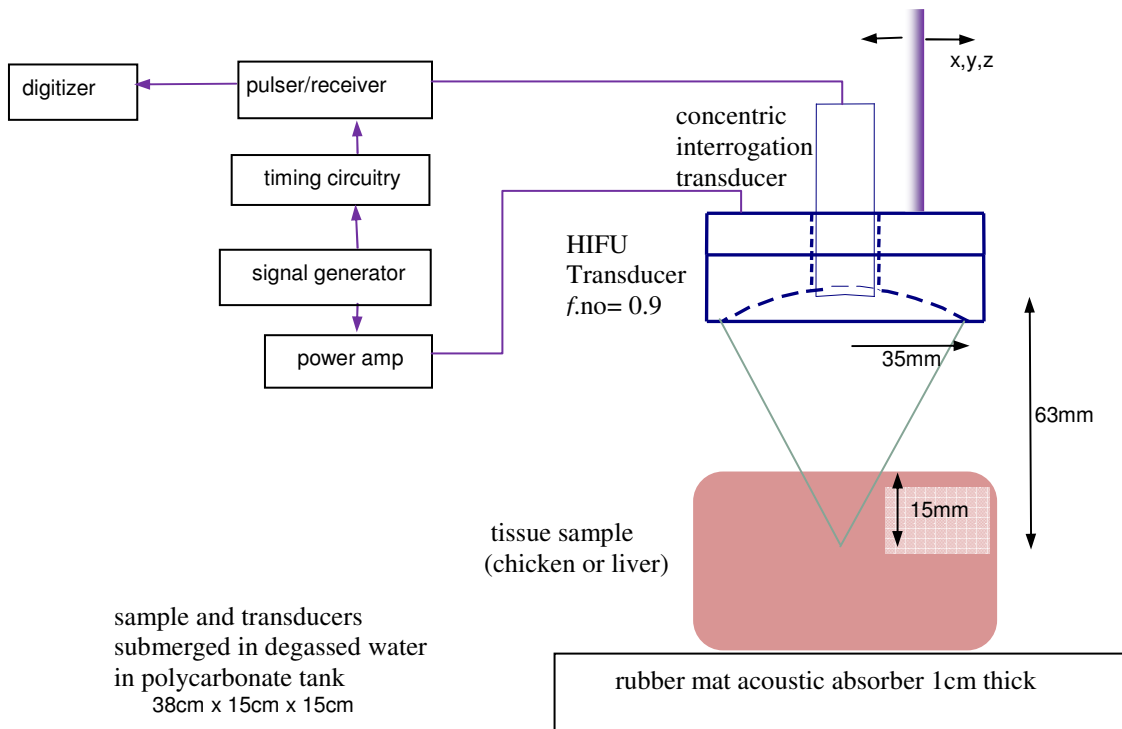


Figure 3.3 Basic schematic of experimental setup for HMI

The depth of the acoustic focus in the tissue was chosen to be 15mm – deep enough to place the lesion entirely below the surface, yet shallow enough for adequate SNR of the backscattered interrogation pulse. Oscillatory motion was induced in the tissue with 3MPa HIFU modulated with a square wave of 40Hz. One HMI measurement consisted of digitized backscatter energy from interrogation pulses fired at a PRF of 1.25kHz, over the course of four HIFU modulation cycles. During lesion formation, these measurements were interspersed with CW HIFU heating phases lasting 2 to 10 seconds each. Backscattered energy was sampled by the Gage card at a rate of

100MHz. Figure 3.4 shows a diagram of the basic timing sequence used during HMI measurements during lesion formation.

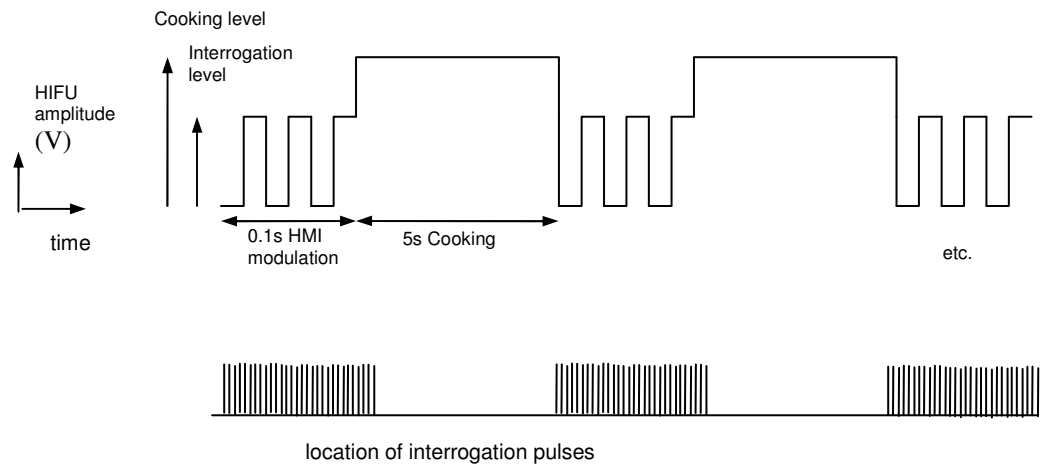


Figure 3.4 Timing diagram of the HIFU voltage and interrogation pulses.

On some data sets, additional interrogation pulses were fired during the heating phases, for the purpose of monitoring cavitation and measuring bulk (non-modulated) motion. During the 5 second heating phases, these extra pulses were fired in groups of two (riding on opposite phase of the HIFU wave, to cancel the nonlinear speed of sound effects described in 8.1.2Appendix E , at a rate of 5 groups per second.

Tissue samples for the bulk of the experiments were chicken breasts purchased at Whole Foods stores, in varieties deemed to have the least processing and elapsed time between slaughter and purchase. This was an attempt to minimize any biological decay that may have altered the tissue properties and produced gas. Some experiments were also done with bovine liver, delivered on ice within four hours of slaughter (Research87 Inc. Boston, MA). Samples were cut 3 to 5cm thick, and 4 to 10cm wide, and degassed for 30 minutes or longer in PBS solution (Cole-Parmer cat. No EW-88068-28) using an aspirating vacuum pump. The smooth outer surface of the breast was facing the

HIFU transducer. Thus, the muscle fiber direction is perpendicular to the HIFU beam. During measurements, walls were placed on the sides of the samples which applied just enough pressure to prevent movement from water currents in the tank.

3.3 Design of system for combined forcing and tracking

3.3.1 Transducer geometry and frequency

A number of factors should be considered for the selection of a transducer used for both lesion production and HMI. Among factors to be optimized for are:

1. Size of focal zone.
2. Desired depth of lesion/HMI
3. Amount of pre-focal heating that can be tolerated
4. Amount of HMI tissue amplitude desired
5. Probability of producing cavitation.

Among the factors that can be chosen to affect these outcomes are:

1. Frequency
2. F-number (=focal distance/diameter)

Higher frequency will produce more heat and force for a given pressure because acoustic absorption increases with frequency. This means lower pressures can be used, which lowers the probability of cavitation. However, the depth of penetration is reduced, also because of higher absorption. Lower f-number means a narrower focal zone. This will lower energy deposition (thus heat) in regions away from the target. A higher ratio of frequency/f-number results in greater sensitivity to tissue inhomogeneities that will spoil the phase summation at the focus. This will reduce the intensity and make the energy deposition less uniform and predictable. Finally, a less tightly focused (larger f-number) beam will produce more displacement for a given intensity, because this intensity is applied to a larger volume. However the focal spot will be larger and there will be more pre-focal heating.

To study these effects, a parametric study was done, showing the displacement amplitude as a

function of both frequency and f-number. To calculate displacement, a Greens function solution in cylindrical coordinates for a point force in an infinite solid is the taken from Nightengale et al. (2001), as refined from the derivation in Timoshenko (1987):

$$disp_z = \frac{F_{point} (1 + \nu) [4z^2(-1 + \nu) + r^2(-3 + 4\nu)]}{8E\pi(r^2 + z^2)^{3/2}(-1 + \nu)} \quad (3.3)$$

where r and z are the distances from the point where the force is applied to the point in space where the displacement value is calculated. The acoustic field was derived using O'Neil's solution for a focused piston radiator. F-number was adjusted by varying the diameter, and leaving the focal distance constant at 63mm (the size of the H102 transducer). From the field calculation the power half-widths of the beam were found in the axial dimension and in the focal plane. The forced region was then approximated as an ellipsoid with these dimensions, with a constant force per volume equal to $2\alpha I_{peak}/c$. The ellipsoid was then divided into 0.05mm voxels, and the displacement at the focus was the sum of the Green's function solutions for each voxel. It will be shown in chapter 5 that this method produces results that are in good agreement with FEM results. Figure 3.5 shows the results for peak intensity set to 1600 W/cm² (which is the approximate intensity in water of the H102 field at peak pressure=7MPa).

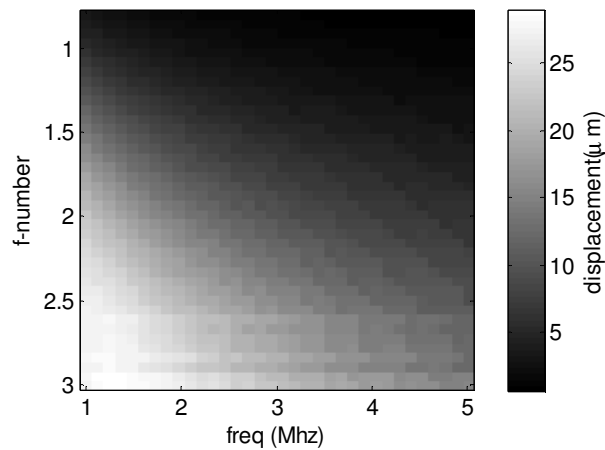


Figure 3.5 Steady state tissue displacement calculated from Green's function solution for a sum of point sources in an infinite solid, vs. transducer frequency and f-number. Peak intensity held constant at 1600 W/cm²

The f-number of the H102 operating at its fundamental frequency of 1.1MHz is 0.95. The plot shows that raising the f-number would produce higher displacement. However, the region of highest displacement (lower left corner of plot) will probably produce much pre-focal heating and large lesions, due to the wider focus. Also note that the peak intensity is reached 30% closer to the transducer here (i.e. the numerator for the f-number is the transducer radius of curvature, rather than distance to peak pressure).

A custom impedance matching box was obtained in order to operate the H102 at its third harmonic frequency. The reason for this was that, theoretically, lower pressures would be required for forcing and heating due to the higher acoustic absorption at 3.3MHz, and this would decrease likelihood of cavitation. However, as shown on the plot, this would result in little or no added displacement. A device was made to block the radiation from the outer portion of the transducer, to increase the f-number, but this was abandoned due to lack of initial success. With or without this block, the waveforms at 3.3MHz exhibited much more nonlinearity than those at 1.1MHz, and it was far more difficult to produce lesions and produce measureable displacement.

3.3.1.1 Transducer mount

Since the HIFU and interrogation fields were less than 1mm wide at the foci, it was necessary to keep them closely and consistently aligned. The cable and connector of the interrogation transducer extending from the H102 was susceptible to bumping and twisting. A gimbal mount (Figure 3.6) was made for the purpose of alignment and structural stability. A 5mm wide soft plastic (LDPE) strip fit snugly between the steel outer shell of the interrogation transducer and the steel inner sheath of the H102. At the end of the gimbal, 4 screws held the transducer alignment in place and provided fine adjustment. The alignment was checked periodically using a ball bearing, and the two foci were usually found to be within 0.1mm.

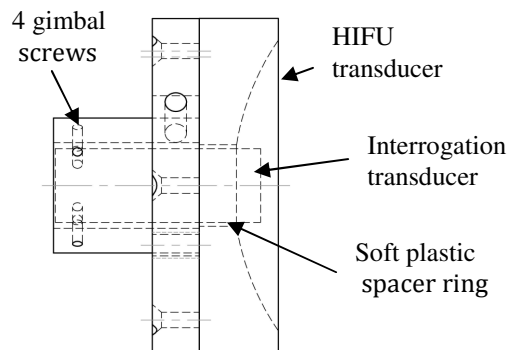


Figure 3.6 H02 HIFU transducer plus polycarbonate mount with two-axis gimbal for positioning interrogation transducer.

3.3.2 Computer and hardware connections and synchronization

The HMI tissue displacement amplitude was typically under $5\mu\text{m}$, which resulted in time-shifts of the backscattered energy of under 10ns. Hence, timing was of critical concern. The Gage digitizer card (and any digitizer) begins digitizing each sample according to its internal clock. Since the tissue motion was derived from cross-correlating successive A-lines of backscattered energy, the time reference point was the start of each interrogation pulse. Thus, the pulser/receiver and the digitizer

needed to be synchronized. The Gage card had a trigger output which was synchronized with the same internal clock that initiated the digitizing. This was connected to the analog trigger input of the pulser and provided synchronization between the interrogation pulses and the digitization. The timing source for the interrogation pulse PRF was the Agilent 33120a, which was connected to the trigger input of the Gage card after a custom delay circuit which controlled when the pulse was fired in each HIFU cycle, for reasons which will be described in the next section. The 1.1MHz HIFU signal was provided by the Agilent 33250. The HMI modulation was made by the HP8116 (labeled “interleaf source”), which made the modulation square wave shown in Figure 3.4 and was connected to the gate of the HIFU source (only the timing of this waveform was used in the generation of the HIFU wave – the amplitude was controlled by GPIB commands from software). Finally, the output of the pulser/receiver was connected to the Gage digitizer after passing through a high-pass filter (5MHz, 60 dB/octave, F5081-5P0-B, Allen Avionics, Mineola, NY), to remove HIFU energy from the backscattered interrogation pulse.

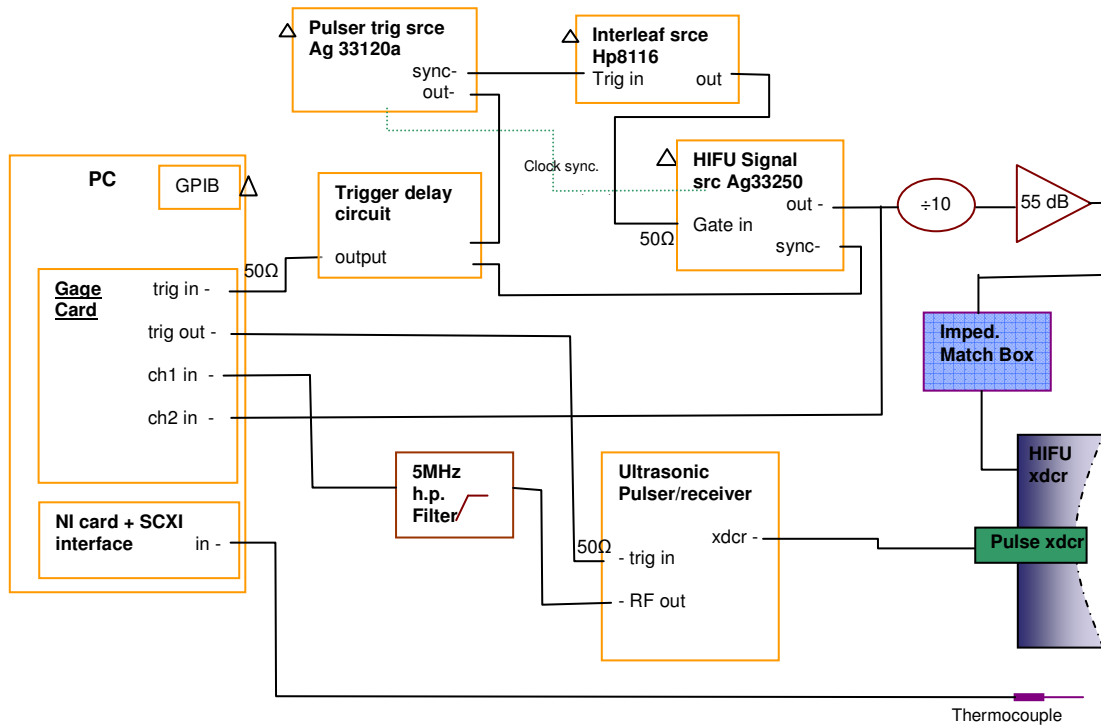


Figure 3.7 Diagram of electrical connections.

3.3.2.1 Software

The entire lesion creation/HMI measurement was controlled by a Matlab (Mathworks, Inc., Natick, MA) routine. The only setting that was not controlled by software was the gain on the pulser/receiver.

3.3.3 Apparent displacement from nonlinear acoustic interactions

Typical HIFU pressure levels can cause a nonlinear time-shift in the interrogation pulse. During each interrogation measurement, the HIFU level was set to 3MPa peak pressure, and was modulated by 4 cycles of a square wave of 40Hz. During the “on” times, the interrogation pulse and HIFU beam propagate together. Figure 3.8 depicts the pressure waveform on axis at the focus, for the case in which the pulse travels on a crest of the HIFU wave (left), and for the case in which the pulse travels in a trough of the HIFU wave (left).

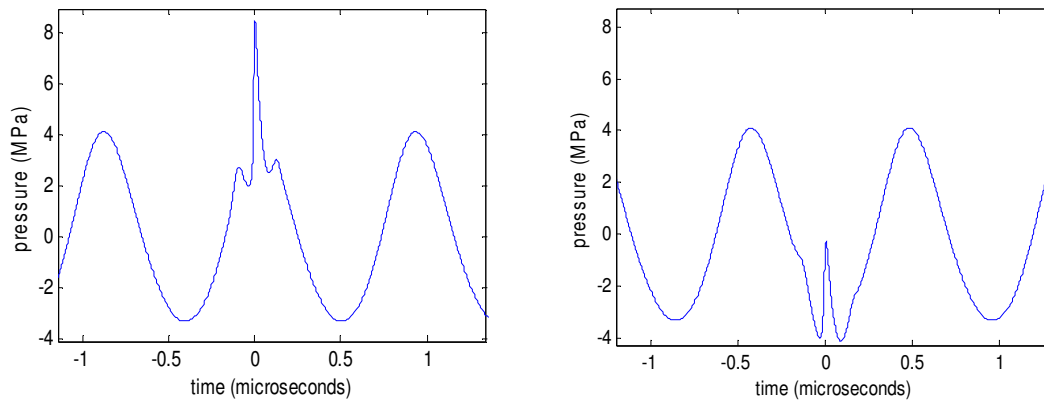


Figure 3.8 Depiction of coincident interrogation pulse and HIFU field, for the case where the pulse propagates (Left) on a HIFU crest, or (Right) on a HIFU trough.

Due to nonlinearity in the acoustic wave equation, the speed of sound is a function of the pressure $c = c_0 + \beta p / \rho_0 c_0$ where p is the local acoustic pressure, c_0 the small-signal (linear) sound-speed, ρ_0 the density and β the coefficient of nonlinearity (~ 3.5 for water, 5 for tissue). If the HIFU wave was planar, the phase relationship between the pulse and the HIFU wave would remain constant. If the pulse were on a 1 MPa crest, it would arrive 65ns earlier at the focal distance (63mm) than a pulse without HIFU. This would translate into an apparent tissue displacement of 49 μ m. The HIFU wave is not planar, and differences in the diffraction between the HIFU and pulse fields results in their phase relationship changing during propagation. In practice, a 6MPa HIFU beam causes apparent tissue motion of about 7 μ m, which is about the same magnitude as the actual observed tissue displacement. A paper was written on this phenomenon (Draudt and Cleveland, 2011), presented as 8.1.2 Appendix E, in which a new technique was shown to mitigate the error. This technique relies on the fact that two different pulses that occur on opposite phases of the HIFU wave will have opposite time-shifts. If data is taken for two opposite phase relationships, the resulting timeshifts (and hence displacements) can be averaged together, thus cancelling out the nonlinear effect.

To this end, a circuit was designed to delay the time that every other pulse was fired with respect to the phase of the HIFU signal. The delay time was exactly one half of the HIFU period. As shown in Figure 3.7, the trigger delay circuit is armed by the pulse from the trigger source generator, and then

emits a trigger when the HIFU source reaches a certain phase. This also triggers an internal flip-flop which changes the phase for the next pulse. The circuit is described and drawn in 8.1.2Appendix B. A portion of the HIFU signal was digitized along with the backscattered pulse, and this provided the information that the analysis software needed to discern which of the two phases each A-line corresponded to. With that information, the software can separate all the A-lines corresponding to each phase, calculate the displacement, and average the results to obtain a result which is un-plagued by the nonlinear timeshift.

3.4 Acoustic fields: measurements and modeling

3.4.1 Calibration

The HIFU transducer was calibrated using a membrane hydrophone (0.2mm active diameter. Precision Acoustics, Dorchester, UK SN1502-031) which used a PVDF film to measure pressure. Also used was an optical fiber hydrophone, which works on the acousto-optic principle. The acoustic pressure changes the optical index of the water. Light in the fiber is reflected back from the fiber tip, the reflection coefficient being a function of the difference in optical index between the fiber and the medium. Corrections were made for diffraction, since for high frequency sound, the fiber presents a reflective wall, causing pressure doubling (software for this correction was provided by Robin Cleveland). Figure 3.9 shows calibration curves of the focal peak acoustic pressure (both positive and negative) vs peak voltage at transducer. The fiber measurements were unstable and two different runs of fiber data are shown. A parabolic fit was applied to the membrane data and served as the standard calibration curve for setting desired pressures in the HMI experiments.

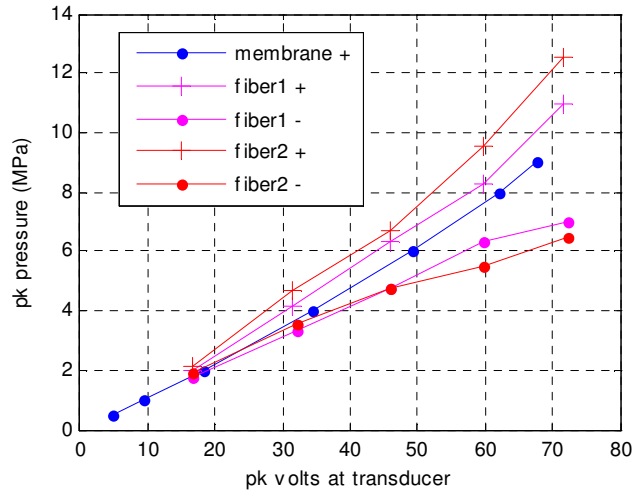


Figure 3.9 Calibration of h102 HIFU transducer with membrane and fiber hydrophones. “+” indicates positive peak pressure, “-” negative.

When specifying acoustic levels for the remainder of this thesis, it is the peak pressure in water that will be used, since that is the measurement that is traceable to standards via our calibrated hydrophone. The focal intensity is not measured in tissue during HMI experiments, and so must be modeled from the peak pressure in water using a series of theoretical considerations and calculations that will be described in following sections.

3.4.2 Field models and measurements

A model for the spatial distribution of the HIFU pressure was needed to predict the temperature due to heating and the displacement due to acoustic forcing. A numerical method known as the angular spectrum technique was used. It is a method to calculate the field in a plane, given the known complex field in a parallel plane at an earlier point in the wave propagation. Used initially in the field of Fourier optics, it involves expanding a complex wave field into a summation of an infinite number of plane waves. Assuming time harmonic waves, the plane wave solutions of the Helmholtz equation $(\nabla^2 + k^2)p = 0$ may be expressed as $p = p_0 \exp(i\omega t - i\vec{k}\vec{r})$. The wave number and

distance vectors may be broken down into components: $\vec{k} = \sqrt{k_x^2 + k_y^2 + k_z^2} = \frac{\omega}{c} + i\alpha$,

$\bar{r} = \sqrt{r_x^2 + r_y^2 + r_z^2}$, where α is the acoustic attenuation. Modeling the diffraction of a continuous

wave of single frequency involves the following steps:

1. Find the complex pressure field of the source on a planar grid of points x, y .

$$p(x, y, t) = p_s(x, y) \exp(i\omega t) \quad (3.4)$$

If only the velocity at the source points is known, convert to pressure using Euler's equation.

2. Take the 2D- Fourier transform of the pressure field, which will decompose the field into plane waves of unique propagation vectors.

$$P(k_x, k_y) = \mathfrak{F}(p_s(x, y)) \quad (3.5)$$

3. Apply a propagation term to each point in the FFT to account for the phase change that each plane wave will undergo on its path to the prediction plane at $z=d$.

$$P(k_x, k_y, d) = P(k_x, k_y) H(k_x, k_y) \quad (3.6)$$

The propagation term is sometimes called the "spatial transfer function" (Saleh and Teich 2006) and for free space is

$$H(k_x, k_y) = \exp(-ik_z d) \quad (3.7)$$

4. Take the inverse Fourier transform.

$$p_s(x, y) = \mathfrak{F}^{-1}(P(k_x, k_y, d)) \quad (3.8)$$

This model uses Fourier methods, so the calculation region is treated as if it repeats in the x and y dimensions to infinity. This causes image sources to appear in the $z=0$ plane at multiples of twice the maximum x or y extents of the calculation region. Thus, to minimize the influence of these image sources, the maximum x and y extents should be chosen to be large enough.

An appropriate ground truth model against which to compare the angular spectrum results is a solution of the Rayleigh integral (time harmonic):

$$p(\vec{r}) = \frac{ik\rho cu}{2\pi} \int_s \frac{\exp(-ikr)}{r} dS \quad (3.9)$$

where k is the wave number, c acoustic velocity, ρ density, u source surface velocity (assumed constant here), r the distance from point on the source to field point, and S the area of the source. For a focused transducer, if the depth of the transducer “bowl” and the wavelength are both small compared to the transducer radius, analytical expressions can be found for the pressure on axis and in the focal plane (O’Neil 1949). One could also divide the region of interest into a grid and numerically evaluate this expression for the entire field, which would be a faster and more accurate alternative to the angular spectrum method. However, it cannot account for a tissue interface between two regions of different impedance and attenuation, which is required for this work, and which is possible with the angular spectrum method. Since the field is approximately linear at lower pressures, the hole in the middle of the h102 transducer is accounted for by subtracting the solution for a transducer of the same size as the hole.

For the case in which the calculation grid extends to 5 transducer radii, and grid spacing 0.16mm, It was found that the mean square error on axis(normalized to peak) between the angular spectrum and O’Neil’s solution was well under 1%. Figure 3.10 shows the comparison on axis and also in the focal plane for the two models. Also are the 1.1MHz Fourier amplitudes of measured pressure fields from the h102. The peak pressure at the focus was 1.23MPa.

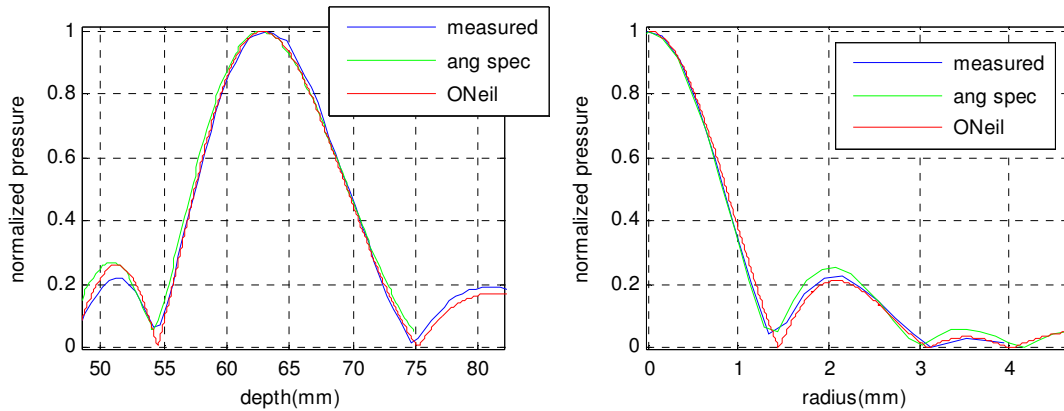


Figure 3.10 Comparison of measured pressure for h102 HIFU transducer to results from the angular spectrum method and O'Neil's solution to the Rayleigh integral. Peak pressure was 1.23MPa.

In order to best match the measurements, the model radius was changed from 35 to 33.1mm. It is reasonable to expect that this is due to the curved transducer surfaced not moving entirely in unison. Discrepancies between the angular spectrum and O'Neil results are seen in the side lobes in the focal plane, and in the first lobe on axis in front of the main lobe. Figure 3.11 shows additional measurements in the focal plane at finer resolution. The fact that the pressure drops to under 1% of the peak attests to the high sphericity of this transducer.

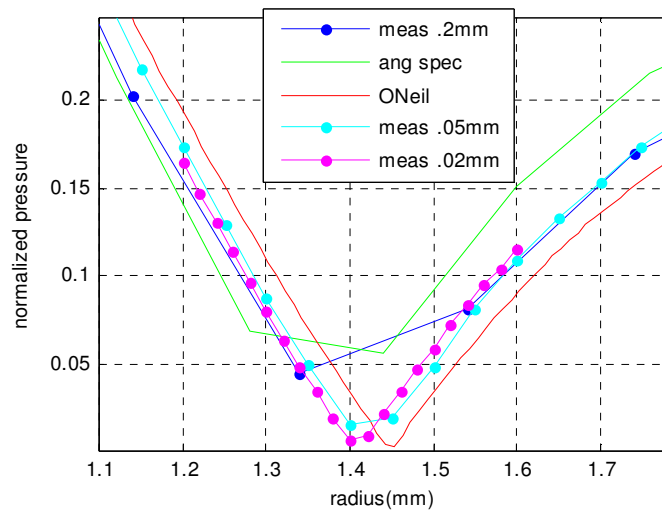


Figure 3.11 h102 focal plane measurements taken in first null, with fine spatial grid.

Finally, Figure 3.12 shows contour plots of the h102 field and the pulser field, as calculated by the angular spectrum method. The beam width of the interrogation beam is seen to be less than the HIFU beam. Thus the A-line data from which displacement will be calculated will reveal motion only along the central portion of the HIFU beam.

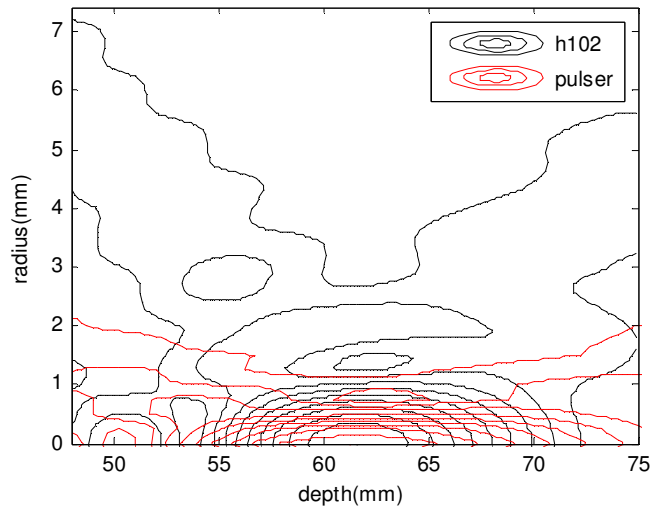


Figure 3.12 Contour plot of acoustic fields of h102 and interrogation transducers, as modeled by the angular spectrum method. Each contour represents 10% of peak pressure.

3.4.3 Fields in media

In order to model the field in tissue, the angular spectrum routine was modified to take into account the difference in sound speed and attenuation between the two media, and the impedance mis-match at the interface between them. The propagation in k-space was stopped at the interface, and converted back into pressure. The transmission coefficient at the boundary was then applied, and the new tissue properties put into effect. The field was then propagated in k-space onto the points of interest inside the tissue. Note that the attenuation of the material is added as the imaginary part of the propagation vector \mathbf{k} .

Figure 3.13 shows the field near the focus for a few tissue parameters. The pressure peak lowers 5% with typical tissue attenuation of 5Np/m/MHz , and at the same time is increased and moved forward due to the increased velocity.

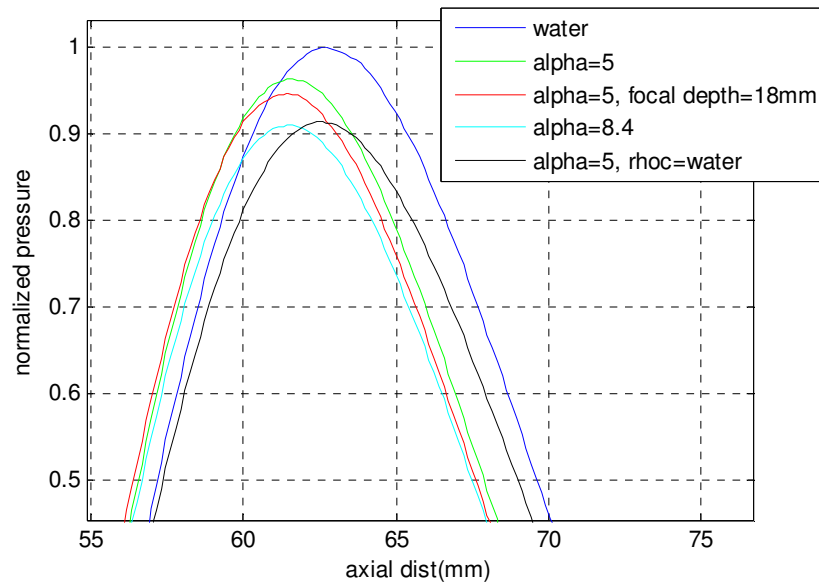


Figure 3.13 Axial pressure for 2-layer angular spectrum model with various parameters.

Inhomogeneities in tissue velocity and attenuation can result in imperfect focusing and therefore less pressure. To investigate this, samples of chicken breast 14 to 18mm thick were placed over the membrane hydrophone, which was placed at the focal point in water (63mm). Figure 3.14 shows the result of scanning the transducer laterally over the sample. The bold blue curve is data without tissue, and the bold orange curve is from the angular spectrum model for a thickness of 18mm and tissue properties $C=1050\text{m/s}$, $\alpha=5\text{Np/m/MHz}$, normalized to the peak pressure in water at the focus. Two perpendicular scans were done on each sample. Chick1, 2, 3 were Whole Foods organic chicken, 18.2, 18.2, 17.8mm thick. Chick 4, 5 was from the Market Basket store(on sale), 16.4mm. Chick1 was later sliced to 14.1mm for the last measurement. The peak pressure was 1.2MPa. This suggests that tissue attenuation is variable, and more than 5Np/m/MHz .

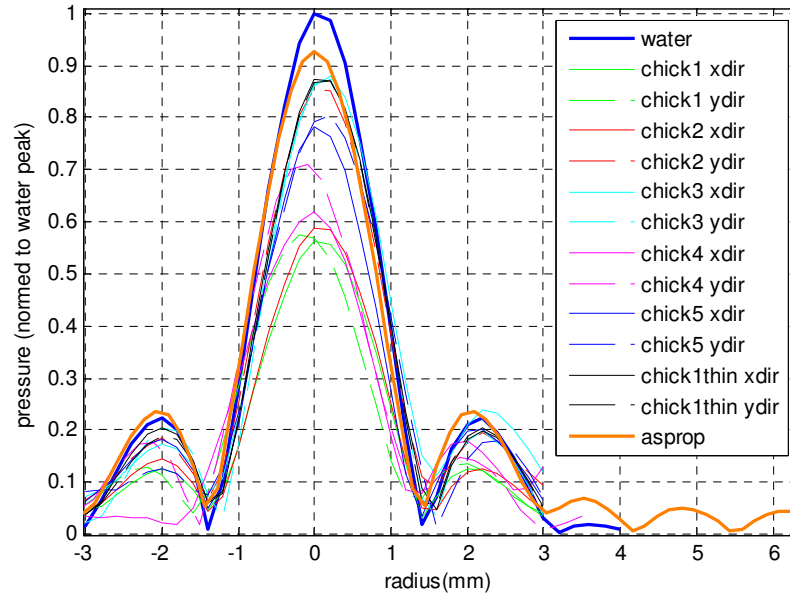


Figure 3.14 Measured fields through chicken tissue at depth=63mm(the focus in water). Thick lines are measured pressure without tissue, and predicted curve from angular spectrum model ("asprop"). All samples are 18mm thick, except for "thin", which is 14mm. The asprop curve is for 18mm thick sample.

3.4.3.1 Intensity

The intensity of an acoustic field of pressure P and particle velocity U is given by

$$I = \frac{1}{2} \text{Re}(PU^*)$$

$$U = \frac{-\nabla P}{i\omega\rho}$$
(3.10)

O'Neil (1949) further refined this expression to $I = \frac{|P|^2}{2\rho c} \nabla(\text{angle}(P)/k)$, noting that this reduces

to $I = \frac{|P|^2}{2\rho c}$ for planar or perfectly spherical waves. On-axis the gradient points in the axial

direction, which allowed him to formulate an analytical expression for intensity, as well as pressure.

The field from the h102 HIFU transducer is neither planar nor spherical, so the intensity was

calculated from a numerical solution of (3.10). To achieve less than 0.5% error from the gradient

operation in Matlab, the grid spacing used to obtain the angular spectrum solution (0.16mm) needed to be interpolated to a grid that was 5 times finer. Figure 3.15 shows the on-axis intensity as calculated from O’Neil’s analytical expression, along with the above numerical gradient method applied to the angular spectrum field. Also shown is the application of $|P|^2/2\rho c$ to the angular spectrum field. At the peak, the numerical gradient method is 6% higher than the O’Neil solution, and 8% lower than the plane wave solution. The discrepancy between the O’Neil solution and the gradient method is a mystery at this point, since the O’Neil and angular spectrum solutions on-axis agree (Figure 3.10), and the same equation (3.10) is used in each to calculate intensity. However, it is superior to the $|P|^2/2\rho c$ estimate, which is used widely in the literature. [Post-publishing note: the above discrepancy was discovered to be a result of a typo in the program that implemented the O’Neil solution. The O’Neil curve is now within 0.5% of the asprop curve.]

If the diameter of the transducer were halved (f-number doubled), the field at the focus would more resemble plane waves, and the discrepancy between O’Neil and $|P|^2/2\rho c$ falls from 16% to 1.5%. The gradient operation on the scalar pressure field yields the vector components of \mathbf{I} , which are later required for the modeling of the displacement field.

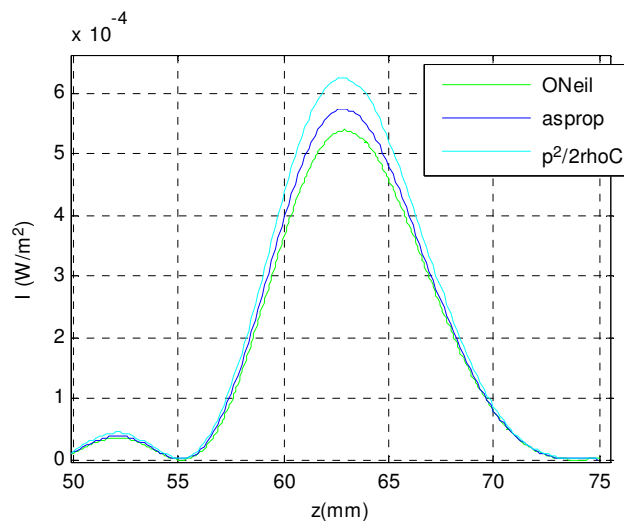


Figure 3.15 On-axis intensity for the h102 transducer without central hole, for a source pressure of 1Pa. Plotted are O’Neil’s analytical expression, the numerical gradient method applied to the angular spectrum field(“asprop”), and the application of $|P|^2/2\rho c$ to the angular spectrum field.

3.4.3.2 Nonlinearity

In the HIFU heating and forcing regimes used in these experiments, acoustic nonlinearity results in waveforms that are significantly non-monochromatic. Since acoustic absorption varies roughly linearly with frequency, the energy in higher harmonics will translate into heat and force more readily than that of the fundamental. Of course the harmonics are attenuated more and will thus propagate less deeply into the tissue, which means that the nonlinear field will have less energy than the linear field as calculated by the angular spectrum model, assuming the same peak pressure in each. A full nonlinear treatment of the field is required in order to model the heating and forcing accurately, however a simplified approach will be used here.

Sarvazyen et al. (1998) and Rudenko et al. (1996) derived expressions for the on-axis radiation force from a focused acoustic beam using the KZK equation. For a given transducer source velocity, a value of 0.3 for the nonlinear coefficient N was found to increase the peak radiation force 12%. $N = \text{focal dist}/\text{shock formation distance}$. The full expression is $N = 63\text{mm} \cdot \beta p_0 \omega / \rho c^3$ where β is the nonlinear parameter for tissue, which equals 4.7 for muscle (Bamber et al. 1998), and p_0 is the pressure at the source. Since the peak pressure used for forcing in the HMI experiments is 3MPa, N is found to be 0.035. This is 9 times smaller than the value in Sarvazyen et al. (1998) which produced a 12% change. In addition, the ratio of focal distance to Rayleigh distance is 5 times less for the h102 which should result in less shock development at the focus, and therefore even less effect on radiation force.

A similar argument can be made for ignoring the nonlinear effects on heating. Also starting with the KZK equation, Curra et al. (2000) derived expressions for on-axis heat rates for values of N . They found a 50% increase for $N=0.73$, but presented no data for smaller N . As with Sarvazyen et al. (1998), the transducer considered had a ratio of focal distance to Rayleigh distance that was much longer than for the h102, so their nonlinear effects will be greater. In the present study, the value of N for HIFU heating pressure of 6MPa equals 0.07. Nonlinearity will be treated by modifying the intensity, according to the method in the next section.

3.4.3.2.1 Numerical treatment of nonlinearity

The angular spectrum method was used to model all acoustic intensity fields in this study, unless otherwise noted. This assumes a monochromatic linear field. Figure 3.16 shows a portion of an actual field measured with the fiber-optic hydrophone placed at the focus in water. The peak pressure was set to 6MPa using the calibration curve in Figure 3.9. It is clear that this is nonlinear, and that the energy in the waveform is less than that of a sine wave of the same amplitude. To arrive at a more accurate value for the nonlinear intensity, the sine wave intensity was multiplied by a correction factor “*Ifac*”, which can be obtained from a measured nonlinear waveform, as the ratio of the mean square power to that of a sine wave of the same peak pressure. One may also account for the higher contribution to heating and forcing caused by the higher acoustic absorption at the higher harmonics. The sine intensity will be approximated as $\langle p^2 \rangle / \rho c = p_0^2 / 2\rho c$, and the frequency dependence of absorption for muscle tissue will be taken as approximately linear (Bamber et al. 1998). To obtain $Ifac = I\alpha / I\alpha(\text{linear})$, we will use Parsival’s theorem: average power = area

under power spectral density(psd), and $\text{psd} = \frac{|X|^2}{f_s N}$ where $|X| = \text{abs}(\text{fft}(x))$ and f_s is sample

frequency. Thus $\frac{\sum x^2}{N} = \frac{\sum |X|^2 \Delta f}{f_s N} = \frac{\sum |X|^2}{N^2}$ using $\Delta f = \frac{f_s}{N}$. We have, $Ifac =$

$I\alpha / I\alpha(\text{linear}) =$

$$Ifac = \frac{\left(\frac{1}{\rho c}\right) \left(\frac{\sum p^2}{N}\right) * \alpha_{IR}(f)}{\frac{p_0^2}{2\rho c} f_0 \alpha_0} = \frac{\left(\frac{1}{\rho c}\right) \left(\frac{\sum |P|^2 \alpha(f)}{N^2}\right)}{\frac{p_0^2}{2\rho c} f_0 \alpha_0} = \frac{\left(\frac{2}{N^2}\right) \sum |P|^2 f}{p_0^2 f_0} \quad (3.11)$$

Where $P = \text{fft}(p)$, p is the measured pressure waveform, $f_0=1.1\text{MHz}$, and $\alpha(f)=\alpha_0 f$ where f is in MHz and α is in Np/m/MHz. $\alpha_{IR}(f)$ above left is actually the impulse response of $\alpha(f)$.

Figure 3.16 (Right) shows the results of this calculation for various measured waveforms. The fiber-optic hydrophone was placed at the focus in water and the peak pressure (burst mode) was varied from 2 to 12MPa. A 15mm thick chicken tissue sample was also placed in front of the fiber. Finally, eq.(3.11) was applied to waveforms calculated by a numerical solution to the KZK equation (from calculations carried out for the results in 8.1.2Appendix E). The lower pressure points taken with the fiber deviate significantly from the trend, possibly from the poor SNR and/or drift of this instrument at these levels. A polynomial curve was fit to these data, as a function of peak pressure, and used as a correction factor for angular spectrum acoustic field data, for use with models of the thermal and displacement fields during HIFU/HMI. It is interesting to note that the inclusion of the effect of higher harmonics on attenuation resulted in a 3.4% increase in I_{fac} , at 6MPa peak pressure and $\alpha=f_0 * 5\text{Np/m/MHz}$.

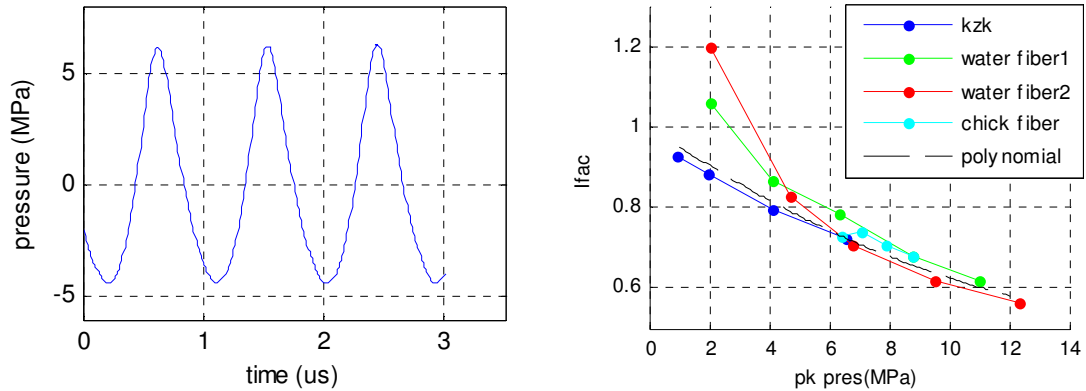


Figure 3.16 Left: pressure waveform at focus, taken by fiber-optic hydrophone. Right: plots of “ I_{fac} ” for various measured waveforms and waveforms calculated by the KZK equation, along with the polynomial function that will be used to yield $I_{fac}(f)$.

Theoretically this analysis needs to be done for every point in the field, and not just at the focus, since shocks increase with propagation distance. To investigate the necessity of this, waveforms at 6MPa peak pressure were obtained from the full KZK simulation at $z = \text{focus}-4\text{mm}$, and $z = \text{focus}+6\text{mm}$. It was found that the values for I_{fac} were close to the calculated polynomial function above at the respective peak pressures, suggesting that the polynomial correction factor could be

applied throughout the entire field, keeping in mind the fact that the correction becomes negligible at positions away from the focus, because the pressure is small.

3.4.4 Conclusion

An angular spectrum model was developed to calculate the HIFU and interrogation acoustic fields. There was good agreement between model and measurement in water at 1.23MPa. The model was modified to calculate the field in tissue, which included the effects of the water-tissue interface. It must be kept in mind that measured fields inside chicken tissue showed considerable sample variability. Experimental results were reported in terms of peak pressure in water, so in order to obtain accurate values for the intensity field in tissue for use in the Parker thermal model, this number was multiplied by a factor derived from comparing the angular spectrum outputs for the HIFU field in water and in tissue. It was next multiplied by a factor accounting for the discrepancy between the $p_0^2/2\rho C$ estimate for intensity and the more accurate expression (3.10), and finally with a pressure-dependant nonlinear correction. The nonlinear correction factor was also used for the FEM models.

3.5 Temperature measurements and comparison with models

3.5.1 Thermocouple measurements showing viscous heating

Thermocouples were inserted into tissue or phantoms so that the wire was either parallel or perpendicular to the HIFU beam. To align the beam to the thermocouple tip, a low amplitude HIFU signal was modulated with a square wave of 1.4Hz. The resulting temperature “saw tooth” wave was monitored as a strip-chart, and could be maximized by steering the beam.

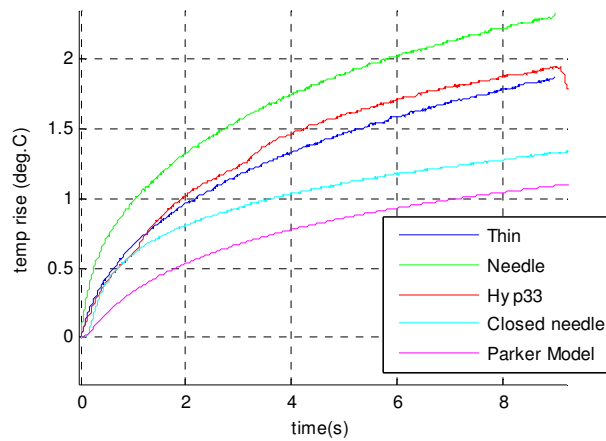


Figure 3.17 Data from four thermocouple types, placed at focus of 0.74MPa HIFU beam. Magenta curve=Parker model prediction.

In this data the open needle has the highest artifact, and the closed needle the lowest. However other insertions produced a range of temperature responses, so it is difficult to conclude from this data which type has the lowest probable artifact.

Figure 3.18 shows a magnified image of the closed and open needles, and wire type. The needles were new and un-used, and had the same stainless steel jacket. The jacket of the closed needle completely covers the wires and junction weld. Finally, Table 3-1 lists the characteristics of the thermocouples. The closed needle type was used for all the subsequent data in this thesis.

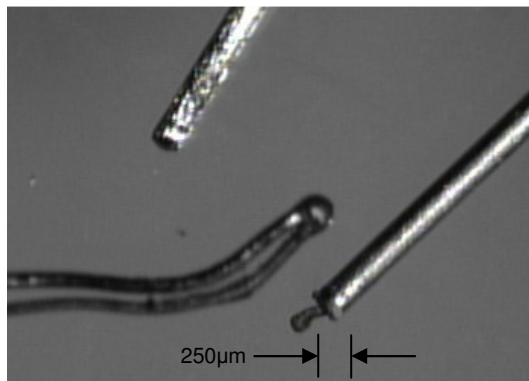


Figure 3.18 Photo of thermocouples used in the lab. Left to right: closed needle, wire, exposed needle.

Name	Thickness. inches (μm)	Response time (s)	Description	Type
Wire	.012 (305)	.22	Rubber insulated, bare at end. 5TC-TT-E-36-36	E
Needle	.010 (254)	.20	Bendable solid wire EMTSS-101E-6	E
Thin	.0005 (12.5)	<.002	Thinner than human hair CHCO-0005	E
Hypo33	.008 (203)	.16	Hard polished hypodermic syringe Hypo-33-1-T-G-60-SMPW-M	T
Hypo30	.012 (305)	.22	Hard polished hypodermic syringe Hypo-30-1/2-E-G-60-SMPW-M	E
Closed needle	0.010"(245)	0.3	Similar to "Needle", but stainless sheath also encloses junction. EMTSS-010(G)-6	E

Table 3-1 Properties of thermocouples used in study. All were obtained from Omega Inc., Stamford, CT. Response times provided by Omega.

3.5.2 Modeling thermocouple mass

One of the only ways to obtain an accurate value for the acoustic absorption of tissue requires measuring the temperature during acoustic heating, and one of the only ways to obtain an accurate temperature measurement is with a thermocouple. As will be seen, the response time of the thermocouple due to its thermal mass cannot be neglected when trying to compensate for viscous heating and obtaining absorption. Figure 3.19 shows the temperature output vs. time for a thermocouple ("Closed needle") suddenly plunged into ice water, showing a response time of about 0.2 sec.

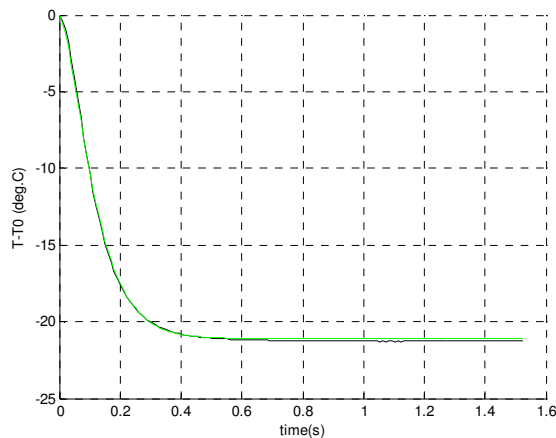


Figure 3.19 Temperature vs. time during sudden plunge of thermocouple into ice water. Black=measurement, green=lumped element model.

Incropera (1990) modeled the thermal mass of a thermocouple junction weld as a low-pass filter. However Figure 3.19 shows that there is a delay in the initial response which will need to be addressed, since the acoustic absorption is most readily manifest in the initial slope of the temperature curve. The particular thermocouple used in this work had a stainless steel jacket entirely enclosing the wires and junction, and it is the thermal mass of this jacket that results in the initial curve seen in the plot. Thus, an additional lo-pass filter as added to the first, as shown in Figure 3.20

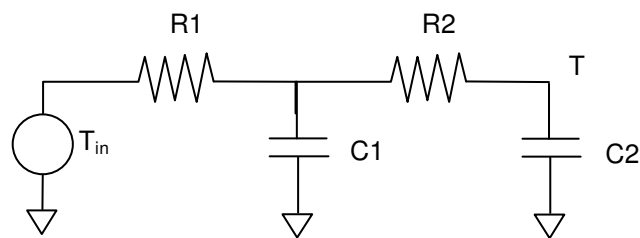


Figure 3.20 Lumped-element model for thermal mass of thermocouple. T_{in} is outside temperature, T is measured temperature, $R1$ is the thermal conduction resistance between the tissue and thermocouple, $C1$ is the thermal mass of the sheath, $R2$ is the resistance between the sheath and the junction weld, and $C2$ is the mass of the weld.

For the simple one-stage RC model, the temperature measured by the thermocouple is given by $T = T_{tis}(1 - e^{-t/\tau})$ where $\tau = RC$ and T_{tis} is the temperature in the tissue around the thermocouple.

This equation can be thought of as a response to a step input as T_{tis} is turned on at time=0. Thus the impulse response can be found by differentiating: $h(t)=\exp(-t/\tau)/\tau$. However, to find the impulse response of both filters, we take the inverse LaPlace transform of the transfer function H , which is

$$H = \frac{1}{1 + sr_2c_2 + sr_1c_2(1 + sr_2c_1 + c_1/c_2)}$$

where s is the complex frequency.

The Matlab symbolic toolbox is used to find the impulse response (using the function called `ilaplace.m`), which is large. The impulse response is then easily added to the Parker model routine, which already uses convolution with an impulse response to get temperature, to yield the predicted thermocouple response to heating from a Gaussian beam. To find the parameters r_1, c_1, r_2, c_2 , the

unconstrained nonlinear optimization method of Matlab's *fminsearch* routine is used to match the ice water curve in Figure 3.19 (the fit is also shown in the figure).

3.5.3 Modeling artifact

Viscous heating (aka thermocouple artifact) plagued every thermocouple measurement in chicken, even when placed at presumed nulls in the field. Figure 3.21 (right) shows the temperature curves for thermocouples placed at the first null at $r=1.5\text{mm}$ and at the first side-lobe at $r=3\text{mm}$. Viscous heating appears during the exposure as an elevated region of short attack and decay time. An effort was made to separate out the artifact using a method close to those of Clarke and Ter Haar (1997) and Yang (2003), who included it as an extra heat source in the heat equation, with arbitrary strength but proportional to the acoustic intensity. The Parker model was modified with an extra Gaussian source in addition to the Gaussian source of the main field, but of smaller radius and length (the Parker model can accommodate finite length sources). This could even be adapted for thermocouple placements off axis. Optimization (via *fminsearch*) was then applied to match a number of parameters to measured curves. These parameters included some or all of the following: absorption, conductivity, artifact radius, length, and strength. Figure 3.21 (left) shows the results of one such calculation, with plots of the separated viscous heat and heating from the field without thermocouple ("bulk").

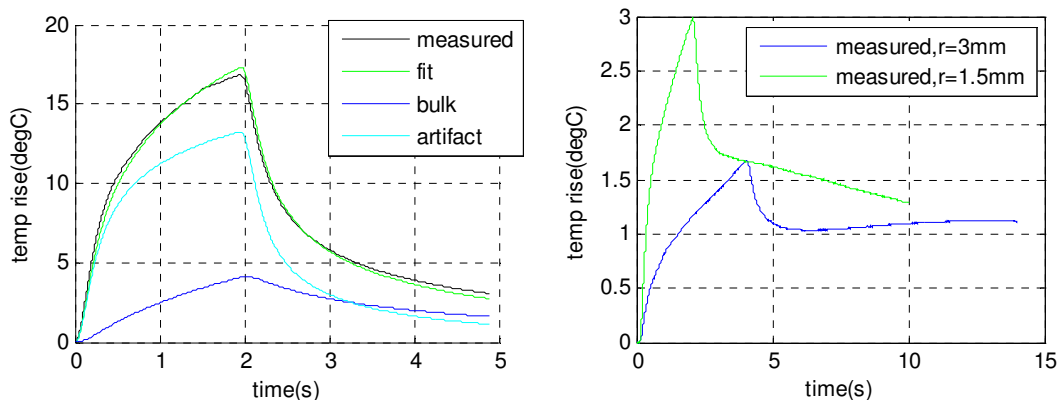


Figure 3.21 Left: Measured temperature at focus in chicken for 4MPa HIFU, along with best-fit curve for artifact and its bulk and artifact components. Right: Measured temp in chicken for 5MPa HIFU taken 1.5 and 3mm from axis, which had durations of 2 and 4 seconds respectively.

It was found that the solutions were not unique, even for as little as two search variables. In other words, good curve fits could be obtained with more than one combination of variables. Many temperature measurements were taken at various power levels and locations, and it was hoped that the absorption could be obtained from analyzing the fit values, but no success was had in finding consistent, unique solutions.

3.5.4 Push-in method

In order to avoid the viscous heating artifact, a method was devised whereby a thermocouple was quickly pushed into the focal zone of the HIFU immediately after it shut off. The resulting curve could then be fit to the basic thermal model, since the thermocouple would enter a region of no viscous heating. The thermocouple was mounted securely on a laboratory xyz translation stage, perpendicularly to the HIFU beam. It was then located with the technique of section 3.5.1. The translation stage had a spring that maintained contact between the moving part of the stage and the position adjustment screw. A 1.47mm thick washer could be placed in the gap, thereby moving the thermocouple in a direction perpendicular to the HIFU beam. Removing the washer resulted in the spring quickly snapping the thermocouple back to the original position. This was repeated prior to measurements, in order to remove sticking points between the thermocouple and tissue. Figure 3.22 shows the results for 2 second 2MPa HIFU exposure in chicken. The blue curve shows viscous heating at the focal spot. The thermocouple was then backed up 1.47mm and the HIFU run again (cyan). The magenta curve shows the “push-in” data, in which the thermocouple was quickly moved from $r=1.47\text{mm}$ to $r=0$ at the end of HIFU.

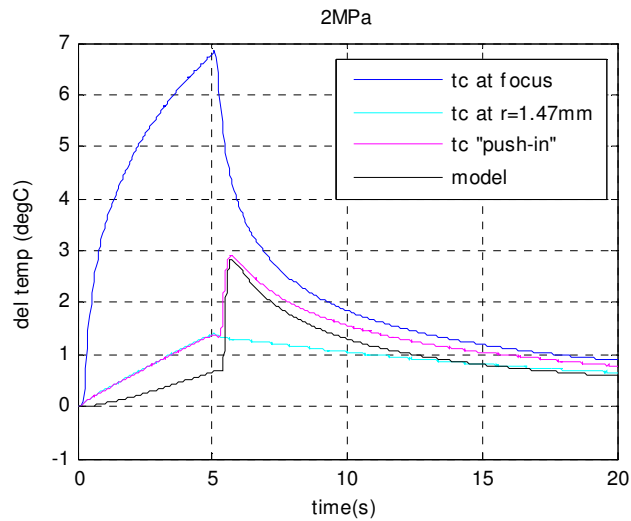


Figure 3.22 Thermocouple curve for a 2MPa HIFU exposure in chicken. The blue curve shows viscous heating at the focal spot. The thermocouple was then backed up 1.47mm and the HIFU run again (cyan). The magenta curve shows the “push-in” data, in which the thermocouple was quickly moved from $r=1.47\text{mm}$ to $r=0$ at the end of HIFU. The black curve is the model, with absorption= 3.4Np/m/MHz .

The Parker model can then be overlaid at this point, but a further addition was made to the model to simulate the push-in. The temperature was calculated at both the original thermocouple placement at $r=1.47\text{mm}$ and at the final placement at $r=0$. The two temperature curves were then stitched together at the time when the thermocouple was snapped to the new location, which was easy to glean from the measured trace. After this stitching, the thermocouple mass filter was applied. The black curve in the figure is from this model, with absorption= 3.4Np/m/MHz . A number of things can be observed. The magenta curve does not overlap the blue after the HIFU is off. This could be caused either by the viscous heating raising the temperature in the tissue, or the thermocouple not returning to the original focus position. There is certainly some of the former, as can be inferred from the different decay rates of the bulk and viscous curves in Figure 3.21. One may also observe that the model curve decays more quickly than the measured. One possible reason for this is that the model does not include the side lobes of the field, the heating from which will slow the conduction of heat from the focal region. Another possible reason is that the value for the thermal conductivity ($0.49\text{W/m}\cdot\text{C}$) is wrong, but this value is quite consistently reported in the literature. Still another possible reason is that the actual HIFU focus is spread out due to tissue inhomogeneity, resulting in a

slower decay of temperature. Finally, one may observe that the measured and modeled curves differ for the HIFU-on time. Again, some of this may be due to the side lobe heating at this radius, but is also caused by viscous heating. Even FEM thermal models that include the side lobes show a more gradual increase in temperature at this radius. It is assumed that any viscous heating here does not affect the following data after the push-in takes place.

Figure 3.23 shows similar results for higher pressure levels, at various exposure times. The discrepancy in the fit of the decay is more than for the 2Mpa data, and so too the HIFU-on data. A finite element model was made for the 20 sec exposure case, and the results closely matched the black model curves, so the side lobes don't appear to be the issue.

Similar studies were done at pressure levels of 3, 4, and 6Mpa. The values for absorption for the best fits were 3.5, 3, and 2.8Np/m/MHz, respectively.

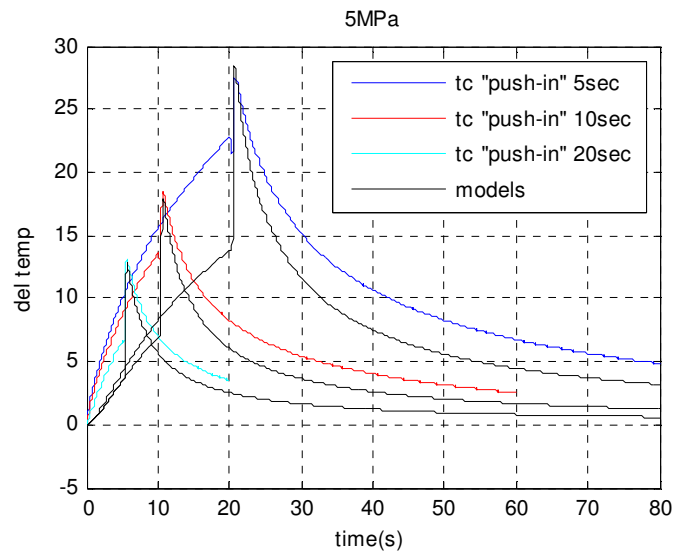


Figure 3.23 Thermocouple “push-in” data for various length 5MPa exposures. Black curves are for model, with absorption = 3Np/m/MHz. ERRATA: legend has blue and cyan curves reversed.

3.6 Tissue Properties

Chicken breast tissue was used in the bulk of the experiments. Chicken doesn't cavitate readily and is fairly homogeneous. It is however quite non-isotropic, which causes the attenuation along the muscle fibers to be increased by a factor of two. All experiments were done with the fibers perpendicular to the HIFU beam, and, when applicable, also perpendicular to other acoustic interrogation devices like hydrophones or B-mode imagers. Although in clinical HIFU applications *In-vivo* tissue is typically saturated (Yang 2003), store-bought tissue has additional gas from processes after death. The tissue samples were degassed to reduce the likelihood of cavitation during HIFU. Because freezing can break down tissue structures and thus cause changes to stiffness, only non-frozen samples were used.

Phantoms were also studied. To mimic the approximate stiffness of tissue, a low concentration of agar was used to make a gel. Silica particles provided scattering, and safflower oil was added to mimic acoustic absorption. (recipe: 100ml water, 1g agar, 0.62g Silica, 33ml oil, 1ml dish soap, for emulsification.). These phantoms were of limited use, principally because the mechanical losses were so low that resonant vibrations were easily excited by vibrations in the building. They also did not hold together well, making custom formulations with embedded simulated lesions difficult.

3.6.1 Attenuation

Measurements were done using the insertion technique, in which samples of uniform thickness <2cm were lightly pressed between two parallel plates containing flush-mounted 19mm dia. unfocused 2.25MHz broadband transducers. There were no reflections from interfaces to consider, and the diffraction losses were small and considered identical for the case of tissue or water (Huang, 2002). The attenuation (Np/m/MHz) was given by $\alpha(f) = \frac{1}{th} \left(\frac{W_1}{W_0} \right)$ where th=sample thickness and W_1, W_0 the Fourier transforms of the received pulses with and without tissue sample. Figure 3.24 shows typical results from one such measurement. In practice the slope of the attenuation line was

not always linear, and when it was it did not usually pass through the origin. This latter fact is somewhat mysterious at this point. The value chosen for attenuation was that of a line passing from the origin to the point on the curve at the peak of the energy spectrum of the pulse.

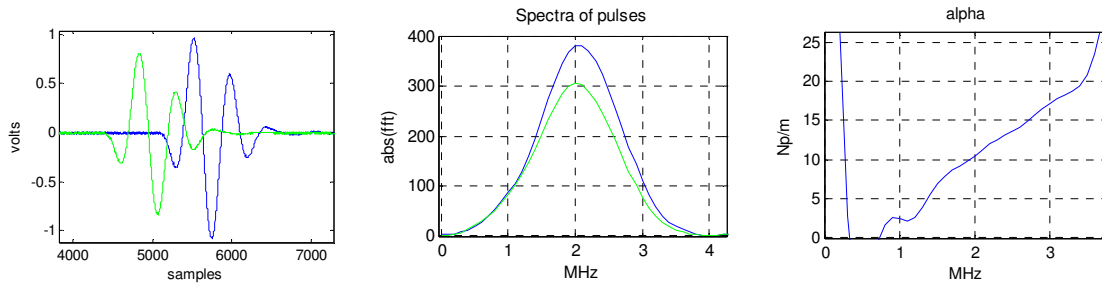


Figure 3.24 Typical output of attenuation analysis of a tissue sample in the parallel plate apparatus. Green and blue waveforms are received pulses with and without sample. Rather than using the slope, the value of attenuation is taken as 5.25 Np/m/MHz, which is the value at 2MHz (spectral peak).

At room temperature, the attenuation was found to be 5 ± 1.5 Np/m/MHz for five different chicken breasts. If measurements were limited to one breast, the variation reduced to ± 0.75 . Attenuation measurements in the literature are notoriously inconsistent, and there are few reported values for chicken tissue. Tyreus (2004) reported 4.5 Np/m/MHz for chicken.

3.6.1.1 Attenuation as a function of temperature

Attenuation varies with temperature, due to changes in protein structure. To measure this, the parallel plate device was immersed in a tank. A needle thermocouple was inserted into the tissue for temperature measurement. Three random positions on the sample were measured at each temperature. The sample was about 20mm thick and 5cm diameter. In the first experiment, hot water was added to the tank at various points. The results are shown in Figure 3.25.

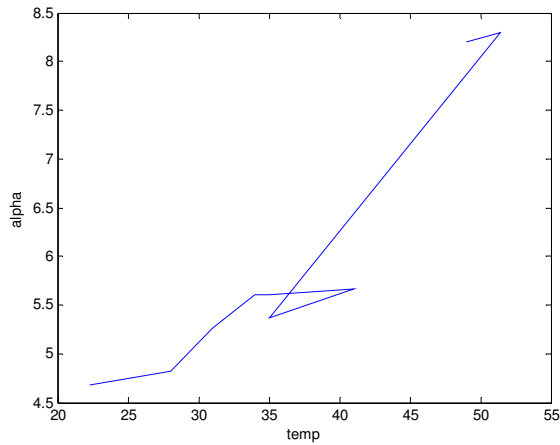


Figure 3.25 Attenuation (Np/m/MHz) vs temperature for chicken sample.

At one point the tissue cooled 5 degrees before the next heating was applied. It is possible that the slope changed between 40 and 50 degrees, but no data points were taken in this region. The experiment was repeated on a new sample, in the Neslab circulating temperature-controlled bath. Results are shown in Figure 3.26.

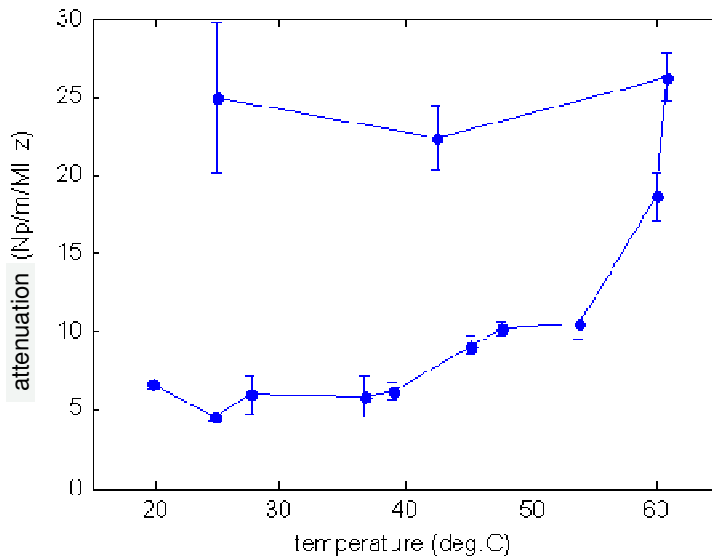


Figure 3.26 Attenuation for chicken sample in controlled water bath. Error bars represent 3 measurement locations at each temperature.

There is a gradual doubling of attenuation from 40 to 55 degrees, followed by a steep increase to 5 times the original value, and then a cooling phase where the high value is maintained.

Similar studies were performed by Damianou (1997) and Tyreus (2004). The former was on canine liver, showing a doubling of attenuation between 50 and 70 degrees C. The later was done on chicken, showing a 2.5 times increase by 60 degrees, and a 7 times increase by 90 degrees. It is assumed that irreversible protein denaturation takes place above 57 degrees (see section 2.1.1) and causes the steep increase.

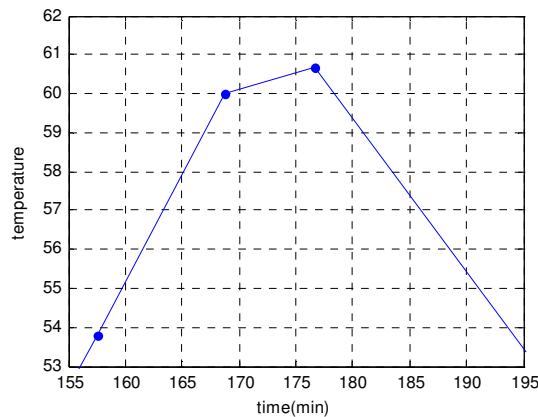


Figure 3.27 clock time vs temperature, for the data in Figure 3.26.

To investigate the time scale over which this denaturation occurs, Figure 3.27 shows the cpu clock time when each data point in Figure 3.26 was taken. This indicates that the point at 60 degrees had been above 57 degrees for approximately five minutes, and the point at 60.5 degrees for 12 minutes. Thus by the time the attenuation reached 25 Np/m/MHz, the temperature had been above the point at which denaturation begins (57 deg.) for 12 minutes. Furthermore, it is evident that the attenuation change from 18 to 26 Np/m/MHz took place over about 8 minutes, while the temperature remained fairly constant. This suggests what was hinted at in section 2.1.1: the changes in protein structure leading to increased stiffness do not occur on time scales less than many seconds or even minutes. This is important for modeling HIFU lesion formation, since the rate of temperature increase would be much faster than the rate of 0.5 degrees per minute used in the method described

here and also by Damianou et al.(1997), Tyreus (2004), or Sapin-de Brosse et al. 2010 (Figure 2.2). During HIFU lesion formation the temperature at the focus reaches and surpasses 57 degrees within a few seconds, and according to the results above the increase in stiffness from protein denaturation would occur many seconds later. This presents a problem for using a functional relationship between stiffness and temperature in the modeling of HIFU lesion formation, unless it contains temporal response information also. Using thermal dose for this purpose, as has often been done in the literature, may be erroneous. Functional relationships between stiffness or attenuation and thermal dose have only been established at low heating rates and for temperatures less than 60 degrees C. Indeed, Damianou et al.(1997) showed that the dependence of attenuation on dose differed substantially for different heating rates, attaining lower levels of attenuation for higher heating rates.

The tissue absorption remains at 25 N/m/MHz as the sample is cooled, indicating irreversible changes from protein denaturing. Samples that were heated to higher temperatures, and even boiled, had similar attenuation values of 25N/m/MHz, suggesting that no further increase in attenuation is seen after the complete protein denaturation.

A cross-section of a HIFU lesion in chicken was measure for attenuation using a surface acoustic microscope. This consisted of a high frequency focused transducer operating in pulse-echo mode, reflecting off a glass slide on which was mounted the 3mm thick tissue sample. Corrections were made for the impedance mismatch at the water-tissue and tissue-glass interfaces, and the acoustic field diffraction was assumed the same for the case with tissue and for the reference case without tissue. The slide was placed at the focal distance in the fluid (PBS solution, to prevent tissue from bloating due to mismatch in salinity). The spectral peak of the digitized echo off glass was 20MHz. A large lesion was made for this study using a long HIFU exposure, measuring 3.5mm in diameter. Figure 3.28 shows the results.

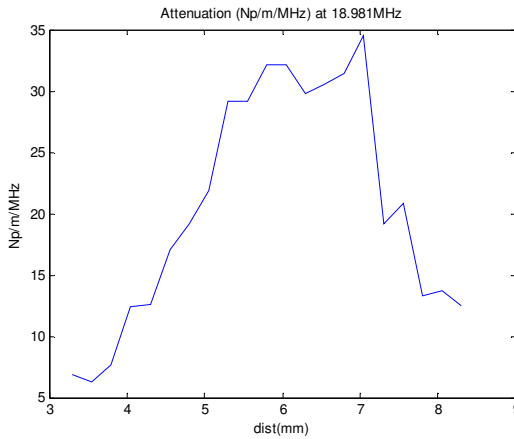


Figure 3.28 Attenuation vs. surface position over a cross-section of chicken tissue with a HIFU lesion. Taken with surface acoustic microscope. The lesion was measured with a ruler to be 3.5mm wide.

Similar to the water bath measurements, the protein denaturation results in more than 5 times increase in attenuation. Although not shown, the calculated attenuation vs frequency was quite linear, extending down to 5MHz. It is interesting to note that the transition to the peak takes place in over 1mm (much larger than the spatial resolution of the instrument), but this is left for further study.

3.6.1.2 Values from the literature

Most studies involve organ tissues, rather than muscle, and only one was found (Tyreus et al. 2004) involving chicken. Table 3-2 shows some values found for chicken, turkey, and a variety of muscle tissue. Also shown are values for the increase due to lesion. The chicken values are in agreement with those found here.

Source	Tissue	Attenuation (Np/m/MHz)	Attenuation Cross-grain	Factor with lesion
Anand and Kaczowski (2008)	turkey breast	14.3	28	
Duck (1990)	muscle	10-16	18-32	
Tyreus et al. (2004)	chicken breast	4.5		5-7
Bush et al. (1993)	porcine liver	8		1.3 to 2.9
Damianou et al. (1997)	canine liver	5		2
Robinson and Lele (1972)	feline brain			5

Table 3-2 Values of attenuation and lesion increase, from the literature

3.6.2 Calculating the absorption coefficient

3.6.2.1 Method#1: Matching temperature measurements to models

In section 3.5.4 the “push-in” method was described, in which a thermocouple was quickly pushed into the HIFU focal zone at the end of heating, in order to avoid any viscous heating artifact. The data was compared to the Parker thermal model. Assuming the tissue parameters of thermal conductivity, heat capacity, density are known, the acoustic absorption could be chosen to match the measured data. When tried on two chicken breasts at various HIFU durations and pressure levels, this method produced values for absorption of 2.8 to 3.5 Np/m/MHz. This is unexpectedly small, being only 56 to 70% of the average total attenuation for chicken (5 Np/m/MHz). However, the failure of the model to reproduce the decay portion of the data casts some doubt on these values.

3.6.2.2 Method#2: Scattering cross-section

The total attenuation has two components – one due to absorption, and one from scattering. Therefore, if one could measure the scattering component and the total attenuation, the absorption could be calculated. A more precise expression is written in terms of the cross section σ , which is equal to power radiated or absorbed/incident intensity. So, $\sigma_e = \sigma_{sct} + \sigma_{abs}$ where the subscript “e” means “extinction”, i.e. total attenuation. To this end the total scattered energy from a tissue sample was measured by sweeping a needle hydrophone through space and integrating the resulting scattered energy. A 1.3cm cube of chicken was placed on a thin rubber mat on top of a metal block. The h102 HIFU xdcr was fired horizontally in the water tank, focused in the middle of the sample. A jig was made to move a pzt needle hydrophone in an arc above the sample, keeping 6cm from the focus. The HIFU was set to deliver 2 cycle bursts at 4.72MPa peak pressure. The hydrophone output was amplified by 28dB and digitized by the oscilloscope. Figure 3.29 shows the setup for the measurement.

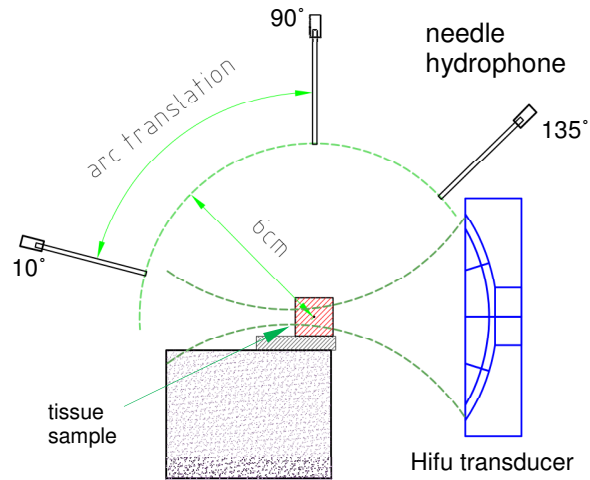


Figure 3.29 Scale drawing of scattering cross-section setup

For purposes of comparing the power in the direct beam and the scattered power, only the uncalibrated voltage signal from the pzt hydrophone is required. The frequency response of the needle is reasonably flat, but not strictly required to be so for the present study. Figure 3.30 shows the scattered waveforms vs. angle.

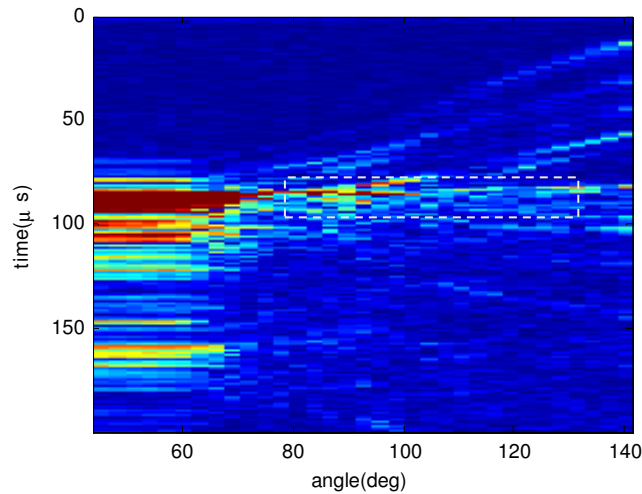


Figure 3.30 Time waveforms from the pzt needle hydrophone vs scattering angle. The white rectangle indicates the region of data used in the study, representing scattered energy from the tissue, without interference from direct energy from the transducer.

Because the excitation is not CW, there will be direct energy from the transducer at all the hydrophone positions. To investigate whether this direct energy could be avoided in the measurements, a simulation of the 2 cycle burst from the h102 transducer was carried out using the “FOCUS” software routines written by R. McGough at Michigan State University (downloaded from <http://www.egr.msu.edu/focus-ultrasound/>). This uses a modified angular spectrum approach. Figure 3.31 shows the modeled wavefront (no sample) at the moment when peak pressure is reached at the focus ($z=0$). Also from the simulation is a plot to match the measured scatter waveforms in Figure 3.30, which shows the location of the direct energy expected to reach the hydrophone location. From this it is seen that the only portion of the scattered data that does not contain direct energy from the HIFU transducer is the region outlined by the rectangle in Figure 3.30. This will contain only the energy of the pulse scattered from the tissue. Figure 3.32 plots the rms value vs angle of just the scattered energy within this window. The data from the baseline case without sample are subtracted from that with sample, to further reduce contributions from direct energy and noise.

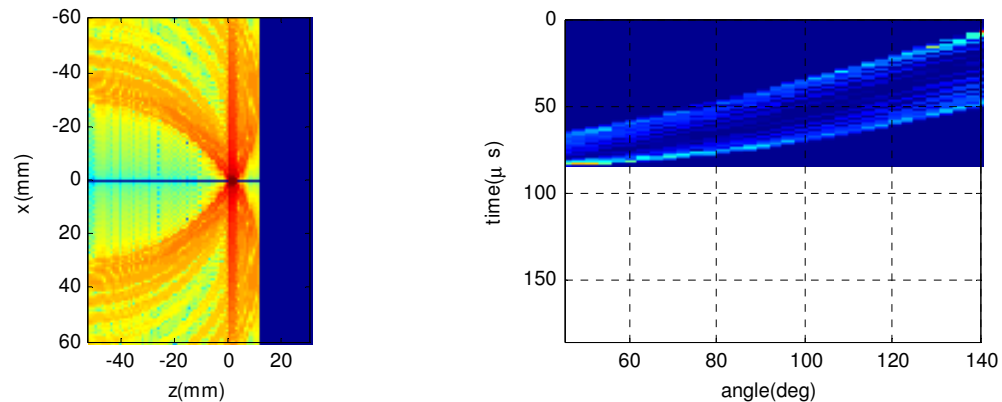


Figure 3.31 “Focus” simulation of 2 cycles from h102. Left: $\log(\text{Hilbert transform})$ of pressure when p_{\max} reaches focus at $z=0$ ($t=43\mu\text{s}$). Right: $\text{abs}(\text{Hilbert})$ of pressure as a function of time and angle for points on an arc 6cm around focus, to match Figure 3.30. The calculation stopped at $80\mu\text{s}$, but would have shown no further energy than shown, for $\text{angle}>60^\circ$.

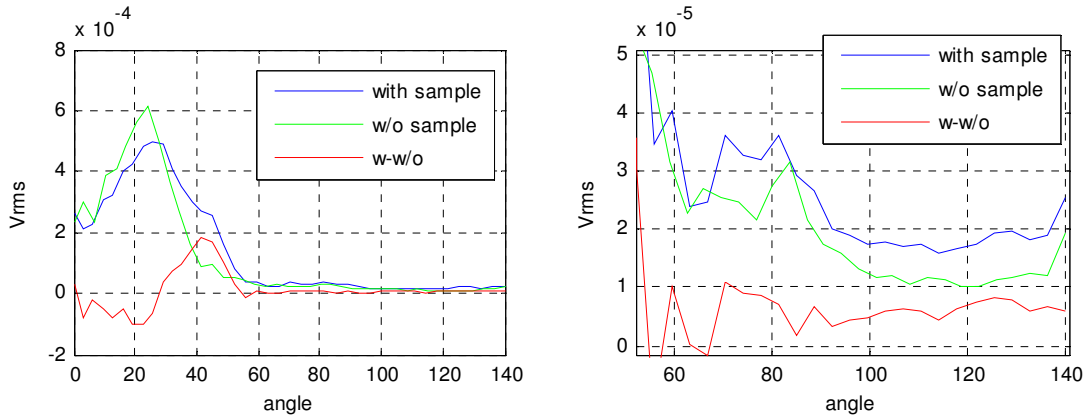


Figure 3.32 RMS voltage of the hydrophone signal vs. angle, during the time window of the arrival of the scattered burst. Red curve is the difference between waveforms with and without sample. Right: zoom in of left plot.

The scatterers in the chicken breast tissue are mostly much smaller than one acoustic wavelength, with the exception of small vessels and other inhomogeneities. For this case the intensity scattering cross-section is proportional to frequency to the fourth power (Rayleigh 1871). Morse and Ingard (1968) further derived an expression for the scattering of these small particles as a function of their density and compressibility. This could be divided into a monopole term, in which the energy is scattered uniformly over all angles, and a dipole term. In the present analysis we will consider the scattering is only from the monopole term, by reasoning that the dipole term would give the curves in Figure 3.32 a substantial slope vs. angle. In contrast, it is seen that the energy in the region where direct sound from the transducer does not come into play ($\text{angle} > 100^\circ$), the angular dependence is fairly flat.

In the following analysis, the Born approximation is used, which states that the scattered energy is simply σ_{scat} times the incident intensity, ignoring incremental degradation of the incident beam by the scattering itself. Furthermore, the contribution to the measured scattered energy of the attenuation of the incident and scattered beams is considered to be negligible.

For a given burst, the total amount of energy lost from the beam will be the sum of that which is scattered and that which is absorbed: $E_{\text{att}} = E_{\text{scat}} + E_{\text{abs}}$. The total energy lost is found by applying the attenuation coefficient to the total beam energy. $E_{\text{att}} = (1 - \exp(-2\alpha_{\text{att}}th))E_{\text{tot}}$ where th is the

sample thickness. Similarly, for absorbed energy, $E_{abs} = (1 - \exp(-2\alpha_{abs}th))E_{tot}$. The total beam energy was found by measuring the peak pressure at the focus in water: $E_{abs} = IA\Delta t = P^2\pi a^2\Delta t/\rho C$ where a is the Gaussian radius of the beam, Δt the duration of the burst, and P is the peak pressure at the focus. Finally, using $E_{scat} = SE_{tot}$, where S will be calculated from our measurements,

$$\alpha_{abs} = \frac{-1}{2th} \ln \left[\exp(-2\alpha_{att}th) + S \right] \quad (3.12)$$

For the total scattered energy, $E_{scat} = \int I \Delta t dA = 4\pi R^2 \langle p^2 \rangle \Delta t / \rho C$ where Δt is the length of the waveform in seconds, and R is the radius (6cm). $\langle p^2 \rangle$ in this case is the average mean square pressure in the windowed region of scattered waveforms taken from 90° to 140°. This can be evaluated in the two prominent energy bands, centered at 1.1MHz, and 2.2MHz. Using a similar approach to that used in section 3.4.3.2.1, $\langle p^2 \rangle$ will be sum of $\text{abs}(\text{FFT}(p))^2$ in the band of interest (including the upper mirrored band), divided by the number of samples in the waveform squared. The bands are defined as where the FFT drops by 25dB, which is .75 to 1.6MHz, and 1.85 to 2.7MHz. After finding E_{scat} and E_{tot} for each band, S is calculated as the ratio of E_{scat}/E_{tot} : $S_{1.1\text{MHz}} = 0.0275$ and $S_{2.2\text{MHz}} = 0.0154$. It was expected that $S_{2.2}$ should be larger than $S_{1.1}$ due to the f^4 dependence of Rayleigh scattering. Finally α_{abs} is calculated from (3.12). For $\alpha_{att} = 5\text{Np/m/MHz}$,

$$\alpha_{abs}/\alpha_{att} = 0.7816 \quad \text{in 1.1 MHz band}$$

$$\alpha_{abs}/\alpha_{att} = 0.9291 \quad \text{in 2.2 MHz band}$$

3.6.2.3 Discussion

In the first method of this section, the thermocouple “push-in” data suggested values for absorption that were considerably less than expected, and the fit to the model that was used to arrive at these values was not good. In the second method, the scatter measurement was only made on one sample, and was based on the assumption that the radiation measured over a small portion of the sphere was representative of the scattering over the entire sphere. The results were however in

keeping with values given in the literature ($\alpha_{abs}/\alpha_{att} = 0.8$ to 1.0). The value for absorption going forward will be taken as $\alpha_{abs} = 0.8\alpha_{att}$.

3.6.3 Sound speed

$C(T)$ was measured from the parallel plate apparatus using the same waveforms as used for attenuation. The equation from Sachse and Pao (1978) is used: $c(f) = \frac{2\pi f th}{(\varphi_0(f) - \varphi(f)) + 2\pi f \tau}$ where th is sample thickness, $\varphi_0(f)$ and $\varphi(f)$ are the phases from the Fourier transforms of the measured pulses without and with sample, and τ is the time delay between the two received pulse waveforms (which was zero). The frequency at the spectral peak was chosen. Figure 3.33 shows the results. The temperature was cycled at one point to examine reversibility.

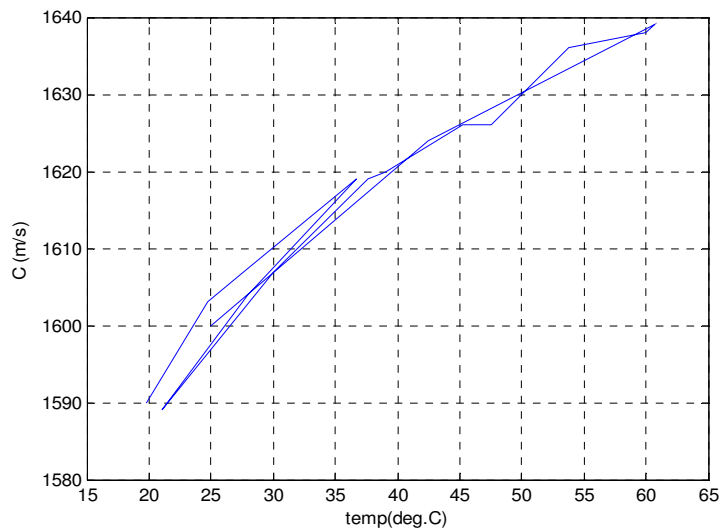


Figure 3.33 Sound speed of chicken breast as a function of temperature in hot water bath. At room temperature (20°), the slope $dC/dT \sim 2.0$

3.6.4 Elastic modulus

The complex shear modulus was measured on a rotating disk rheometer (AR2000 TA Instruments, New Castle, DE). The tissue was cut into 5mm thick, 40mm diameter pucks, and placed on the flat surface of the rheometer, which contained a Peltier heater/cooler capable of fast and accurate temperature control. A 40mm diameter aluminum disk was brought in contact with the sample, it's normal force being adjusted either manually or automatically, to about 1N. The rheometer then performed the following steps: The disk was oscillated at a given frequency with a constant amplitude of 1.5×10^{-4} radians. The torque was measured by a transducer, and the shear modulus calculated from the torque and known shear strain. Corrections are made in the rheometer software for instrument friction and inertia. The shear modulus is given by $G = \frac{\text{torque } th}{\varphi J}$ where φ is the angular displacement, th sample thickness, and J the moment of inertia of cylinder sample ($=\pi R^4/2$). In the standard Voigt model for viscoelasticity, the viscous loss is given by the loss tangent $= \tan(G''/G')$ where G'' and G' are the real and imaginary parts of G . This model does not include material inertia, and so cannot account for standing waves that develop if the sample is too thick. When this happens a dip will appear in the curve of $G(f)$, since such waves occur at specific frequencies. The first such expected resonance occurs at thickness = one quarter wavelength $h = \frac{\lambda}{4} = \frac{1}{4f} \sqrt{\frac{G}{\rho}}$. At the HMI modulation frequency of 40 Hz, this will be reached for a soft tissue like liver with a stiffness of about 1kPa, at thickness=6.25mm. Chicken tissue is stiffer, and the samples in this study were kept below 5mm. Some studies in the literature, e.g. Kobayashi (2008), Kiss(2004) report $G(f)$ curves for tissue that have resonant dips or even go below zero. These are probably suspect and due to standing waves.

Since the rotating disk plate was made of aluminum, a 2.8mm thick disk of dense foam (thermal conductivity 0.033W/m²K) was glued to the surface of the disk with 5-minute epoxy to minimize the thermal gradient in the sample. The sample, foam, and disk assembly was modeled in the Comsol finite element package, which revealed that the temperature at the top of a 5mm thick tissue sample

reached 92% of that at the temperature-controlled bottom plate, and it took 3.4 minutes to reach 90% of this value.

In HMI/lesion experiments the direction of the muscle fibers was perpendicular to the HIFU beam. Unfortunately, because it used a rotating disk, this rheometer could not isolate the same shear force orientation as in the tissue during HIFU. For example, if the HIFU beam exerts force in the z direction, the shear forces will be τ_{xz} and τ_{yz} . The disk exerts shear force in two directions, e.g. τ_{xz} and τ_{xy} (disk axis along x) or τ_{yz} and τ_{yx} (disk axis along y).

Figure 3.34 shows the results for four samples. The blue curve was eventually used for the making of the generalized Maxwell visco-elastic FEM model (chapter 4). To investigate thermal effects, samples were run at room temperature, then 40° or 50°, then back to room temperature. Results are shown in Figure 3.35. A reversible softening of about 30% is evident.

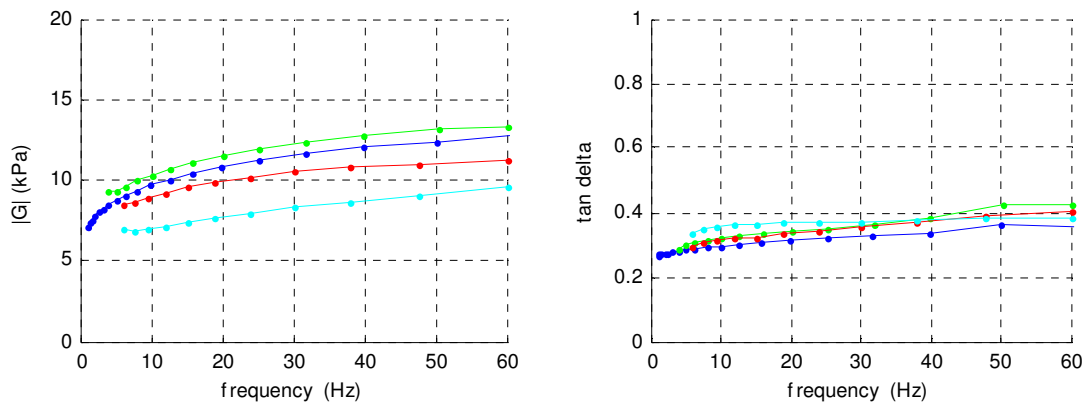


Figure 3.34 Shear modulus of four chicken samples Left: magnitude, Right: tan(phase) i.e. “loss factor”

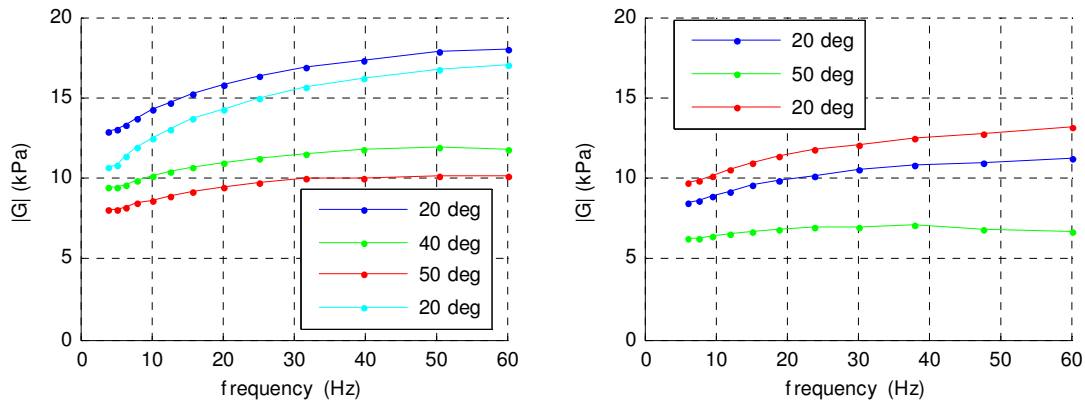


Figure 3.35 Stiffness of chicken samples showing effect of cycling temperature 20°C to 50°C to 20°C. Left and Right: two different samples.

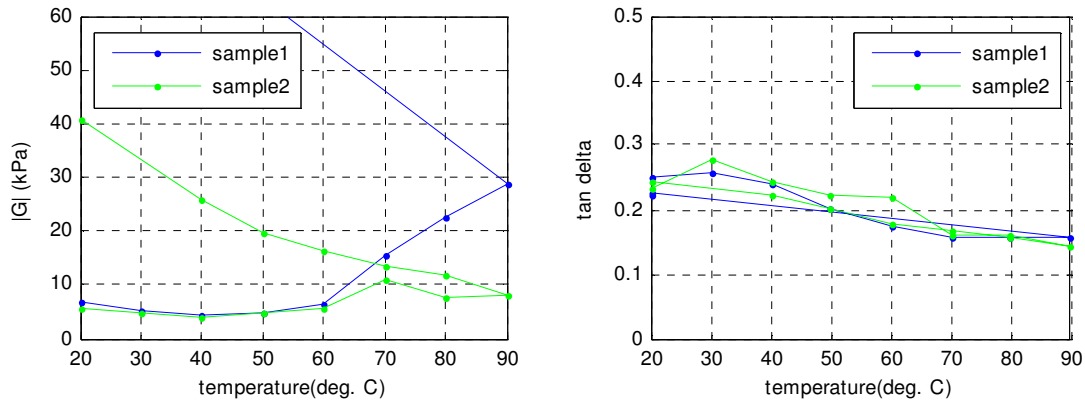


Figure 3.36 Shear modulus vs. temperature for two samples, taken on different days. Rheometer oscillation frequency was 10Hz. Sample #1 had 10 min. wait time between points, sample #2 had 5min wait time. The curve for sample#1 reached 88kPa upon returning to 20 degrees. Left: magnitude, Right: tan(phase) "loss factor".

Samples were next subjected to lesion-forming temperatures. Figure 3.36 shows measured stiffness vs temperature results for two tissue samples. Sample #1 had a 10 minute wait time at each 10 degree temperature measurement point, while sample #2 had a 5 minute wait time. The loss factor changed only 25% and appeared to be reversible with temperature. The peak in $|G|$ for sample#2 at 70°C would appear to be spurious. The data there showed a sudden increase in normal force in the rheometer, perhaps due to tissue thermal expansion. The overall shape of the curve resembles those of Sapin-de Brosses et al. (2010) (see section 2.1.1). The stiffening that occurs after 57°C they attribute to collagen myofibrillar shrinkage. Stiffness continues to rise irreversibly with

temperature after denaturation starts. The stiffness rises still further upon cooling. As with the results of Sapin-de Brosses et al. (2010), the stiffness during cooling is approximately linear with temperature, the slope depending somewhat on the ultimate stiffness attained during the heating cycle. The fact that the sample taken at a slower heating rate reaches higher stiffness is consistent with the arguments in section 3.6.1.1 regarding the dependence of $\alpha(\text{Temp})$ on heat rates. This supports the argument made in section [2.1.1], that attenuation and also stiffness change with temperature, but the dependence is a function of heating rate. The data presented here, taken at heating rates on the order of 1°C per minute may not be suitable for use in modeling HIFU lesion formation, with significantly higher heating rates.

3.6.4.1 Uncertainties

Tay et al. (2006) found that measurements for liver stiffness from the literature vary widely, from 5 to 170kPa. It is thus difficult to find trusted numbers with which to compare. Tissue itself exhibits considerable variability, and the amount of time required to take rheological data prohibited measuring more than a few samples. Also, stiffness of tissue within a living organism may be different than a thin slice of ex-vivo tissue. Lastly, the sample stiffness was somewhat affected by the downward force of the rotating disk. Even though this was automatically adjusted, the process appeared to be incremental and slow, and may not have kept up with the changes brought about by tissue thermal expansion.

3.6.4.2 Values from the literature

Table 3-3 shows values from literature for the increase in shear modulus caused by lesion. In some cases decrease caused by warming was also reported. Stiffness data was less represented in the literature than attenuation, and no data was available for chicken or other fowl.

Source	Tissue	Stiffness decrease with warming <60°C	Stiffness increase with lesion
Wu et al. 2001	Bovine muscle	0.5	3
Lizzi et al. 2003	liver		5
Kiss et al. 2004	liver		10
Sapin-de Brosse et al. 2010	Bovine muscle	0.2-0.5	1 to 1.3
“	Bovine liver		4
Orescanin et al. 2009	Porcine liver		2-3

Table 3-3 Values from literature for increase in shear modulus caused by lesion

3.6.5 Tissue properties used in models

The average value of $|G|$ for eight runs at 40Hz was 12kPa. This will be used for the shear modulus at 20 degrees in subsequent models. Figure 3.37 shows the base curve used in the models, which will be multiplied by the value for G at 40Hz. (It is assumed here that the approximate shape of the temperature dependence curve shown in Figure 3.36 for a rheometer frequency of 10Hz also applies at the MHI modulation frequency used throughout this work, 40Hz). The value of the drop of at 40 degrees (30%) was found from the average of five runs on different tissue samples. However the rise from 60 to 90 degrees (400%) was based on only three samples with considerable measurement variability. Some of this may be due to problems inherent to measuring a tissue sample that is undergoing thermal expansion/contraction and liquid evaporation, and some may be due to sample variability, but the bulk of the variation may be due to different heating rates used in the measurements.

As mentioned in the sections on stiffness and absorption, and in section 2.1.1, measured curves for $G(T)$ and $\alpha(T)$ were taken at heating rates much slower than found in HIFU, and may be overestimates. The protein changes resulting in the ultimate values for stiffness and absorption may require many seconds or even minutes, even for instantaneous of heating (assuming temperature is not significantly over boiling temperature, so that no other processes occur, akin to searing or burning). To account for this in the modeling, alternate curves for $G(T)$ and $\alpha(T)$ are proposed Figure 3.37. For lack of measurements at high heating rates, the values for ultimate stiffness and absorption

can only be guessed, and are here taken to be twice the initial values. Three arguments for the choice of a factor of two for the attenuation increase are as follows: 1) Angular spectrum modeling suggests that any more than a factor of 2 would cause a large shadow in the interrogation field, which is not seen in practice, 2) FEM thermal modeling predicts that any higher value than 2 would cause a very fast ascension to boiling, which is probably not occurring, and 3) one “push-in” thermocouple data run revealed results before and after a lesion was made that were consistent with a factor of 2 increase in acoustic absorption.

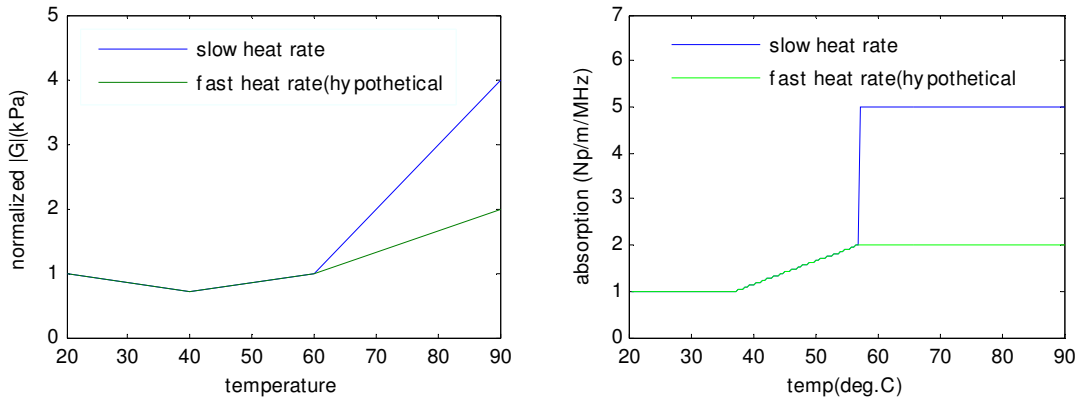


Figure 3.37 Values for $G(T)$ and $\alpha(T)$ used for FEM models, normalized to the value at 20°C. The measured curves were simplified into linear segments that could be easily incorporated into the FEM model. Also shown are the alternate hypothetical curves for the high heat rates found in HIFU.

Table 3-4 lists values of tissue properties used in the models. The density and sound speed were measured in the lab, and the values for specific heat, thermal conductivity, and Poisson’s ration were found from the literature, and showed little variability across sources.

$\rho=1040 \text{ kg/m}^3$	density
$C=1585 \text{ m/s}$	speed of sound
$E=18\text{kPa (static)}$	Young’s modulus
$E=36\text{kPa (40Hz)}$	Young’s modulus (dynamic). 20°C
$C_v=3600 \text{ kJ/kg-}^\circ\text{C}$	Specific heat
$k= 0.49 \text{ W/m-}^\circ\text{C}$	Thermal conductivity
$\nu=0.495$	Poisson’s ratio

Table 3-4 Material properties used for chicken breast

3.7 Validation and preliminary results

3.7.1 Magnetostrictive micro-shaker

Early HMI measurements revealed that the displacement amplitude at the tissue surface was the same as that at the focus, 15mm below. This was surprising, and to verify that the apparatus and software were working properly for displacement measurement at the HMI modulation frequency, a mechanical transducer was designed to impart a known oscillatory amplitude at a point within a tissue sample or phantom. Figure 3.38 shows the transducer, which was attached to a pin with a 2mm spherical head. The pin could be translated at 40Hz with an amplitude of $5\mu\text{m}$, and was molded into an agar gel phantom loaded with graphite particles. Figure 3.38 shows the transducer, which was attached to a pin with a 2mm spherical head. The pin could be translated at 40Hz with an amplitude of $5\mu\text{m}$, and was molded into an agar gel phantom loaded with graphite particles.

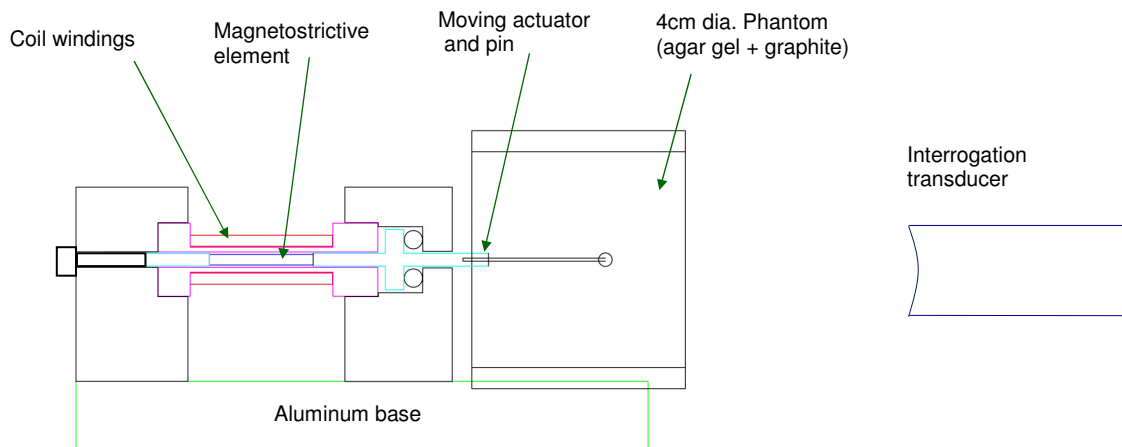


Figure 3.38 Scale drawing of magneto-strictive vibration exciter. Pin with 2mm head translates horizontally within a gel phantom, and the motion is measured using speckle tracking with the 7.5MHz interrogation transducer.

A calibration measurement of the transducer operating at 40Hz was made using a laser doppler vibrometer (LDV) (Polytek GmbH, Waldbronn, GE., controller=OFV 3001, scanner head=OFV303) aimed at the pin, prior to the gel being poured. After the gel cured, the LDV was again used to measure the motion at a point on the pin axis at the surface of the gel, 15mm from the pin. The

transducer and phantom were then immersed in water and the 7.5MHz HMI interrogation transducer was focused on the pin head and took pulse/echo A-lines at a rate of 2.5kHz. After being digitized, the A-lines were input to the speckle-tracking algorithm, the first line serving as the reference line. Figure 3.39 shows the displacement vs. time waveforms measured by the speckle-tracker at the pin head and at the surface. Also shown are the displacements measured by the LDV. The LDV data at the pin head was made prior to the gel, but the motion of the pin is expected to be the same with or without the gel. The LDV and ultrasonic waveforms were taken at different times, so the phase needed to be matched on the plot to aid in comparison. The agreement is good.

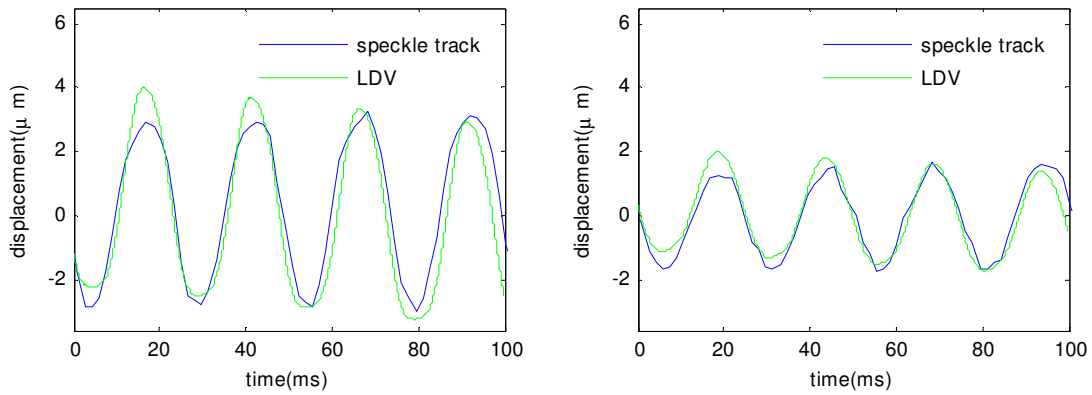


Figure 3.39 Displacement vs. time as measured by the LDV and the ultrasound pulse/echo speckle-tracker. Left: at the pin head. Right: at the surface of the phantom.

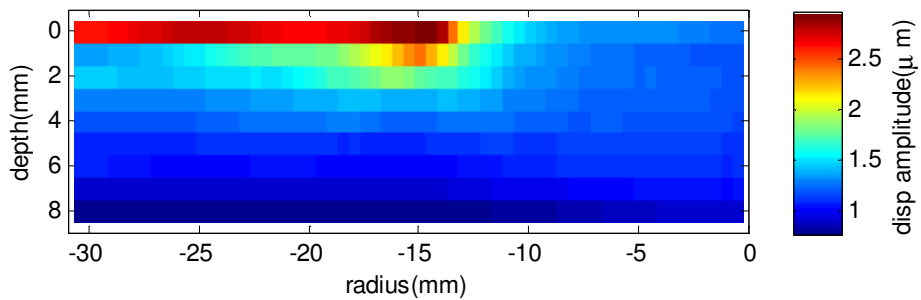


Figure 3.40 Displacement amplitude at 40Hz vs depth measured by speckle-tracking. The interrogation beam was translated from 0 to 8mm in steps of 1mm over the phantom surface. The translating pin head is at a depth of 15mm. The region of high amplitude behind this spot is anomalous, since the pin head blocks further penetration of the interrogation beam.

Figure 3.40 shows the displacement amplitude at 40Hz vs depth measured by speckle-tracking. The interrogation beam was translated from 0 to 8mm in steps of 1mm over the phantom surface. The region of high amplitude behind this spot is anomalous, since the pin head blocks further penetration of the interrogation beam. The amplitude in the gel falls steadily between the pin head and the surface. Note that the entire region has displacement over $1\mu\text{m}$, and, though not shown, the phase is constant, meaning the frequency was far below any inertial resonance of the pin-phantom system.

3.7.2 Displacement data from HIFU forcing modulated at 40Hz

3.7.2.1 “Push runs”

Frequently it was desired to measure the tissue response to harmonic forcing without appreciable heating or lesion formation. The setup described in section 3.2 is used, but 10 interrogation pulses are delivered, and there is no heating phase. This type of data will be referred to as a “push run”. Figure 3.41 shows an example for a chicken sample, with the usual HMI peak pressure of 3MPa. Positive displacement is in the direction away from the HIFU transducer. The oscillations are seen to be maximum near the focus at 15mm into the tissue, and are still quite strong at the surface. As will be shown, this is due primarily to the pre-focal energy in the HIFU field, but also to the surface force caused by the small acoustic impedance mismatch between tissue and water. The motion is not symmetric about zero, indicating that viscosity does not permit the tissue to recover to original position in between the “on” portions of the modulation.

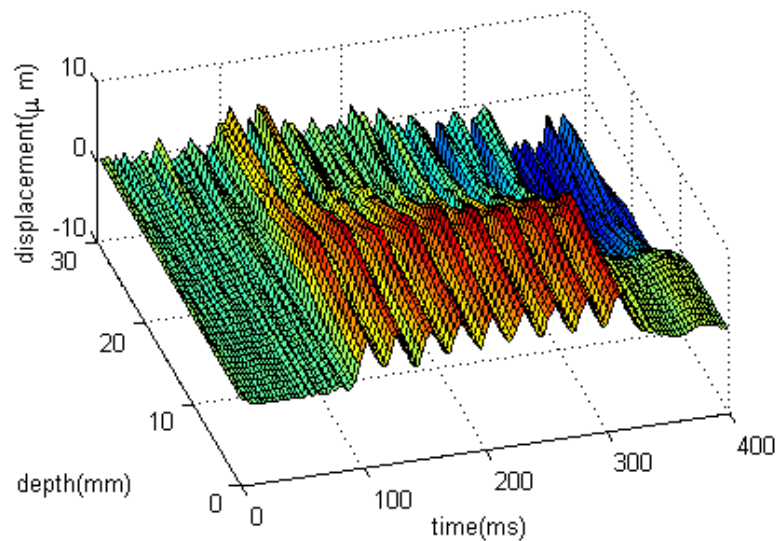


Figure 3.41 Displacement vs. time vs. depth during a 10 cycle “push run”. The sample was chicken, and forcing wave was 3MPa peak pressure 1.1MHz HIFU, modulated at 40 Hz.

Note that the displacement after the last forcing cycle is negative for tissue deeper than the focus. This is the result of an increase in sound speed near the focus caused by heating. It is clear that heating causes apparent displacements at least as large as the HMI displacements, and, for the case of lesion-making intensity, many times larger. Measuring this apparent displacement is one way of finding the temperature with the sample. Called “apparent displacement thermometry”, this method has many problems, and was abandoned for use in this research. The location of the “drop-off” is seen to be at a depth of 13mm, which is about the focal point, since the tissue velocity and attenuation result in a 1.5 mm shift in the focus (see Figure 3.13). The Fourier amplitude at the oscillation frequency during the ten cycles is shown vs depth in Figure 3.42. Note that the amplitude does not drop to zero by 30mm, which is near the rubber mat at the bottom of the sample. This is erroneous, and due to poor SNR in the echo signal at depths deeper than 25mm. The depth at which the displacement data could no longer be trusted was fairly consistent for the HMI experiments with chicken, and was identified by a separate parameter reported by the speckle tracker routines for degree of correlation.

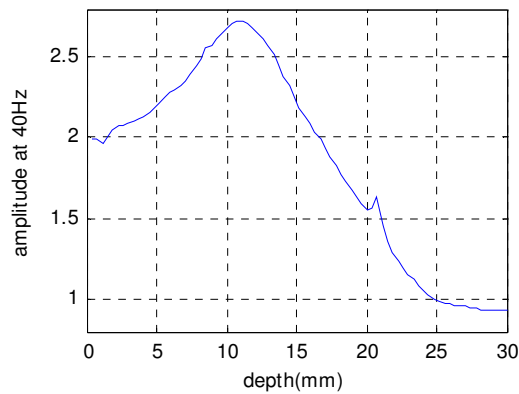


Figure 3.42 Fourier amplitude of the oscillations in Figure 3.41, vs depth into tissue.

3.7.2.2 HMI during lesion formation

To monitor HMI amplitude during lesion formation, several of these “push runs”, reduced to 4 modulation cycles in length, were interspersed with 4 to 5 second heating phases, where the HIFU intensity was turned up to “cooking” level, and the 40Hz modulation was disabled. Figure 3.4 showed a schematic of the timing sequence. The data was processed and the Fourier amplitude of each 4 cycle interrogation, like the one shown in Figure 3.42, were displayed sequentially, in the form of a 3-d mesh or a color image, like that shown in Figure 3.43. One interrogation was always taken prior to heating, to give a baseline. Interrogations were also taken after the heating was done, to provide information during the cooling phase. A heavy black line was drawn at the top to indicate the time duration of the heating phase.

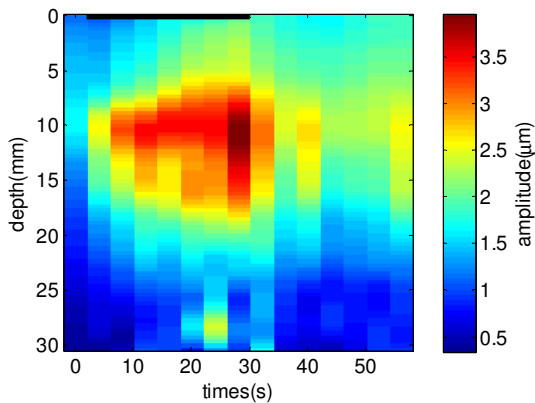


Figure 3.43 Typical results of HMI interrogations during lesion formation. Each vertical line is the Fourier amplitude of the HMI displacement vs. depth, for one interrogation. Interrogations occur every 4 to 5 seconds, and are interspersed with HIFU heating. One interrogation was always taken before the start of heating, and usually many were taken after heating stopped. The black line on top indicates the entire duration of the heating.

3.7.2.3 Relationship between displacement amplitude and HIFU pressure

To examine the dependence of amplitude on forcing pressure, several push runs were taken on the sample, at peak pressures of 1.5, 2, 4, and 6MPa. The amplitude at peak depth is shown in Figure 3.44. A parabola is fit to the points, showing that the amplitude is proportional to the square of the pressure, as expected (since the force is proportional to intensity).

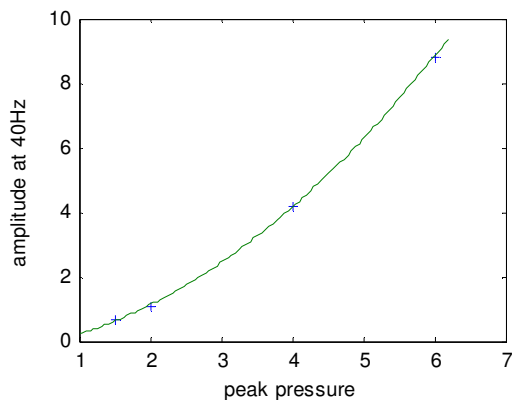


Figure 3.44 Displacement amplitude at 40 Hz at peak depth, for 4 separate push runs at varying HIFU peak pressure. Also shown is a parabolic fit.

3.7.2.4 Error due to signal to noise ratio of pulse/echo signal

As mentioned above, the received signal from the interrogation pulse became too weak to be unusable past a certain depth. Figure 3.45 shows the SNR as a function of depth for the A-lines in one push run. The lines were first divided into 20 segments to represent different depths. Each segment was compared to that of the next A-line in the data set, taken about 1ms later in time. SNR was found for each segment via $20 \cdot \log_{10}(\text{rms}(\text{line1})/\text{rms}(\text{line1-line2}))$. This process was repeated for 8 different pairs of A-lines taken from a full push-run (consisting of 2000 lines), and variations between the 8 are shown as error bars. The 8 lines were taken pre- HIFU, since that would shift the data as a result of forcing and temperature.

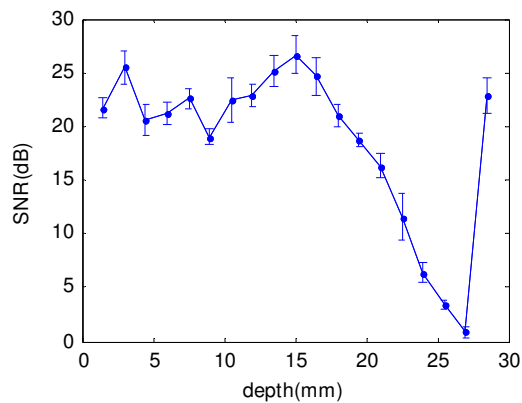


Figure 3.45 SNR vs. depth for 8 pairs of A-lines from a typical push run in chicken

The SNR drops below 5dB at around 23mm, but recovers at the end, where there is a strong echo from the bottom mat. Below 5dB the speckle trackers showed low degree of correlation and produced noisy or erroneous data. This did not usually occur for depths less than about 25mm, and these depths were usually not of interest. When they were, the pulser prf was adjusted to take more A-lines per second, and lines (of the same phase w.r.t HIFU) were averaged together to improve SNR.

Another source of error was in the numerical processing. For example, finding the Fourier amplitude at the modulation frequency was found to give up to 4% change when the number of modulation periods sampled was not an integer.

The A-line data was all passed through a 5MHz high-pass filter (9th order Butterworth), which had an impulse response lasting about 0.8 μ s. Thus, every bit of backscattered energy was given an extra few oscillations at about 5MHz. However, when HMI data was taken with the filter removed, there was no detectable change in the measured displacement.

4

Bubbles

4.1 Background and theory

The presence of gas bubbles will affect HIFU lesion formation and detection in a number of ways. Inertial cavitation may dramatically enhance acoustic heating and cause lesion formation at higher rates and in different regions than expected. Boiling will limit temperature by absorbing heat as latent heat of water, and may result in bubbles so large that the HIFU beam is partially blocked and reflected. Bubbles have a high acoustic impedance mismatch with water or tissue and thereby enhance acoustic forcing. They will also affect HMI because they may produce strong transient echoes of the interrogation pulse, destroying the line-to-line correlation required for speckle-tracking. These effects will be discussed in this chapter, as well as results of modeling and measuring their presence in the HMI data.

4.1.1 Cavitation

Generally, gas bubbles may form in liquids and solids by chemical reactions or by dissolved gasses coming out of solution due to a lowering of pressure or increase in temperature (Crum 1982). Once present, bubbles can grow if the local or ambient pressure is decreased below the vapor pressure of

the gas in the liquid. The negative pressure of high amplitude acoustic waves can initiate bubble formation in this way. The formation and subsequent oscillation of bubbles by acoustic excitation is referred to as acoustic cavitation (Leighton 1994). One form of acoustic cavitation, called inertial cavitation, occurs when bubbles grow to several times their initial size and then collapse violently. Driven by the inertia of the surrounding fluid, the density and temperature can momentarily reach very high levels, emitting an intense pressure pulse and even light (Frenzel and Schultes 1934, Suslick et al. 1990). Non-inertial cavitation is referred to as stable cavitation.

4.1.2 Linear and nonlinear oscillations and scattering

At small amplitude, bubbles oscillate linearly, like damped harmonic oscillators. The resonance frequency is determined by the “spring” of the pressure of the gas in the bubble, and the mass of the fluid layer surrounding the bubble.

$$\omega_0 = \frac{1}{R} \sqrt{\frac{3YP_0}{\rho}} \quad (4.1)$$

Where R is the equilibrium bubble radius, Y the polytropic constant, P₀ the equilibrium pressure in the fluid, and ρ is the fluid density. For a 1μm bubble in water, this is 3.3MHz. When a bubble is excited by an acoustic wave, the subsequent oscillations will re-radiate sound (i.e. scatter). The single bubble scattering cross section, defined as the total scattered power divided by the incident acoustic intensity, is given by Leighton (1994):

$$\sigma_{scat} = \frac{4\pi R^2}{\left[(\omega_0/\omega)^2 - 1 \right]^2 + \text{damping}} \quad (4.2)$$

Below resonance, the power radiated is proportional to ω⁴, as expected for small scatterers (Rayleigh scattering).

At large amplitude the oscillations can be highly non-linear and even chaotic. A number of models have been proposed for describing non-linear bubble oscillations. In this work a numerical solution

will be found for a modified Keller-Miksis equation, following the approach of Hilgenfeldt et al.

(2000):

$$\left(1 - \frac{\dot{R}}{c}\right) R \ddot{R} + \left(1 - \frac{\dot{R}}{3c}\right) \frac{3}{2} \dot{R}^2 = \left(1 + \frac{\dot{R}}{c}\right) \frac{1}{\rho} (p(R, t) - P(t) - P_0) + \frac{R}{\rho c} \frac{d}{dt} p(R, t) - 4v \frac{\dot{R}}{R} - \frac{2\zeta}{\rho R} \quad (4.3)$$

where v , ρ and c are the kinematic viscosity, density, and speed of sound of the liquid, respectively;

and ζ is the surface tension of the gas/liquid interface. P is the pressure of the acoustic wave, and p is the internal pressure in the bubble. Once $R(t)$ is thus calculated, the scattering power may be derived from the expression for the pressure radiated from a spherical source (Vokurka 1990):

$$p(r, t) = \rho \left[\frac{1}{r} (R^2 \ddot{R} + 2R \dot{R}^2) - \frac{R^4 \dot{R}^2}{2r^4} \right] \quad (4.4)$$

Usually the second term is ignored, since it quickly falls to zero with r . The solution of (4.3) can reveal the sharp collapsing in radius found in inertial cavitation, which results in spikes of pressure.

4.1.3 Expected bubble size

Once bubbles are formed they can either dissolve back into solution, or grow with each acoustic cycle by a process known as “rectified diffusion” (Eller & Flynn 1965). They may also break apart if they become a-spherical in shape (Eller & Crum 1970, Maksimov & Leighton 2001). Yang et al (2004) used theory for these two processes, along with nonlinear bubble oscillation models and other physics pertaining to bubbles in fluid, to predict the range of allowable bubble sizes in high pressure ultrasound fields. Figure 4.1 shows their plot of thresholds for allowable bubble sizes in an acoustic field of 2.5MPa peak pressure at a frequency of 1MHz, as a function of bubble equilibrium radius and fluid viscosity. The horizontal lines labeled “a” and “b” represent the predicted size evolution of a bubble starting at 50nm, for two different fluid viscosities. For the higher viscosity, the bubble grows via rectified diffusion until it reaches a theoretical limit where the process can no longer add gas to the bubble. This limit depends on the dissolved gas concentration in the fluid. Lines for this limit are drawn for various concentrations. For example, “RD20” represents the limit for 20% gas concentration. For the bubble “a” at the lower viscosity value, the shape instability threshold (“SI”) is reached when it grows to about 1 μ m.

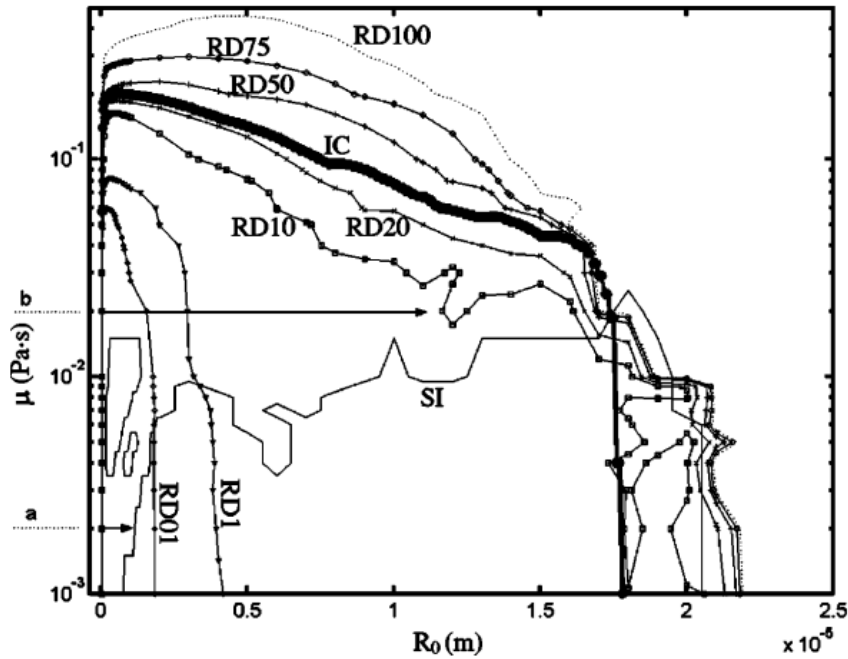


Figure 4.1 Plot of bubble size thresholds as a function of equilibrium radius and fluid viscosity, from Yang et al. (2004), for an ultrasound excitation of 2.5MPa peak pressure at 1MHz. “SI” is the shape instability threshold. “IC” is the limit beyond which inertial cavitation can no longer occur, and “RDxx” are the maximum growth levels for rectified diffusion, for various percent gas concentration xx in the fluid.

Thus, assuming the gas in the chicken or liver tissue used in this study is from 50 to 100% saturated, we may expect bubbles to grow up about 17 μ m, if the viscosity is over about 0.01 Pa-s. If it is below this, the bubbles will not get bigger than about 1 μ m before they become unstable. Bubble growth via rectified diffusion is a rapid process, so the maximum size will be reached in <2sec. We may thus infer that all the bubbles in an area with a given acoustic intensity will be of approximately the same size. Finally, when considering what bubbles may be present during HIFU, it must be kept in mind that there could also be cavities made by boiling.

4.1.4 Bubble effects on heating and acoustic forcing

The affects of bubbles on HIFU heating and forcing are numerous. First of all, they can greatly enhance HIFU heating through the re-absorption of energy scattered from inertial cavitation

(Hynynen 1991, Malcolm and ter Haar 1996, Holt and Roy 2001). Also, bubbles can diminish or re-direct the acoustic field through reflection and scattering. In a study of HIFU with in-vivo rabbit thighs, Rabkin et al. (2006) observed that thermal damage and hyper-echogenicity (on B-mode images) occurred in front of the focal zone and moved backwards during exposure. This they hypothesized was due to ultrasonic energy being blocked and reflected by bubbles at the focus. In a different experiment, Bailey et al. (2001) put samples of in-vitro bovine liver in a pressurized vessel to reduce the growth of bubbles and noticed that this prevented the backward growth of heat damage, reinforcing the conclusion that the backward growth was due to bubble reflection. Rabkin et al. observed that the cavitation-enhanced heating was always accompanied by hyper-echogenicity, which they hypothesized could have been due to vapor cavities (i.e. boiling), although it remains uncertain as to whether boiling always leads to hyper-echogenicity, nor whether hyper-echogenicity always indicates boiling.

In addition to removing significant portions of the HIFU beam by reflection or scattering, boiling affects the heating process by putting energy into latent heat. This will tend to keep the temperature constant once boiling starts. In their thermal models of HIFU heating, Meany et al. (2000) treated boiling by re-distributing the heat energy that *would have* been deposited beyond the boiling bubbles into a 5mm sphere around the point at which boiling began. Mast et al. (2005) took this approach one step further by limiting the temperature to the boiling point of 100 °C until all the latent heat of boiling was used up, at which point they allowed the temperature to rise as usual. They reported that this step had little effect on the modeled temperature results. In the case of the present study, the time required to convert all of the water in the HIFU focal region to vapor can be approximated with a simple calculation. The HIFU pressure is taken to be 7MPa, and the focal volume to be $11.7 \times 10^{-9} \text{m}^3$. For a tissue acoustic absorption of 5Np/m/MHz , the rate of heating per volume is 2.1 J/s (Watts). If the latent heat of water is $2.26 \times 10^6 \text{ J/kg}$, and heat conduction ignored, the time required to boil a volume of water the size of the focal region would be about 10s, once boiling began. However it may be assumed that the original heating rate would be diminished due to reflections and

scattering from the boiling bubbles.

The most significant effect of bubbles on HMI is the added force due to the impedance mismatch between the gas inside the bubbles and the tissue. The radiation force on a gas bubble in water is $F_{bub} = 2I/c * \pi r^2$ (Erpelding et al. 2005) where I is the incident intensity, and r is the bubble radius. The number and size of bubbles needed to create the same volumetric force as that due to acoustic attenuation can be calculated using equation (2.7): $2\alpha I/c = F/vol = n/vol * F_{bub}$. The relationship then becomes $r^2 N = \alpha/c$ where r and N are the bubble radius and number per volume, and α is the attenuation, which for chicken is about 5.5 Np/m. Evaluating the total force in the acoustic focal volume, it would take 17,000 1 μ m bubbles to make the same force as that due to attenuation. Similarly, 170 10 μ m bubbles and 1.7 100 μ m bubbles would be required.

Finally, sufficiently large void fractions due to bubbles will change bulk tissue properties like soundspeed (Commander and Prosperetti 1988), which would have a significant effect on HMI calculations. However it is doubtful that such large void fractions will be made during HIFU lesion formation.

4.1.5 Dissolution time

In order to deduce bubble size by observations of decreasing echogenicity in time (after HIFU is turned off), the dissolution time may be solved using

$$\dot{R} = \frac{D(c-c_0)}{\rho} \left[\frac{1}{R} + \frac{1}{\sqrt{\pi D t}} \right] \quad (4.5)$$

where R is bubble radius, D is the diffusion constant (=2e-9 for nitrogen or oxygen in water), c_0 is the gas saturation concentration, and c the gas concentration. Figure 4.2 shows the results as a function of initial radius and gas concentration. It is observed in many lesion experiments that regions of increased echogenicity develop during HIFU, and then diminish within 10 seconds. If it is assumed that the gas concentration in tissue is between 50 and 100%, the figure shows that the initial bubble radius is less than 30 μ m. Note that this calculation assumed there is no water vapor inside the bubble. This may not hold for bubbles produced by boiling.

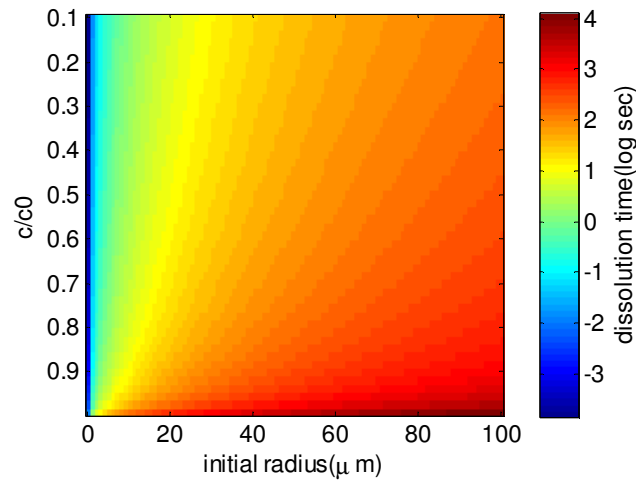


Figure 4.2 Bubble dissolution time vs. gas concentration and initial bubble size, for bubble of either nitrogen or oxygen, in water.

4.2 Modeling scattering from cavitation bubbles

During the lesion/HMI experiments, the backscattered interrogation pulse signal often showed signs of possible bubble activity, in the form of increased echogenicity, higher harmonic content, and loss of line-to-line correlation. If these could be attributed to bubble size, number, and type of cavitation, it would aid in the interpretation and modeling of thermal and HMI behavior during lesion formation. Various bubble sizes were modeled using Matlab's PDE routines to solve the modified Keller-Miksis equation(4.3). The pressure inputs to the model were digitized waveforms of the exact HIFU and interrogation pressure fields used for interrogation and lesion-making in the HMI experiments, derated for propagation through the tissue. Once the values for $R(t)$ were found, the resulting pressure waveforms at the interrogation transducer could be calculated. To check the model output, the scattered pressure was calculated for a large bubble (60um), which is not expected to exhibit nonlinearity, and this agreed with values predicted by linear bubble scattering theory (equation (4.2)).

The pressure radiated from the bubble was calculated using (4.4). After derating this value for attenuation in the tissue, a transfer function was applied between the pressure at the focus of the interrogation transducer and the voltage signal from the interrogation transducer. To find this

function, a pulse from the transducer was measured in water by the membrane hydrophone and converted to Pascals. Then the membrane was replaced by a reflecting steel block and the received voltage was measured by the interrogation transducer. The ratio of the measured pressure at the focus to the voltage from the echo provided an approximate sensitivity function for the interrogation transducer. Finally, the modeled signal needed to reflect the 35dB gain from the pulser/receiver and the 5MHz hipass filter. The latter was a 9-pole Butterworth filter, for which the impulse response was calculated using the Matlab signal processing toolbox. The impulse response had a ringdown time of about $0.6\mu\text{s}$, which tended to add oscillatory rings to any short-lived spikes in the interrogation signal, such as those from inertial cavitation.

Figure 4.3 shows the response of bubbles of various initial size (R_0) to a 1.2MPa pulse from the interrogation transducer. The viscosity for chicken was chosen to be $2\text{e-}2$ Pas. The calculation was also done for the viscosity of blood ($3\text{e-}3$ Pas), yielding larger amplitudes by a factor of 2. The center frequency of the excitation pulse was 6MPa, at which frequency the resonant bubble size is $0.54\mu\text{m}$. Also shown is the resulting voltage after the hipass filter for a $1\mu\text{m}$ bubble. Bubbles sizes up to $100\mu\text{m}$ were also modeled, yielding similar waveforms which scaled with bubble size.

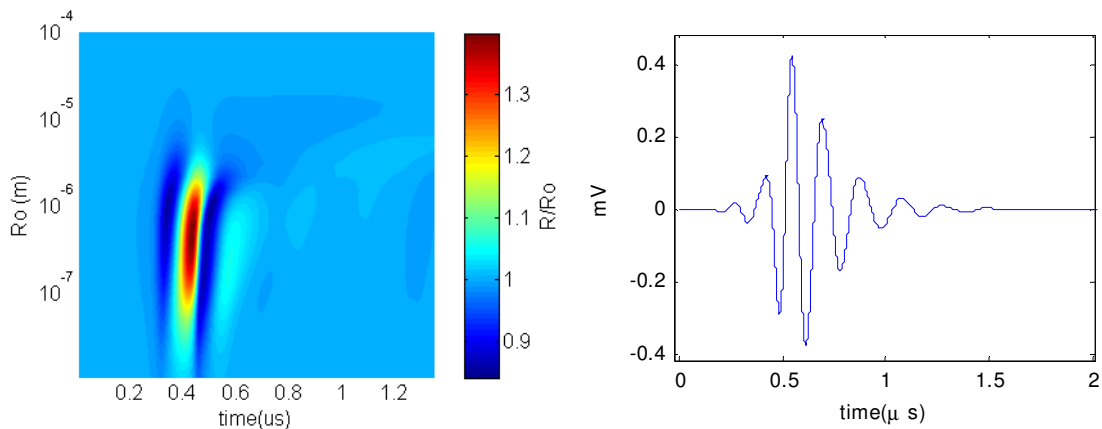


Figure 4.3 Calculated response of a bubble to a 1.2MPa pulse from the interrogation transducer. Viscosity = 0.02 Pa s. Left: size vs initial size, Right: calculated voltage signal from a $1\mu\text{m}$ bubble. Larger bubbles were calculated up to $100\mu\text{m}$, and the response scaled with radius.

The effect of bubble scattering on the spectrum of the interrogation signal from the tissue may also provide a clue to the presence and size of bubbles. The spectra of the calculated voltage signal

were derived from the same simulation as the data in Figure 4.3. Results are shown in Figure 4.4, along with the measured spectrum of the backscattered signal from chicken tissue without signs of bubbles. It is evident that the bubble scattering adds about 10dB to the spectrum between 8 and 14 MHz.

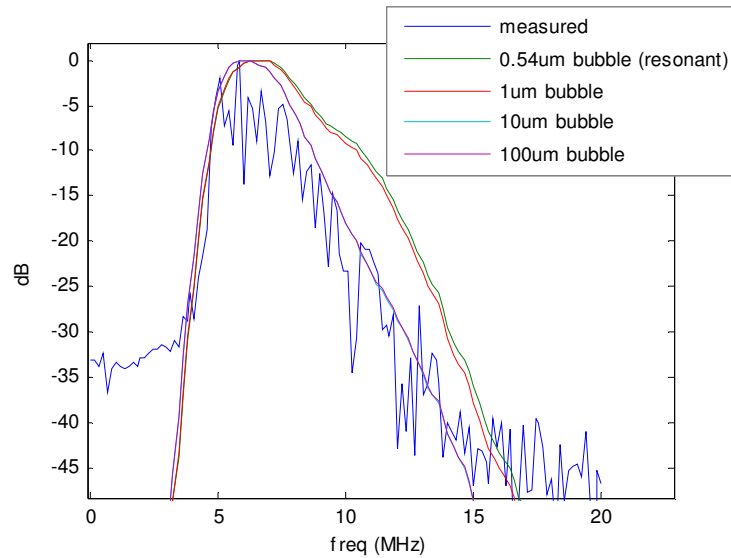


Figure 4.4 Normalized spectrum from measured backscattered interrogation pulse from chicken, along with calculated spectrum from nonlinear bubble scatterers. Viscosity=0.02 Pa s

The scattering model was repeated for the case of a HIFU excitation of 7MPa. Figure 4.5 shows $R(t)/R_0$ for various initial bubble sizes. Figure 4.6 shows data for just the 1 μ m and 8 μ m bubbles. The largest expansion ratio is seen for the 1 μ m bubbles. If the simulation were allowed to progress further in time a more steady pattern would emerge. The 1 μ m bubble would collapse once every HIFU cycle, and the 8 μ m bubble would collapse every 4 cycles.

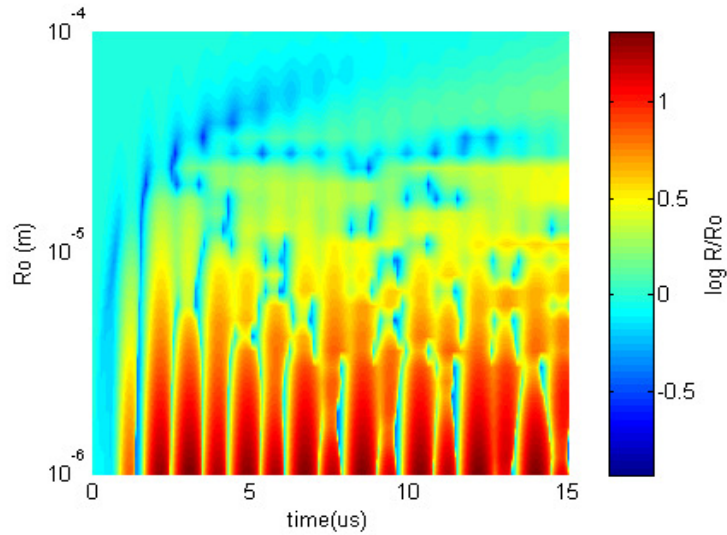


Figure 4.5 Modeled values of $R(t)$ for various initial bubble sizes in response to a 7MPa HIFU wave. The viscosity for this simulation was 0.02Pa s

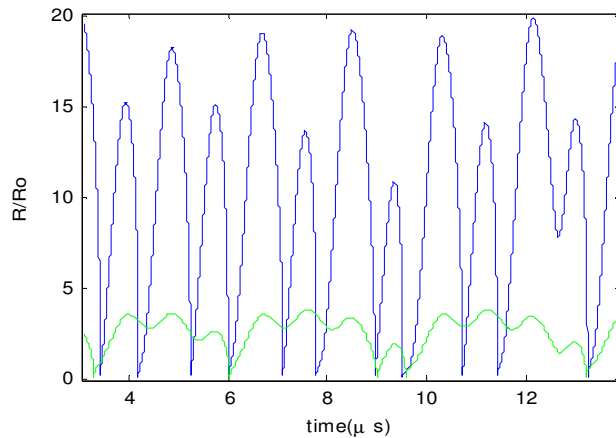


Figure 4.6 Oscillations in bubble radius $R(t)$ caused by a 7MPa 1.1MHz HIFU wave, plotted for initial bubble radii of 1 μm (blue) and 8 μm (green).

Each collapse emits a short pressure pulse. The pressure from these collapses, calculated by equation (4.4), results in a series of spikes in time. Once again, the re-radiated pressure is derated for propagation through the tissue, and passed through the transfer function of the interrogation transducer, the amplifier, and the hipass filter. The resulting voltage signal is shown in Figure 4.7. The calculated pressure pulses are well over 50MPa at the bubble. However the physical assumptions of the model and the assumption that the bubble remains perfectly spherical, may not hold at the point of collapse, as does the assumption of linear wave propagation of these pulses. For

these reasons, the predicted received voltages in Figure 4.7 are an overestimate. Nevertheless, the basic result of the nonlinear bubble scattering model is that pressure spikes will be generated if inertial cavitation occurs, and these spikes will far exceed the acoustic pressure scattered from bubbles that are not inertially collapsing. For the smallest bubbles modeled the spikes are strongest, and come every cycle of the HIFU excitation (presuming they survive each collapse). Inertial collapses from larger bubbles are seen to occur at integer multiples of the HIFU period.

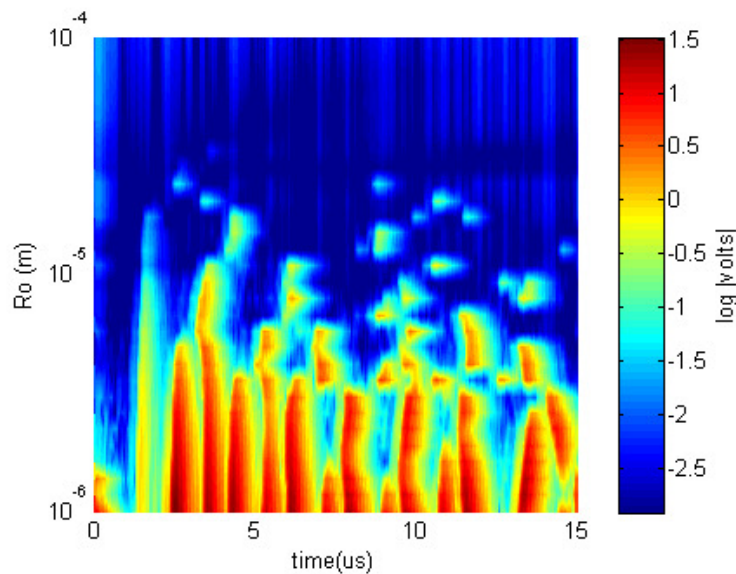


Figure 4.7 Calculated voltage after the hipass filter for the same model as Figure 4.5. This is intended to show relative voltage levels for various size bubbles. The magnitude is inaccurate due to the uncertainty of the size of each pressure pulse created during inertial implosions.

The spectra of the voltage signals are shown in Figure 4.8. The model was carried further out in time in order to allow a steady state to be reached. Around the resonant bubble size ($\sim 3\mu\text{m}$) there is an increase in broadband energy as well as harmonics and half-harmonics of the HIFU frequency.

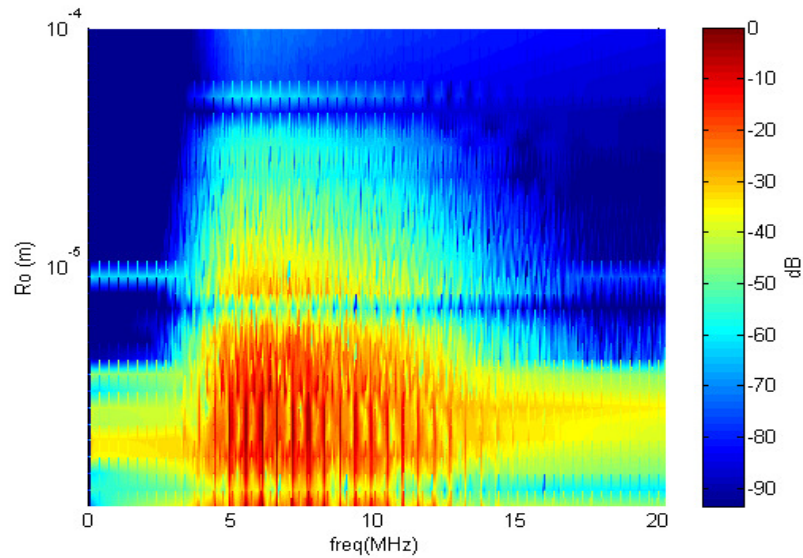


Figure 4.8 Spectra of the voltage signals from the scattering of 7MPa, 1.1MHz HIFU wave off various size bubbles.

4.3 Observations

The purpose of this section will be to present and classify evidence of bubbles occurring in the HIFU lesion/HMI experiments, and to examine potential bubble effects on HMI, AOI and thermal modeling. The main source of data in the HMI experiments is the pulse/echo data from the interrogation transducer.

4.3.1 Lesion/HMI case studies

Figure 4.9 shows data from a 7MPa, 36s HIFU exposure in chicken tissue in which HMI data was taken in accordance with the description in section 3.2 of the experimental setup and timing sequence. The A-lines from the interrogation transducer are presented in plots (a) and (b), and show a growth in echogenicity at certain depths in the tissue. The duration within the A-line of these echoes is less than one microsecond. According to Figure 4.3, that is the expected response duration of one bubble, together with the ring-down time associated with the hipass filter. It is thus expected

that these regions of increased echogenicity correspond either to one bubble, or to a group of bubbles clustered in a region of space less than 0.4mm. The HIFU focus was at a depth of 15mm, which corresponds to 20 μ s on the horizontal axis of pulse/echo time. As outlined in section 3.2, the occurrence of A-lines is not linear with time. Hifu heating periods lasted 4s each and comprised 40 lines. HMI interrogation periods lasted 0.1s and comprised 128 lines. Three or more bubbles appear to grow between 20 and 26 μ s in depth, one of which persists after the HIFU stops at line #1600. The dissolution time on the others takes place within one 4s "heating phase" (HIFU is off here, so there is no heating), so their expected size is less than 15 μ m, according to Figure 4.2. According to the analysis for Figure 4.1, rectified diffusion cannot account for bubbles much larger than 15 μ m, suggesting that the bubble at 22 μ s which persists over 18s must be due to boiling. Another bubble is seen to form and disappear at a depth of 28 μ s. Plots (c) and (d) are spectrograms of line #1200 and #1550 (each element Hamming windowed, with 50% overlap with the next). At line #1200, where the deepest bubble echo is strongest, there is some evidence of a more broadband echo at the deep bubble location. At line #1550, the strongest echo is at 25 μ s, and there is a strong broadband signature associated with it. The HMI results for this run are shown in Figure 4.10. There is a marked region of higher displacement amplitude which coincides with the location of the deepest bubble, indicating that this region is being forced considerably more than the surrounding tissue. According to the analysis of section 4.1.4, this would result from a bubble at least 100 μ m in radius. The fact that the echo from this region, and the HMI displacement, diminishes before the end of HIFU may be due to the region being shielded by the shallower bubble(s) at 22-25 μ s.

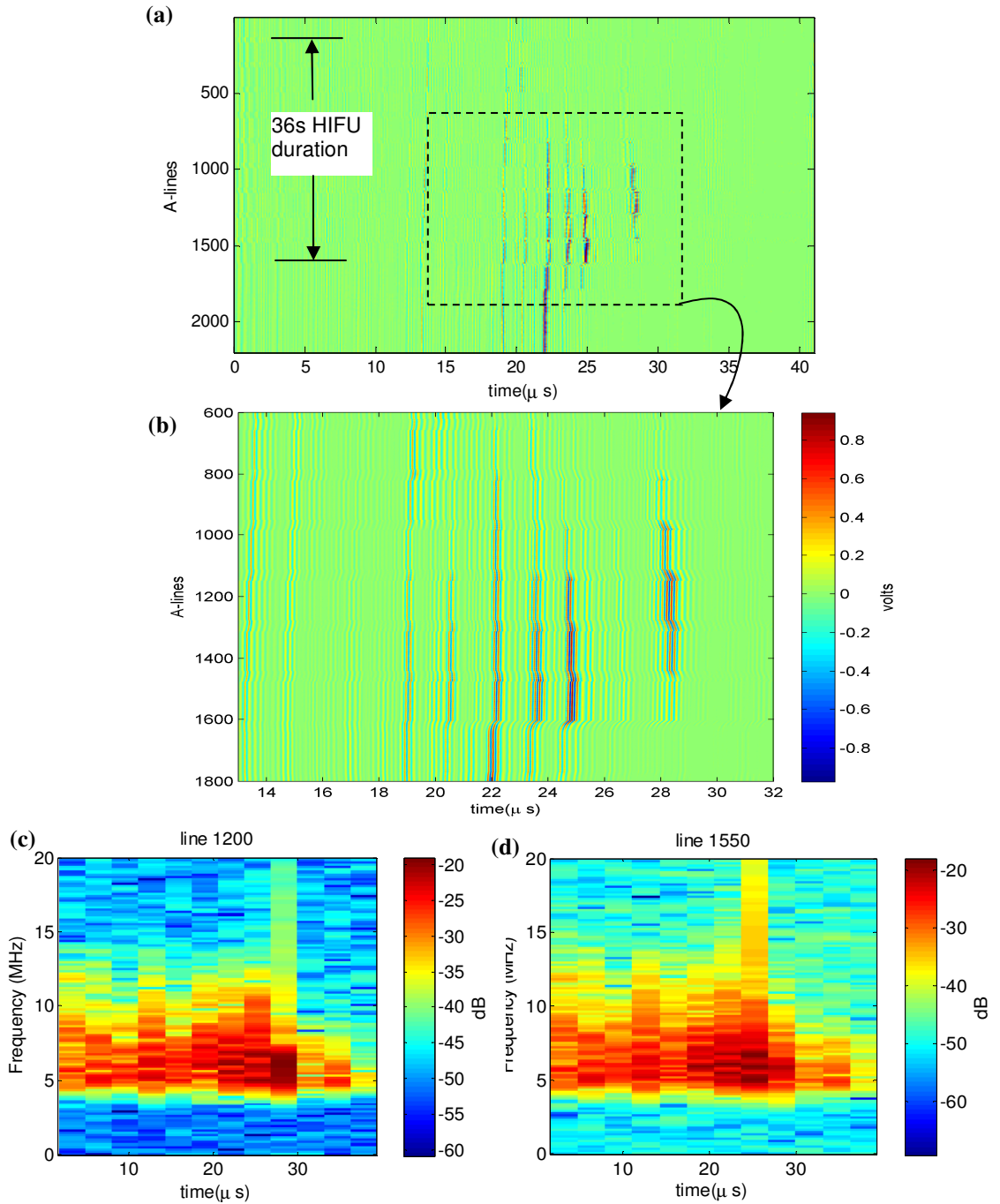


Figure 4.9 Data from a 7MPa, 36s HIFU exposure. (a) A-lines from interrogation transducer, showing growth of region of increased echogenicity, possibly caused by scattering from bubbles. (b) zoom-in. (c) spectrogram of A-line #1200. (d) spectrogram of A-line #1550.

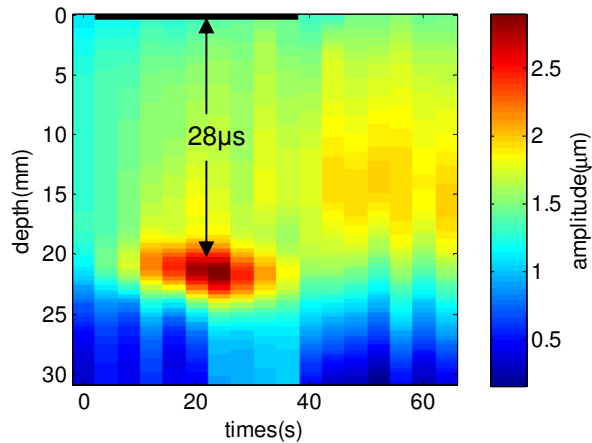


Figure 4.10 HMI results for the data shown in Figure 4.9. The black bar over the top indicates the HIFU on-time.

Figure 4.11 shows the results of another lesion run in chicken, taken with an 8MPa 36s HIFU exposure. An interesting phenomenon is seen during the heating phase around line #1457. Plot (b) contains the spectrogram of this line, showing an increase in bandwidth at 20 μ s, and an abundance of harmonics of the HIFU frequency occurring at all times. This is energy from the HIFU beam scattered back to the interrogation transducer. There is, of course, no information available to reveal the depth of the origin of this energy, since the HIFU wave is continuous, unlike the interrogation pulse. Plot (c) shows a portion of the line (#1457), revealing periodic spikes occurring every HIFU period. The ring-down from the hipass filter can be seen after each spike. The Fourier spectrum of a pulse train such as this is a pulse train in frequency, and the harmonics extend upward in frequency to a point defined by the width of the pulses. The energy in line #1457 is thus consistent with a bubble, or perhaps a group of bubbles, undergoing inertial collapses every HIFU cycle. The nonlinear scattering model shows that bubbles less than 3 μ m exhibit this behavior. None of the other heating periods produced these harmonics in the backscatter spectra, even those associated with the region between lines 500- 1000, which has a stronger echo. It may be inferred that the origin of the HIFU backscattered energy in line #1457 is from the region around 20 μ s, because this is where a

broadening of the interrogation spectrum is seen. Note that the spectral signature of the cavitating bubble may look different for a CW excitation as compared to a single pulse. For a single pulse, and for CW excitation that produces inertial collapses randomly distributed in time, the spectrum will be broadband, with no HIFU harmonics. However, for a CW excitation that produces periodic inertial collapses, the energy will be concentrated in frequency space only at harmonics of the collapse period. The energy in line #1457 contains both types of excitation, CW HIFU and single pulse. It is commonly accepted that the best indicator of inertial cavitation is a broadband spectrum, and the best indicator of non-inertial cavitation is the occurrence of harmonics and subharmonics (ter Haar 2004). The harmonics seen in this work are clearly from periodic pressure spikes caused by collapsing bubbles, so it may be that this sort of behavior is not seen in other tissue types or experimental approaches. For evidence of *subharmonics* caused by periodic spikes, and other interesting bubble phenomena, see 8.1.2 Appendix F.

In the HMI data, increased motion can be seen at the focus after the first heating period, but then it falls at the same time the first increase in echogenicity is seen at 19 μ s. This is possibly due to shielding from these bubbles. No increase in tissue displacement is associated with the rise in echo strength, as might be expected from increased force on bubbles.

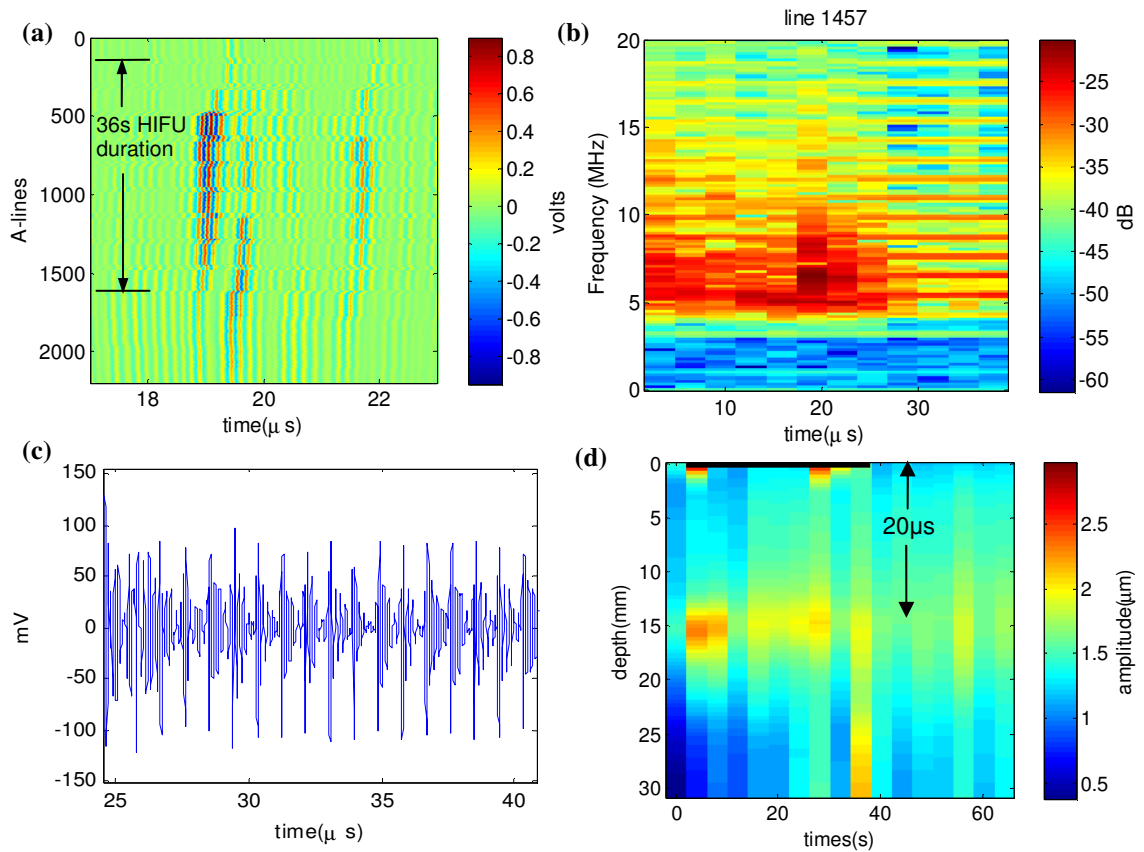


Figure 4.11 8MPa 36s HIFU exposure in chicken. (a) A-lines showing the only region of increased echogenicity. (b) spectrogram of line #1457. (c) time trace of a portion of line #1457, showing periodic spikes. (d) HMI displacement. Black bar over top indicates HIFU on-time.

4.3.2 Harmonic content of backscattered Hifu from chicken, without cavitation

In order to be able to distinguish between the spectral signature of bubble scattering to that of the HIFU wave scattered from tissue without bubbles, short (33 cycle) HIFU bursts of various pressures were launched into chicken tissue, and the backscattered energy received by the interrogation transducer. The backscatter waveforms were viewed on an oscilloscope triggered at the PRF of the bursts. These waveforms appeared steady, so it was inferred that no bubble activity was present during the short bursts. Figure 4.12 shows the harmonic content of the received signals on the interrogation transducer, relative to the fundamental frequency of 1.1MHz. Note that the transfer function of the interrogation transducer is far from flat, but this was left uncorrected

because the spectra of the A-lines taken during lesion/HMI experiments are measured on the same transducer. The sensitivity of the interrogation transducer peaks at 6MHz, and is down 12 dB at 1.1MHz.

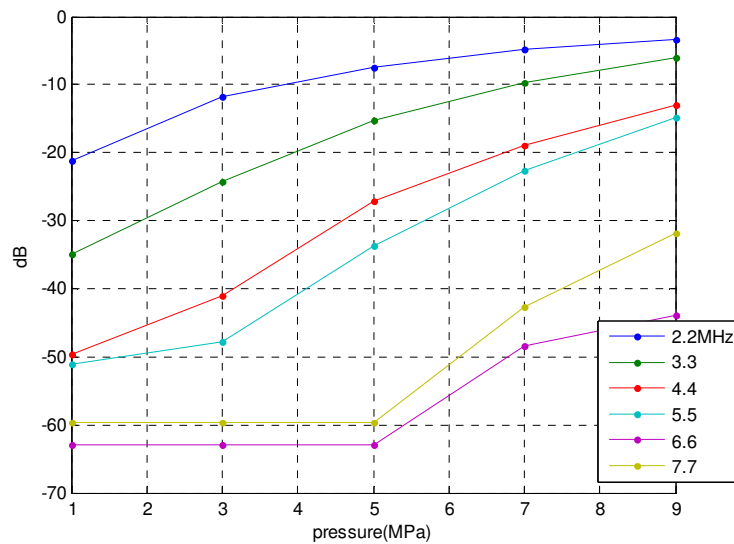


Figure 4.12 Harmonic content, relative to fundamental, of 33 cycle bursts backscattered from chicken at various pressure levels.

There is a steady rise in harmonic content with pressure. Although some of this could be from nonlinearities in the transfer function of the transducer, the majority is from nonlinear acoustic propagation. The relative harmonic content in this plot agrees with data from a computer simulation using the KZK equation (data not shown. See 8.1.2 Appendix E for description of simulation). Harmonics below 5.5MHz are usually filtered out by the 5MHz hipass filter. At 7MPa (the usual pressure used to make lesions in this work), the harmonics decay at approximately 6dB intervals. It appears that this interval may be higher for harmonics above the 6th. This serves as independent confirmation that the harmonics seen in Figure 4.11b are not from HIFU scattered from non-bubble tissue scatterers.

4.3.3 Relative occurrence of bubble-related phenomena

Hundreds of lesion/HMI runs were performed, and the results are presented in chapter 6 . In addition to the HMI tissue displacement amplitude, plots were generated of the A-lines and their spectrograms and assembled in order to assess the detectability of lesions with HMI. From observing this data, it is possible to make the following observations about bubbles and their effects.

In one class of data, an increase in echogenicity was usually seen with lesion-making pressures (i.e.>5MPa). Much of this extra echogenicity decayed after the Hifu turned off. In this class, there was seldom an occurrence of multiple harmonics. In another class of data, runs with greatly increased echogenicity over many depths usually occurred with HIFU pressures above 8MPa and the echoes usually did not decay with time after the cessation of HIFU. Broadband spectra and multiple harmonics were usually present in these runs, and the HMI data was usually strong and random, often with regions of ten-fold increase in displacement. The HMI data was also noisy due to diminished degree of correlation between successive A-lines. On runs in which a B-mode imager was also employed, regions of extra echogenicity could be seen. This was not true for the first class of data, for which the increased echoes decayed with time (suggesting bubbles were small enough to dissolve quickly).

Broadband regions were seen in the spectrograms of most of the runs. However, as seen with the bubbles occurring from 22 to 25 μ s in Figure 4.9, they were often uncorrelated with tissue motion. Finally, less commonly observed phenomena included cases in which bubble shielding was clearly present, or cases in which regions of increased HMI displacement were correlated with increased echoes.

4.4 Conclusions:

In this chapter, results of calculations were presented which showed likely bubble sizes, bubble size vs. dissolution time, expected force on a bubble, and expected time and frequency signatures of

bubble-scattered energy. Measurements of backscattered energy during lesion/HMI runs were analyzed and it was shown how features revealed information about the size of bubbles and their effect on HMI measurements. This study helped in the interpretation of the results of the HMI displacement analysis; for example it showed when data could be untrustworthy due to the presence of boiling; when bubble shielding may have influenced the displacement pattern, and when isolated regions of high displacement were possibly caused by bubbles.

5

The Finite Element Model

5.1 Introduction

A finite element model was made to simulate the HIFU lesion process with concurrent harmonic motion imaging, in order to check the measured results and provide insight into the various contributing processes. Separate models were made to solve the acoustic wave equation, heat equation, and solid elasticity equations. The acoustic, thermal, and displacement fields were permitted to interact, taking into account the temperature-dependant tissue properties of acoustic absorption and shear modulus. Previous attempts to model ARFI and HMI involved just the elastic model, assigning either “cooked” or “uncooked” values to the stiffness of a designated lesion area (Lizzi et al. 2003). Konofagou et al. (2001), and Haw (2008) also modeled the increased absorption of the lesion. A recent numerical study by Heikkila et al. (2010) includes both thermal and mechanical models, allowing for the modeling of lesion evolution, rather than just solutions for pre and post lesion. However, this didn’t consider the added attenuation to the sound field of the forming lesion. It will be shown that this is a significant factor.

5.1.1 The finite element method

A brief overview of the finite element method is presented here. The software package used was Comsol (Burlington, MA) . The program allows manipulation of the underlying differential equations, so various models for visco-elasticity can be employed. Finite element analysis usually consists of the following steps:

1. Divide the modeled geometry into polygonal elements, and write an approximate solution for each element in terms of the field values at each vertex(node) of the element.

2. Develop an algebraic system of equations for all nodal values in the mesh, incorporating continuity and boundary conditions. Nodal values, and sometimes their derivatives, are continuous across element boundaries.

3. Solve the system for all nodal values. The final form of the system of equations to be solved has the form

$$[K]\{u\} = \{F\} \quad (5.1)$$

Where $[K]$ is a matrix containing property information about the domain, for example stiffness for structural problems, dielectric permittivity for electrostatic problems. $\{u\}$ is the field variable and describes system behavior, e.g. displacement for structural problems or electric potential for electrostatic problems. $\{F\}$ describes the “action” acting on the system, e.g. force in structural problems or charge in electrostatic problems.

The Comsol software package uses the principle of virtual work to solve structural mechanics problems. This states that, after imposing a small displacement δu , the resulting strain energy equals the work done by surface and body forces.

$$\int_{vol} \sigma_{ij} \delta e_{ij} dV = \int_{surf} T_i^n \delta u_i dS + \int_{vol} f_i \delta u_i dV \quad (5.2)$$

Here the strain δe is derived from displacement δu via $\delta e_{ij} = \frac{1}{2}(\delta u_{i,j} + \delta u_{j,i})$, where standard index notation is used. Within each element, the field variable $u(\mathbf{r})$ is interpolated as a function of the values u_i at the nodes of the element:

$$u(\bar{\mathbf{r}}) = \sum_{i=1}^N u_i \psi_i(\bar{\mathbf{r}}) \quad (5.3)$$

Where u_i are the values of u at the nodes, and ψ_i are known as interpolation functions, or shape functions. These are simple linear (or sometimes higher order polynomial) functions that equal 1 at node i , and 0 for the other nodes of the element. After inserting the expression for $u(\mathbf{r})$, equation (5.2) can be expressed as

$$\{\delta u\}^T ([K]\{u_i\} - \{F\} - \{Q\}) = 0 \quad (5.4)$$

where

$$\begin{aligned} [K] &= \int [B]^T [C][B] dV && = \text{stiffness matrix} \\ \{F\} &= \int [\psi]^T \{f\} dV && = \text{body force vector} \\ \{Q\} &= \int [\psi]^T \{T\} dS && = \text{loading vector} \end{aligned} \quad (5.5)$$

Here \mathbf{C} is the usual elasticity matrix for the material and \mathbf{B} consists of derivatives of the shape functions, which are constants for linear shape functions. The virtual work term δu , can be dropped because (5.4) must hold for arbitrary values of δu . Equation (5.4) must be solved for each element. Of course, the elements are connected, so each nodal value u must have be the same for all elements that it is part of. Thus, the final step is to transfer the nodal coordinates of each element to one set of master coordinates, and incorporate (5.4) for each element into one large matrix, which is then solved numerically. The results are values of u at all the nodes in the domain.

5.2 The general model

This section describes the acoustic, thermal, and mechanical models. In the experiments the tissue samples were about 4cm thick, with the acoustic focus placed at a depth of 1.5cm. They were approximately rectangular, with sides of 5cm or more. Since the acoustic field was axisymmetric, the tissue is modeled as a 4cm tall, 6cm diameter puck. A representative mesh is shown in Figure 5.1. In general the mesh needs to be fine enough for model convergence, but coarse enough to enable solution with limited computer memory. The mesh was generated automatically by the program, but local density and element shape could be controlled. The computer used was a PC with an Intel 2.4GHz Core2 Quad 660 processor and 3.25GB RAM, running the WindowsXP operating system.

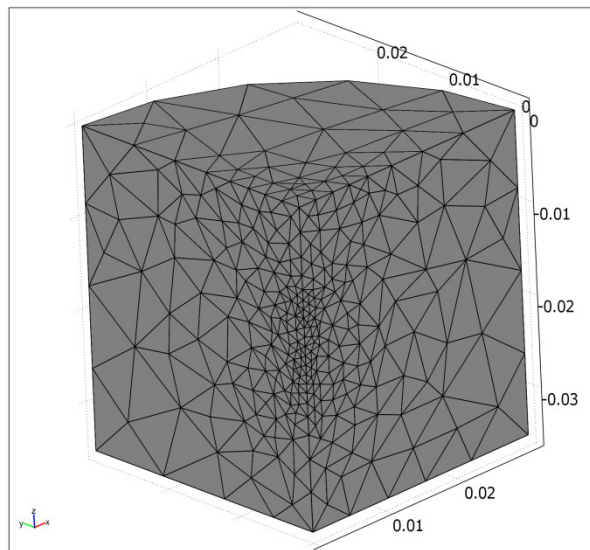


Figure 5.1 Mesh for the basic 3d model Units are meters.

Both 3-d Cartesian and axisymmetric models were made. The later requires much less memory and processing time, and was the only option for the large models combining acoustic and thermal fields, and time-evolving tissue parameters. Figure 5.2 shows the axisymmetric mesh, together with a colored map of the acoustic field, which is imported from a text file from the Matlab angular spectrum routine. Comsol interpolates this onto the FEM mesh.

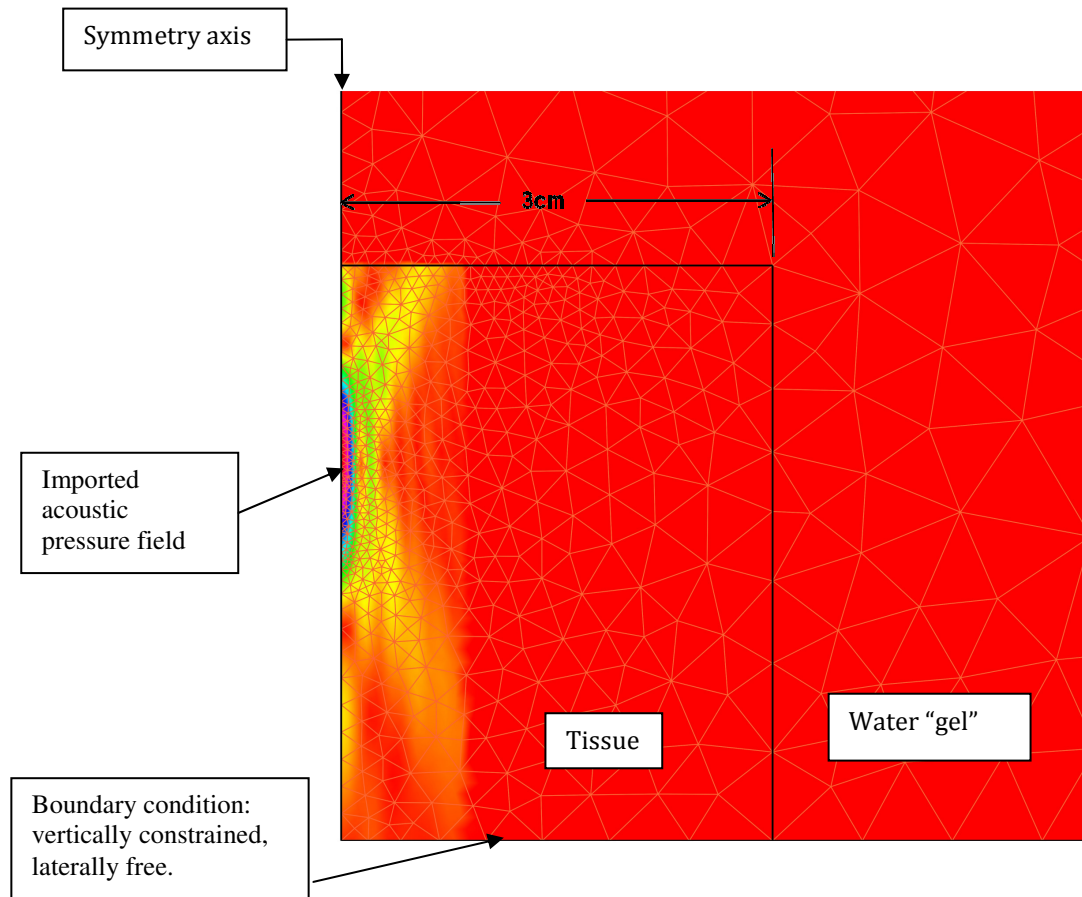


Figure 5.2 Mesh for 2-d axisymmetric models, with imported acoustic field

5.2.1 Acoustic modeling

The FEM model requires the magnitude of the acoustic intensity for the heat source in the thermal model, and the vector components of intensity for the force source in the mechanical model. The acoustic field was calculated in Matlab using the angular spectrum technique, and the spatial distribution of the scalar fields I_r and I_z were imported into Comsol.

Nonlinearity in the acoustic field will result in a lower overall intensity for a given peak pressure than is calculated from the linear angular spectrum model. This is treated in the same way as for the

Parker model (see section 3.4.3.2.1). The intensity is multiplied by a correction factor in the form of a 2nd order polynomial in pressure. The peak pressure for each simulation is input as a target peak pressure in water. This and the nonlinear correction factor then multiply the interpolated pressure field to achieve the predicted field in the tissue. The acoustic field in the model could be further manipulated by lesion formation (see section 5.4.1) in the combined model. The acoustic field was only imported into the axisymmetric models. In the 3-d models, which were only used for test purposes, the acoustic forcing was modeled as a constant volume force over an ellipsoid at the focus, and the surface acoustic radiation pressure was modeled as a constant pressure over a disk.

5.2.2 Thermal modeling

The thermal model solves the heat equation in time for purely conductive heat transfer,

$C_p \frac{\partial T}{\partial t} + \nabla \cdot (-k\nabla T) = Q$, where Q is the volumetric heat source given by $Q(r,z)=2\alpha I(r,z)$ (equation (2.2)), where α is the acoustic absorption. In the combined model, the acoustic absorption was allowed to vary with temperature, and thus had r , z , and t dependence. Even though the program was solving for temperature, the value for acoustic absorption could be entered by the user as an equation with dependence on temperature.

5.2.2.1 Bubbles: shielding and boiling

In some cases the temperature solution rose above 100 degrees C. It is reasonable to assume that boiling would occur at this point, thus limiting further temperature rise until all the water was converted to vapor. This was implemented in the FEM model by entering a temperature dependence for the input acoustic heat source which tapered to zero as the temperature neared 100 degrees. In the results section this treatment is compared to the case where no such limitation was implemented. Ter Haar (2000) and Mast (2005) reasoned that, once boiling started, the bubbles would scatter acoustic energy into the surrounding tissue. They modeled the situation such that all the heat energy that was deposited for $z > z_0$, $t > t_0$ (where t_0 is the time of first appearance of 100°, and z_0 is the depth there), was applied to a sphere of a few millimeters in diameter. No attempt has

been made to model other effects of boiling or cavitation, such as added heat from inertial cavitation, added forcing due to impedance mismatch, or shielding.

5.2.3 Mechanical modeling

As previously described, Comsol uses the principle of virtual work to solve the linear elastic solid differential equation $\varepsilon = C\sigma$ where ε and σ are the 6 element strain and stress vectors, containing the normal and deviatoric parts, and C is the 6x6 compliance matrix. The input forces to the model were those of the acoustic radiation force.

5.2.3.1 Volume force

Inside the tissue, the volume force was given by $\vec{F}(\vec{r}, t) = \frac{2\alpha\vec{I}(\vec{r}, t)}{c}$, where α in this case is total attenuation. It was difficult to import the acoustic intensity field calculated by the angular spectrum technique into the 3-d test models, so the force was input as a constant value over an ellipsoid that coincided with the half-power contour of the acoustic main lobe. The value for this force was calculated so that the total force delivered was equal to that delivered by the entire main lobe of the acoustic field as calculated by the angular spectrum method.

5.2.3.2 Surface force

As the acoustic wave passes from the coupling fluid (water) into the tissue, it will impart a surface force at the interface due to the impedance mismatch. It was shown in section 2.2, that the effective pressure due to this effect is $P_s = \left\{ (1 + R^2) - T^2 \frac{\rho_1 c_1^2}{\rho_2 c_2^2} \right\} \frac{p^2}{\rho_1 c_1^2}$ where R and T are the pressure reflection and transmission coefficients.

As mentioned, the acoustic field from the angular spectrum method was not used in the 3-d test models, so the surface force was applied as a constant value over a 14mm diameter disk, such that the total force delivered was the same as that from the calculated acoustic field.

5.2.3.3 Boundary conditions

The tissue was bounded on the top and sides by water, which in Comsol was modeled as a gel solid with the density of water, a Poisson's ratio of 0.495, and a low shear modulus (50Pa). The actual tissue samples rested on a rubber mat, and there was little or no traction at the interface with the mat. Thus a "roller" boundary condition was applied there, allowing free lateral motion and no normal motion.

5.2.4 Surface motion and surface tension

As will be evident in the modeled and measured output, the motion at the water-tissue interface has approximately the same amplitude as that at the focus. Other authors (Konofagou et al. 2001, and Haw 2008, Heikkila et al. 2010) applied a fixed boundary condition at the surface of the tissue, and in experiments attempted to pack the tissue tightly in holders, with taught mylar or cellophane acoustic windows. It was found in the present study that a taught cellophane holder could reduce the surface motion by a maximum of 30% over the free case, and this membrane seemed more rigid than any conceivable biological skin in an in-vivo FUS/HMI application. It was thus decided to allow the tissue surface to be free in the water bath, and was modeled as a free interface.

5.2.4.1 Viscoelasticity

Damping in structures is often treated by specifying the spring constant as complex and equal to $K(1+i\chi)$. This treatment is referred to as hysteretic or structural damping, and χ is referred to as the loss factor, loss tangent, or "tan δ ". Damping in thick liquids or solids that creep is referred to as viscous damping. A common model for viscoelasticity is the Kelvin-Voigt model, which adds a factor η to the linear restoring force factor K, proportional to velocity:

$$\begin{aligned}\sigma(t) &= E\varepsilon(t) + \eta\dot{\varepsilon}(t) \\ \sigma(\omega) &= E\varepsilon(\omega) + i\omega\eta\varepsilon(\omega) \quad (\text{harmonic time dependence})\end{aligned}\tag{5.6}$$

where σ is stress, ε strain, E elastic modulus, and η is the effective viscosity. One can see this is analogous to hysteretic damping in that $E = \sigma/\varepsilon = E_{real} + i\omega\eta$. The loss factor is then

$$\chi = \frac{E_{imag}}{E_{real}} = \frac{\omega\eta}{E_{real}} \quad (5.7)$$

For nearly incompressible materials like tissue, the losses come mostly from the shearing motion, therefore in what follows only the shear modulus is modified: $G_{eff} = (1+i\chi)G$. Damping is difficult to model numerically for large systems. A method that is widely used to facilitate numerical solutions is called proportional, or Rayleigh damping, in which it is assumed that damping is proportional to a linear combination of the stiffness and mass. For illustration, a single degree of freedom system with viscous damping is described by:

$$m \frac{d^2u}{dt^2} + c \frac{du}{dt} + ku = f(t) \quad (5.8)$$

In the Rayleigh damping model, the damping parameter c is expressed in terms of the mass m and the stiffness k as

$$c = \alpha m + \beta k \quad (5.9)$$

Comsol is programmed to use either Rayleigh or hysteretic (loss factor) damping. Hysteretic damping only applies to time-harmonic models, whereas Rayleigh damping can be used for either time-harmonic or transient models. If only the loss factor is known, values for the Rayleigh damping coefficients can be set to $\alpha=0$ and $\beta = \chi/\omega$. This is called “equivalent viscous damping”, and these values can be obtained by starting with the Voigt model equation (5.6) and Newton’s law $\sigma = \rho \frac{\partial^2 \varepsilon}{\partial t^2}$ to obtain (5.8) in terms of σ and ε . It was found that both of these damping methods when used in the 3d basic time-dependant model produced identical results.

A more complete model for tissue viscoelasticity is the generalized Maxwell (GM) model, which consists of an equilibrium stiffness E_e in parallel with a number of viscoelastic elements (Figure 5.3). This can capture behavior of most real materials, since damping is usually a function of frequency [Findley, 1989]

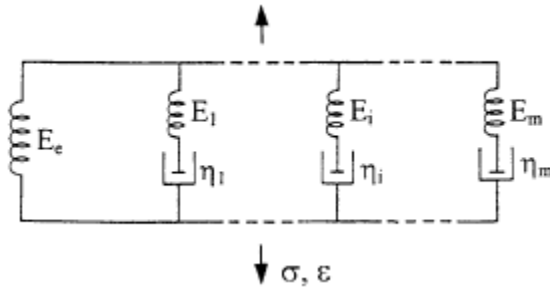


Figure 5.3 Generalized Maxwell model, consisting of a number of spring-dashpot elements.

The constitutive differential equation for each spring-dashpot pair is

$$\dot{\epsilon}_i = \frac{\dot{\sigma}_i}{E_i} + \frac{\sigma_i}{\eta_i} \quad (5.10)$$

where E_i is the stiffness of the i^{th} spring and η_i is the viscosity. The total value for the elastic modulus E is (Park 2001)

$$E(t) = E_e + \sum_{i=1}^m E_i e^{-t/\rho_i} \quad (5.11)$$

where $\rho_i = \eta_i / E_i$ is the relaxation time of the i^{th} element. If time-harmonic inputs are assumed, then E can be expressed as $E = E' + iE''$ where

$$E'(\omega) = E_e + \sum_{i=1}^m \frac{\omega^2 \rho_i^2 E_i}{\omega^2 \rho_i^2 + 1}$$

$$E''(\omega) = \sum_{i=1}^m \frac{\omega \rho_i E_i}{\omega^2 \rho_i^2 + 1} \quad (5.12)$$

Implementation of this into the Comsol model involves augmenting the basic constitutive equations with a separate constitutive equation for each Maxwell element. The values for E_i and ρ_i are found by fitting eqn. (5.12) to measured dynamic modulus curves (Figure 3.34).

5.2.5 Tissue parameters used

Tissue properties used in the models were described in (Section 3.6.5), and are summarized in Table 5-1.

$\rho=1040 \text{ kg/m}^3$	density
$C=1585 \text{ m/s}$	speed of sound
$E=18\text{kPa (static)}$	Young's modulus
$E=36\text{kPa (40Hz)}$	Young's modulus (dynamic). 20°C
$C_v=3600 \text{ kJ/kg-}^\circ\text{C}$	Specific heat
$k= 0.49 \text{ W/m-}^\circ\text{C}$	Thermal conductivity
$\nu=0.495$	Poisson's ratio
$\chi=0.34$	Loss factor at 40Hz

Table 5-1 Material properties used for chicken breast

5.3 Validation and exploration of the model

5.3.1 Validation of thermal model

The FEM thermal model output was compared to that of the Parker model (section 2.1.2). Each model included the same corrections for acoustic nonlinearity and tissue attenuation. Figure 5.4 shows the temperature at the focus, for a 4MPa exposure lasting 5 seconds in chicken tissue. Since the Parker model assumes a Gaussian beam and the FEM model uses the acoustic field calculated by the angular spectrum method, an extra FEM simulation was performed on a Gaussian beam for a more precise comparison. The Gauss widths of the beams were chosen so the half-pressure points were the same as those of the angular spectrum field.

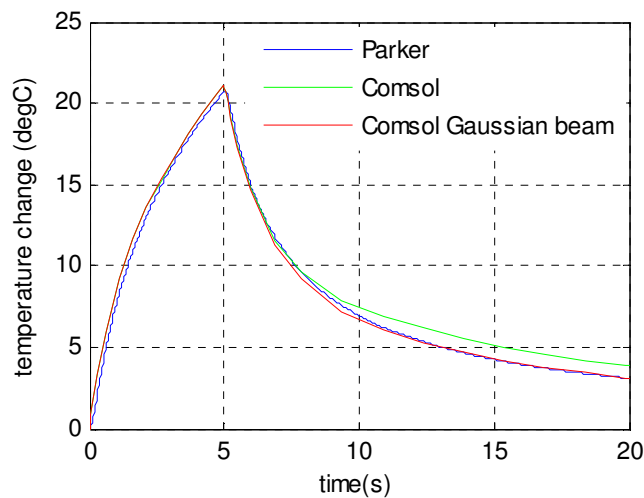


Figure 5.4 Temperature response to 4MPa, 5 sec exposure at 1.1MHz for absorption=5 Np/m/MHz. Results are shown from the Parker model, the FEM thermal model using the acoustic field calculated from the angular spectrum method, and the FEM thermal model for the same Gaussian beam used in the Parker model.

There is excellent agreement between the curves. It can be seen that the FEM model with the full field takes longer to decay. This is due to the presence of side lobes in the acoustic field, which result in higher temperature at radii just outside the main lobe, slowing the conductivity of heat from the main lobe region.

5.3.2 Green's function validation of elastic model

To ensure that the elastic model was implemented properly, the output was compared to that of a Greens function solution for a distribution of point force sources. The Greens function solution in cylindrical coordinates for a point force in an infinite solid is the same as that used in section 3.3.1. A model was made in Matlab for the case of a uniform volume force applied over an ellipsoid roughly the size of the HIFU focal zone (semi-axes $a, b=0.8\text{mm}$, $c=5\text{mm}$). The ellipsoid was divided into voxels of 0.1mm and the Greens function solution summed over all points. The force per volume was $F=2.48e3\text{ N/m}^3$, the Young's modulus $E=18.5e3$, and Poisson's ratio $\nu=0.495$. If a point on the solution grid overlapped a source point, the Green's function yielded infinity. Therefore, for each solution point, any source point that was within $3e-5\text{m}$, was ignored.

In Comsol, the axisymmetric model was chosen, and the infinite solid for which the Green's function is derived was modeled as a cylinder of 20cm radius and 20 cm thickness. The outer round surface boundary was held stationary. Results for displacement along the major axis are shown in Figure 5.5. There is a 5% discrepancy at the origin, which could be caused by the coarseness in grid size for either model, or the fact that the FEM model space was not an infinite solid.

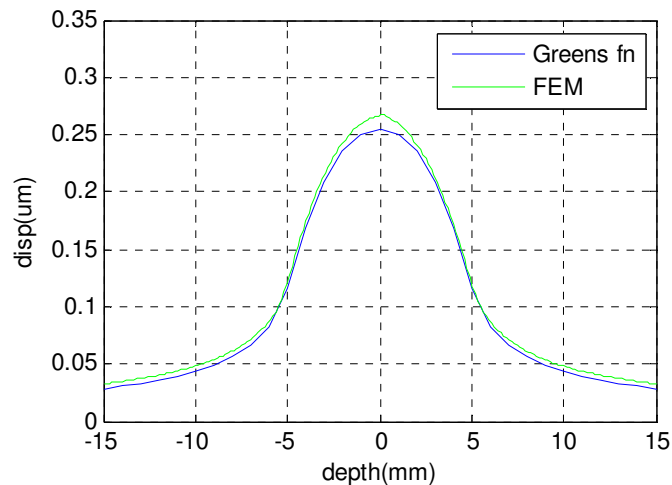


Figure 5.5 Comparison of Green's function solution and FEM solution for the case where the HIFU is applied into an infinite solid.

5.3.3 Effect of mesh size

The mesh size for the FEM model needed to be controlled in order to run within the memory capacity of the computer (which had the maximum memory possible for the operating system; 3.5Gbytes). To study the effect of mesh size on the model results, the basic elastic model was run with varying mesh resolution.

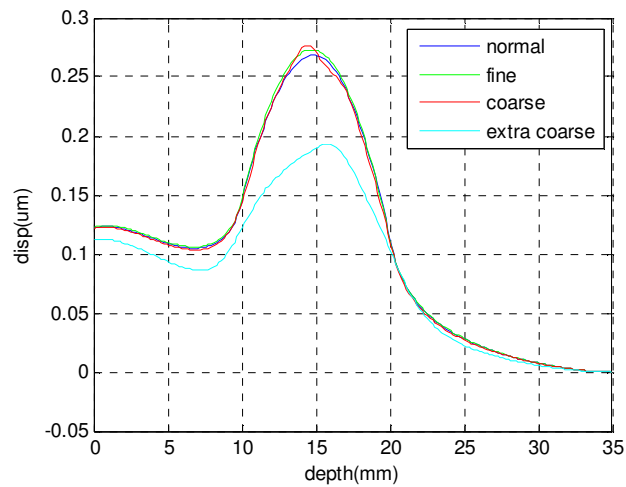


Figure 5.6 Effect of mesh size on axisym static solution. The labels “normal” etc. are Comsol designations, and elements in critical regions were limited in size as follows: fine: 0.25mm, normal: 0.5mm, coarse: 1mm, extra coarse: 2mm

Figure 5.6 shows the axial displacement results for the four meshes shown in Figure 5.7. Significant deviation was not seen until the “extra coarse” size, which has 2mm elements at the focus. Thus, the rest of the results shown in this thesis are for a course mesh, with elements chosen to be less than 1mm in size in regions of significant heating or forcing.

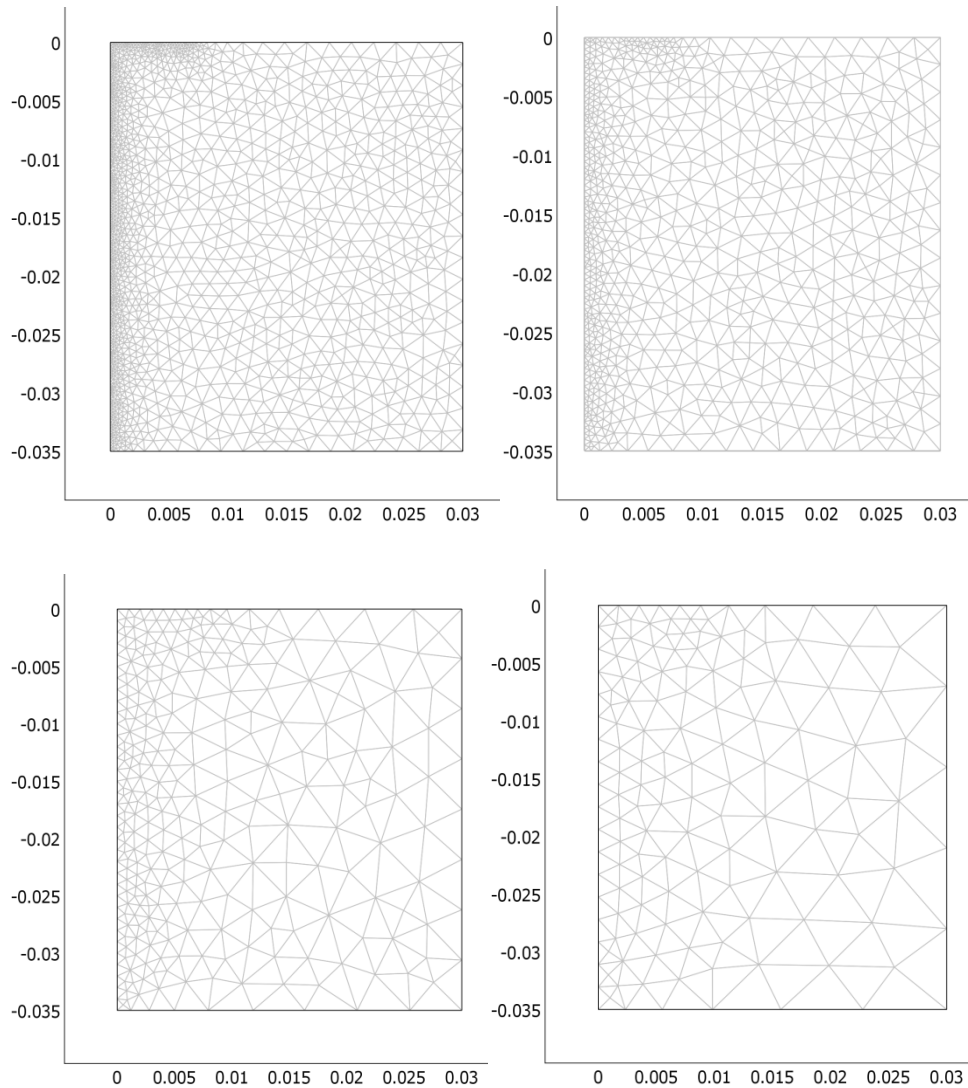


Figure 5.7 The various axisymmetric grids used in the grid size study. Units are in meters. From upper left to lower left, the designated sizes, along with the length of the tightest mesh in each, were: fine(0.25mm), normal(0.5mm), coarse (1mm), extra coarse(2mm).

5.3.4 Comparison of the model types – 2D axisymmetric, 3D, and 3D Generalized Maxwell

5.3.4.1 Simplifications and model types

The object of this section is to compare the outputs of the five model types and justify the use of the simplest model, the axisymmetric time-harmonic. There are simplifications in this model over

other model types, which will be studied and justified. The model types, in order of descending complexity are:

1. 3-d Cartesian, time dependant, with generalized Maxwell (GM) viscoelasticity.
2. 3-d Cartesian, time dependant, with Rayleigh damping.
3. 3-d Cartesian, time-harmonic with loss-factor damping
4. 3-d cylindrical, time dependant, with Rayleigh damping.
5. 3-d cylindrical, time-harmonic, with loss factor damping.

It was necessary to use model #5 when the mechanical, thermal and acoustic models were combined, because it uses less computer resources than models #1-#4. The GM model could not be implemented on the axisymmetric models due to Comsol-related mathematical limitations in expressing the differential equations in cylindrical form.

The 3-d Cartesian models incorporated a simplified acoustic field, since the fully modeled field could only be easily imported into the axisymmetric model. The acoustic volume force was applied uniformly within an ellipsoid at the focus. The semi-axes were 0.8mm X 5mm, and were calculated such that the ellipsoid volume times the force per volume at the peak is equal to the total integrated volume force in the main lobe of the modeled field. The surface force at the tissue-water interface was applied uniformly over a disk of 14mm diameter, calculated to give the same total surface force as that of the integrated acoustic field. Other simplifications over the final more realistic models were the exclusion of acoustic nonlinearity, the bounding of the side and top with air instead of water, and the fixing of the bottom boundary. These simplifications did not affect the validity of the conclusions of this comparison study.

Figure 5.8 (top) shows a comparison between the GM model and the 3-d time-dependant model. Unlike the GM model, the models with loss-factor or Rayleigh damping have single-valued inputs for the elastic modulus and damping. The force input to the time-dependant models was a square wave with a DC offset, which resembles the actual forcing function applied in experiments. To facilitate eventual comparison with time-harmonic models, which treat all energy as sinusoidal at one frequency, the time-dependant model was also given an input force modulated by a sine wave of

40Hz., with the same peak-peak amplitude as the square wave(Figure 5.8). For the 3d model, the Young's modulus used is that of the tissue at 40Hz; 36kPa. Results are also shown for 18kPa, to gain further understanding.

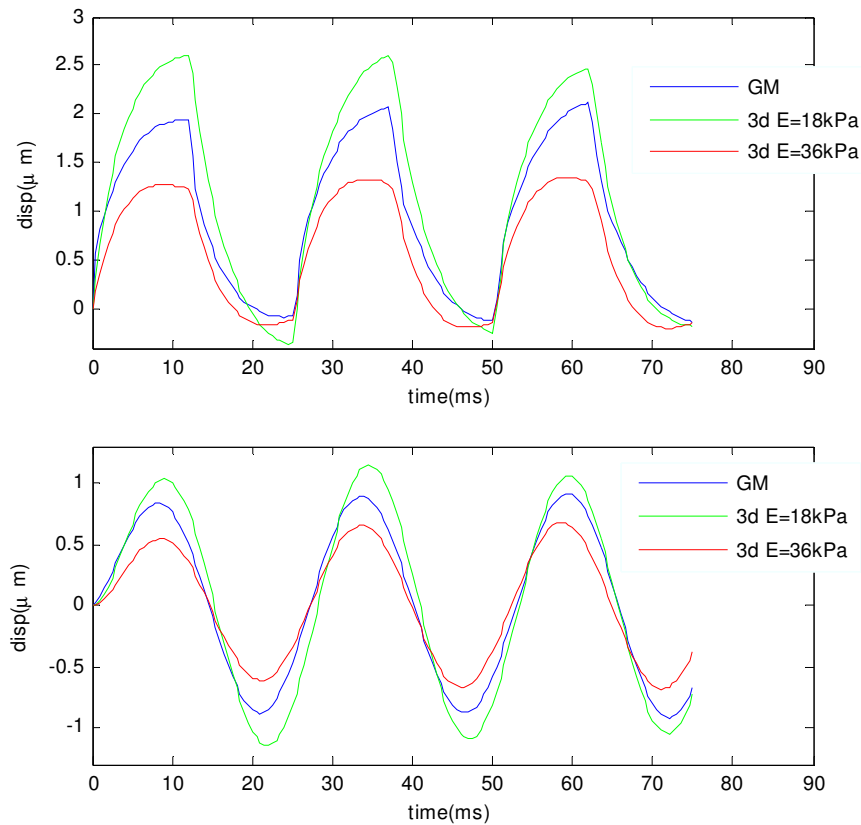


Figure 5.8 FEM model output for axial displacement at a depth of 13mm, which is the location of maximum displacement. Top: force applied as square wave from 0 to F_0 . Bottom: force applied as a sinusoid. blue: general Maxwell model, green: 3d model with $E=18\text{kPa}$, red: 3d model with $E=36\text{kPa}$

Both the amplitude and shape of the GM curve falls between those of the two curves for the 3-d Rayleigh damping model. This suggests that if the GM model, and the measurements used to create it are accurate, the value for stiffness measured at 40Hz is too large. Other than that, the GM model does not show any fundamentally different behavior than that of the basic 3d model. It will thus be assumed that the GM model offers no advantage over models using simpler damping methods.

We next turn to a comparison of time-dependant and time-harmonic models. Figure 5.9 shows the amplitude of the motion on axis for the 3d time-harmonic model with sinusoidal excitation

(labeled “3d”). The amplitude at $dpeth=13mm$ is $0.7\mu m$, which is the same as the eventual value reached in the 3d, $E=36kPa$ curve in Figure 5.8. This shows that the time-harmonic model can be used in place of the time-dependant model with no significant loss in accuracy. Also shown in Figure 5.9 is the output of the axisymmetric model, which overlaps with the 3d model well enough to conclude that the axisymmetric model can be used instead of the 3d Cartesian model with no significant loss in accuracy. The ability to use the time-harmonic, axisymmetric model will reduce computational requirements and thus enable realistic additions to the model, and coupling with a thermal model.

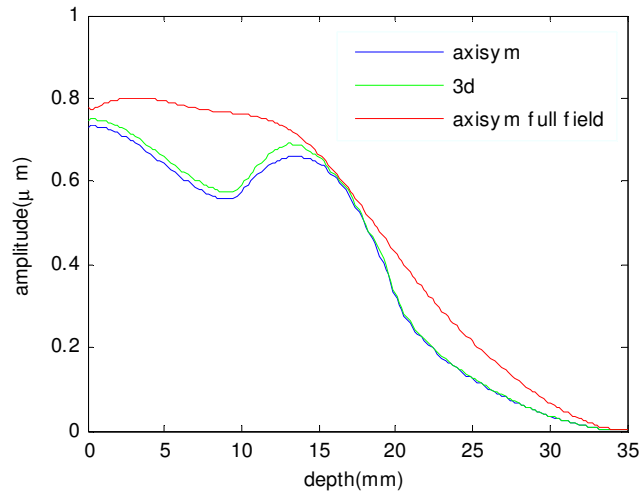


Figure 5.9 Fourier amplitude vs depth for time-harmonic solutions of the axisymmetric model, 3d basic model, and axisymmetric model with full acoustic field and water bounding top and sides. All models had $E=36kPa$.

The final curve shown in Figure 5.9 is the output of the axisymmetric model with the force from the full acoustic field, rather than from the simplified ellipsoid and surface disk. It is evident that the momentum transferred by the acoustic field prior to the focus, although spread over more area, results in significant displacement between the surface and the focus.

5.3.5 Comparison to measured data from “push runs”

Data is presented below for 27 “push runs” from experiments on three different chicken breasts. As described in section 3.7.2.1, a “push run” was a non-heating, non-cavitating interrogation consisting of 3MPa peak pressure HIFU modulated by turning it on and off 10 times at a rate of 40Hz. Figure 5.10 shows the motion at the focus for four randomly chosen runs, as calculated using the speckle-tracking techniques described in section 3.1. These plots represent some of the rather large variation between samples.

As an important aside, recall that in the Kelvin-Voigt model there is an exponential time constant for the rise and fall in strain due to a constant stress, which is equal to the viscosity divided by the elastic modulus. The decay time seen on these plots is roughly 10ms. It is evident that this is long enough (viscosity is high enough) that the tissue does not recover its initial position in time for the next forcing pulse; resulting in a net DC offset of the displacement curves, and a reduction of AC amplitude. This is significant for HMI, which only measures the AC amplitude. It is usually assumed that the AC amplitude is a function of tissue stiffness, and viscosity is not considered. However, since the basic model for viscoelasticity (Kelvin-Voigt) is essentially a lowpass filter (equation (5.6), the viscosity will reduce the amplitude for frequencies above the cutoff frequency ($=1/\text{decay time}$).

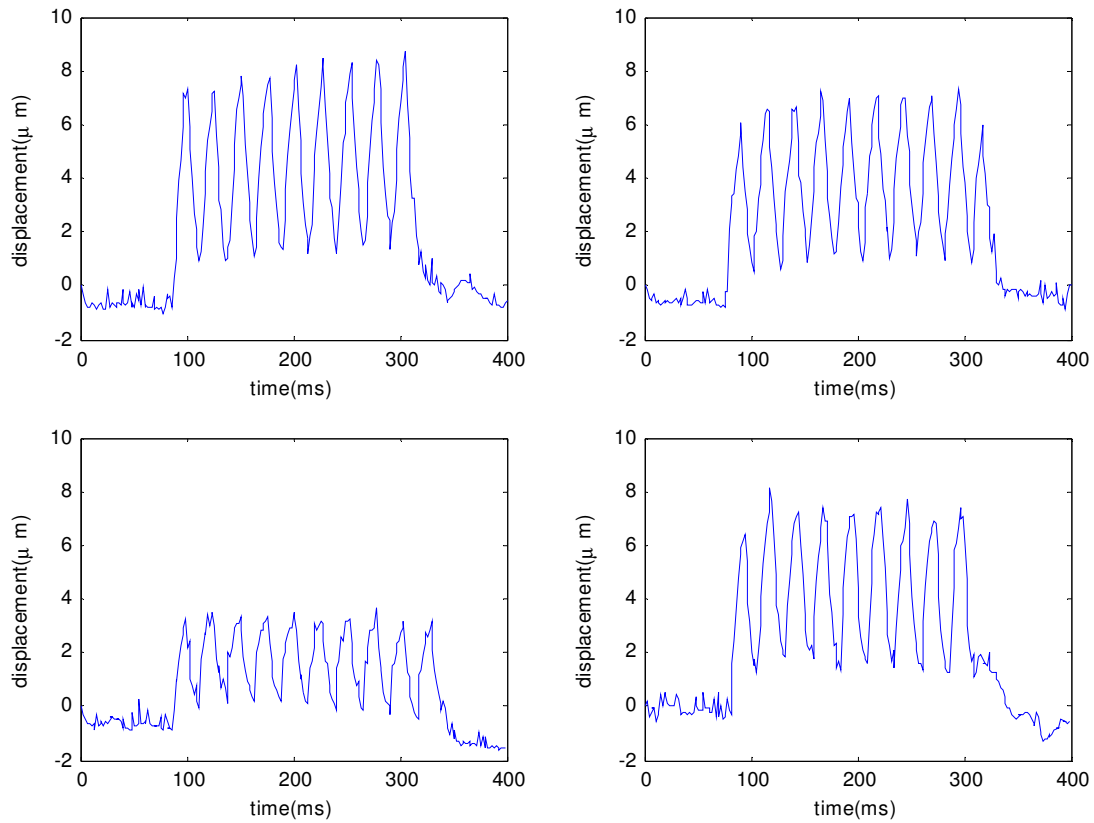


Figure 5.10 Four waveforms selected at random from 27 push-runs. Top two are from breast#1, bottom two from breast #2. These are from the segments of the A-lines representing a depth of 13mm into the tissue.

The Fourier amplitude at 40Hz was calculated for all 27 runs and plotted in Figure 5.11. Again, substantial variation is seen. However the variation was less on breast #3, in which there was a smaller distance between interrogation points. Note that the amplitude at depths above 25mm sometimes did not taper toward zero, as is predicted in models and expected from considering that the bottom of the sample was between 30 and 40mm. This was found to be the result of poor SNR of the backscatter data at depths greater than 24mm.

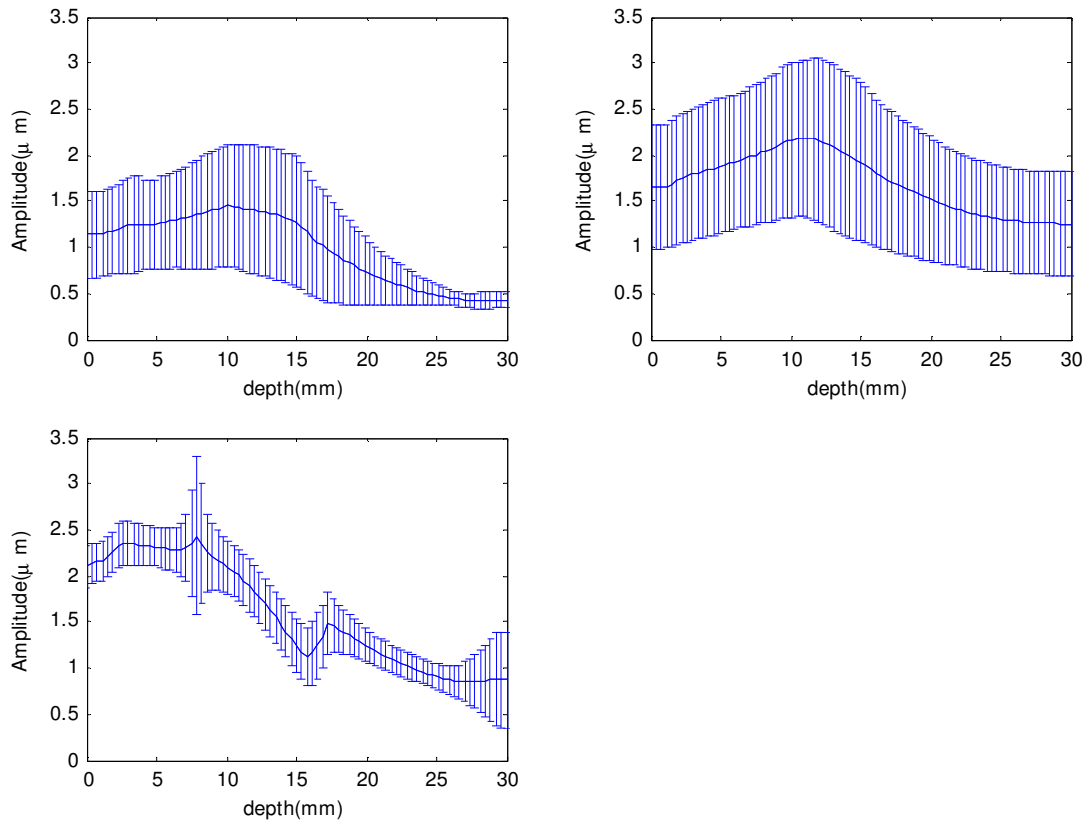


Figure 5.11 Fourier amplitude of displacement vs depth into tissue, along with standard deviation, for breasts #1, 2, and 3. The first two each contain data from 8 runs spaced >10mm apart. The third plot is for 11 runs spaced 1mm apart.

Figure 5.12 shows the measured motion at the focus for one of the runs on the first breast, along with the output of the axisymmetric, time-harmonic model with the full acoustic field. The model output does not agree well with the measured waveform. A better match to measurement could be obtained by adjusting the tissue properties. Absorption was changed from 4 to 9Np/m/MHz, stiffness from 36kPa to 18kPa, and Rayleigh damping parameter from 1.35e-3 to 4e-3. Based on these parameters the model is within the expected variation of the experiments. The changes to the parameters are more than seem reasonable, and it is a mystery as to what may be the cause of the discrepancy between measured and modeled displacement. Nonetheless they will be investigated as one possibility of tissue parameters in the following studies.

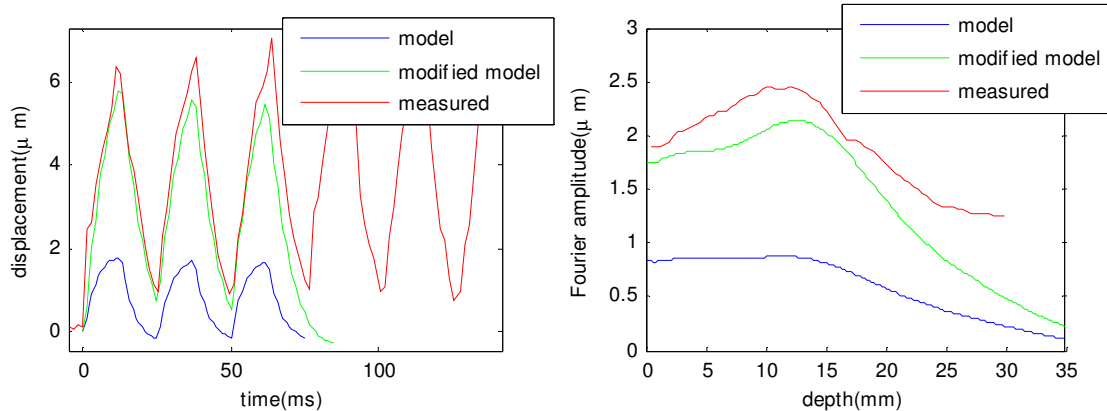


Figure 5.12 Measured waveform compared to model output. Left: time waveform at focal depth. Right: Fourier amplitude vs. depth into tissue. Model output is shown for nominal values (absorption=4 Np/m/MHz, Young's modulus = 36kPa, Rayleigh damping factor = 1.35e-3), and for modified parameters (absorption=9 Np/m/MHz, Young's modulus = 18kPa, Rayleigh damping factor = 4e-3)

It is interesting to note that Heikkila et al. (2010) used Comsol to model a similar HMI experiment, and also got displacements that were considerably smaller than measured values (in their case 50%). They noted the discrepancy, and also that they had no explanation.

5.3.6 Comparison to measurements in raised temperature bath

To investigate the effects of temperature, push-runs were done on samples as the temperature of the water bath was increased. The amplitude is expected to rise by the time the temperature reaches 40 degrees because of decreased stiffness. The motion is expected to rise further as the absorption increases at temperatures above 40 degrees, causing more force. Figure 5.13 shows the measured and modeled amplitude for 4 temperatures. As mentioned before, the overall amplitude is less than half of that measured. The measurements rise with temperature, as predicted, but not as fast as the model. One possible reason is that the temperature inside the tissue may not have reached that of the water bath at the time of measurement.

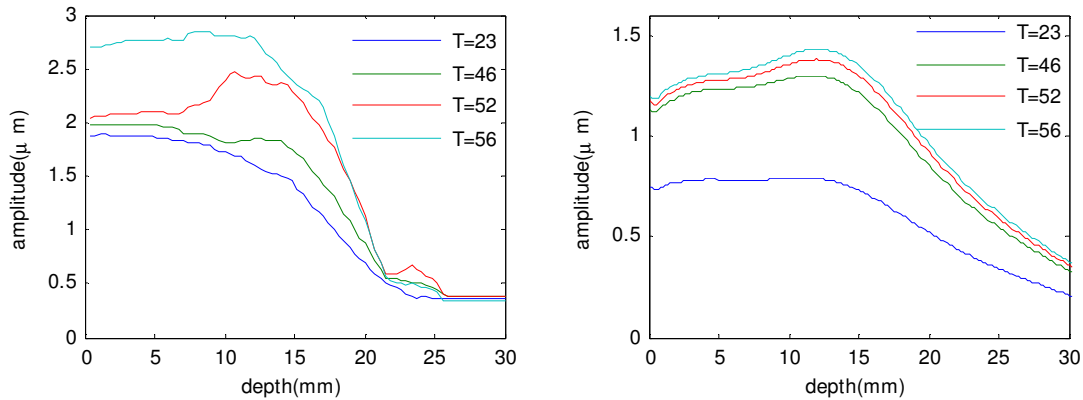


Figure 5.13 Push runs amplitude vs water bath temp. Left: measured. Right: FEM model.

5.3.7 Selected effects of stiffness and absorption on displacement

At his point it is necessary to discuss the fact that the values of stiffness and acoustic absorption vary with temperature (see section 2.1.1). Figure 3.37 gives simplified curves for the measured values of $G(T)$ and $\alpha(T)$, and also alternatives to the measured values, which are an attempt to take into account the fact that the actual stiffness and absorption changes from protein denaturation occur over time spans longer than the 28 second lesion exposure used here. Results will be shown for both the measured and modified curves for $G(T)$ and $\alpha(T)$.

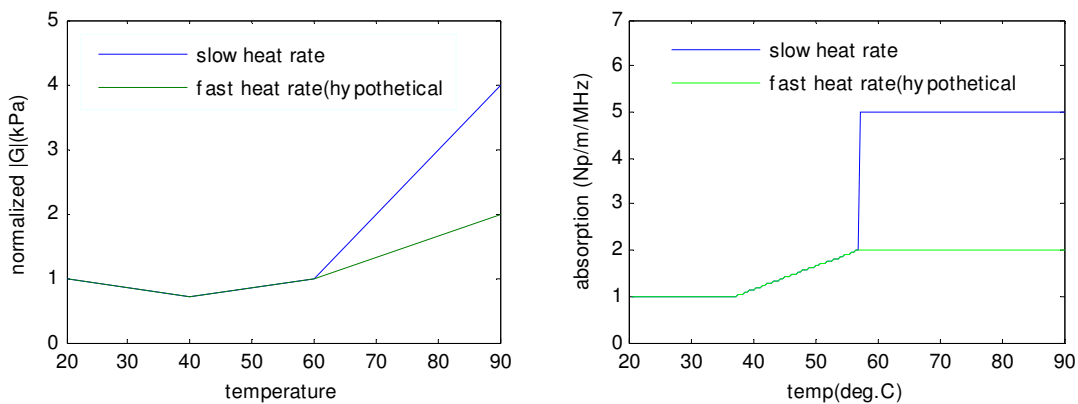


Figure 5.14 Simplified curves for measured values of $G(T)$ and $\alpha(T)$ used for FEM models, normalized to the value at 20 degrees C

Note that in the mechanical model the force is proportional to total acoustic attenuation, and not just absorption. In section 3.6.2.3 it was found that the attenuation was approximately 20% higher

than the absorption. Thus the attenuation used in the models will be represented as absorption * 1.2. Since they share the same symbol “ α ”, the text will be explicit in when absorption or attenuation are being used. In general, only acoustic heating will involve absorption.

Since there are a number of effects resulting from temperature-induced changes to stiffness and absorption, it is worthwhile investigating each one individually. Firstly, the stiffness affects the tissue displacement approximately inversely. Since tissue is near incompressible, the stiffness acts principally in shear, meaning that a forced region will move according to the stiffness of the tissue *on either side of it*. Thus the increase in stiffness of a lesion will not affect the displacement until it grows outside of the acoustic focal region. Secondly, increased absorption will have three significant affects: 1) it will accelerate heating, 2) it will decrease acoustic intensity, and 3) it will increase acoustic forcing.

To investigate just the mechanical effects, the simplified model was used which treated the acoustic field as just a force acting on a surface disk and on an ellipsoid at the focus. Stiffness and absorption were varied in another ellipsoid which simulated the lesion. Two lesion sizes were considered; a “small” one, which occupied just the acoustic focal region(10mm long x 1.6mm wide), and a “large” one, which resembled actual lesions after 28sec exposure to 7MPa HIFU (12mm long, 5mm wide). Values were chosen for absorption and stiffness from Figure 3.37, at 40°C (tissue softened) and at 90°C (lesion formed).

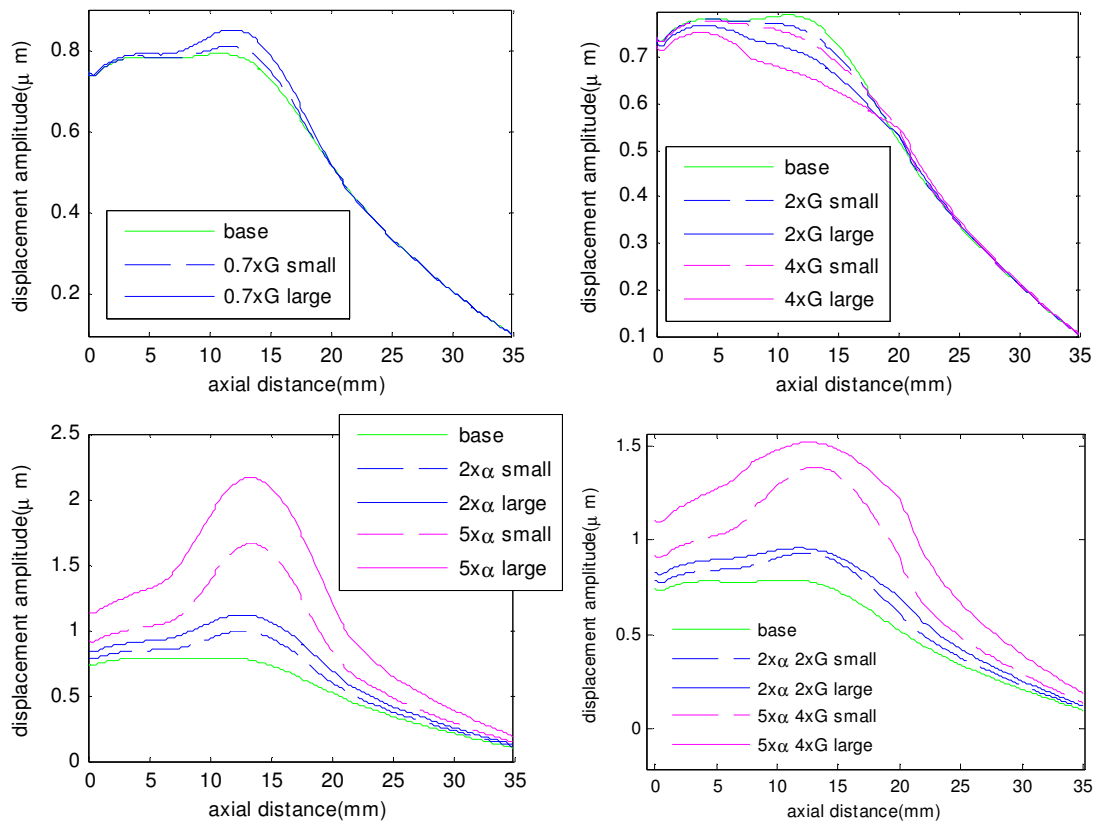


Figure 5.15 Effects of changing stiffness and absorption inside a “small” and “large” lesion. (a): initial softening, in which G drops 30%. (b): final stiffening, in which G changes either 2x or 4x. (c): increasing attenuation, either 2x or 5x. (d): both increased attenuation and stiffness.

Figure 5.15 shows the results. The dominant effect is the 5x increase in attenuation, which produced large displacement at the focus due to a five-fold increase in the force. Increased stiffness in the lesion resulted in a reduction in displacement only for the large lesion, as expected, and also in a “flattening” of the response curve. Due to the lesion, the axial displacement at the focus no longer conformed to the force concentration there. It has been suggested in the literature (Lizzi et al. 2003, Konofagou et al. 2001) to assume that the increase in absorption plays a minor role compared to the increase in stiffness, but the present study suggests the opposite is true.

5.4 The combined model of HMI during lesion formation

To simulate the HMI measurement as the lesion forms, models for the acoustic, thermal, and displacement fields are coupled. Figure 5.16 shows a schematic of the elements of the model.

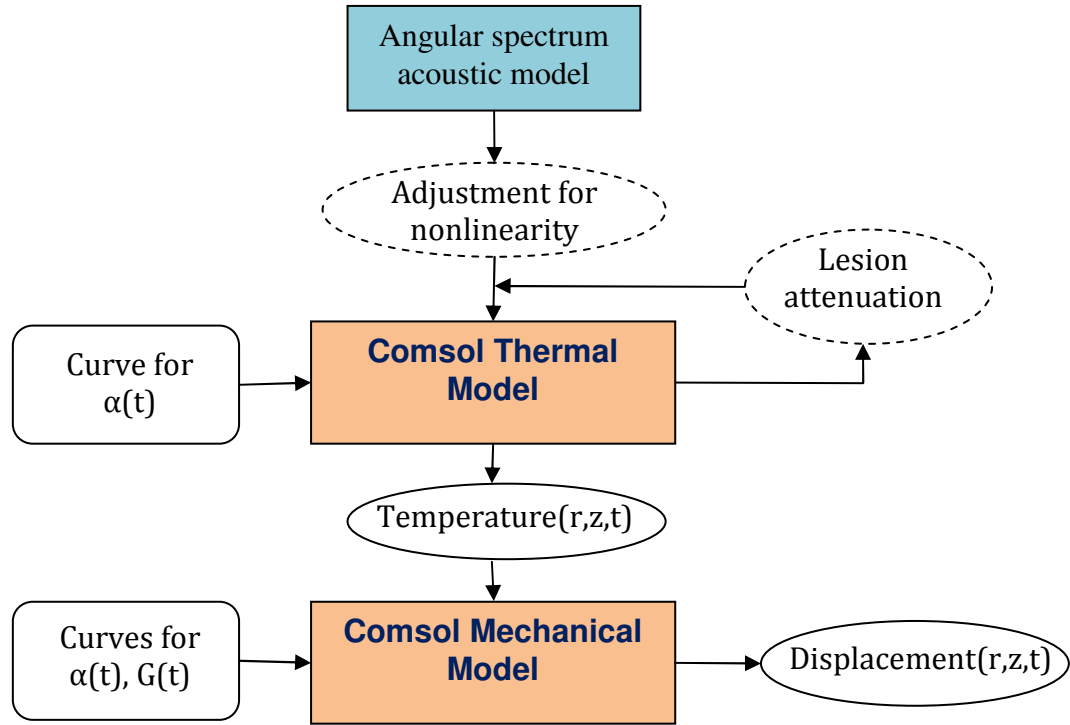


Figure 5.16 Schematic of the combined FEM model

5.4.1 Acoustical considerations in the combined model

The acoustic intensity field is imported into Comsol from a text file output of the 2-layer angular spectrum model described in section 3.4.3. A nonlinear correction factor is applied according to section 3.4.3.2.1. The acoustic intensity will be further attenuated by the lesion as it forms. This was accomplished in the FEM thermal and mechanical models by defining the volume where temperature was $>57^{\circ}\text{C}$, as a lesion. For all points in the model mesh with depths below the top of the lesion, the intensity was multiplied by $\exp(-2\alpha_1 f_0 x)$ where α_1 was the difference between the final lesion attenuation and the healthy tissue attenuation, f_0 was the HIFU frequency, and x the distance between

the depth of the top of the lesion and that of the point in question. Here it is assumed that the interaction between diffraction and attenuation is weak. The full curve for $\alpha(T)$ could not be incorporated into the FEM model due to program restrictions. To examine the accuracy of this treatment of attenuation, the resulting intensity was compared to a more accurate model for lesion attenuation. This was made from a modified angular spectrum model. As with the normal angular spectrum method, the field was propagated in k-space, but only up to the top of the pre-defined lesion location. Then, for each axial grid point ($\Delta z = 0.16\text{mm}$), the field was converted back to pressure, and at those points within the pre-defined radial boundary of the lesion, the attenuation factor of $\exp(-\alpha f_0 \Delta z)$ was applied. The field was then converted back into k-space and propagated one more grid point, and the process repeated until the end of the lesion. The assumption made is that the acoustic field within the lesion is planar locally over a distance Δz . A comparison of these two methods is shown in Figure 5.17. For this plot, the lesion is defined as the region $r < 2.25\text{mm}$, $56\text{mm} < z < 67\text{mm}$. The healthy tissue attenuation was 5Np/m/MHz , and the lesion attenuation was 25Np/m/MHz .

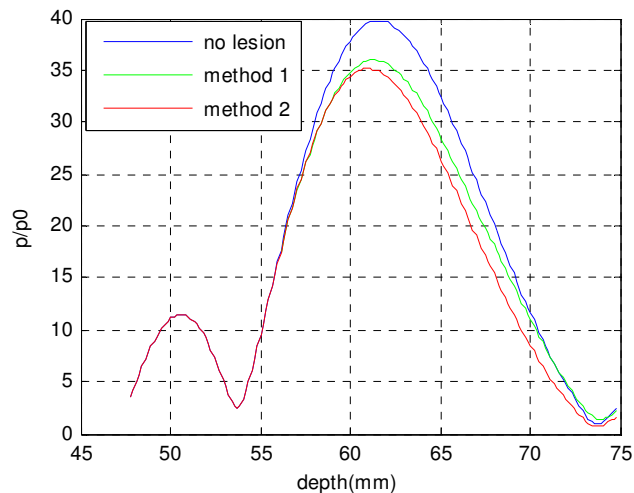


Figure 5.17 Axial pressure field with simulated lesion. Method 1 is modified angular spectrum, method 2 is simple application of $\exp(-\alpha x)$ to the no-lesion curve, starting at top of lesion(56mm).

The method used in the FEM combined model is within 10% of the more accurate modified angular spectrum model.

5.4.2 Thermal considerations in the combined model

The FEM thermal model calculates the temperature field in time, using the intensity field as the heat source. As time progresses, the intensity changes with temperature due to changes in the acoustic absorption. In addition, changes in acoustic absorption result in changes to the heat source for the thermal model. The values for $\alpha(T)$ are given in Figure 3.37. After the solution is calculated, temperature fields at representative times during the lesion formation are chosen and saved to disk, for importation into the mechanical FEM model.

5.4.3 Mechanical considerations in the combined model

The mechanical model uses the same intensity field as the thermal model, but uses the separate components I_r and I_z for the force vector. Since the spatial distribution of α and G depend on spatial distribution of temperature, a separate solution of the mechanical model is run for each temperature field output from the thermal model. $\alpha(T)$ is allowed to modify the intensity field, exactly the same as it did during the thermal model. It also is a factor in the force source. $G(T)$ is multiplied by 3 and input into the tissue Young's modulus of the model.

5.5 Combined model results

5.5.1 Combined model effect of changes in acoustic field

The reduction in the acoustic field from the added attenuation of a typical lesion was shown in Figure 5.17. To examine the effect on displacement of applying the lesion attenuation to the acoustic field, the displacement at the end of a 28 second exposure to 7MPa HIFU was compared to that of no lesion attenuation (Figure 5.18). The effect is clear, and is thus a necessary part of the model.

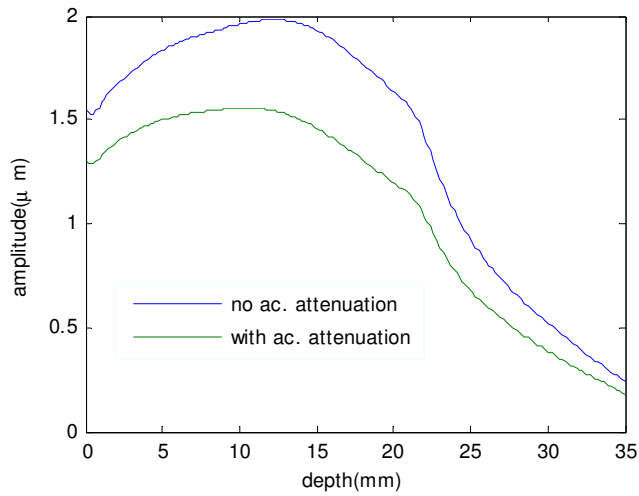


Figure 5.18 Amplitude after 28 sec exposure, with and without extra attenuation of acoustic field by lesion. $\alpha_{\text{lesion}} = 5x \alpha$.

5.5.2 Combined model effect on temperature

Figure 5.19 shows the effect of including $\alpha(T)$ in the heat source, rather than just the absorption of healthy tissue. The modified values for $\alpha(T)$ (Figure 3.37) are also included, where the absorption is only allowed to reach 2x that of healthy tissue. The extra attenuation in the forming lesion causes a 75% to 240% increase in final temperature, for ultimate values of α that are either 2x or 5x that of healthy tissue.

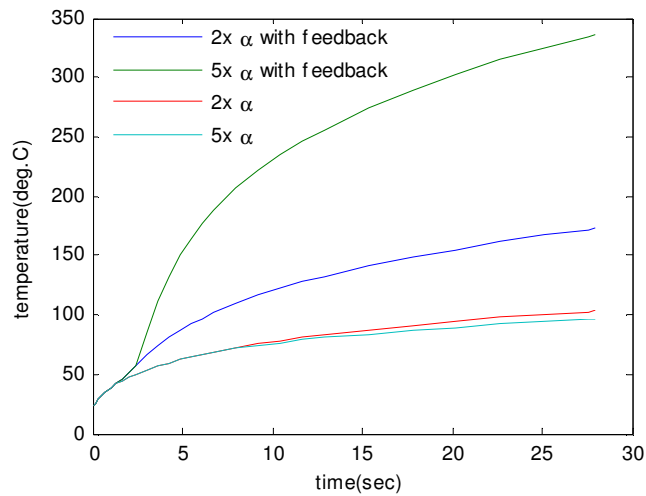


Figure 5.19 Temperature at focus for 28 sec 7MPa exposure. Final lesion absorption = 2x or 5x healthy tissue. "Feedback" refers to whether the increased acoustic absorption of the lesion is included in the heat source.

Because boiling will limit the temperature to around 100°C., the heat source was automatically reduced in the model to simulate the absorption of energy into latent heat of vaporization. This was done by applying a linear reduction to the heat source as a function of temperature (over a span of 3°C.), once temperature reached 100°C. Spatial distributions of temperature after 28 seconds at 7MPa are plotted in Figure 5.20 to show the effect of this treatment of boiling. Under these experimental conditions, actual lesion sizes ranged from 3 to 5mm in diameter. Using 57°C. as a lesion formation threshold, the model output of Figure 5.20(d) most closely matches the experimental data. In this simulation the lesion had double the absorption and the temperature was limited to 100°C.

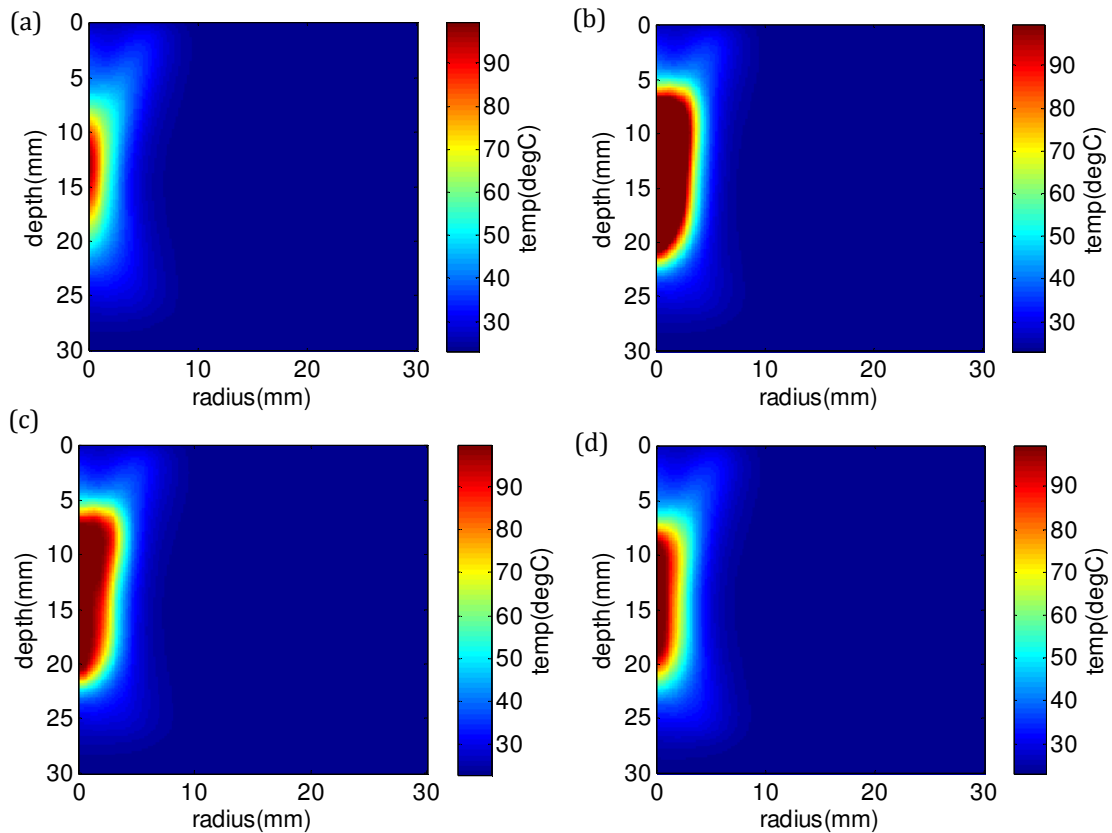


Figure 5.20 Temperature at end of 7MPa 28s exposure. a) no feedback, b) feedback included from increase in lesion absorption (5x healthy), c) feedback plus heat absorption from boiling, d) feedback with final $\alpha=2x$ healthy, with boiling. Note that the color scale saturates at 100°C.

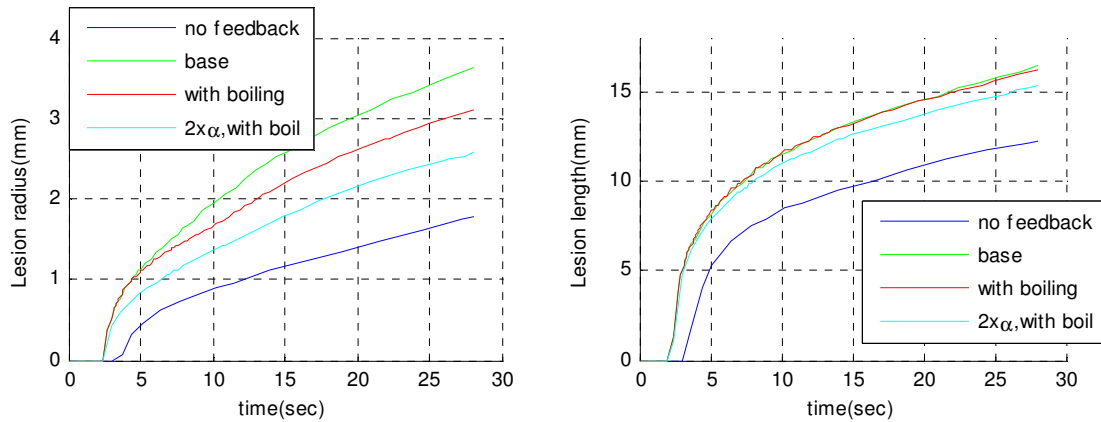


Figure 5.21 Lesion size, defined by when temperature is over 57°C. Left: radius at center, Right: length, for the four cases in Figure 5.20. “Base” refers to un-modified tissue parameters, and no special treatment of boiling.

The lesion radii and lengths are plotted in Figure 5.21 for the four cases in Figure 5.20. Analogous to plot (d) in Figure 5.20 and the final curve in Figure 5.21 (“2x α , with boil”), has the best match with actual lesions made under the same conditions (7MPa for 28 sec). It is reasonable to expect that this curve is most realistic, treating the final value of alpha as the “modified” version, in which the protein denaturation does not reach its final value during the short duration of lesion formation.

5.5.3 Combined model effect on displacement during lesion sequence

This section presents results that were the final goal of the FEM work; HMI displacement during lesion formation. Figure 5.22 shows the Fourier amplitude of the tissue displacement on the acoustic axis, vs depth. Lines are plotted for different times during lesion formation, and also made into a topographic-style plot similar to those produced from typical post-processing of experimental data.

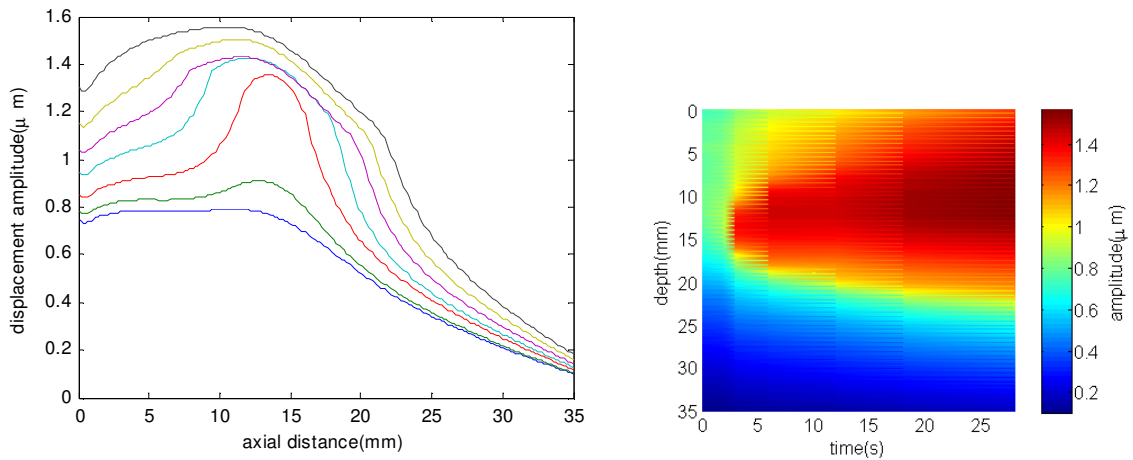


Figure 5.22 Amplitude vs. depth at times during lesion sequence $t=0, 2, 3, 6, 12, 18, 28$ sec. Shear modulus $G=12\text{kPa}$, absorption= 4Np/m/MHz , Rayleigh damping parameter $\beta=1.35\text{e-}3$. Final lesion absorption $\alpha_F=5\alpha$, final stiffness $G_F=4xG$.

By 3 seconds there is a strong increase at the focus mainly due to α rising with temperature. By 6 seconds the lesion radius, as shown in Figure 5.21, has grown outside the acoustic field (half-power radius = 0.7mm), so the higher stiffness begins to broaden the profile. The profile continues to broaden as the lesion grows, and continues to rise due to higher forcing from higher values of absorption α .

Figure 5.23 shows the results for the modified values of $\alpha(T)$ and $G(T)$, in which protein denaturation is delayed. The pattern is unchanged, but the magnitude of the increase in displacement is less, due to the smaller increase in $\alpha(T)$ and $G(T)$.

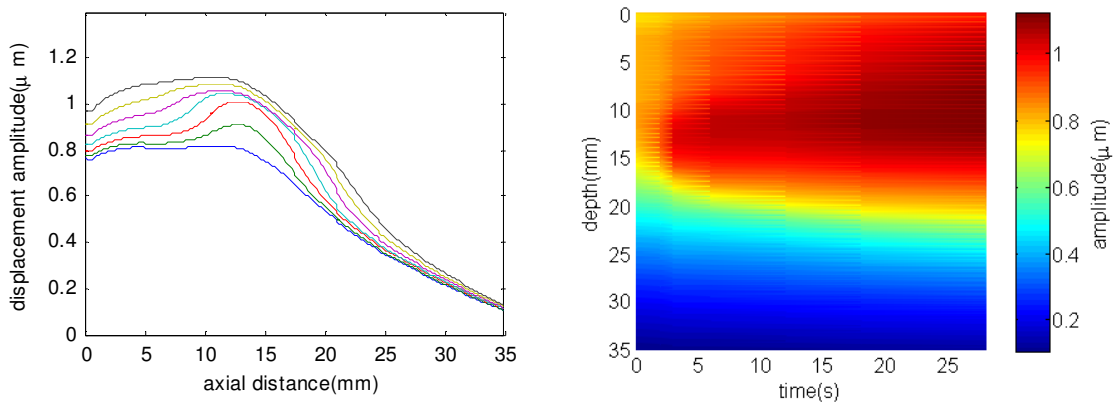


Figure 5.23 Amplitude vs. depth at times during lesion sequence $t=0, 2, 3, 6, 12, 18, 28$ sec. Shear modulus= 12kPa , absorption= 4Np/m/MHz , Rayleigh damping parameter $\beta=1.35\text{e-}3$. Use "modified" parameters for slower protein denaturation (Figure 3.37) $\alpha_F=2\alpha$, $G_F=2xG$.

Figure 5.24 shows the case in which the “alternate” set of tissue parameters were used in order to match measured displacements (Figure 5.12). Shear modulus changed from =12kPa to 6kPa, room-temperature absorption from 4Np/m/MHz to 9Np/m/MHz, and Rayleigh damping parameter from $\beta=1.35e-3$ to $4e-3$. The temperature effects were incorporated by using the modified parameters for slower protein denaturation: $\alpha_F = 2x\alpha$, $G_F = 2xG$. These parameters resulted in an overall amplitude increased, but the same basic pattern remains; an early increase near the focus, followed by a broadening.

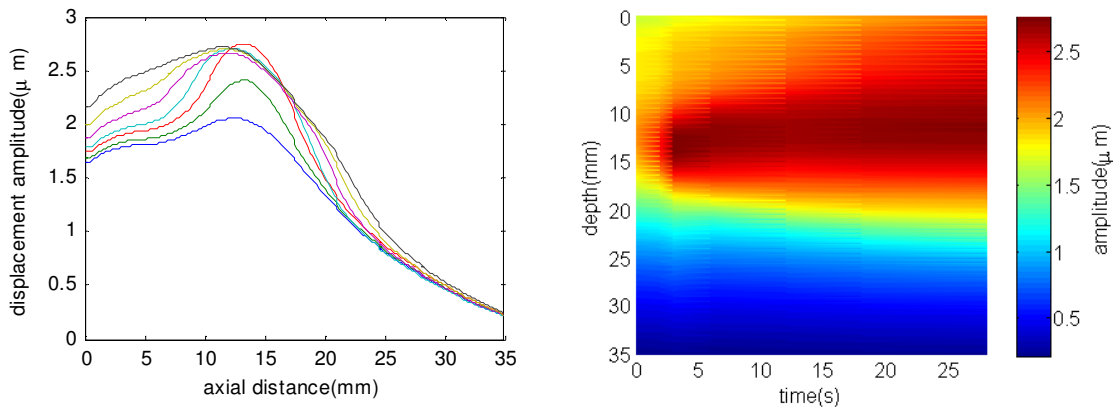


Figure 5.24 Amplitude vs. depth at times during lesion sequence $t=0, 2, 3, 6, 12, 18, 28$ sec. Alternate tissue parameters to match measured values (Figure 5.12). Shear modulus changed from =12kPa to 6kPa, Healthy absorption from 4Np/m/MHz to 9Np/m/MHz. Rayleigh damping parameter from $\beta=1.35e-3$ to $4e-3$. Also use the “modified” parameters for slower protein denaturation (Figure 3.37): $\alpha(T)$ final =2x healthy, $G(T)$ final = 2x healthy.

Experimental HMI/lesion data usually included the period of time after the HIFU was turned off, to gain further insight into the influence of temperature evolution on HMI amplitude. This was simulated in the FEM models, but not presented here. The results showed that the profile of the amplitude vs. depth at the end of HIFU persisted after the HIFU was turned off, in cases where a lesion was made (i.e. the temperature got above 57°C.). According to measurements, the lesion stiffness rose substantially during cooling, but the absorption remained the same. This is expected, since the effects of changes in absorption are much more than those of changes in stiffness, and also

it is the stiffness of the tissue surrounding the lesion that affects the amplitude, rather than the stiffness in the lesion itself.

The results of the three studies shown above are consistent with those of Figure 5.15, in which a simplified model was used to examine individual effects of absorption and stiffness. Increased absorption in the focal region leads to higher amplitude there, and increased stiffness leads to a broadening of the amplitude vs. depth. Each model shows that a five-fold increase in absorption, as would be required if the slow heating-rate rheometer measurements were used for $G(T)$, approximately results in a doubling of amplitude. Since the values for lesion attenuation and stiffness are uncertain and vary to some degree with each tissue sample, the two parameters were varied systematically in the combined model. Figure 5.25 Modeled displacement amplitude for various values of final attenuation and stiffness. The three rows represent final values of attenuation of 5x, 2x, and 1x initial attenuation, from top to bottom. Color scale ranges are 0-2 μm , 0-1.3 μm , and 0-1 μm , respectively. Final stiffness values are 1x, 2x, and 4x for the columns, from left to right, and further prove that changes in attenuation affect displacement much more than proportional changes in stiffness. Increasing stiffness just results in 18% less displacement but similar shape. Increasing alpha increases maximum displacement by 100%, and concentrates displacement around the focal depth.

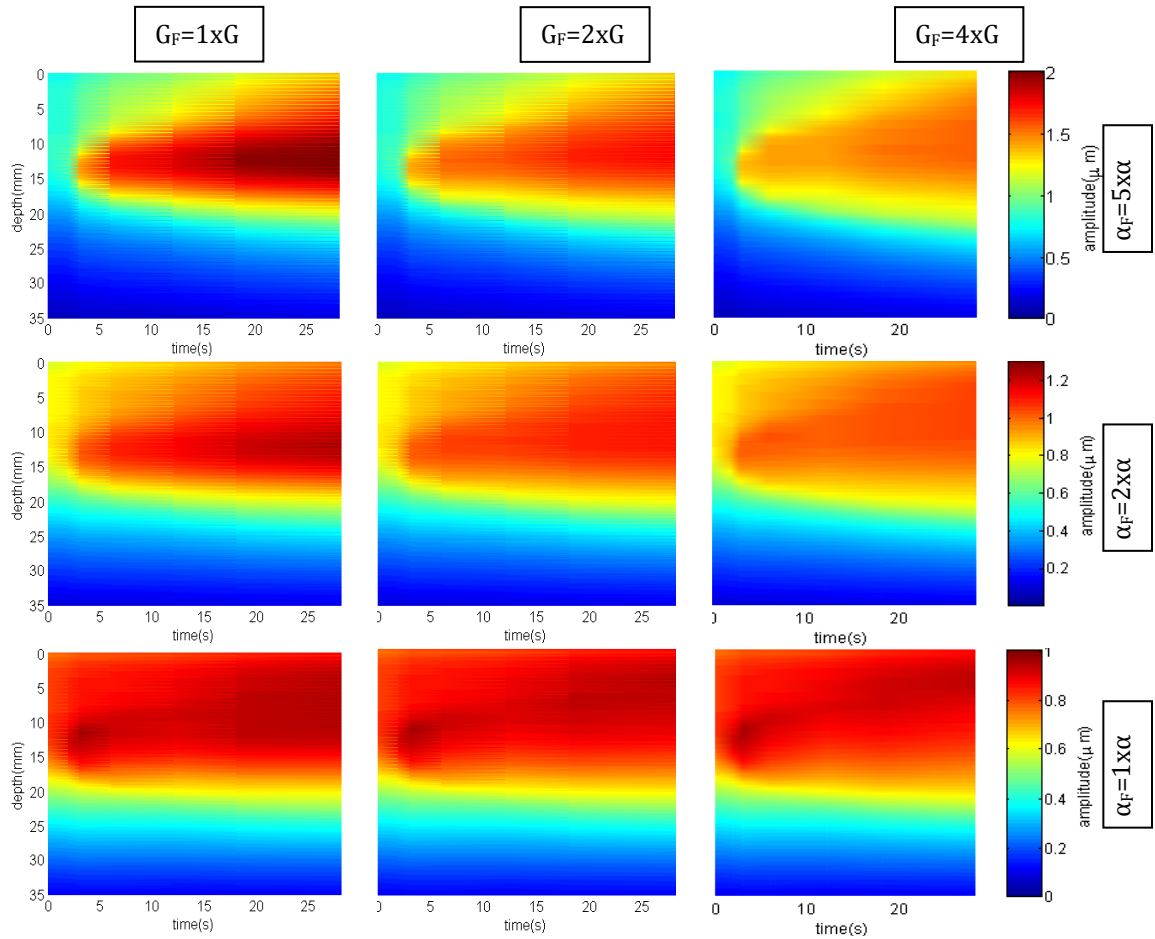


Figure 5.25 Modeled displacement amplitude for various values of final attenuation and stiffness. The three rows represent final values of attenuation of 5x, 2x, and 1x initial attenuation, from top to bottom. Color scale ranges are 0-2 μm , 0-1.3 μm , and 0-1 μm , respectively. Final stiffness values are 1x, 2x, and 4x for the columns, from left to right.

5.5.4 Conclusions

An FEM model was made to simulate the HIFU lesion process with concurrent HMI measurements. Since the acoustic attenuation and tissue stiffness are functions of temperature, models for the acoustic field, temperature field, and displacement needed to be coupled to simulate the HMI displacement. The model also accounted for acoustic nonlinearity in the HIFU field. The simulated displacement amplitudes are about 50% of those measured. In section 3.5.4 it was seen that measured temperatures were lower than predicted by models, until the value for acoustic

absorption is brought below 4Np/m/MHz . Thus it seems unlikely that the cause of the large underestimate of displacement (Figure 5.10) can be explained by an underestimate of tissue absorption.

Exploration of the individual effects of increased absorption and also increased stiffness revealed a similar pattern as produced by the combined model using three different sets of tissue parameters: as the focal region heats up, increased absorption leads to higher amplitude there, and increased stiffness leads to a broadening of the amplitude vs. depth. The initial increase in displacement at the focus could be caused by both the initial softening which occurs at about 40°C , and the increased absorption which begins at around the same temperature. These are both signs of the early stages of protein denaturation. The broadening pattern with depth occurs later, when the stiffness from the later stages of protein denaturation grows outside of the focal width, and may be a good indicator of when a substantial lesion has been made.

6

HMI Results and Comparison with FEM

6.1 Lesions produced in chicken

Figure 6.1 shows a photo of a typical HIFU lesion in chicken. This shows the results of the method used to prepare for measuring the size of the lesion. The tissue was first cut across the lesion, in order to localize it laterally. An axial cut was then made down the middle of the lesion and the two pieces pushed together in order to create a longitudinal cross-section. Measurements were taken from the cross-section using a ruler. Lesion size and depth will be annotated as three numbers $axb@c$: where a is width (i.e. diameter), b length, and c distance from sample surface to top of lesion, all in millimeters. For example, the size of the lesion in the photo is 3mm x 11mm @ 5mm.

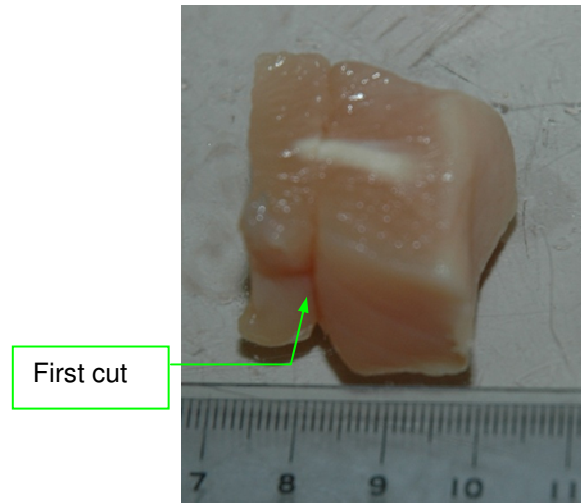


Figure 6.1 Cross-section of a typical lesion made by the H102 transducer, with focus placed 15mm below surface. The lesion was made in a larger sample, then cut into a cube for photograph.

During the course of this research, over 200 lesions were made. Peak pressures (in water) used to make lesions were between 5 and 9MPa, and durations from 15 to 80 seconds. Figure 6.2 shows the diameter as a function of pressure and duration for all lesions produced during one four day period of experiments. There is significant variability. Note there were several at 5MPa that produced no lesion. This motivates the need to have feedback on lesion formation; even in a simple ex-vivo model, constant acoustic exposure doesn't result in a reproducible lesion. Variability will likely be greater for an in-vivo situation with intervening layers.

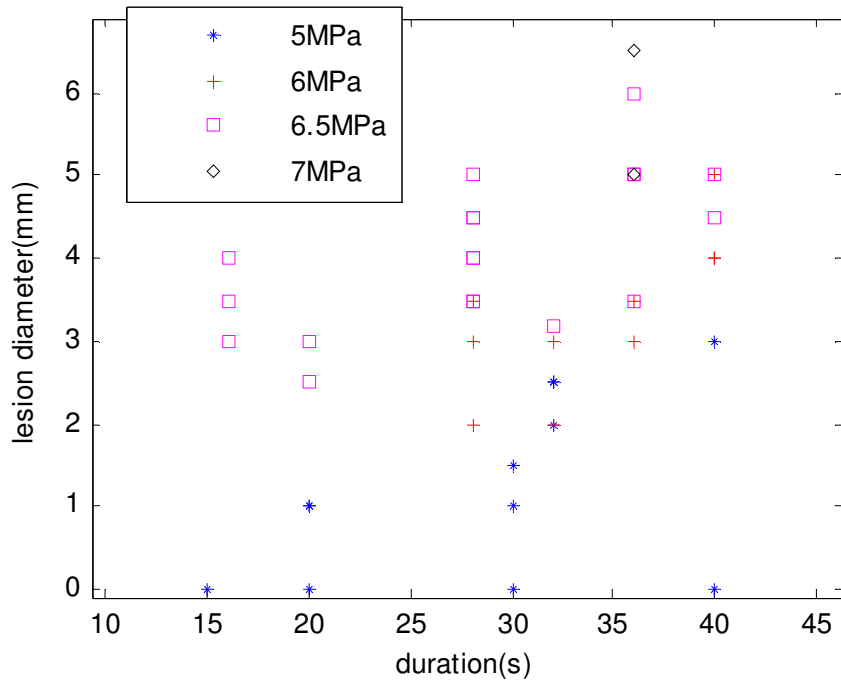


Figure 6.2 Diameters of lesions made in chicken as a function of duration and peak pressure (in water). Note there are many overlapped points.

6.1.1 HMI results during lesion formation

As described in section 3.3, HMI interrogation during lesion production consisted of four cycles of modulation at 40Hz. Interrogations were interleaved with 4 second heating periods. For each HMI interrogation, the Fourier amplitude was calculated as a function of depth, akin to an A-line. The lines were stitched together to produce a 2-d image of displacement as a function of depth in the tissue and insonation time. HMI interrogations continued to be taken for 20 to 60s after the HIFU shut off, at the same time intervals. During this cool-down phase, it is expected that if a lesion has been made, the attenuation inside the lesion will remain at the value reached during heating, and the stiffness will rise even higher. Also, any tissue outside the lesion that had been softened by the heat will cool and return to original stiffness. Together these are expected to result in less amplitude after the HIFU is turned off. The broadening of the focal maximum caused by the stiffness in the lesion is expected to remain.

To reiterate the main results of the FEM modeling, heating from HIFU will cause increased HMI amplitude in the focal region first due to tissue softening, then due to the increase in absorption in the lesion. As the lesion grows beyond the width of the HIFU field, the focal maximum in amplitude vs depth will broaden due to increased stiffness in the lesion. Thus, the expected signs of lesion formation are a rise in amplitude at the focus, followed by a broadening of the peak vs. depth. The broadened peak should sustain after the cessation of HIFU, but may be diminished. Note that amplitude will increase solely due to tissue warming, so increased amplitude does not in itself indicate lesion formation.

Figure 6.3 shows the results of 6 different lesions, all made in the same chicken breast. The pressure and duration for all was 7MPa, 28 seconds, the same as that modeled by the FEM simulations. Black lines at the top of each figure represent the lesion-making heating time. In Figure 6.3(a) there is an increase in displacement at a depth of 10mm starting soon after insonation. The displacement increases both towards the transducer and away, extending from 4mm to 18mm at the end of the insonation, with a peak amplitude of 35 μ m. Once the HIFU is stopped however, the displacement returns to close to base line. Figure 6.3(b) shows similar behavior except the region of high displacement is centered at 15mm, and the peak is only 1.5 μ m.

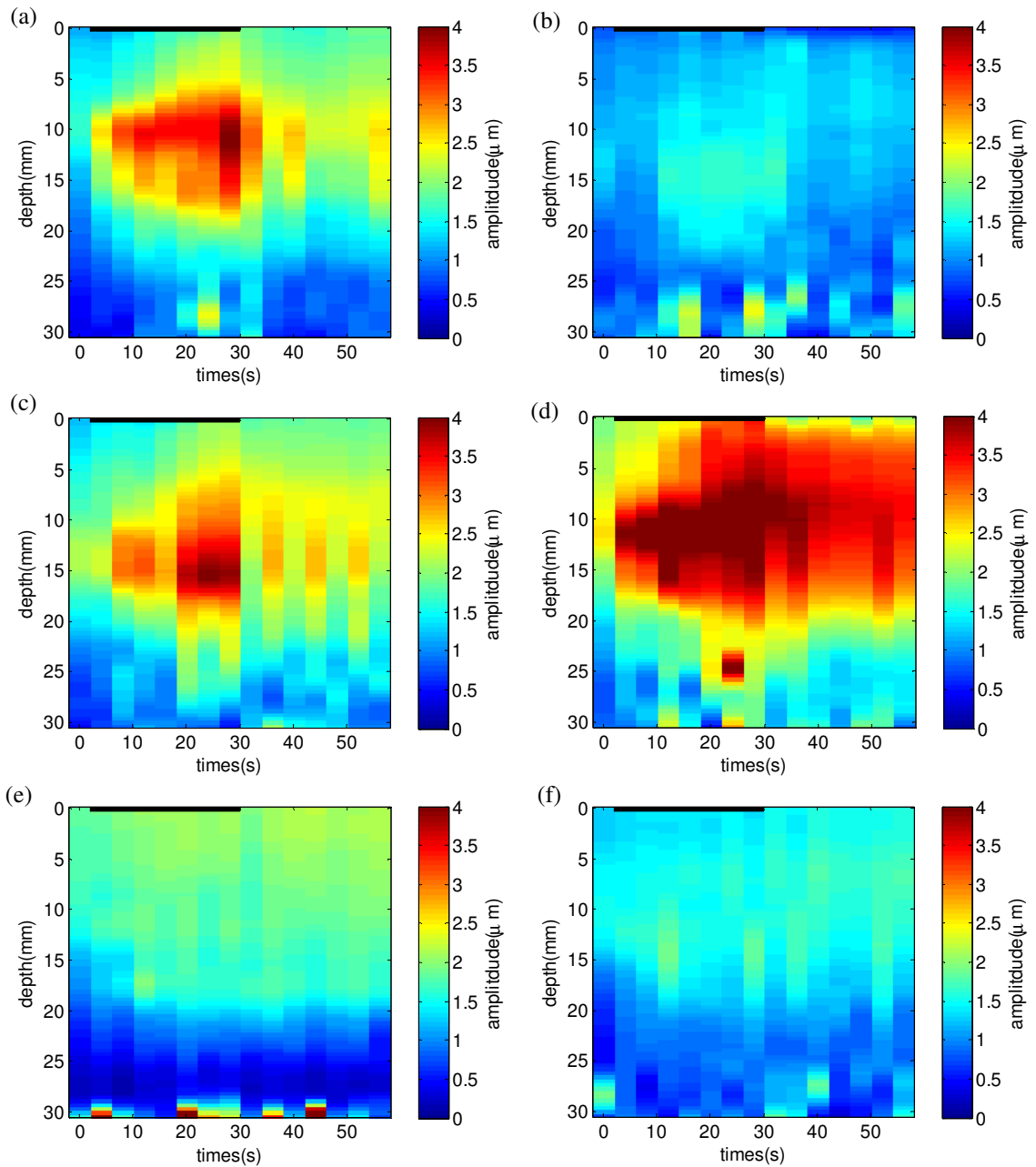


Figure 6.3 HMI results for 6 lesions made on the same chicken breast with HIFU peak pressure of 7MPa, lasting 28 sec. The sizes of the lesions were (a)3.5mm x 10mm @ 7mm, (b) 4mm x 13mm @ 5mm, (c)4.5mm x 11mm @ 7mm, (d) 3.5mm x 11mm @ 7mm, (e)4mm x 13.5mm @ 7.5mm, (f)5mm x 13mm @ 7mm. Black lines on top indicate the heating phase.

There is a rising and broadening vs. depth in (a), (c), and (d), similar to the FEM results (compare to Figure 5.22 to Figure 5.24). The broadened peak remains after cessation of HIFU in (d), and, to a smaller degree, in (a) and (c). In (b) there is a rise at the focus, but no significant broadening. In (e)

there is a rise near the surface, and perhaps a smaller rise near the focus. In (f) there is a small rise at the focus, but the pattern is intermittent in time. In most of these data sets there is a drop in displacement after the HIFU stops. At first glance this would suggest that the changes to stiffness and/or attenuation in the tissue are reversible. However, lesions were made, so irreversible changes should have occurred. There are two factors that may account for the apparent reversibility. One is that there was reversible softening in the tissue around the lesion, as would be expected in the first stages of protein denaturation; and the other is that bubbles could have contributed to extra forcing and displacement amplitude, which dissolved soon after HIFU stopped. Evidence for the latter could be found in comparing cases (a) and (d). In (a) there was some increase in echogenicity during HIFU (as with most all lesions) which soon disappeared after HIFU. In (d) the increased echogenicity did not disappear so much. The results from these 6 lesions are similar to the majority of all the lesions made, in that a clear manifestation of the basic pattern of rising amplitude followed by broadening peak vs depth, can be seen in only a portion of the lesions made. It is difficult to answer why the rest did not show the pattern.

In order to observe the difference between lesion-producing runs and runs that did not produce lesions, many exposures were made using a “threshold” peak pressure of 5MPa. At this level lesions were made in only about half the samples. The robustness of the method of detecting lesions by the pattern of rising amplitude followed by broadening, can be addressed by answering two questions: 1) Are there some lesions that occur without the pattern? And 2) Is there data in which the pattern arises, but no lesion is formed?

Figure 6.4 shows results from 6 runs taken on the same breast, with a peak pressure of 5MPa and durations from 17 to 50s. Only runs (a) – (d) produced lesions. The size of the lesion from (a) was 2.5mm x 9mm @ 10mm. The amplitude peak is seen, but not sustained during cool-down. However, the post-hifu level is overall more than the initial. The lesion size from (b) was 1.5mm x 7mm @ 12mm. A broad peak suddenly appears at one point during heating, which is sustained. The lesion size from (c) was 1mm x 1mm @ 9mm. The peak rises, and sustains. The lesion size from (d) was

large, at 5mm x 12mm @ 18mm. There is a rise and perhaps subtle broadening, which is not sustained. However, the post heating level is overall more than the initial. In (e), no lesion was made. The amplitude rises in a broad fashion, with no initial narrow peak, and the level is sustained. In (f), the heating duration was short (15s), and no lesion was made. There is a rise at the focus, but the amplitude after heating cannot be distinguished from the initial. One other run (not shown) produced no lesion, and had no rise in amplitude at all.

The answer to the first question, are there some lesions that occur without the pattern, appears to be yes, since case (b) has no initial rise, but rather transitions directly to a broad peak, much like case (e), in which no lesion was made. Also, cases (a) and (d) have only subtle broadening, at best.

To answer the second question, does the pattern ever manifest without a lesion forming, the answer is “almost”. Case (e) looks quite a bit like the rise-and-broaden pattern, but the initial rise is not narrow, like it is in a large majority other data in which increased amplitude is observed.

Various attempts were made at creating a type of metric that could describe the amplitude pattern with a single number that could be correlated with the presence or size of lesions, such as subtracting pre and post-lesion data, or differentiating the data with respect to time. None of these produced a metric that could predict lesion formation in chicken breast.

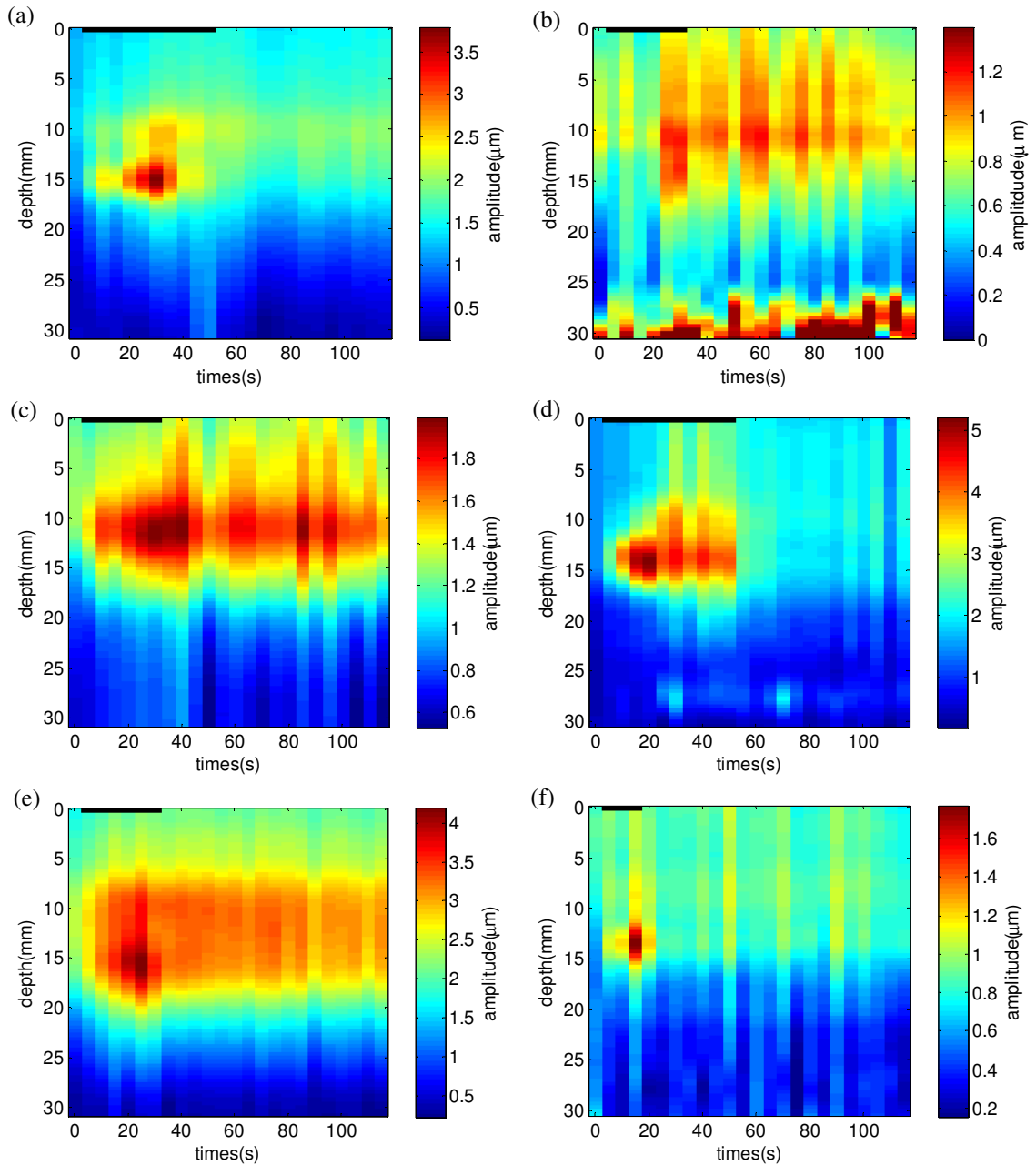


Figure 6.4 Data from 6 runs, all taken on the same chicken breast, at a peak pressure of 5MPa. (e) and (f) did not produce lesions. The lesion sizes of the others were (a) 2.5mm x 9mm @ 10mm, (b) 1.5mm x 7mm @ 12mm, (c) 1mm x 1mm @ 9mm, (d) 5mm x 12mm @ 18mm

6.1.2 Results for liver

Studies similar to those performed in chicken were done with fresh bovine liver. In liver there were more instances of data that was obviously affected by vessels or cavitation than in chicken. However it was easily seen when this occurred, and these data sets were discarded from further analysis. Therefore the evaluation of the robustness of HMI for lesion detection in liver is only considered for cases where there was no occurrence of cavitation and vessels, as evidenced by either poor line-to-line correlation or highly localized displacement. Figure 6.5 shows data from runs taken at 5MPa for 70 seconds. The top two plots show data for which no lesion was made Case (b) shows some rise and broadening, so here is an example of a “false” manifestation of the target pattern. Of the remaining 4 lesion data sets, all have a broadening except the bottom right, which has a constant narrow peak near the focus, and also large motion near the surface. Thus, as with the chicken data; there are results which show the target pattern, and produced a lesion (d and e); but there are also results which show the target pattern but have no lesion(b), and results that don’t show the pattern, but have a lesion(f).

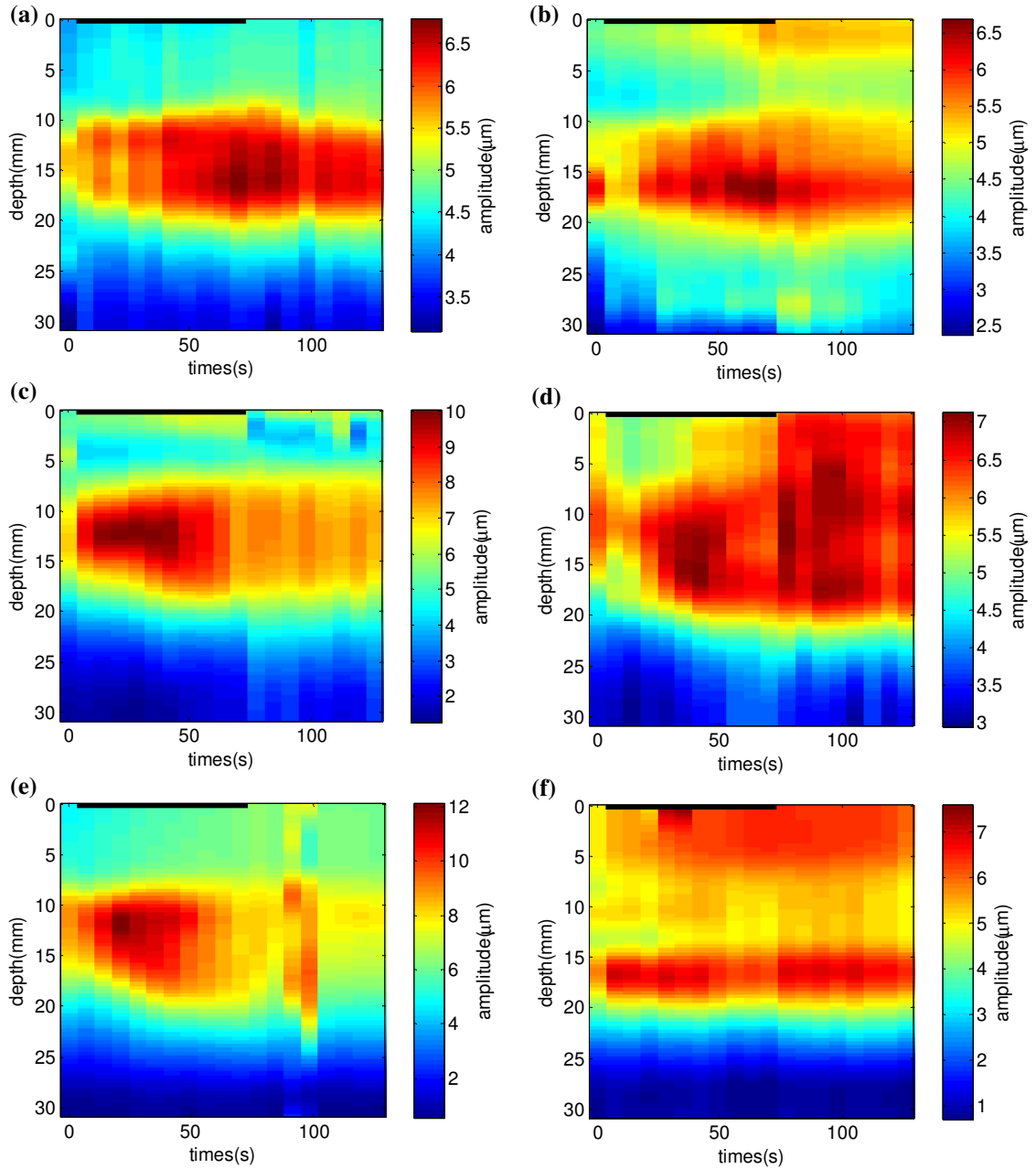


Figure 6.5 HMI data for fresh liver. All 5MPa, 70s, Lesion sizes were (a)no lesion, (b) no lesion, (c) 2mm x 10mm x 7mm, (d) 1mm x 2mm x 9mm, (e) 5mm x 10mm x 6mm, (f) 3.5mm x 7mm x 9mm

6.1.3 Results at 3.3MHz HIFU frequency

The HIFU transducer could be operated at its third harmonic, 3.3MHz, with a custom impedance matching transformer. Much effort was placed into making lesions and measuring HMI at this

frequency, since theoretically they could be made at a lower pressure due to higher tissue absorption, and therefore induce less cavitation. It was found however, that higher pressures were needed to make lesions. At 1.1MHz, lesions were reliably made at a derated focal pressure of 6.4MPa. However at 3.3MHz, lesion production required a calculated focal pressure of at least 7MPa. This was probably due to tissue inhomogeneities, which had more of an effect on the 3.3MHz HIFU than the 1.1MHz. Cavitation was thus much more prevalent during lesion/HMI runs, and the HMI data was usually too noisy to be of use. However there were some runs that showed the pattern of rising displacement near the focus, followed by a broadening with depth. However, among the data not corrupted by cavitation, there was nothing to indicate that lesion development could be observed any more accurately at this frequency than at 1.1MHz.

6.2 Bulk motion, thermal apparent displacement, and bubbles

In order to illustrate features associated with bulk motion, thermal apparent displacement, and bubbles, one data set will be examined in detail. Figure 6.6 shows all the A-lines of a data set in which a lesion of size 5mm x 13mm @ 6mm was produced in chicken with a 7MPa, 40 sec. HIFU exposure. As described in section 3.3, additional interrogation pulses were usually fired during the heating phases, for the purpose of monitoring cavitation and measuring bulk (non-modulated) motion. During the 4 second heating phases, pulses were fired in groups of two (riding on opposite phase of HIFU wave, to cancel nonlinear sound speed effects), at a rate of 5 groups per second. There are 40 lines thus produced during a 4 second heating period, and 125 lines during a 0.1 second interrogation (taken at 1.25kHz). Thus the "heating" lines show up in the plot as narrow strips every 165 lines like the one at line #490. During the heating the tissue was subjected to constant acoustic forcing of higher magnitude than during the HMI interrogation periods, and the resulting motion can be seen as a trend to the right on the plot (away from the HIFU and pulse transducers) in the region around sample #2000 (fast time), which is the HIFU focus. However, increasing temperature results in higher acoustic velocity, therefore shorter travel time for the interrogation pulses. This causes a leftward movement on the plot, which competes with the forcing. The result seen in this plot is a net

rightward movement at the focus, but some leftward motion before the focus. Thermal expansion will also cause motion in the tissue, which is probably seen in this plot as the leftward trend of the echoes near the surface. A sudden movement to the left can be seen at the end of heating (line #1778). This is the bulk “snap back” of the tissue after the cessation of the constant HIFU force. The HMI modulations cannot be seen at this scale, but when zoomed in they appear as wiggles of an amplitude of one or two samples. There is a leftward trend in these wiggles, caused by the tissue momentarily “snapping back” from the previous heating phase, but not enough to spoil the AC component used for measuring HMI displacement. This illustrates the advantage of the HMI method; it is immune to bulk motion caused by thermal apparent displacement, thermal expansion, bulk forcing, and other net motion of the tissue as expected in a clinical application.

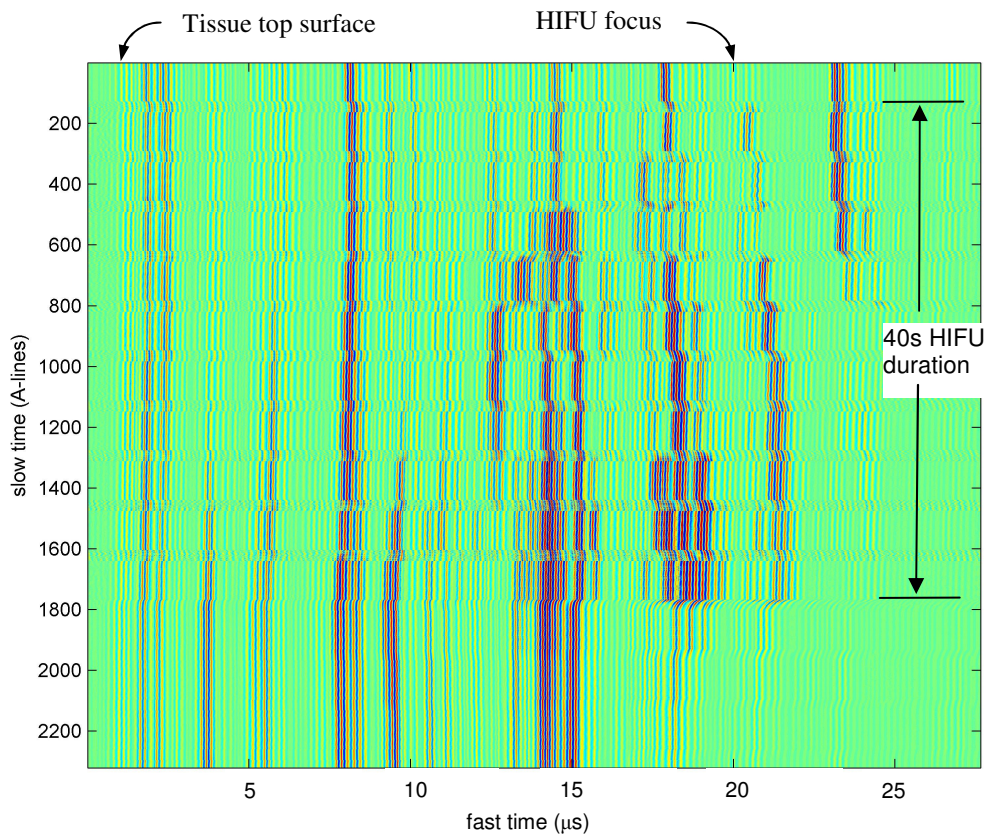


Figure 6.6 All A-lines from a data run in which a lesion of size 5x13x6 was produced in chicken with a 7MPa, 40 sec. HIFU exposure.

The increase in echogenicity at certain depths is probably from bubbles forming due to boiling or cavitation. The first group of A-lines occurs before the first heating, so the regions of stronger echoes there are either tissue inhomogeneities or bubbles that were not removed during degassing. During heating there is an increase in echogenicity in three regions, at sample number 1400, 1800, and 2100. The latter two disappear within 4 seconds after the end of heating, but the first showed little sign of diminishment, even at the end of the run 55 seconds later. If these echoes are bubbles, this suggests the latter two groups are small bubbles which dissolve quickly ($<15\mu\text{m}$, Figure 4.2), and the first group are much larger, perhaps the result of boiling.

Figure 6.7(a) shows the HMI data for this run. There is an increase near the focus, but it is short-lived. It is possible that bubbles shielded the focal zone, but the size and depth of the lesion was similar to lesions produced with little evidence of bubbles. Shown in Figure 6.7(b) are spectrograms of selected A-lines taken during heating periods (each time window in the spectrograms was Hamming-windowed, and there was 50% overlap between windows). The data from the first A-line shows the backscattered spectrum begins at 5MHz, due to the high-pass filter. The upper end is defined by the sensitivity of the interrogation transducer, which falls 20dB by 13MHz. After the first HIFU heating phase the spectrogram looks similar, but at the end of HIFU there is an increase in broadband energy near the focus, and many harmonics of the HIFU frequency at all times. The broadband scattering of the pulse remains immediately after the cessation of HIFU. This suggests that the interrogation pulse was scattered by bubbles near the focus, and the HIFU was scattered by bubbles at an unknown depth (since the HIFU is CW). As seen in Chapter 4, these strong HIFU harmonics, which only occurred in a minority of the lesion runs, were probably due to inertial cavitation. This is corroborated by the fact that spikes were seen on the A-line once every period of the HIFU fundamental. The data sets that showed HIFU harmonics, and also those showing a large amount of increased echogenicity usually had HMI data with localized spikes in motion or erratic patterns. These were discarded from further analysis. However, most of the data, while not showing

harmonics from inertial cavitation, did show some increased echogenicity and extra broadband energy near the focus, possibly indicating some form of cavitation.

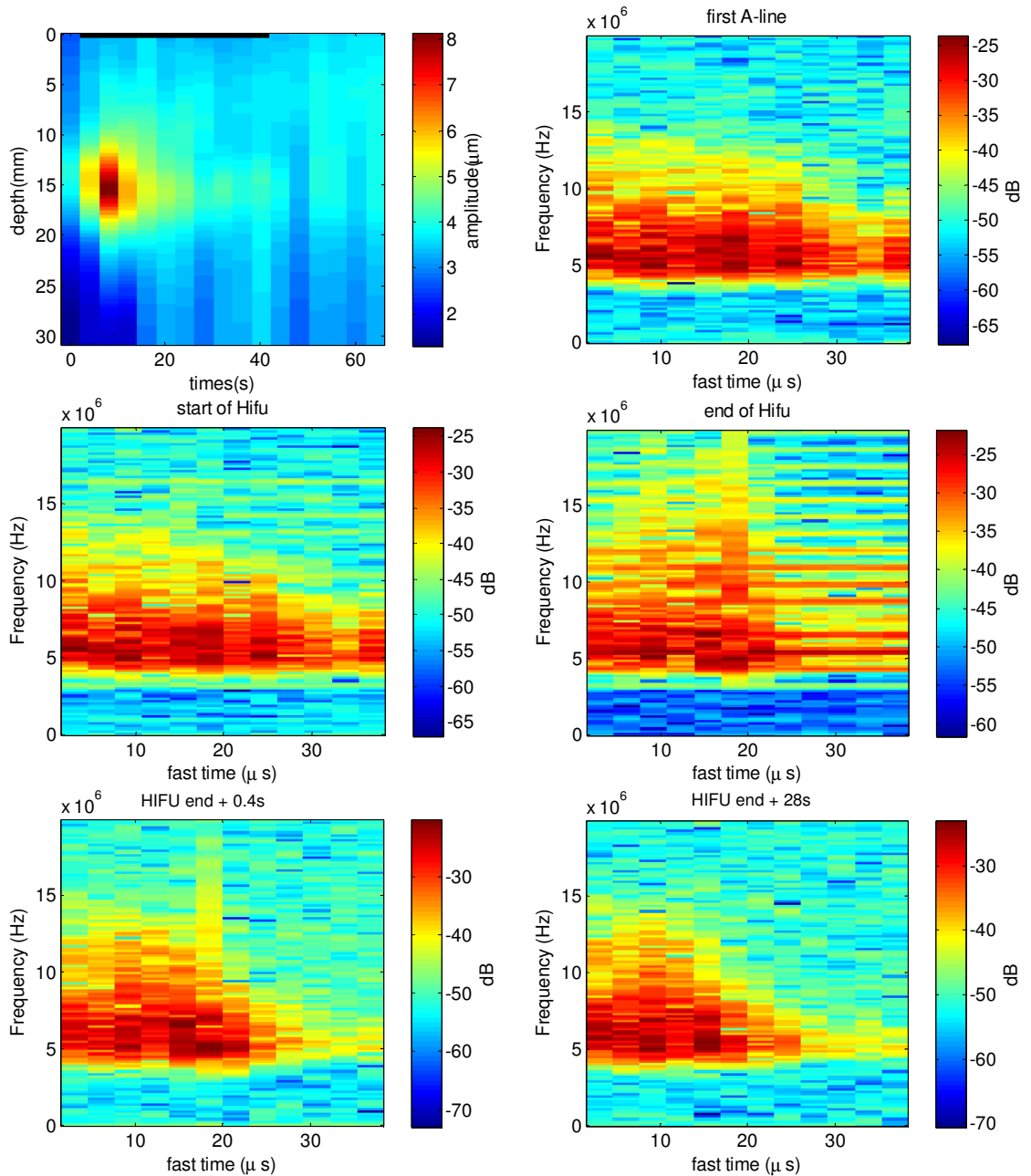


Figure 6.7 Data from same run as in Figure 6.6. Upper left: HMI data. The rest are spectrograms taken of the A-lines during the heating periods. The HIFU focus is at $20\mu\text{s}$.

6.3 Conclusions

The measured pattern of HMI amplitude vs. depth did not consistently agree with the pattern predicted by the FEM. Of 65 lesions, 26% showed the pattern; 21% showed central region of displacement that either narrow or wide, but did not change over the course of the HIFU exposure; and 52% were either too noisy to be considered, or exhibited a pattern of constant uniform displacement over the first 10 to 15 mm of depth. There were only five instances where no lesion was made at the threshold pressure of 5MPa, and no instances above that. At 5MPa, the HMI data for these 5 did not show the rising-broadening pattern, with the exception of one. In order to be useful, the 26% of runs which showed the rising-broadening pattern would still need to be shown to predict the actual lesion size and initiation time. This will be investigated in chapter 7, where acousto-optic imaging is combined with the HMI method. However, it can be concluded that, in this particular application of HMI, it appears that there was too much variability in the data to reliably monitor lesion formation.

Most of the data showed some increased echogenicity and extra broadband energy near the focus, suggesting that lesion formation was usually, if not always, coincident with some bubble formation and/or excitation. However, this did not seem to be correlated with the presence or non-presence of the predicted target pattern of the HMI amplitude vs. depth. It is not entirely certain that the increased echogenicity was caused by bubbles, but in lieu of other mechanisms (e.g. heat related), it is the most likely cause. The thermal model suggests that boiling temperatures are likely reached with the HIFU pressure levels used to make lesions in this work. Perhaps the boiling makes small bubbles that only modestly increase backscattering, without producing significant shielding or inertial cavitation.

7

Combined Acousto-Optic Imaging and HMI

7.1 Background

Acousto-optic imaging, like conventional refractive optic imaging, creates spatial images based on the optical properties of matter. However it can create maps of optical properties in optically diffusive media with the use of an ultrasound beam (Dolfi and Micheron 1989, Marks et al. 1993, Leutz and Maret 1995). Acoustic waves can influence light because they induce fluctuations in local density, which in turn affects the optical index of refraction, absorption, and scattering. As an example, a diffraction pattern may be observed when photons from a laser are passed through a grating pattern of high and low optical index set up by acoustic standing waves (Raman and Nath, 1935). Acoustic waves also induce fluctuations in particle displacement, which affect the phase of photons scattered from those particles. For precise descriptions of these mechanisms of the acoustic interaction with light, see Thurston and Mason (1976), Leutz and Maret (1995), Korpel (1997), Kempe et al. (1997), Sakadzic and Wang (2005). Upon emerging from a diffuse medium, there is no way of telling the path taken by photons. However, if they passed through an acoustic wave at some point, the path would have been changed by the mechanisms listed above. Photons with altered paths, so called “tagged” photons, would appear with a different phase than they would have had

without the acoustic wave. If the amount of tagged photons could be somehow measured, then this signal would be a measure of the amount of the acoustic “tagging” in the specific region of the acoustic energy, which can be made fairly small via focusing. Any process or property that affects the magnitude of the acousto-optic interaction or the number of tagged photons could thus be mapped in space with the resolution of the size of the acoustic focal zone (Murray et al. 2004; Ramaz et al. 2004). Two such properties are optical absorption and scattering. Both of these increase when a thermal lesion is made in tissue, so acousto-optic imaging may be effective in monitoring FUS lesion formation. Various methods have been developed to detect tagged photons, including the use of single speckle detectors (Dolfi and Micheron 1989, Lev et al. 2000), parallel multiple speckle detection using a CCD to improve the signal-to-noise ratio (Leveque 1999), photorefractive holography and interferometry (Murray et al. 2004), and a nonlinear narrowband optical filter achieved by a spectral hole burning crystal (Li et al. 2008).

7.1.1 Detecting tagged photons with a photo-refractive crystal

This thesis describes experiments which used the interferometric method used by Murray et al. (2004), in which tagged photons are detected using a photo-refractive crystal (PRC). The basic setup is shown in Figure 7.1. The tissue sample was illuminated with infrared laser light from a CW Nd-YAG laser ($\lambda=1064\text{nm}$, intensity at tissue= $200\text{mW}/\text{cm}^2$), and the scattered light was collected by a 3 inch diameter lens and directed into a 7mm cubic GaAs photorefractive crystal. A full description of the physics involved in the crystal is beyond the scope of this thesis, however a simplified explanation follows. The beam from the sample (“signal beam”) interferes with the reference beam to form a stationary three-dimensional pattern of optical intensity in the crystal. This in turn liberates charges which re-distribute according to this pattern, and give rise to local changes in optical index through the electro-optic effect. The result is a diffraction grating which matches the interference pattern of the two waves. This diffracts energy from each wave along the path of the other, in a process called two-wave-mixing (Figure 7.2). For example, when the grating is

established, energy from the reference beam will be diffracted in the direction of the signal beam, with the same complex wavefront as the signal beam. This results in more light at the photodetector.

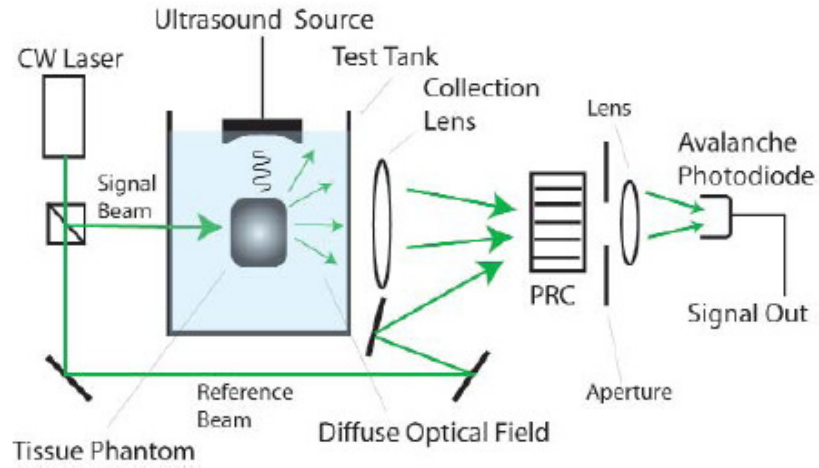


Figure 7.1 Schematic of the acousto-optic experiments

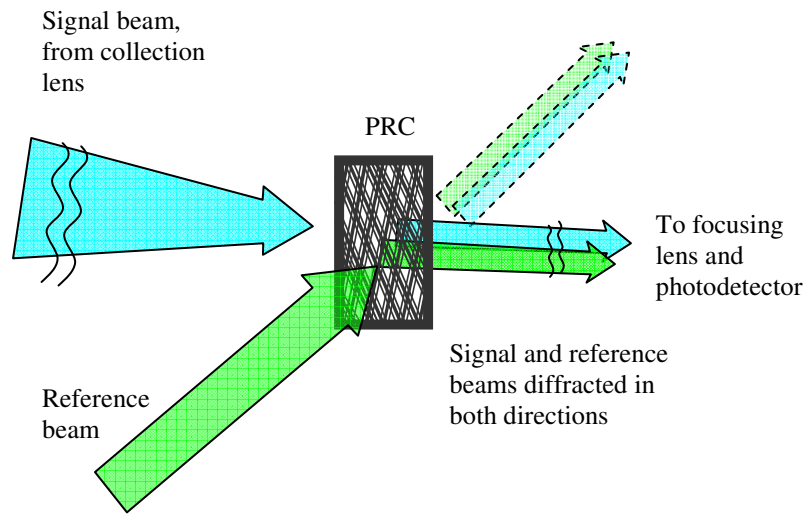


Figure 7.2 Schematic of the action of the PRC. A grating is made by the interference of the two beams which diffracts each in the direction of the other.

At the exit of the crystal the intensity is given by (Delaye et al. 1995),

$$I_{se} = \exp(-\alpha L) I_{so} (|\exp(\gamma L) - 1|^2 + 1) + 2\text{Re}\{[\exp(\gamma L) - 1]^* \exp[i\varphi_a \sin(\omega_a t + \chi_r)]\} \quad (7.1)$$

where I_{so} is the intensity of the signal beam before entering the crystal, α and L are the optical absorption and length of the crystal. γ is the efficiency, or gain coefficient, of the two-wave-mixing in the crystal (prime and double-prime being the real and imaginary parts). γ is increased by the strength, or “depth” of the diffraction grating, and this increases the two-wave-mixing (TWM) efficiency. As a photon passes through the acoustic field, it will accumulate phase changes every time it scatters from particles moving with the acoustic field. It will also accumulate phase changes when it encounters optical index changes induced by the acoustic field. The accumulated change to the photon phase can thus be written as $\varphi_a \sin(\omega_a t + \chi_r)$ where φ_a is the magnitude of the photon phase change, ω_a is the acoustic frequency and χ_r is the *phase of the acoustic modulation to the photon phase*. Equation (7.1) can be written as the sum of two terms, an “AC” term which contains the acoustic frequency ω_a , and a “DC” term which does not (Blonigen et al. 2005):

$$I_{se}^{DC} = \exp(-\alpha L) I_{so} \{ (|\exp(\gamma L) - 1|^2 + 1) + 2[\exp(\gamma' L) \cos(\gamma'' L) - 1] J_0(\varphi_a) \} \quad (7.2)$$

$$I_{se}^{AC} = 4 \exp(-\alpha L) I_{so} \exp(\gamma' L) \times \sin(\gamma'' L) J_1(\varphi_a) \sin(\omega_a t + \chi_r) \quad (7.3)$$

These equations represent the intensity at the detector for one optical path only. The total intensity will be the sum over all paths incident on the detector. In this summation, it is assumed that each value of φ_a is <1 radian and therefore the values of the Bessel function J_0 will occur before the first minimum in the function. However, the values of χ_r will be distributed randomly through all phase

space, and this will effectively eliminate the AC term. We are left with the DC term, which is proportional to $J_0(\varphi_a)$, a measure of the number and degree of acoustically-tagged photons.

7.1.2 Lesion optical properties

Thermal lesions in tissue have increased optical absorption and scattering over healthy tissue. Among the mechanisms for increased absorption is an increase in concentration of chromophores due to protein coagulation (Cilesiz and Welch 1993, Yaroslavsky et al. 2002). The increase in scattering results from the higher concentration of scattering sites caused by a decrease in the effective size of the scatterers (Nilsson et al. 1998). Figure 7.3 qualitatively shows the increase in absorption in a thin, back-lit cross-section of a lesion in chicken, which appears darker than the surrounding tissue. Also shown is the white color of the lesion as a result of the increase in scattering.

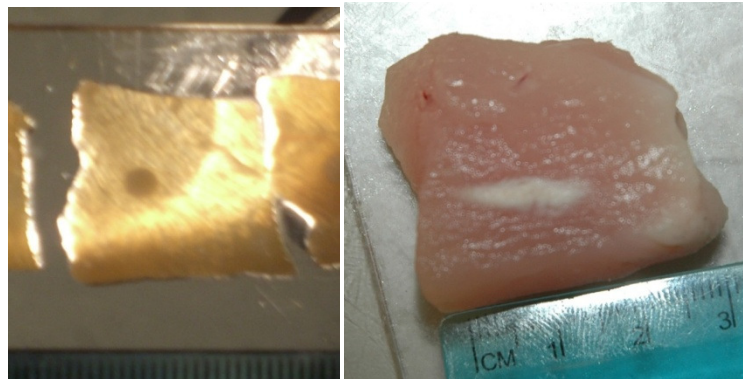


Figure 7.3 Left: increase in absorption in a thin, back-lit cross-section of a lesion in chicken, which appears darker than the surrounding tissue. Right: Lesion appears white as a result of the increase in scattering.

7.2 Detection of lesions with pulsed ultrasound

Lesions were detected, post formation, with a similar approach to that used by Sui et al. (2004). Figure 7.1 showed the optical components, and Figure 7.4 shows the physical setup with the location of the acoustic sources and tissue sample in the water tank. Figure 7.5 is a photo of the setup taken immediately prior to HIFU exposure, showing the chicken tissue in the sample mount. Figure 7.6 shows the approximate size relationship between the ultrasound focus and the light field. For

adequate SNR for the acousto-optic (AO) signal the laser was not expanded before the tissue sample, as might be expected for imaging a region of tissue. The majority of the scattered laser light emerged from the sample from a fairly small area 1 to 2 cm in diameter, which was imaged onto the surface of the PRC. It was found that the TWM gain decreased as the angular distribution of the light grew, and this was another reason to image only a small region of the tissue. The optically-modulating pulsed ultrasound field was created using a diagnostic ultrasound array transducer, which was driven by an ultrasound imaging machine (Analogic 2300). The system created 5 MHz pulsed ultrasound which had a spatial extent of 0.3mm in the acoustic propagation axis and 0.8mm beam width. The tissue samples were store-bought chicken breast, cut into a 4 cm x 4 cm x 2 cm pieces and then degassed for 40 min. in phosphate buffered saline solution.

As an ultrasonic pulse traverses the illuminated tissue, the flux of modulated (tagged) photons increases, resulting in a drop in voltage from the photodetector. The profile of this AO signal essentially tracks the local intensity of the illuminated region (typically Gaussian). If the pulse traverses a sub-region of higher optical absorption, such as a HIFU lesion, there will be less local photons available to “tag”. This will diminish the AOI signal, and result in a blip in the overall decrease in photodetector output, giving it a characteristic “W” shape. The ultrasound array is electronically steerable and by firing a sequence of acoustic pulses in different directions it is possible to create a 2D image of the AOI data. However for this study, restrictions in the set-up meant that the multiple lines were achieved by mechanically translating the sample. An AOI scan was obtained prior to HIFU exposure. To obtain sufficient SNR it was necessary to average the AO signals for 10^4 acoustic pulses. The sample was also imaged with the ultrasound scanner in standard B-mode.

Lesions were made in the center of the sample (focal depth=16mm) with the same 1.1 MHz HIFU transducer used in the HMI work. The peak pressure was 8MPa, and the duration was 6s. After HIFU treatment the sample was re-imaged with AOI and B-mode ultrasound.

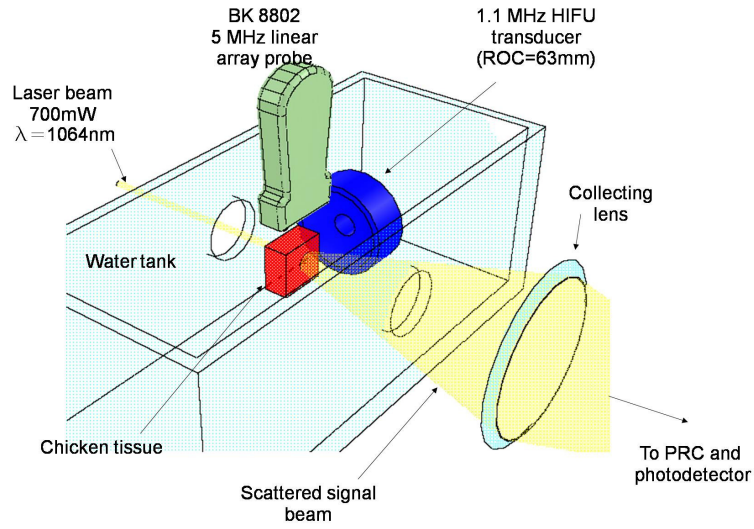


Figure 7.4 Experimental setup. The light passes through transparent windows into and out of the tank. Drawing is to scale, with depth perspective.

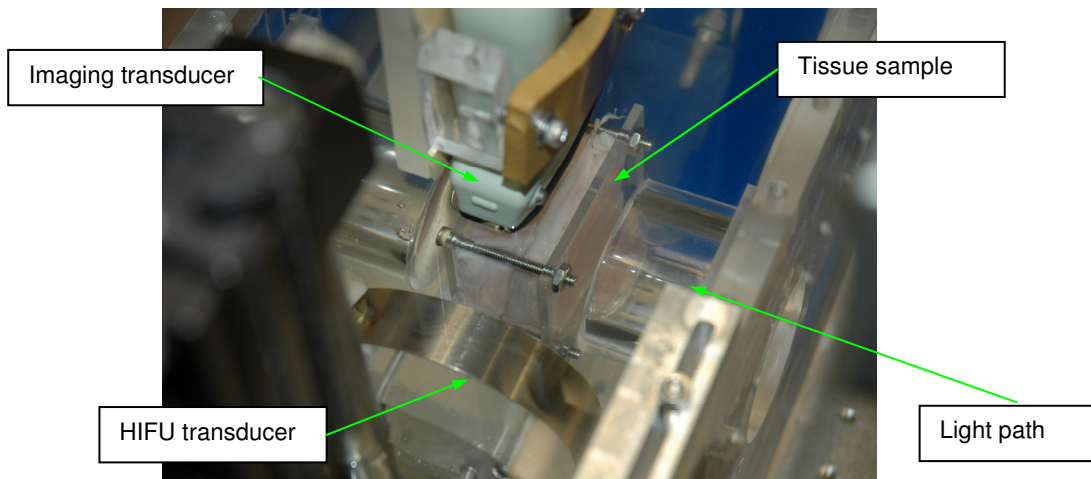


Figure 7.5 Photo of tissue sample mount, plus HIFU and imaging transducer

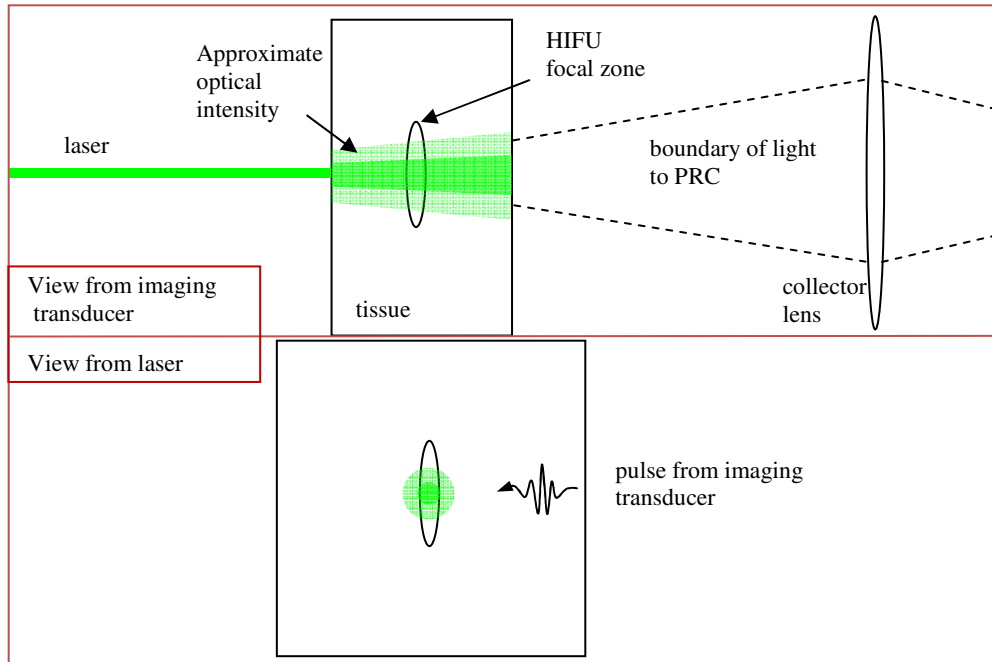


Figure 7.6 Cartoon depicting the approximate size of the acoustic and light fields.

7.2.1 Results

Figure 7.7 shows time waveforms from the photodetector for a scan line through the center of a lesion. The width of the pre-lesion AOI dip, shown in Figure 7.7(a), is $5 \mu\text{s}$, which, based on the speed of sound in the tissue, corresponds to a physical distance of 7.7 mm. This is the optically illuminated region and comprises the effective field of view of the AO setup. Figure 7.7(b) is the post-lesion waveform, showing a central region where the AOI effect is less. The width of the central blip is proportional to the width of the lesion region of increased optical absorptivity. By subtracting the two waveforms the resulting trace, Figure 7.7(c), is essentially a 1-D line plot of the optical property contrast through the lesion. A 2-D image can be constructed by stacking the individual lines scanned across the sample (just as is done to create a B-mode ultrasound image). The result is an optical image of the interior of a diffuse medium, with a resolution determined by spatial extent of the acoustic pulse (typically of order 1 mm).

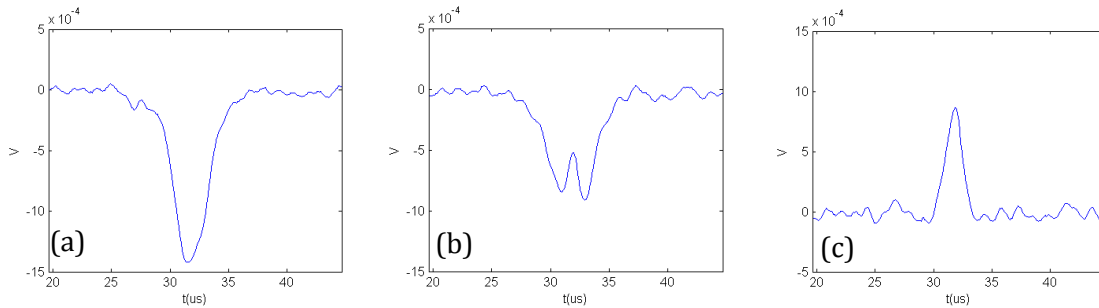


Figure 7.7 Photodetector waveforms for acoustic pulses directed through the center of HIFU lesion in chicken. (a) pre-lesion, (b) post-lesion, (c) difference.

Figure 7.8 shows the resulting image for one lesion. The dotted line shows the location of the HIFU focal region, as determined by -6 dB pressure contours. The AO image indicates that the lesion “grew” toward the HIFU source—possibly caused by bubble shielding. Shown at right is a B-mode image taken of the same sample, within five minutes post sonication. The dashed line indicates the region of the AOI image at left, and a similar oval marks the focal region. No evidence of the lesion can be seen, consistent with the known difficulty in detecting HIFU lesions with standard ultrasonic imaging. Any gas bubbles that may have been created during the HIFU insonation have dissolved by the time the B-mode image was taken, or are too small to show up. The experiment was repeated on three separate chicken breasts. Table 7-1 Position and size of three lesions measured with pulsed AOI method, compared with post-dissection manual measurements. The location of the start of the lesion was within 1 mm for the two methods. The AOI measurements for lesion length thus agree with the manual measurements, within the error bounds which are estimated to be ± 2 mm. The lesion widths were not measured accurately, presumably due to the finite width of the ultrasound pulse.

Lesion number, method	Start (mm)	End (mm)	Length (mm)
1 AOI	-2	7	9
meas.	-1	9	10
2 AOI	-3	11	14
meas.	-3	14	17
3 AOI	-1	7	8
meas.	-2	7	9

Table 7-1 Position and size of three lesions measured with pulsed AOI method, compared with post-dissection manual measurements.

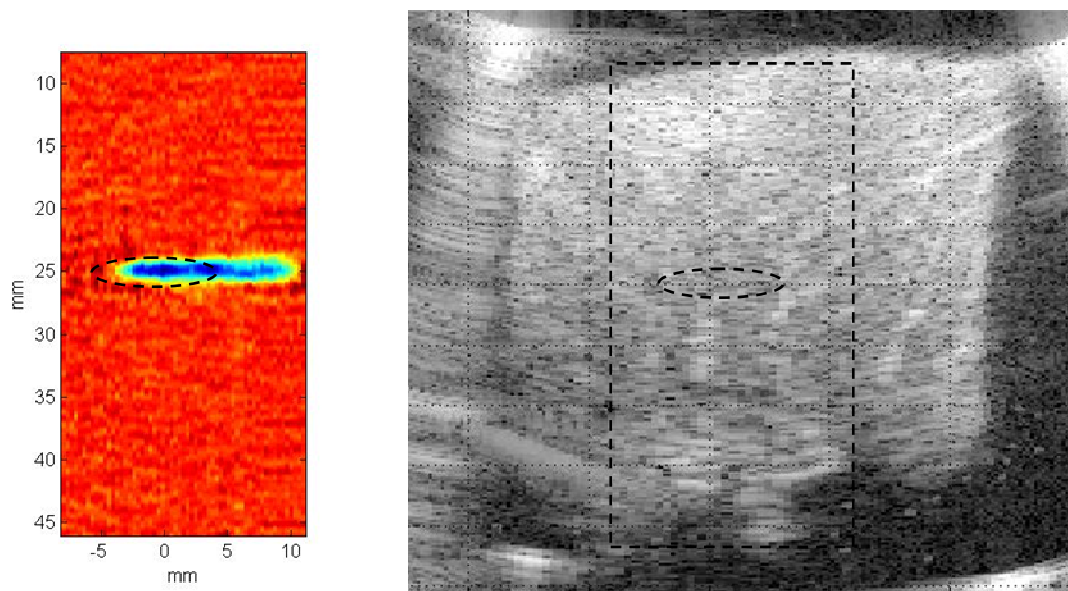


Figure 7.8 Left: AOI image of HIFU lesion in chicken breast. The HIFU focal zone is shown by the dashed oval. The tissue was scanned in increments of 1/3 mm in the horizontal dimension. Right: A standard B-mode ultrasound image of the same tissue where the dashed rectangle represents the area of the AOI image shown at left. The lesion was not visible in the B-mode image. Lesion was 4mm thick, 14mm long.

7.3 Detection of lesions with CW ultrasound

The pulsed ultrasound method described in section 7.2 required over 30s of averaging time for each location, making this approach incapable of monitoring lesion formation in real-time. It was

hypothesized that using the HIFU transducer to create the acousto-optic effect in CW mode would improve the signal-to-noise ratio. The spatial resolution along the ultrasound beam afforded by the short pulse length ($\sim 3\text{mm}$) would be forfeited since the HIFU was now CW. The resolution would now be determined by the size of the HIFU focal zone, which is 10mm long. Because the same acoustic source could be used for both the AOI excitation and the lesion heating, “Imaging” the lesion in space was no longer necessary, since the AOI signal was a measure of the optical properties at the exact lesion location.

In preparation for this work, the AOI signal was measured for various ultrasound burst lengths. The 1.1MHz HIFU transducer was used to fire 1MPa peak pressure bursts of 5 to 50,000 cycles into an acrylamide gel phantom loaded with glass microspheres for scattering. The avalanche photodiode (APD) photodetector output is shown in Figure 7.9. The depth of the signal drop increased when the HIFU duration changed from 5 to 50 cycles because a larger portion of the optical field was affected by the ultrasound. However after this number of cycles the increase was caused by another mechanism, associated with the PRC response time. The diffraction grating of the PRC requires a finite time to be written, and this response time decreases with the intensity of the optical fields. For the approximate intensities used in this work the response time was measured to be 10 to 15ms (Lai, 2011). It is this delay which makes the PRC able to detect changes in the optical field (i.e. the tagged photons). If there were no such delay, the grating would continuously adapt to the optical fields and there would be no change in output. Thus it is usually desired to induce and detect changes in the number of tagged photons lasting much less than the PRC response time. For the case of CW ultrasound, there is an initial drop in the APD output as described in section 7.2 – the new light field no longer matches the grating, so the TWM gain drops. The grating starts to adapt to the new light field, and if this field were stable in time, the original APD level would be restored. The new light field is not stable, however, since the tagged photons have a phase modulation that is changing at the ultrasound frequency. As a result the grating becomes weaker, so the TWM gain becomes weaker, and the APD level further drops. This is the cause of the continuing drop seen in figure Figure 7.9,

which, for the case of the 10,000 cycle burst, can be seen to have a time constant similar to the independently measured PRC response time of 10-15ms. The drop in output levels-off eventually, because the grating settles to the configuration made by the un-tagged photons, which still make up the majority of the optical field.

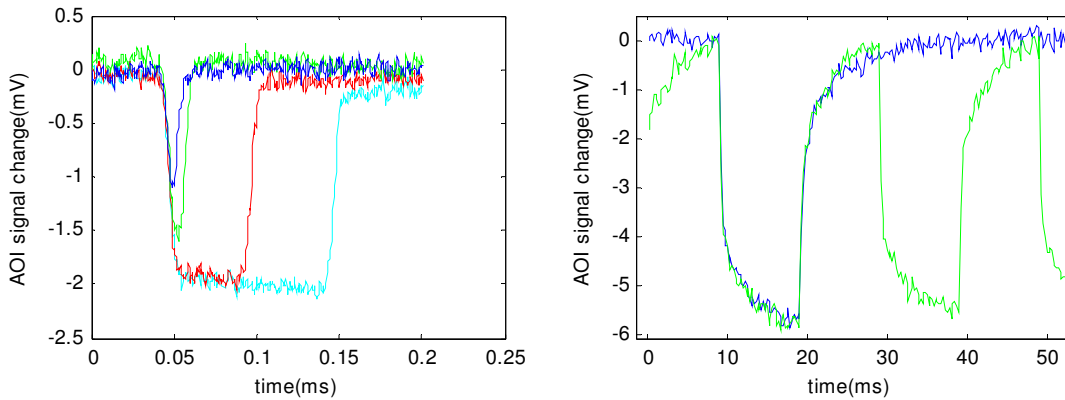


Figure 7.9 Left: Photodetector(APD) voltage for 1.1MHz, 1MPa acoustic excitations lasting 5, 10, 50, and 100 cycles. Right: Output for 10,000 cycles, at both 1% and 50% duty cycle.

The initial drop is about 2mV, and the further drop caused by grating degradation is another 4mV. When the ultrasound is turned off, there is a sudden increase in the APD signal, as the optical fields that made the original grating are restored. However, the grating has changed somewhat, so the restoration is not complete. The grating then re-adapts to the field, restoring the original APD level. This drop in output for long ultrasound bursts was also observed by Gross et al. (2009), who further investigated the use of this phenomenon as a quantitative measurement of PRC response time. In a modified approach, their method recorded tagged photons as an increase in output light level, rather than a decrease. The grating decay thus detracted from their signal, whereas it actually benefits the present detection scheme, since it is shown here to increase the AOI signal change by 200%.

The biggest improvement to the SNR comes with the introduction of a lock-in amplifier after the APD output. Since a 50% duty cycle imposed on the CW ultrasound bursts allows the grating to restore (as shown by the green curve at right in Figure 7.9), the lock-in amplifier can now measure the amplitude of the rising and falling of the APD signal if its reference frequency is set to the pulse

repetition frequency (PRF) of the ultrasound modulation. The lock-in effectively multiplies the input with a sine wave of the reference frequency, and the output is a DC voltage level proportional to the Fourier component of the input at the reference frequency. The depth of the drops in the APD signal were a function of the number and degree of tagged photons, and this could now be monitored in real time, thanks to the superior noise rejection of the lock-in. Figure 7.10 shows the AOI experimental setup with the addition of the lock-in amplifier.

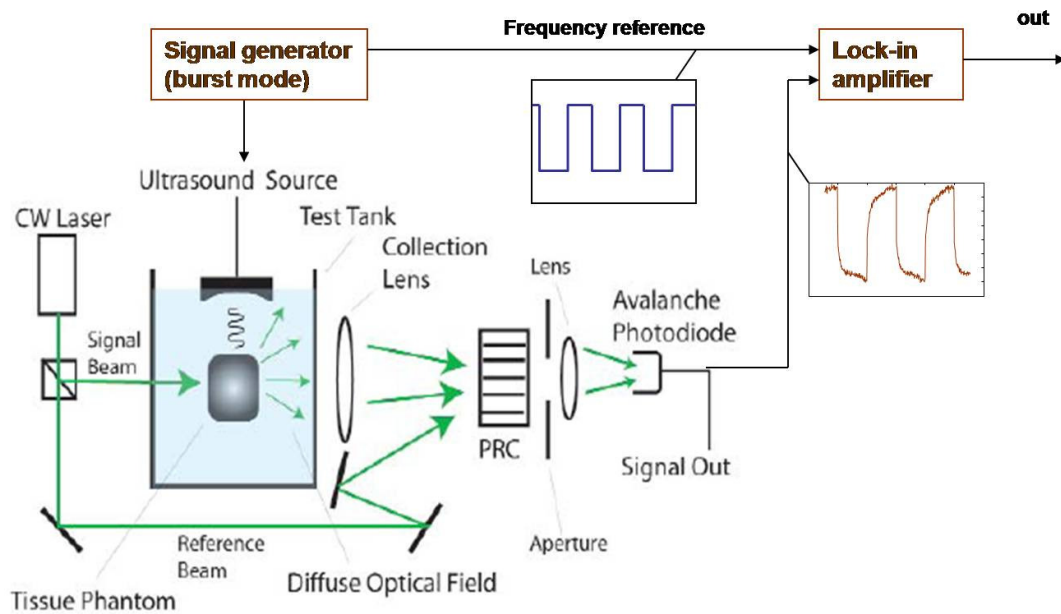


Figure 7.10 Schematic of addition of the lock-in amplifier to the AOI experimental setup.

7.3.1 Results

Tissue samples were prepared and mounted the same way as in the pulsed ultrasound experiments. Figure 7.11 shows the lock-in (LI) output during a 1.1MHz HIFU exposure of 8MPa. The PRF was 50Hz and the duty cycle was 50%. Starting at 8s the output drops, indicating a drop in tagged photons. It is theorized that this is due to the increase in optical scattering and absorption in the lesion. The continuing drop presumably reflects the growing lesion size.

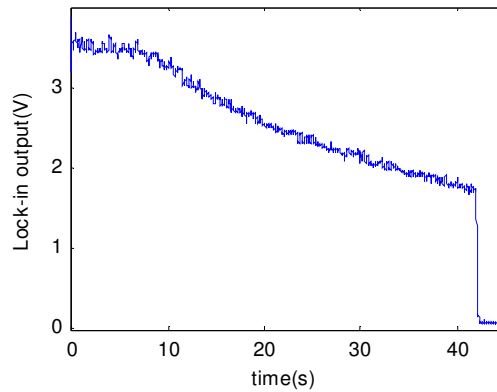


Figure 7.11 Lock-in output during 8MPa HIFU exposure in chicken

My colleague, Puxiang Lai, performed similar AOI measurements on lesions made with various peak pressures and durations (Lai et al. 2009 and Lai 2011). The lesion volumes were calculated “post-mortem” by photographing a longitudinal cross-section of the lesion and using image-processing routines to identify the discolored region. Cylindrical symmetry was then assumed for the volume calculation. The drop in LI signal at the end of the exposure was normalized to the initial level, and is plotted against lesion volume in Figure 7.12.

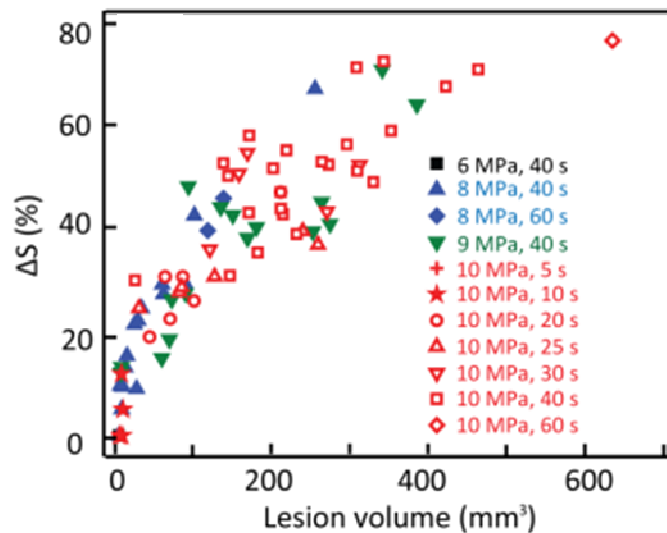


Figure 7.12 Per-cent drop in LI signal for indicated HIFU exposure peak pressures and durations, in chicken breast. (from Lai 2011)

There is good correlation between the LI signal drop and the lesion volume. Over 100 lesions were measured. The LI signal drop showed better correlation with lesion volume than did the values for HIFU pressure and duration, which are a notoriously poor predictor of lesion growth. The reason for the nonlinear curve seen in the data is probably that the larger lesions grew outside the HIFU focal zone, which is the only area where photons are acoustically-tagged.

7.4 AOI and tissue motion

Optical modulation from ultrasound can also be caused by secondary effects like bulk motion from the acoustic radiation force, and the formation of bubbles. Using a PRC and CW ultrasound source, Xu et al. (2007) observed a non-zero AOI signal 0.1ms after the end of a short ultrasound burst. They reasoned that this was caused by residual tissue motion from acoustic forcing (note that their ultrasound bursts were short enough that the PRC response time was not a factor). This post-HIFU AOI signal was found to correspond with local stiffness in the medium. Bossy et al. (2007) used a CCD camera and digital speckle correlation techniques to detect tagged photons, and also recorded non-zero AOI signals after ultrasound bursts. These they showed were correlated with the persistence of shear waves.

One of the goals of the present research was to combine Acousto-Optic Imaging and Harmonic Motion Imaging in the detection of lesion formation. As will be described in the next section, this was achieved by using the same modulated HIFU source for both the AOI and HMI. Since the acoustic pulse/echo speckle-tracking apparatus could measure tissue motion, the effects of tissue motion on the acousto-optic effect could be investigated. Figure 7.13 shows the APD output for a 2MPa, 500 cycle HIFU burst in bovine liver. Unlike the data for the similar excitation in the acrylamide phantom (Figure 7.9), there is considerable signal after the HIFU burst. This is similar to curves reported by Bossy et al.(2007). Their hypothesis is that the rise after the burst, and subsequent slow decay, is from a shear wave propagating away from the focus. Since it causes tissue motion, the shear wave is able to modulate photons as it propagates outside of the ultrasound focal region. Our data is

consistent with their hypothesis. The signal from the HIFU burst itself is also visible, suggesting that the optical modulation from the bulk tissue motion is roughly the same magnitude as the modulation caused by the previously described mechanisms (fluctuations in optical index, particle displacement of the acoustic field). No pulse/echo speckle-tracking data was available for these experiments.

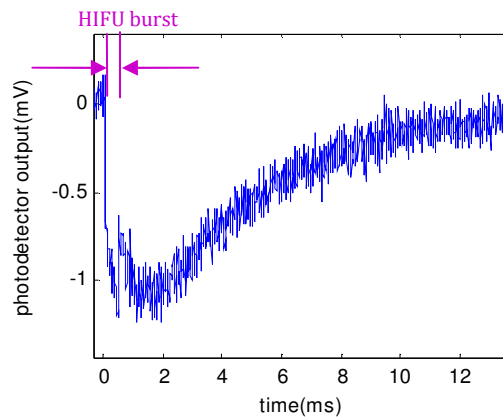


Figure 7.13 APD output for a 2MPa, 500 cycle HIFU burst in bovine liver.

The experiment was repeated for chicken breast tissue under various HIFU pressures and burst lengths. Figure 7.14 through Figure 7.16 show results for burst lengths of 400, 1,980, and 14,000 cycles (the latter is the same duration as the bursts in the 40Hz modulated HIFU signal used in the HMI studies). The left-hand plots show the acousto-optic (AO) waveforms which have been averaged for better SNR. The bursts were fired continuously at a 1% duty cycle. The right-hand plots are of the tissue displacement at the ultrasound focus, measured by the same ultrasound pulse/echo speckle-tracking technique used in the HMI work. These were not averaged, and represent the displacement from a single HIFU burst. Only the last HMI data set, for 14,000 cycles, shows the expected tissue displacement, rising and falling with a time constant of about 10ms, consistent with the rheometer measurements and HMI data. The amplitudes are proportional to the square of the pressure, as expected. The displacement data from the shorter bursts has a much steeper initial slope, followed by the 10ms rate of decay. The cause is unclear, but this initial steepness can also be seen at the very beginning of the plot for the longer 14k cycle burst.

On the AO data plots, the short, thick line drawn in the AO plots shows when the HIFU burst occurred in time. The first thing to notice is that at this scale and number of averages there is no visible drop in signal during the HIFU burst. This suggests that the bulk tissue motion in this experiment has a far greater effect on modulating the photon phases than the acoustic field. Furthermore, the AO signal begins to drop *after* 400 cycles. It is possible that shear waves propagate outward from the focus, both toward and away from the direction of the laser, thus affecting progressively more of the optical field. The next thing to notice is that there appears to be a saturation in the drop in APD output as the pressure is increased, and the pressure at which the saturation occurs decreases for longer burst lengths. We may expect that shear waves would remain longer for higher excitation levels, but the time constant of the recovery of the AO signal seems to be the same for the different pressure levels once saturation has been reached. Finally, the initial slope of the AO curve for the 14k cycle, 1MPa excitation seems to follow the expected time constant of 10ms., but the higher pressures have a faster attack time, suggesting some other mode of behavior. These curves represent some of the more mysterious results of this research, and more work needs to be done to find a basic mechanism for what causes the slow rise and fall times, and the saturation with pressure. It is important to understand the effects of the induced tissue motion on the AO signal, if a time-modulated HIFU wave is to be used to obtain acousto-optic information. The recovery time of the APD signal for the 14k cycle burst is much longer than the burst itself. This will result in a greatly reduced AC amplitude of the APD time waveform at 40Hz for a 50% duty cycle burst train, which is what the lock-in measures as the system output.

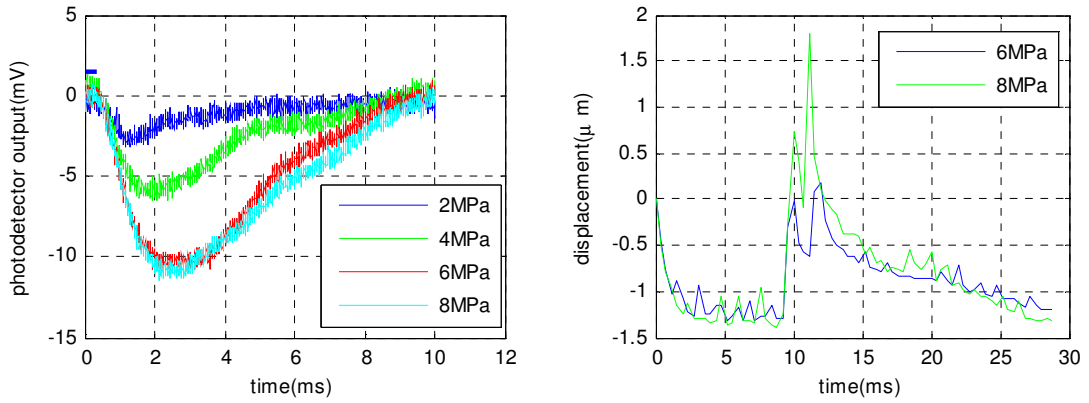


Figure 7.14 Response to 400 cycle HIFU burst. Left: AO interaction, Right: displacement measured by ultrasound speckle tracking.

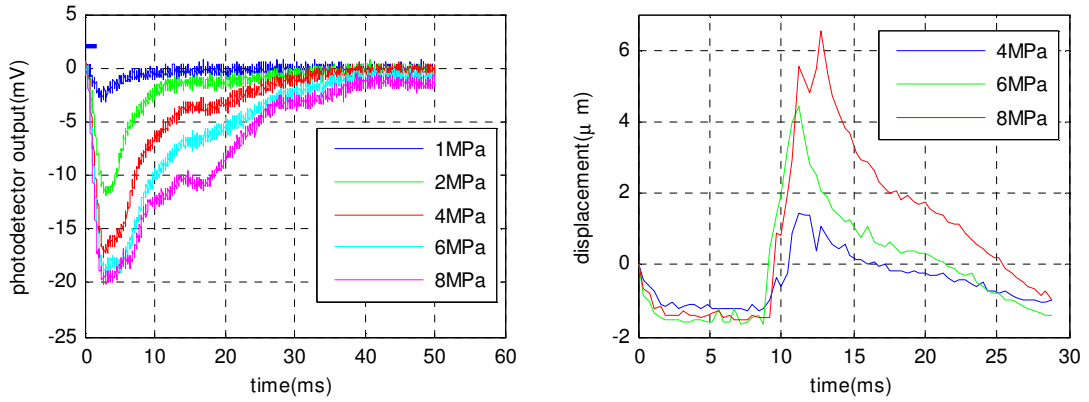


Figure 7.15 Response to 1980 cycle HIFU burst.

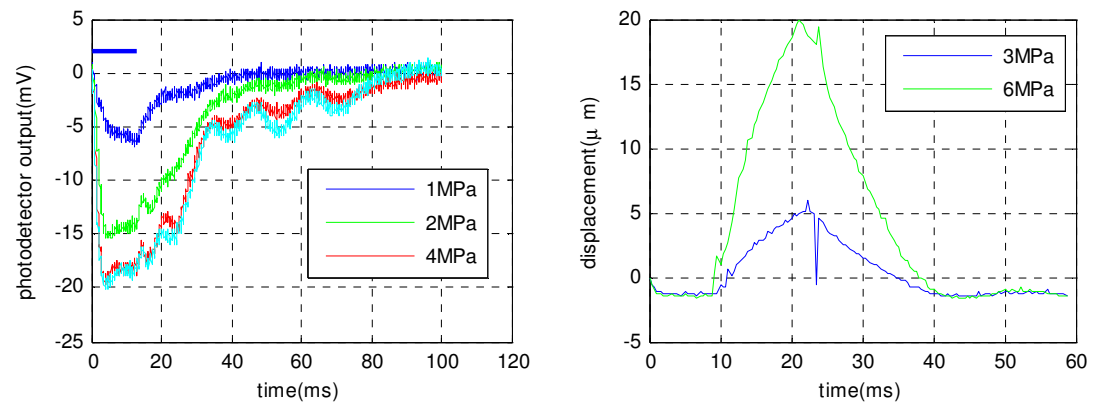


Figure 7.16 Response to 14,000 cycle HIFU burst.

7.5 Combined Harmonic Motion Imaging and Acousto-Optic Imaging

HMI and AOI were done at the same time during HIFU lesion formation, in order to assess the merits of each and to shed new light on each technique with the help of the results of the other. Technically this was straightforward, since the only equipment the two methods shared was the HIFU transducer, and the 40Hz modulated HIFU beam was integral to each. One required modification was to change the duty cycle of the heating phase of the HMI method from 100% to 50%. This simply meant longer exposure times, which should not affect the basic process nor the data obtained. Another modification to the HMI setup was the mounting geometry of the tissue. This had to change from a free-standing 4cm thick sample with the large face (6 to 20cm dia.) toward the HIFU transducer, to a 4x4x2cm sample with the smallest face toward the HIFU transducer (see Figure 7.5). Although the muscle fiber direction was kept consistent between these two arrangements, the boundary conditions for the elastic displacement problem were different. The FEM model showed this to have some effect, but not enough to alter the basic patterns of displacement vs. depth during lesion formation. Figure 7.17 shows the results of 20 of the lesions made under the combined AOI/HMI regime. This is analogous to the results without HMI (Figure 7.12), and shows similar correlation between drop in LI signal and lesion volume.

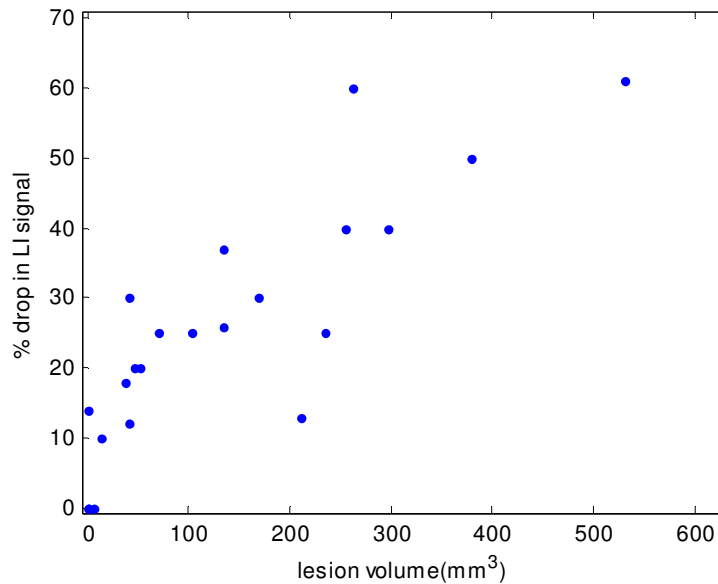


Figure 7.17 Percent drop of LI signal as a function of lesion volume for the combined AOI-HMI experiment.

For each lesion made, the same procedure for HMI was followed which produced the data in chapter 6. The output of the lock-in was recorded, along with the overall light level received from the APD. Since it is estimated that at least half of collected photons pass through the acoustic focus, the received light level will markedly drop when a lesion is formed. This will serve as important baseline information, since it was shown in the last section that a significant portion of the changes seen in the AO signal are caused by tissue motion. Figure 7.18 through Figure 7.22 contain data for five cases, showing HMI amplitude vs. depth vs. time, as was done in chapter 6, along with the lock-in signal. Also shown are time traces for the overall light level received at the APD, and HMI amplitude and integrated acoustic backscattered energy for just the region around the acoustic focus. The Fourier amplitude of the tissue motion shown in the upper plot of the figures is a measure of the motion only along the line of the pulse interrogation field. It is thus not able to reflect how much energy is in the shear waves that are thought to cause much optical modulation. As a primitive measure of the level of excitation given to the shear wave, the Fourier amplitude of the tissue motion was integrated over a 10mm depth around the acoustic focus. It is this motion that gives rise to the shear waves. Finally, the RMS level of the backscattered interrogation pulse was also calculated for the 10mm focal region,

as a measure of bubble activity. Bubbles will be discussed at the end of the chapter. It was desired to see what correlation existed between the time traces of the AO signal, the overall light signal, the averaged HMI data, and the RMS backscatter signal. Each had its own scale and offset, so just the region of change was plotted for each, normalized to 1. The sign of the AO signal and overall light signal was reversed, so that a change in these signals was registered as a positive number. This way of plotting these four parameters is only sensitive to departures from a linear, monotonic trend. In other words, if each variable simply rose linearly from beginning to end, all the lines would overlap and no contrasting behavior could be identified. However this was not a problem, as the trends were usually not linear. The third plot in each figure is the Hilbert transform of the backscattered energy, which will also be discussed in the section about bubbles.

The HMI and lock-in data will be discussed first. Figure 7.18(a) shows the “ideal” HMI pattern discussed in chapter 4: the displacement near the focus increases first, followed by a broadening with depth. The LI trace begins to change at the time when this broadening begins. However the LI trace for lesion in Figure 7.19 starts to change in a region of little change in the HMI pattern. In Figure 7.20 the LI curve begins to change at a time after the HMI broadening is seen. In Figure 7.21 the HMI motion occurs principally in the shallow region of the sample, but the motion and LI signal both start immediately after the HIFU begins. The final data set, in Figure 7.22, shows a case where no lesion was made. As predicted, there is some rise in HMI displacement near the focus, but no appreciable broadening. There is no change in the LI signal, other than noise. Since the overall light level tracks the LI signal very well, it can be assumed that the changes correspond to lesion formation. The author is aware of no other mechanism that would decrease the light level, other than possibly light scattering from bubbles, but the correlation with bubble activity is not apparent. Therefore this data shows that the HMI patterns do not contain consistent information that correlates with lesion formation.

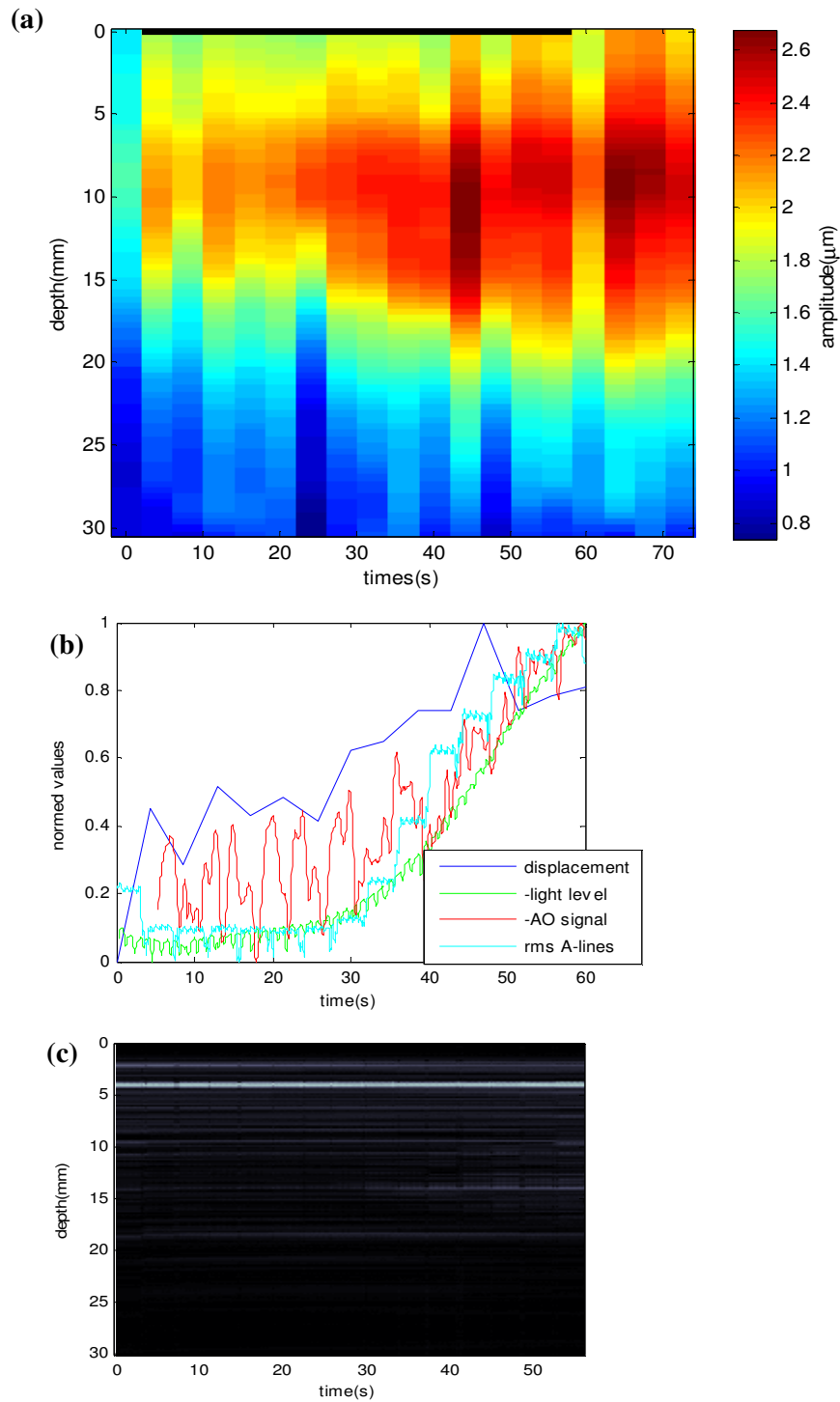


Figure 7.18 Data for a lesion measuring 3mm wide by 8mm long, made with a 8MPa, 60s HIFU exposure at 50% duty cycle. (a) HMI data showing tissue displacement Fourier amplitude at the modulation frequency of 40Hz. (b) Normalized curves for 1: Average displacement amplitude over 10mm focal zone, 2: total light level*1, 3: lock-in output*1, 4: RMS of backscattered interrogation pulse over 10mm focal zone. (c) Hilbert transform of backscatter. All time scales are aligned.

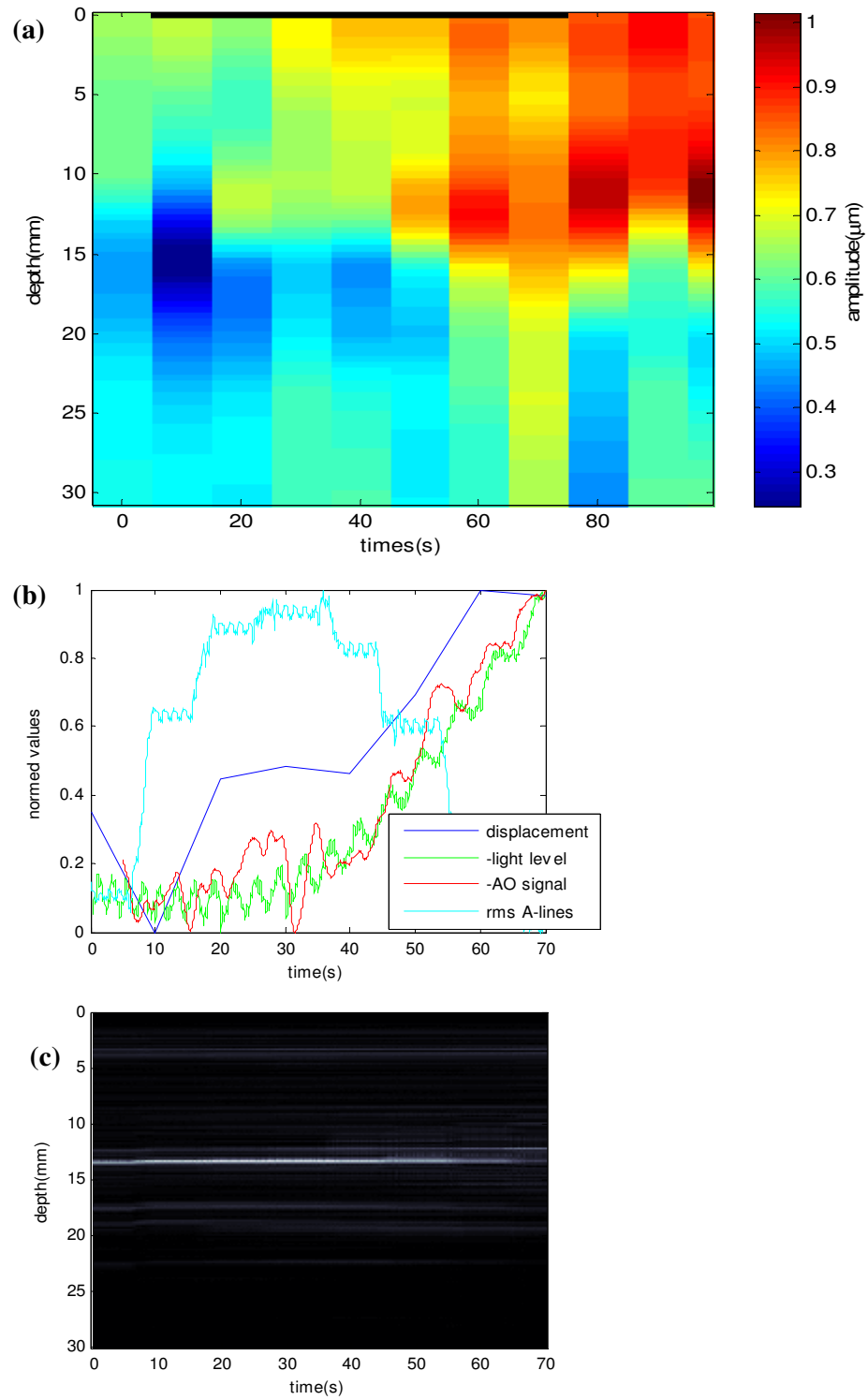


Figure 7.19 Data for a lesion measuring 3mm wide by 11mm long, made with a 6MPa, 70s HIFU exposure at 50% duty cycle.

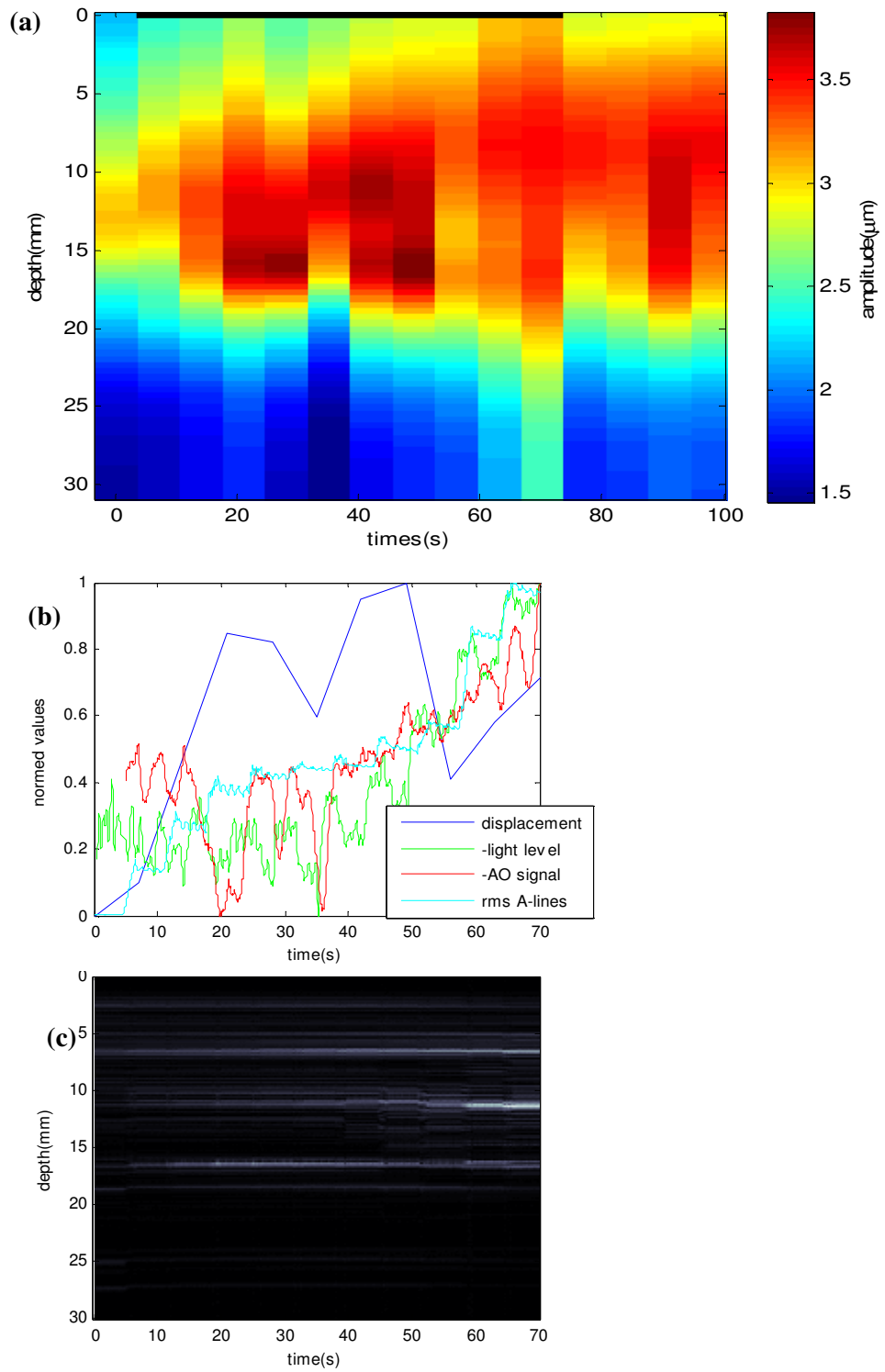


Figure 7.20 Data for a lesion measuring 4.5mm wide by 10mm long, made with a 7MPa, 70s HIFU exposure at 50% duty cycle.

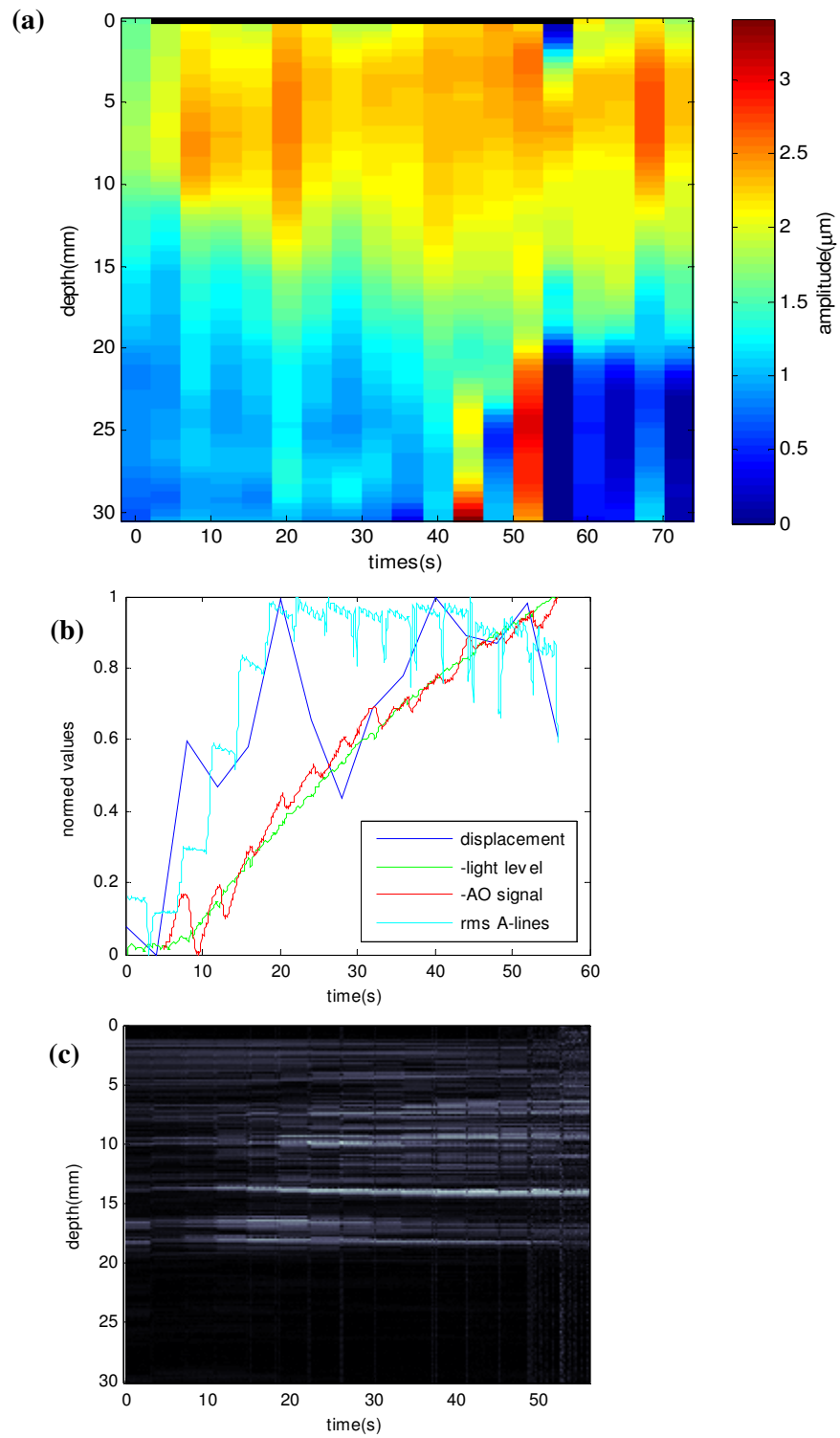


Figure 7.21 Data for a lesion measuring 5mm wide by 15mm long, made with a 9MPa, 56s HIFU exposure at 50% duty cycle.

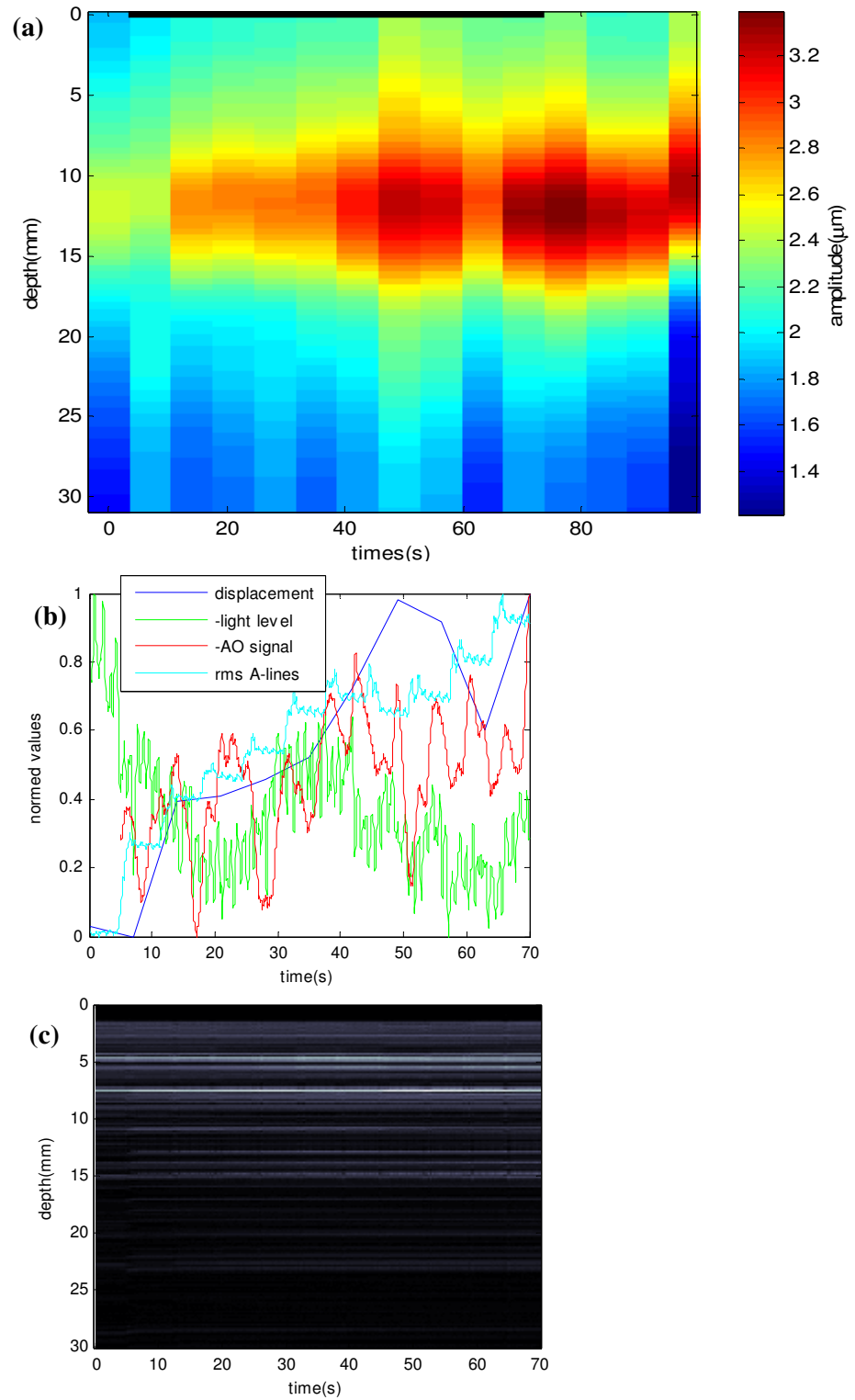


Figure 7.22 No lesion found. 6MPa, 70s HIFU exposure at 50% duty cycle.

In the previous section data was presented which suggested that tissue motion, in particular long-lasting motion thought to be from shear waves, caused a large optical modulation. However in order to be registered with the lock-in method, the motion effect would need to occur and be finished within one cycle of the acoustic modulation at 40Hz., so that it could contribute to successive cycles. It is not clear that this will be the case, nor is it clear how much the LI signals during lesion runs are affected by tissue motion. The plots of the averaged Fourier component of displacement amplitude throughout the 10mm focal region were intended to address this question. Note that tissue motion would be expected to boost the LI output, which is in opposition to the effect of the increased optical absorption of the lesion, which decreases the LI output. In Figure 7.18 and Figure 7.19 there is a delay of about 30s in the LI curves, followed by an upward curve. No change at 30s is evident in the displacement curves. Also, it can be seen in Figure 7.20(a) and (b) that the displacement has a considerable rise and fall. This is not reflected in the LI data. Thus there is not consistent correlation between the LI signal and the average displacement. The effect of tissue motion on AOI is thus ambiguous in this data, and warrants further research.

It is conceivable that bubbles can affect optical modulation. Bubbles scatter light at least as strongly as the other particles in tissue, if not more (Zhang 1998). The bubbles oscillate with the acoustic field, and this oscillation will produce a phase modulation in scattered photons. This would increase the LI signal. However the *amount* of photon scattering would also increase with more and larger bubbles, and, as with the increased scattering from the lesion, this would reduce the LI signal. So it is not clear what the total effect of bubbles will be on the LI output. From the results of chapter 4 it may be assumed that the increases in backscattered energy observed in nearly all of the interrogation A-lines taken during lesion runs are due to bubbles, for the following reasons: Broadband bursts are often seen in spectrograms of A-lines which correspond with the regions of increased backscatter amplitude, and strong bursts of HIFU harmonics are observed to correspond with times when there is a sudden jump in the amplitude in these regions. Also there is often an exponential decay in this amplitude after the HIFU is turned off, indicating slow dissolution of the

bubbles. Figure 7.18 through Figure 7.22 show a steady growth in the RMS level of the backscattered energy near the focus, which is assumed to be due to bubbles. However, like the curves for growth in displacement, the curves of the increase in RMS level do not correlate well with changes in LI signal or HMI displacement.

7.6 Conclusion

The data correlations, or lack thereof, of these five data sets resemble those from the data of 20 more lesions studied. The LI signal tracks the overall light signal very well, even when patterns of bubble activity and tissue motion are different. This suggests that the existence and number of bubbles is small and they don't much affect the light level or photon phase modulation. Also, even though tissue motion may have a strong modulating effect on the light, it seems un-correlated with the LI signal. Because the LI signal is so well correlated with the overall light level in these experiments, and seems uncorrelated with tissue motion and bubbles, the acousto-optic method used in this study seems to be a robust way of detecting changes in optical absorption/scattering due to HIFU lesion formation.

8

Conclusions and Future Work

Harmonic Motion Imaging and Acousto-Optic Imaging were investigated for the monitoring of HIFU lesions during formation. They were applied simultaneously in order to assess their relative merits and reveal extra information about each. A significant potential source of error was discovered with the HMI method, due to acoustic nonlinearity, which was solved with a technique to alter the phase relationship of the HIFU and interrogation pulse beams.

An FEM model was made to simulate the HIFU lesion process with concurrent HMI measurements. Since the acoustic attenuation and tissue stiffness are functions of temperature, models for the acoustic field, temperature field, and displacement needed to be coupled to simulate the HMI displacement. The model also applied a correction for acoustic nonlinearity in the HIFU field. The simulated displacement amplitudes were about 50% of those measured. It was seen that measured temperatures were lower than predicted by models, until the value for acoustic absorption is brought below 4Np/m/MHz . Thus it seems unlikely that the cause of the large underestimate of displacement could be explained by an underestimate of tissue absorption.

Exploration of the individual effects of increased absorption and also increased stiffness revealed a similar pattern as produced by the combined model using three different sets of tissue parameters: as the focal region heats up, increased absorption leads to higher amplitude there, and increased stiffness leads to a broadening of the amplitude vs. depth. The initial increase in displacement at the

focus could be caused by both the initial softening which occurs at about 40°C, and the increased absorption which begins at around the same temperature. These are both signs of the early stages of protein denaturation. A broadening pattern with depth occurs later, when the stiffness from the later stages of protein denaturation grows outside of the focal width, and may be a good indicator of when a substantial lesion has been made.

In the experimental data there were many examples of HMI data during lesion formation with the pattern described in the preceding paragraph. However there were many instances where this was not the case. Of 65 lesions, 26% showed the pattern of HMI amplitude vs. depth shown in the FEM studies; 21% showed a central region of displacement that was either narrow or wide, but did not change over the course of the HIFU exposure; and 52% were either too noisy to be considered, or exhibited a pattern of constant uniform displacement over the first 10 to 15 mm of depth. In some cases the HMI lesion pattern was evident but no lesion was made. At the threshold pressure of 5MPa, 5 of 19 data runs produced no lesions, and for higher pressures, all runs produced lesions. At 5MPa, the HMI data for 4 of the 5 lesion-less runs did not show the rising-broadening pattern. And perhaps more importantly, even if the percentage which showed the pattern were much larger, it was not clear that the data had the potential to predict the actual size and initiation time of the lesions. It can be concluded that, in this particular application of HMI, it appears that there was too much variability in the data to reliably monitor lesion formation.

When AOI was combined with Harmonic Motion Imaging , it was found that the AOI system output (from the lock-in amplifier) correlated well with the actual lesion sizes, and also with the overall light level; but not with the harmonic displacement amplitude nor the RMS backscatter level, which was thought to represent bubble activity. This suggests not only that the AOI was superior to HMI for lesion monitoring, but that the AOI was at least somewhat insensitive to tissue motion and bubble activity.

8.1 Suggestions for future work

8.1.1 HMI

This work involved one HIFU transducer f-number (0.95) and two frequencies (1.1 and 3.3MHz). It was shown that changing these parameters may significantly alter the HMI amplitude, size of lesion, propensity for cavitation, depth of penetration, and immunity to tissue inhomogeneities. Other values for f-number and HIFU frequency should be explored to see if the HMI results can be improved.

A better way of measuring the temperature in the lesion is needed. The “push-in” thermocouple technique was free from viscous heating artifact, but the measured temperatures could only be modeled by using unrealistically low values of acoustic absorption. A great deal of effort was placed in the apparent displacement thermometry technique, but the results were not robust, probably due to the difficulty of obtaining the slope of the noisy displacement vs. depth curves. For any proposed thermal measurement techniques or model, it would be useful to validate with MRI, which is accepted to be accurate.

The temperature dependence of absorption and stiffness was measured in a quasi-static system. For the modeling a HIFU system in which the heating rates were high, values had to be guessed. A method of measuring these properties in real time during HIFU is necessary for modeling the expected HMI displacement during lesion formation.

8.1.2 AOI

The single burst studies in chicken revealed unpredicted AOI results, and suggest that tissue motion has a strong and complex effect on the AOI signal. This has also been reported by others. More research into this is needed to determine whether the AOI signal observed during lesion formation is affected more by tissue optical properties than by tissue motion. Secondly, since it is

possible that some degree of cavitation accompanies the majority of HIFU lesions, and it is important to know the effects of bubbles on the AOI signal.

In Gross et al. (2009), optical frequency modulators were added to the AOI system which resulted in the PRC grating being constructed from the tagged photon optical field, rather than the un-tagged photon optical field. It may be beneficial to employ this method for lesion detection, since, the modulation for AOI lock-in could come from a simple shift in the HIFU phase, rather than turning the HIFU on and off with 50% duty cycle. This would deliver more power to the heating. This would also eliminate the extra factor of tissue motion.

Finally, to obtain adequate SNR in a clinical application, where through-transmission may not be possible, where blood will absorb more of the light, and where scattered light from a larger region of tissue will need to be collected; much more laser power will be needed. In order to keep light below safety levels, short pulses of light from a high powered laser could be used (Rousseau et al. 2009).

Appendix A Equipment list

1.1 MHz Hifu transducer model H102	Sonic Concepts, Bothell, WA
7.5 MHz interrogation transducer I4-0710-S-SU-F57M	Olympus (Harrisonic), Waltham, MA
5MHz hipass filter	Allen Avionics, Mineola, NY
Pulser/receiver 5077 PR	Panametrics, Waltham, MA
Power amp. 75A250A. 75 W, 10 kHz - 250 MHz	Amplifier Research Souderton, PA
Signal generator models 33250A and 33120a	Agilent Technologies, Loveland, CO
Timing pulse generator HP8116	Hewlett Packard
High speed digitizer card 200MHz, 14 bit model 14200	Gage Applied Inc. Lockport, IL
General purpose digitizer card AT-MIO-16E-1, 12-bit,	National Instruments
Signal conditioner unit for thermocouples SCXI1120	National Instruments
Oscilloscope LT264	LeCroy, Chestnut Ridge, NY
Computer with WindowsXP P4 2.8GHz, 1Gbytes Ram	Custom built
Circulating water heater RTE210	Neslab, Woodland Hills CA
Membrane hydrophone 15um, 0.2mm SN1502-031	Precision Acoustics Ltd. Dorchester, UK
Needle hydrophone (pzt) N10-3	Dapco, Ridgefield, CN
Fiber-optic hydrophone FOPH500	RP Acoustics, Leutenbach, Germany
B-mode ultrasound imaging machine model 2300	Analogic, Peabody, MA
Array probe transducer for B-mode. Mod.8802 (5MHz)	BK Medical, Wilmington, MA)
“ “ Mod.8805 (12MHz)	“ “
Nd-YAG laser IRCL-700-1064-S	CrystaLaser, Reno, NV, USA)
GaAs photo-refractive crystal	MolTech GmbH, Berlin, Germany

Appendix B Timing Circuit Diagram

This appendix describes the circuit that was built to adjust the timing relationship between the HMI interrogation pulses and the HIFU wave. The requirements were:

1. Upon receiving a trigger from the interrogation pulse trigger source generator, issue a new trigger when the HIFU signal reaches a certain phase.
2. On each consecutive trigger, alter the phase of the HIFU on which the trigger is issued by 180°.
3. If no HIFU wave is present (is in the post-heating phase of each HMI run), issue a new trigger anyway.

Figure B-1 shows a schematic of the circuit, containing the part numbers used.

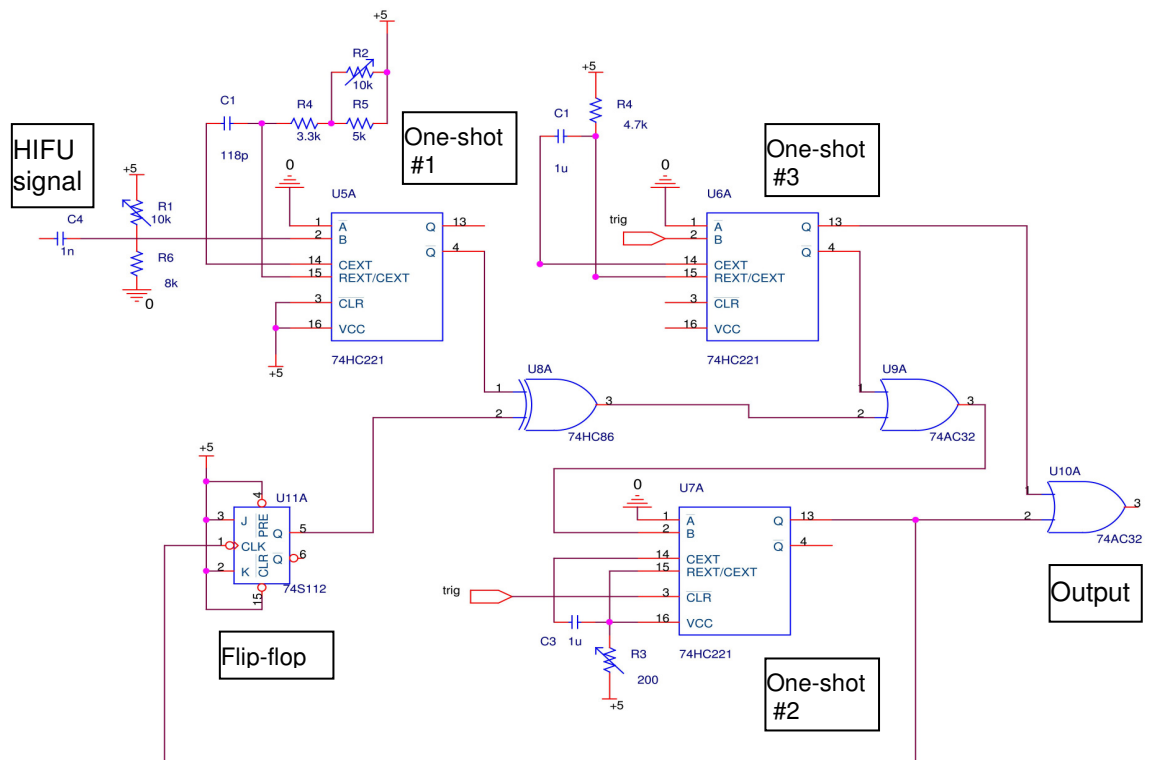


Figure B-1 Diagram of circuit built to synchronize the HIFU wave and interrogation pulses. Note: the plotting process erased the bar above the lower "Q" in each output pair.

Three multivibrator chips were used in the "one-shot" configuration, and a flip-flop chip was used to alter the HIFU phase for each trigger. The purpose of the first one-shot was to generate a square wave from the input HIFU signal. The HIFU signal frequency was either 1.1 or 3.3MHz, and had

amplitudes ranging from 0.6V p-p to 10V p-p. The part chosen (74HC221) had a Schmitt-trigger input, and was the only chip of those considered that could accomplish the task. Megahertz frequencies necessitated the use of non-standard “fast” chips. Of these, most of the op-amps and comparator chips had serious degradation in function for inputs outside the range of 0.5 to 5V p-p, and/or had throughput delays or hysteresis that were too high. The potentiometer on the external R/C timing network for this chip needed to be adjusted to give a 50% duty cycle output square wave at either 1.1 or 3.3MHz.

The output of the first stage was sent, after an XOR and OR gate, to a second one-shot chip which issued the final output trigger, provided it had been “armed” by the interrogation trigger. The length of the output pulse is the total delay added to the input trigger in order to synchronize with the HIFU signal. A third one-shot generated a delay of a few HIFU cycles after the input interrogation trigger was detected. This window was used to limit the timespan of the HIFU signal seen by the second one-shot, and also to issue a final trigger if no HIFU wave was present.

The flip-flop chip and the XOR gate were used to flip the phase of the HIFU square wave every other trigger pulse. The final trigger was used to initiate digitization and was sent to the Gage fast A-D card, which actually triggered on the trailing edge of the signal.

Appendix C Design of Magnetostrictive Shaker

In order to provide a known vibration source for testing the HMI speckle tracking measurement system, it was desired to make a transducer which could deliver a 6 to 14 μ m oscillation at 40Hz, on a round pin-head encapsulated in a gel phantom; all under water. A magnetostrictive material was chosen called Terfenol (Etrema Products inc. Ames, IA) that expands under a magnetic field. The Terfenol was a square prism 2mm x 2mm x 20mm, and was mounted in an aluminum base (Figure C-1) and surrounded by a cylindrical coil to provide the magnetic field.

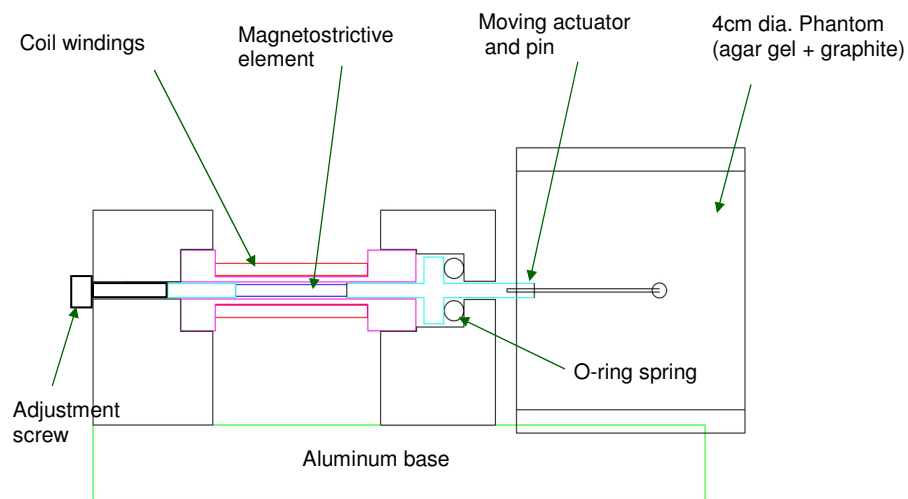


Figure C-1 Scale drawing of magnetostrictive vibration exciter. Pin with 2.5mm head translates horizontally within a gel phantom,

Figure C-2 shows the material properties of induced strain vs applied magnetization H (in Oersteds). The different colored lines correspond to pre-loading pressure, in KSI (kilo-pound force). Some pre-loading is required to make the motion more linear, but some strain is sacrificed in the process. The desired strain was $14\mu\text{m}/2\text{cm} = 7\text{e-}8$. If the applied load was 4KSI, the chart shows that approximately 800 Oersteds would be needed. The length of coil was 26mm, and the number of turns was approximately 300. +/- 1 Amp of current was applied, using an audio-frequency power

amplifier (pa-119 Labworks Inc., Costa Mesa, CA). To provide the amp with its minimal operating load, two 5 Ohm power resistors were connected in series to the coil. 1Amp yields an H field of $300/26e-3 = 11.5k$ A-turns/m = 144 Oersteds. The intersection of that H value and the $700 e-6$ requirement is closest to the blue curve of 1KSI pre-loading. This loading was provided by compressing the terfenol against a rubber O-ring, using an adjustment screw. The amplitude of the displacement for a 40Hz sin wave current of +/- 1 Amp could be viewed on an oscilloscope using the laser-doppler vibrometer aimed at the head of the pin. The adjustment screw was turned until the waveform became sinusoidal in shape, without appreciable distortion.

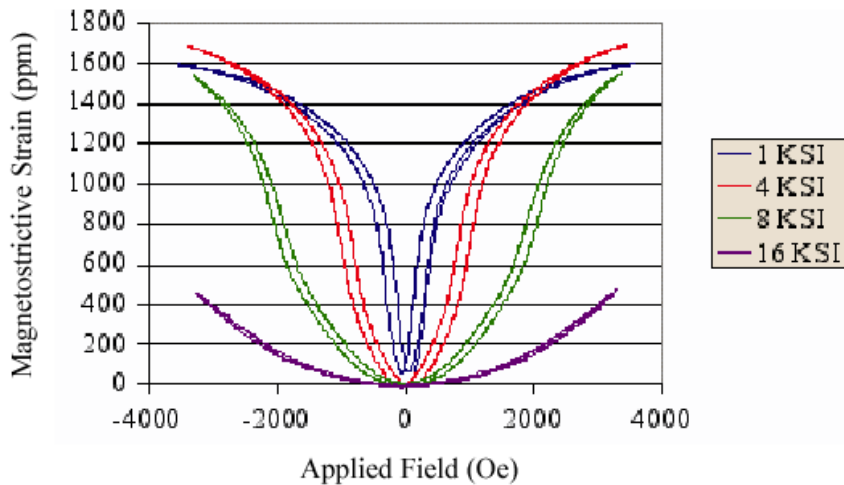


Figure C-2 Magnetostrictive performance specification for Terfenol alloy.

Appendix D Code

The following is a C program written for Matlab, for the gradient-based speckle tracking algorithm. This can be readily implemented by following instructions in the first comment.

```
#include "mex.h"
#include <stdio.h>
#include <math.h>
/*
myelatoC.c
C mex file version of Matlab speckle tracker routine "elasto.m" written by M.Richards
and P.Barbone. Call in matlab via myelatoC(alines, nelelem, reg, difu), where alines
are two or more A-lines, arranged as columns, nelelem is the number of elements
desired, reg is the regularization constant, and difu is 1 or 0, depending on whether
lines are compared successively, or just to the first line. The regularization constant
gets normalized to 500*rms(line)^2, so try a value of 1 first. Some C notes: mxArray
is the matlab data type. mxArraySize is a variable type used instead of int, for
dimensions of mxArrays. To compile, just type mex program.c. To check that the
default compiler is LCC (or change it), type mex -setup.
*/

void mycalc(double *alines, int nelelem, double reg, double *u, int linelen, int nlines, int difu)
{
    int i,j,iline,ielem,iinte,cnt=0;
    int usz1=nelelem+1, usz2=nlines;
    double norm=1;
    double eforce1, eforce2, estif11, estif12, estif21, estif22;
    double shapetwo1, shapetwo2, Xmaterial, Xspatial, disp, ldiff, lgradient;
    int pix;
    double pixpos,seg1,seg2,seg3,seg4,ppm4,ppm3,ppm2,ppm1,delu,bet, normsum;
    double lgradsqrd;

    double dispresol = (1.0*linelen-1)/(nelelem+2); //1.0 is to convert to double! fix this?
    double RegOverRessq = reg/(dispresol*dispresol);
    int ninte = floor(dispresol+1.0);
    double step=2.0/(ninte-1);
    double rmslinesq=0.0;

    mxArray *MXsg = mxCreateDoubleMatrix(ninte,1, mxREAL);
    double *sg=mxGetPr(MXsg); //this is the extra step to make sg a useful pointer.
    // atanga,b,c are the diagonals of the atang matrix (wich is a band-diagonal matrix)
    mxArray *MXatanga = mxCreateDoubleMatrix(usz1,1, mxREAL);
    double *atanga=mxGetPr(MXatanga);
    mxArray *MXatangb = mxCreateDoubleMatrix(usz1,1, mxREAL);
    double *atangb=mxGetPr(MXatangb);
    mxArray *MXatangc = mxCreateDoubleMatrix(usz1,1, mxREAL);
    double *atangc=mxGetPr(MXatangc);
}
```

```

mxArray *MXaload = mxCreateDoubleMatrix(nelem+1,1, mxREAL);
double *aload=mxGetPr(MXaload);
mxArray *MXuthisline = mxCreateDoubleMatrix(usz1,1, mxREAL);
double *uthisline=mxGetPr(MXuthisline);
mxArray *MXthisline = mxCreateDoubleMatrix(linelen,1, mxREAL);
double *thisline=mxGetPr(MXthisline);
mxArray *MXline0 = mxCreateDoubleMatrix(linelen,1, mxREAL);
double *line0=mxGetPr(MXline0);
mxArray *MXgam = mxCreateDoubleMatrix(usz1,1, mxREAL);
double *gam=mxGetPr(MXgam);
mxArray *MXuupdate = mxCreateDoubleMatrix(usz1,1, mxREAL);
double *uupdate=mxGetPr(MXuupdate);

// End of declarations. This compiler apparently won't take
// further declatations after any assignment statement.

for (i=0;i<linelen;i++) rmslinesq += *(alines+i) * *(alines+i);
RegOverRessq *= rmslinesq*500.0/linelen; //normalize reg const to 500*rms(l)^2

for (i=0; i<ninte; i++) { //set sg
*(sg+cnt)--1.0+i*step;
cnt++;
}

cnt=0;for (j=0;j<usz2-1;j++) for (i=0;i<usz1;i++) *(u+cnt)=0.0; cnt++; //set u to 0
for (i=0;i<linelen;i++) *(line0+i)=*(alines+i); //set line0

for (iline=1;iline<nlines;iline++){ //step through lines (note this starts with the line after the
baseline zero line)
norm=1.0;
for (i=0;i<usz1;i++) *(uthisline+i)=0.0; // set uthisline to 0's
for (i=1;i<linelen;i++) *(thisline+i)=*(alines+(linelen*iline)+i); //set thisline
if (difu!=0) for (i=1;i<linelen;i++) *(line0+i)=*(alines+(linelen*(iline-1))+i); /*set line0 to
last line, if differential,line-to-line desired.*/
cnt=0;
while (norm>.005 & cnt<500) { /*if convergence not met at cnt=500, terminate
optimizing loop*/
cnt++;
for (i=0;i<usz1;i++) *(atanga+i)=0; // set atanga to 0
for (i=0;i<usz1;i++) *(atangb+i)=0; // set atangb to 0
for (i=0;i<usz1;i++) *(atangc+i)=0; // set atangc to 0
for (i=0;i<usz1;i++) *(aload+i)=0; // set aload to 0

for (ielem=0;ielem<nelem;ielem++){ //ielem loop =====
eforce1=0.0;eforce2=0.0;
estif11=0.0; estif12=0.0; estif21=0.0; estif22=0.0;
for (iinte=0;iinte<ninte;iinte++){ //iinte loop: step through data pts in element=====
shapetwo2=0.5* *(sg+iinte);shapetwo1=-1.0*shapetwo2;
shapetwo1 += 0.5;shapetwo2 += 0.5;
Xmaterial=shapetwo1*(ielem+1)*dispresol;
Xmaterial+=shapetwo2*(ielem+2)*dispresol;
disp=shapetwo1 * *(uthisline+ielem);

```

```

disp += shapetwo2* *(uthisline+ielem+1);
Xspatial=Xmaterial;
Xspatial += disp;
// do lmaterial for line0-----
pixpos=Xmaterial+1.0;
pix = floor(pixpos)+1;
seg1=(line0+pix-3);seg2=(line0+pix-2);seg3=(line0+pix-1);seg4=(line0+pix);
ppm4=pixpos-pix-1.0;ppm3=ppm4+1.0;ppm2=ppm4+2.0;ppm1=ppm4+3.0;
//ppm4" means pixpos-4
ldiff = seg1*(-1.0/6.0)*ppm2*ppm3*ppm4;
ldiff += seg2*0.5*ppm1*ppm3*ppm4;
ldiff += seg3*(-0.5)*ppm1*ppm2*ppm4;
ldiff += seg4*(1.0/6.0)*ppm1*ppm2*ppm3;

// Now do lmaterial and gradient for thisline-----
pixpos=Xspatial+1.0;
pix = floor(pixpos)+1;
seg1=(thisline+pix-3);seg2=(thisline+pix-2);seg3=(thisline+pix-
1);seg4=(thisline+pix);
ppm4=pixpos-pix-1.0;ppm3=ppm4+1.0;ppm2=ppm4+2.0;ppm1=ppm4+3.0;
//ppm4" means pixpos-4
ldiff -= seg1*(-1.0/6.0)*ppm2*ppm3*ppm4;
ldiff -= seg2*0.5*ppm1*ppm3*ppm4;
ldiff -= seg3*(-0.5)*ppm1*ppm2*ppm4;
ldiff -= seg4*(1.0/6.0)*ppm1*ppm2*ppm3;

lgradient = seg1*(-1.0/6.0)*ppm3*ppm4;
lgradient += seg1*(-1.0/6.0)*ppm2*ppm4;
lgradient += seg1*(-1.0/6.0)*ppm2*ppm3;
lgradient += seg2*(1.0/2.0)*ppm3*ppm4;
lgradient += seg2*(1.0/2.0)*ppm1*ppm4;
lgradient += seg2*(1.0/2.0)*ppm1*ppm3;
lgradient += seg3*(-1.0/2.0)*ppm2*ppm4;
lgradient += seg3*(-1.0/2.0)*ppm1*ppm4;
lgradient += seg3*(-1.0/2.0)*ppm1*ppm2;
lgradient += seg4*(1.0/6.0)*ppm2*ppm3;
lgradient += seg4*(1.0/6.0)*ppm1*ppm3;
lgradient += seg4*(1.0/6.0)*ppm1*ppm2;

// calculate force, stiffness, (lmaterial-lspacial)*lgradient
ldiff *= lgradient;
eforce1 += shapetwo1*ldiff;
eforce2 += shapetwo2*ldiff;
delu = *(uthisline+ielem+1)-*(uthisline+ielem);
eforce1 += RegOverRessq*delu;
eforce2 -= RegOverRessq*delu;
lgradsqrd=lgradient*lgradient;
estif11 += shapetwo1*lgradsqrd*shapetwo1 + RegOverRessq;
estif12 += shapetwo1*lgradsqrd*shapetwo2 -RegOverRessq;
estif21 += shapetwo2*lgradsqrd*shapetwo1 -RegOverRessq;
estif22 += shapetwo2*lgradsqrd*shapetwo2 + RegOverRessq;
} // end iinte loop

```

```

// update the aload vector and atang (band-diagonal matrix)
*(aload+ielem) += eforce1;
*(aload+ielem+1) += eforce2;
*(atangb+ielem) += estif11; *(atangc+ielem) += estif12;
*(atanga+ielem+1) += estif21; *(atangb+ielem+1) += estif22;

} //end ielem loop

// Solve system [atang](uupdate) = (aload). Gauss elim on tridiagonal matrix
// From "Numerical Recpies in C++" 2nd ed. 2002 p.54
bet=*(atangb);
if (bet == 0.0) mexErrMsgTxt("error1 in tridiag routine");
*(uupdate)=*(aload)/bet;
for (j=1;j<usz1;j++) {
    *(gam+j) = *(atangc+j-1)/bet;
    bet = *(atangb+j) - *(atanga+j) * *(gam+j);
    if (bet == 0.0) mexErrMsgTxt("error2 in tridiag routine");
    *(uupdate+j) = (*(aload+j) - *(atanga+j) * *(uupdate+j-1))/bet;
}
normsum=*(uupdate+j-1) * *(uupdate+j-1);
for (j=(usz1-2);j>=0;j--){
    *(uupdate+j) -= *(gam+j+1) * *(uupdate+j+1);
    normsum += *(uupdate+j) * *(uupdate+j);
}

norm=sqrt(normsum);
//mexPrintf("norm=%g \n",norm);
for (j=0;j<usz1;j++) *(uthisline+j) += *(uupdate+j); // Add uupdate to uthisline
//norm = 0.0;

} // end norm loop
if(cnt>499) mexPrintf("Max loop iteration of 500 reached at line %d. norm= %f \n",iline,norm);

for (j=0;j<usz1;j++) *(u+((iline-1)*usz1)+j)=*(uthisline+j); //put uthisline into u matrix
if(difu==1 & iline>1) //update u matrix
    for (j=0;j<usz1;j++) *(u+((iline-1)*usz1)+j)+=(u+((iline-2)*usz1)+j); /*put uthisline into
    u matrix, adding it to previous u, since it's ongoing*/

} // end iline loop

} // end mycalc function

/*+++++*/

/* the gateway function */
void mexFunction( int nlhs, mxArray *plhs[],
                 int nrhs, const mxArray *prhs[])
{
    //input function looks like u=myelastoC(alines, nelelem, reg, difu)
    //output is matrix u
    double *alines,*u;
    double reg;
    int nelelem, difu;

```

```

int linelen, nlines;

/* check for proper number of arguments */
/* NOTE: You do not need an else statement when using mexErrMsgTxt
   within an if statement, because it will never get to the else
   statement if mexErrMsgTxt is executed. (mexErrMsgTxt breaks you out of
   the MEX-file) */
if(nrhs!=4)
    mexErrMsgTxt("4 inputs required.");
if(nlhs!=1)
    mexErrMsgTxt("One output required.");

/* check to make sure the first input argument is a scalar
if( !mxIsDouble(prhs[0]) || mxIsComplex(prhs[0]) ||
   mxGetN(prhs[0])*mxGetM(prhs[0])!=1 ) {
    mexErrMsgTxt("Input x must be a scalar.");
} */

/* create a pointer to the input matrix alines */
alines = mxGetPr(prhs[0]);

    /* get the scalar input */
nelem = mxGetScalar(prhs[1]);
reg = mxGetScalar(prhs[2]);
difu = mxGetScalar(prhs[3]);

/* get the dimensions of the matrix input */
linelen = mxGetM(prhs[0]);
nlines = mxGetN(prhs[0]);
if(nlines>linelen)
    mexErrMsgTxt("nlines needs to be second dimension of input matrix.");

/* set the output pointer to the output matrix */
plhs[0] = mxCreateDoubleMatrix(nelem+1,nlines-1, mxREAL);

/* create a C pointer to a copy of the output matrix */
u = mxGetPr(plhs[0]);

/* call the C subroutine */
mycalc(alines, nelem, reg, u, linelen, nlines, difu);

```


Appendix E Nonlinear effects on HMI

The following is a copy of a paper submitted in February 2011 to the journal "Ultrasound in Medicine and Biology", which was conditionally accepted at the time this thesis was written.

Impact of Nonlinear Distortion on Acoustic Radiation Force Elastography

Andrew B. Draudt and Robin O. Cleveland
Department of Mechanical Engineering,
Boston University,
Boston, MA 02215.

Abstract

High intensity focused ultrasound (HIFU) produces an acoustic radiation force that induces tissue displacement. The displacement can be measured by launching a separate interrogation pulse and monitoring time shifts in the backscattered signals. If the interrogation pulse occurs simultaneously with the HIFU, the arrival time of the backscatter will be biased because nonlinear processes associated with the HIFU change the local sound speed. Measurements of the pressure field using 1.1MHz HIFU and a 7.5MHz interrogation pulse in water showed that the nonlinearly induced apparent displacement (NIAD) of the interrogation pulse varied with the HIFU pressure, propagation distance, and phase relationship between the pulse and the HIFU. A nonlinear simulation employing the KZK equation predicted NIADs that agreed with experiment. Experiments with chicken breast demonstrated a NIAD similar to that measured in water. The NIAD was mitigated by averaging displacements for two interrogation pulses 180 degrees out-of-phase relative to the HIFU.

Key words: Lesion monitoring, HIFU, FUS, Radiation force, Elastography, Tissue ablation, Ultrasound, HMI, ARFI

INTRODUCTION

In ultrasound-stimulated vibro-acoustography, a focused ultrasound beam is used to impart radiation force into tissue in order to induce bulk motion. This motion is then detected by secondary means, typically using acoustic imaging. Fatemi and Greenleaf (1998) used this phenomenon to image plaques in excised blood vessels. They employed two focused beams of slightly different frequencies (3 MHz, 3.007 MHz) to produce a radiation force at the difference (beat) frequency of 7kHz. The HIFU beam was scanned throughout the vessel, and the acoustic emissions from the resulting tissue motion were recorded by a remote hydrophone. The plaques were effectively imaged because the plaque was stiffer and vibrated with less amplitude. Nightingale et al.(2001) used short 7.2MHz bursts(5 μ s long, 2MPa amplitude) to push the tissue, and interspersed B-mode interrogation pulses to measure the displacement—a technique they referred to as “acoustic radiation force imaging” (ARFI). ARFI has been implemented on clinical ultrasound machines in order to qualitatively image tissue stiffness (Nightingale et al. 2002). A related method referred to as Localized Harmonic Motion (LHM) imaging (Konofagou and Hynynen 2003) involves amplitude-modulating a CW HIFU forcing wave to produce tissue oscillations at the modulation frequency (typically 10 to 200Hz). As with ARFI, the motion is measured with interrogation pulses, usually fired from a separate concentrically mounted transducer. The interrogation pulses are fired at a PRF of thousands of Hz, and the backscattered signal from each pulse is cross-correlated with that of the previous pulse to find the tissue displacement. Quantitative measurements of stiffness can also be made by measuring the velocity of shear waves that result from the forcing (Palmeri et al. 2008).

This manuscript is motivated by the desire to detect and monitor lesion formation when HIFU is used for focused ultrasound surgery. Lesions do not appear in conventional B-mode imaging because their ultrasonic scattering coefficient is the same as that of healthy tissue (Bush et al. 1993). When lesions are formed by HIFU the cooked tissue is 2 to 10 times stiffer than un-cooked, (Sapin-de Brosse et al. 2010; Kiss et al. 2004; Wu et al. 2001) and if the changes of stiffness can be measured then it would be possible to detect lesions. For example, ARFI has been used to image HIFU lesions in ex-vivo tissue (Lizzi et al. 2003, Fahey et. al 2004) and LHM to detect HIFU lesion formation in in-vitro bovine liver (Maleke and Konofagou 2008). In the LHM paradigm considered here the acoustic wave of the lower frequency pushing beam (HIFU) and the higher frequency imaging beam are transmitted simultaneously. In the linear acoustics regime the two waves propagate independently of each other, however, if the amplitudes are high enough then a nonlinear interaction can occur. For example, if a low frequency pump beam and high frequency carrier are transmitted simultaneously then as the pump beam distorts through nonlinear propagation it will frequency-modulate the higher frequency carrier (see, e.g. pp 76-84, Blackstock et al. 1998). In the LHM case the high frequency imaging beam is a short (~ 2 cycle) pulse and if it sits on the peak positive pressure of the HIFU it will travel slightly faster than the background sound speed whereas if it sits on the peak negative pressure it will travel slightly slower than the background sound speed. These time shifts will be interpreted by the cross-correlation processing as tissue displacement, but this will be an artifact of the nonlinearity and not a real displacement.

Here it is shown, through measurement and simulation of the acoustic field in water, that the temporal shifts associated with nonlinear distortion result in apparent displacements of the same magnitude as might be expected from the displacements induced by the forcing. Ex vivo experiments in tissue demonstrate that the apparent displacements do occur in ARFI-type scenarios and are in good agreement with the simulations. Finally, a signal processing strategy is proposed that can mitigate the artifact associated with the nonlinear distortion.

METHODS

Experimental Set-up

The experimental set-up for the pressure measurements is depicted in Figure 1. The HIFU beam was delivered by a 1.1MHz focused transducer (H-102, Sonic Concepts, Bothell, WA. USA) which was a single element piezoelectric source (63mm radius of curvature and 33.1mm aperture diameter) with a 20 mm hole in the center for an interrogation transducer to be placed. The interrogation pulse was generated by a 7.5MHz center frequency broadband transducer with a 57 mm focal length and 16mm element diameter (I4-0710-S-SU-F57M, Olympus-NDT, Waltham, MA. USA). The interrogation transducer was placed such that its focal spot coincided with the focus of the HIFU source. The transducers were rigidly mounted to a single translation stage to allow them to be moved in a water tank. The focal zone (based on half the peak pressure) for the HIFU beam was 10mm long in the axial direction and 1.6mm wide, and for the interrogation transducer was 20mm long and 1.16mm wide.

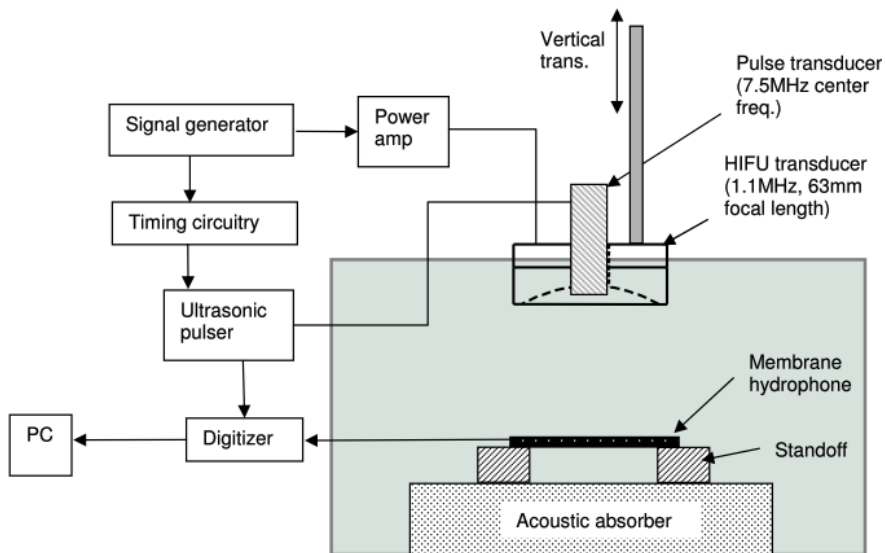


Figure 1. Schematic of the experimental set-up for pressure measurements.

The HIFU source was driven by a signal generator (Agilent 33250A, Palo-Alto CA. USA), and amplified by a power amplifier (75A250A, Amplifier Research, Bothell, WA). The interrogation transducer was excited by an ultrasonic pulser/receiver (5077, Olympus/Panametrics, Waltham, MA). The timing of the interrogation pulse relative to the HIFU was controlled by a pulse generator (8116, Hewlett Packard, Andover, MA). The pulse generator was triggered by the HIFU signal generator and was programmed to wait a specific time before sending a trigger pulse to the pulser/receiver. This allowed the interrogation pulse to occur at any time during the cycle of the HIFU waveform. In experiments in tissue it was necessary to change the phase between the interrogation and HIFU beams by 180 degrees for each successive pulse. A custom circuit was designed for this purpose, since the pulse generator described above was not capable of doing this fast enough.

The acoustic field was measured by a PVDF membrane hydrophone (0.2mm dia. active area, 15µm bilaminar membrane hydrophone, Precision Acoustics, Dorset, UK). The hydrophone was calibrated (NPL, Teddington, UK) from 500 kHz to 20 MHz. The hydrophone was mounted to stand-offs that sat on top of an acoustic absorber that was placed at the bottom of the tank. This arrangement ensured that reflections from the absorber or bottom of the tank did not interfere with the measurements. The hydrophone signal was digitized at a sampling rate of 250MHz by a digital oscilloscope, (LT264, LeCroy, Chestnut Ridge, NY. USA), averaged 63 times, and stored for analysis.

Nonlinear Theory

In finite-amplitude acoustics the amplitude of the sound field manifests itself as a change in the local sound speed. For a nonlinear progressive plane wave the phase speed of the waveform is (Blackstock et al. 1998)

$$c = c_0 + \beta p / \rho_0 c_0 \quad (1)$$

where p is the local acoustic pressure, c_0 the small-signal (linear) sound-speed, ρ_0 the density and β the coefficient of nonlinearity. By inspection of Eq.(1) the compressive phase of an acoustic wave ($p>0$) will travel faster than the small-signal sound speed and the rarefaction phase ($p<0$) will travel slower. The correction is small, as the assumption in finite-amplitude acoustics is that $|p|/\rho_0 c_0^2$ is small (in the experiments considered here less than 0.005), but over long enough propagation distances its effects can become appreciable. For the case of a low amplitude high frequency signal and a high amplitude low frequency pump wave the distortion results in frequency modulation of the high frequency signal (Blackstock et al. 1998). In LHM the high frequency signal is a short high frequency pulse and therefore exists only over a short duration of the HIFU wave, so the distortion of the HIFU wave will primarily translate the interrogation pulse rather than modulate it.

The time shift for the case where the interrogation pulse reflects off a target at a distance x can be estimated by means of eqn.(1). The time-of-flight to the target will be x/c , where c is the nonlinear phase speed due to the HIFU wave. However for the return journey the time-of-flight will be x/c_0 because after reflecting off the target the interrogation pulse will be propagating counter to the HIFU wave. Therefore for the return trip the interrogation pulse will thus spend about the same amount of time in the compression phase of the HIFU as in the rarefaction phase, and the nonlinear effects should cancel out. The total travel time of the interrogation pulse can therefore be expressed as:

$$TF = 2x/c_0 - \frac{\beta p x}{\rho_0 c_0^3} \quad (2)$$

where the first term represents the time-of-flight expected from linear theory and the second due to nonlinear distortion. Based on the standard imaging formula that the distance of a target is $TF \cdot c_0/2$ then the apparent displacement associated with the nonlinear distortion is

$$AD = \beta p x / 2 \rho_0 c_0^2 \quad (3)$$

For a 1 MPa amplitude plane wave propagating in water ($c_0=1485$ m/s, $\rho =998$ kg/m³ and $\beta=3.5$) the crest will have a phase speed 1487.5 m/s and the apparent time shift will grow linearly with propagation distance at a rate of ~ 1 ns/mm. For example, over a propagation distance of 63 mm the nonlinear distortion will result in a time shift of 67 ns. A time shift of 67 ns corresponds to $AD=50$ μ m, which is on the order of the displacements expected in LHM. It can be seen from Eq. 3 that the AD increases linearly with the pressure amplitude of the HIFU wave.

The nonlinear distortion that the HIFU wave suffers will eventually lead to the production of a shock in the waveform. For a plane sinusoidal wave the shock formation distance is $\rho_0 c_0^3 / \beta \omega P$, where P is the source amplitude. As the HIFU wave propagates past the shock formation distance, portions of the wave will be absorbed at the shock front. This implies a fundamental limit to the distance at which LHM can be employed where the forcing and imaging are done simultaneously. For the case of a 1 MPa, 1.1 MHz ultrasound wave in water the shock formations distance is 134mm and for distances beyond this the interrogation pulse is in danger of being absorbed at the shock front.

Numerical Model

The analysis above assumed that the sound field could be modeled as a plane wave. In practice both the HIFU and interrogation transducers produced focused diffracted beams with high enough amplitude for nonlinear effects to be important. In order to model this scenario the KZK equation was employed which models nonlinearity, diffraction (in the paraxial/parabolic approximation) and thermoviscous absorption of acoustic beams (Hamilton and Morfey 1998). For a beam propagating in the z-axis the KZK equation can be expressed as:

$$\frac{\partial p}{\partial z} = \frac{c_0}{2} \int_{-\infty}^{\tau} \nabla_T^2 p d\tau' + \frac{\beta}{2\rho_0 c_0^3} \frac{\partial p^2}{\partial \tau} + \frac{\delta}{2c_0^3} \frac{\partial^2 p}{\partial \tau^2} \quad (4)$$

Here $\tau=t-z/c_0$ the retarded time frame and δ the diffusivity of sound. For the case of an axisymmetric field the transverse Laplacian is given by $\nabla_T^2 = \left(\frac{1}{r} \frac{\partial}{\partial r} + \frac{\partial^2}{\partial r^2} \right)$ where r is the radial distance from the z -axis. In this paper the KZK equation was solved in the time domain using the Texas-code (Lee and Hamilton, 1995). In these simulations the properties of the medium were taken to be $c_0=1485$ m/s, $\rho_0=998$ kg/m³, $\beta=3.5$ and $\delta = 4.45 \times 10^{-5}$ m²/s, which resulted in an attenuation coefficient of 0.262 Np/m at 1 MHz. The computational grid extended in the radial direction from 0 to 69.4 mm with a grid step of 116 μ m (600 grid points total). The temporal discretisation was 0.45 ns (2000 points per HIFU cycle and 266 points per interrogation pulse cycle) and the grid extended in the time domain from -17.27 μ s to 13.6 μ s. The marching step in the axial direction was 32.1 μ m for the first 100 steps and then 64.3 μ m for the rest of the simulation.

The sources used in the experiments consisted of spherically curved elements in order to effect the focusing. For the KZK equation this source condition needed to be mapped to the front aperture plane of the transducer and in this case focusing can be approximated by applying a phase shift across the source, as a function of r . The waveform used for the source was a tone burst given by:

$$p = p_0 \exp\{-(2ft_s/n)^{2m}\} \sin(2\pi ft_s) \quad (5)$$

where n is the number of cycles, m controls the smoothness of the window, and t_s is the temporal behavior in the source plane: $t_s(r) = t - G \frac{r}{2\pi f} \left(\frac{r}{a} \right)^2 + t_0$ where $G = \pi a^2 f / c_0 x_F$ is the focusing gain of the source, x_F is the focal length, and t_0 is an offset to effect the phasing between the forcing and interrogation transducers.

In order to determine appropriate source conditions, the predicted axial field from the KZK equation, with nonlinearity turned off, was compared with the exact linear solution for a focused

radiator (O'Neil 1949). The presence of the hole was accounted by invoking Babinet's principle and subtracting the field from a focused transducer equivalent to the size of the hole in the HIFU transducer. The source conditions were then varied until the KZK equation simulations gave the best match to the O'Neil predictions. For the HIFU source the physical parameters used for the O'Neil prediction were: frequency 1.1 MHz, radius of curvature 63.3 mm, aperture radius 33.1 mm and a hole of radius 10 mm for the ARFI transducer. Optimization of the source conditions for the KZK equation resulted in values $a = 34.7$ mm, $x_F = 64.3$ and there was an axial offset between the numerical grid and physical space of 1.1 mm. The tone burst parameters in Eq. (5) where $n = 8$ and $m = 4$ for the HIFU source. Figure 2a compares the linear field generated by the KZK simulation to that predicted by the O'Neil solution for the HIFU transducer.

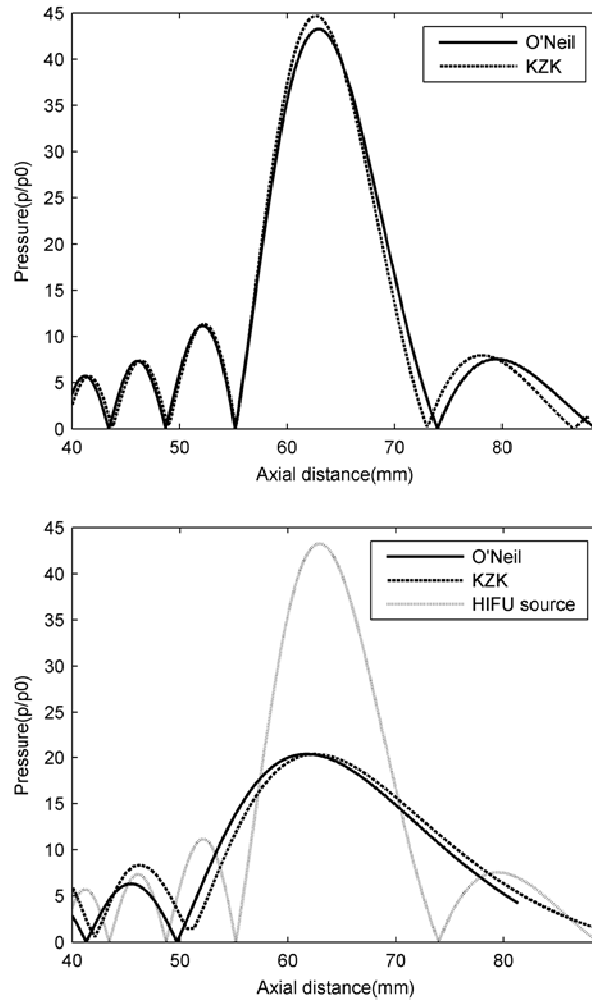


Figure 2. (a) Normalized peak pressure vs. axial distance from the surface of the HIFU transducer, for the O'Neil solution and the KZK prediction. The pressure was normalized by the effective source pressure $p_0 = \rho_0 c_0 u_0$ where u_0 is the source velocity. (b) Normalized peak pressure of the interrogation pulse vs. axial distance from the surface of the HIFU transducer. Also shown is the field of the HIFU source for comparison.

The parameters employed for O'Neil predictions of the interrogation source were: 7.7 MHz frequency, 57 mm radius of curvature, and 8.5 mm aperture radius. In the experiments the interrogation source was placed so that it was confocal with the HIFU source (i.e. it was offset 6.33 mm from the surface of the forcing transducer). For the KZK simulations the interrogation source had to be mapped to the same plane as the HIFU source and it was found that using $x_F = 56.2$ mm and $a = 9.1$ mm yielded the best match between the KZK simulation and the O'Neil prediction for the interrogation source. The interrogation waveform was generated using Eq. (5) with $n = 1.2$ and $m =$

3 yielding a pulse similar to what was measured experimentally. Figure 2b compares the O'Neil and KZK predictions for the 7.7 MHz component of the interrogation source. Also shown is the axial plot for the HIFU source, to illustrate that the differences in the size and frequency of the two sources mean that the diffracted fields are different. For example, the main lobe of the interrogation transducer covers the first pre-focal and the first post-focal lobe of the HIFU. This has ramifications for the nonlinear shifting of the interrogation pulse because every time the field of the HIFU transducer passes through a null the phase changes by 180 degrees and therefore the interrogation pulse will change from sitting on a peak to sitting in a trough. That is, if the interrogation pulse sits on the crest of the HIFU wave at the focus (63 mm), it should sit on the trough at 53 mm due to the phase change of the field of the HIFU transducer. This means that the plane wave analysis above cannot model the details of the diffracted fields as the interrogation pulse will be advanced over some portions of the propagation path and retarded in others.

Data processing

The difference between the arrival time of the interrogation pulse with and without HIFU wave were calculated with standard cross-correlation techniques (Walker and Trahey 1994). Briefly the A-lines were divided into segments corresponding to a distance of 0.375mm and there was 85% overlap between segments. The segments for data with the HIFU present (HIFU-on) were cross-correlated with the corresponding segments in the baseline (HIFU-off) A-line, giving arrival time change as a function of depth into the tissue (and thus tissue displacement vs. depth, if constant sound-speed was assumed). In order to increase the accuracy of the cross-correlation, the data for the interrogation pulse with HIFU on were processed to subtract off the HIFU wave before comparing to the HIFU-off interrogation pulse. For this reason it was necessary to measure (and simulate) waveforms for the HIFU wave alone in order to subtract it off. (Note that in typical LHM applications, the HIFU is removed via lowpass or bandpass filtering. The effect of these filters will be uniform for all the A-lines, so are not considered in this paper) After cross-correlation the three points around

the peak were fit to a parabola to further refine the peak location in time. The same processing was applied to both the measured and simulated data.

RESULTS

Hydrophone data

Pressure measurements were made for four different phase shifts between the interrogation pulse and the HIFU wave. The phase shift was defined in terms of arrival at the focus, not the physical phase at the source. In this work the four phases are referred to as: 0° when the interrogation pulse was in the trough of the HIFU wave, 90° when the interrogation pulse was on the negative-going zero crossing, 180° when it was on the crest, and 270° when it was on the positive-going zero crossing. At each axial distance and HIFU pressure, three waveforms were measured and simulated: 1. Pulse alone. 2. HIFU burst alone. 3. Pulse and HIFU burst together.

For the pressure measurements the length of the HIFU tone burst was either 12 or 24 cycles which was long enough for the HIFU source to reach steady state but short enough to ensure that reflections didn't pollute the signal. Figure 3 shows simulated and measured interrogation pulse waveforms at the focus for the case of a phase of 90° , for which the time difference between pulse arrival time with and without HIFU beam was the greatest. The HIFU wave peak pressure was 6MPa. Cross-correlation of the waveforms resulted in a 3.5ns shift for the simulated data and a 3.0 ns shift for the measured data. Note that at the focus the interrogation pulse was riding on the zero crossing of the HIFU wave and therefore by the plane wave analogy from Eq.(1) the pulse should not have been shifted. The actual delay of ~ 30 ns indicates that the pulse spent a significant portion of its propagation in the negative phase of the HIFU wave. Note also that the amplitude of the interrogation pulse was high enough that it underwent nonlinear distortion, which was also captured in the simulations.

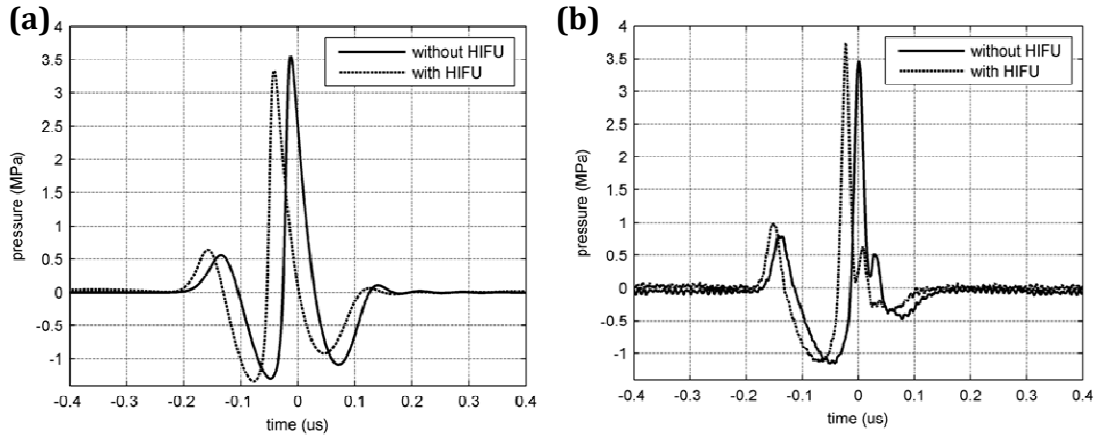


Figure 3. Interrogation pulse waveforms at the focus of the HIFU source (63mm) for a HIFU focal pressure of 6 MPa and a pulse phase of 90° . (a): simulated. (b): measured. The waveform with HIFU beam has the HIFU wave subtracted out. The difference in pulse arrival time caused by the HIFU beam in this case was 28ns for the simulation and 22ns for the measurement.

Figure 4 shows the simulated and measured time difference at the focus for each phase as a function of HIFU pressure level. The time difference is seen to linearly increase with pressure under these conditions, consistent with the prediction of Eq. (1). Note that the maximum time difference does not occur at phases of 0° or 180° , as would be expected if the HIFU beam and interrogation pulse were planar.

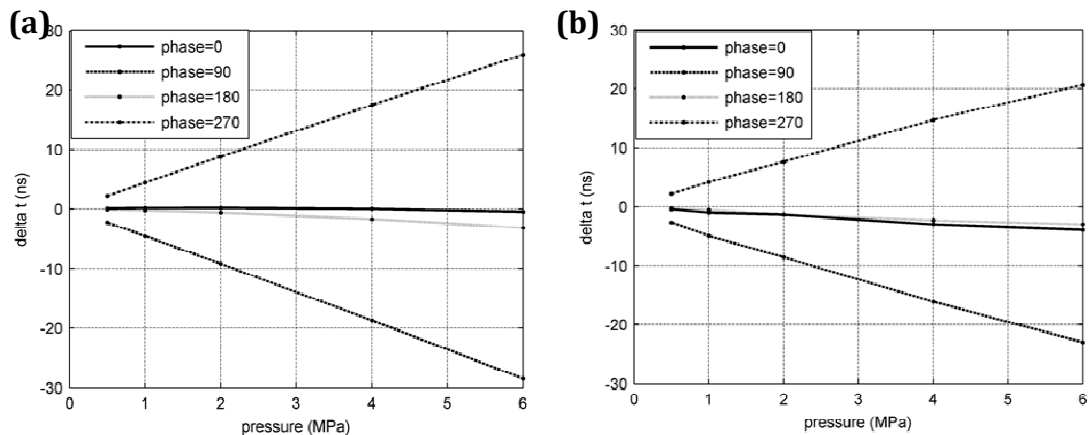


Figure 4. Nonlinearly-induced change in pulse arrival time at the focus of the HIFU source for the four phase relationships between the interrogation pulse and HIFU wave. (a): simulated. (b): measured.

Figure 5 shows the arrival time difference of the four phases as a function of axial location along the beam for two levels of HIFU pressure; 1 MPa and 6MPa. A number of observations can be made;

1. The measured results approximately share the same pattern as the simulation.
2. The basic pattern increases with pressure.
3. The patterns of phases 0° and 180° apart are nearly symmetric about zero, as are the patterns of 90° and 270° .

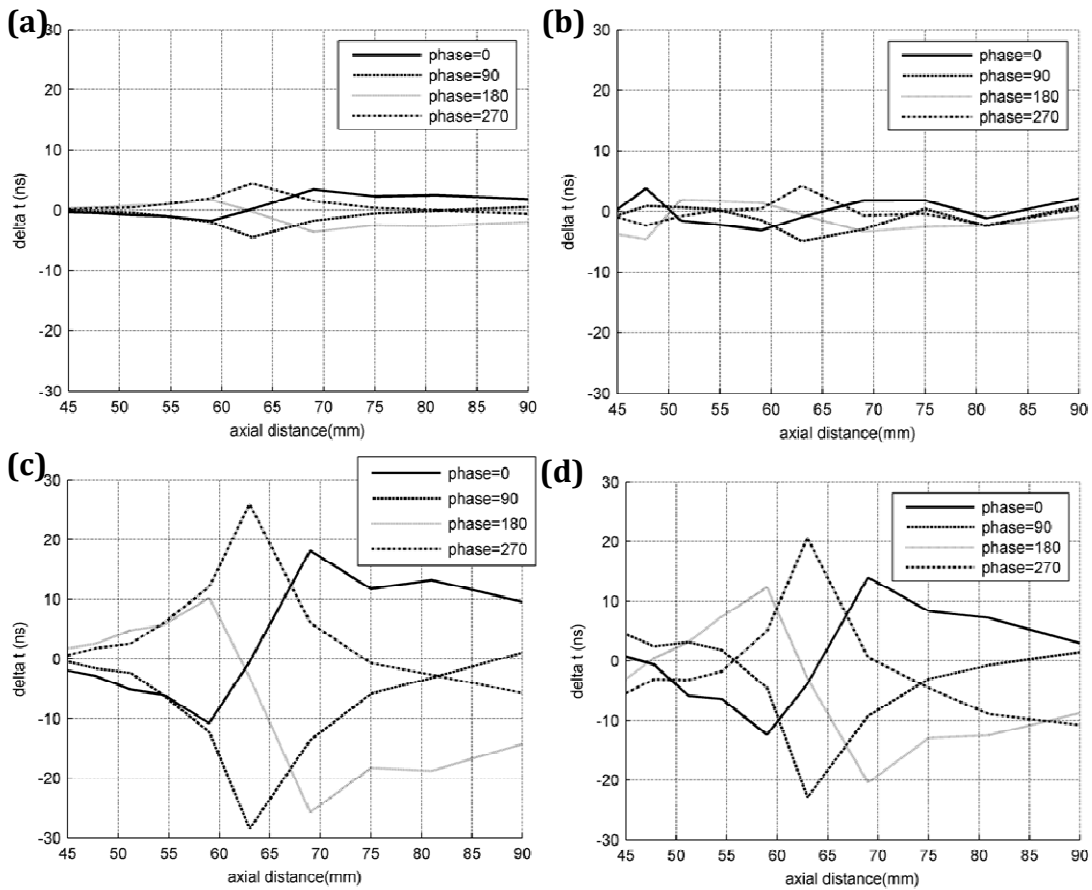


Figure 5. Nonlinearly-induced change in pulse arrival time vs. position for all four pulse phases. Upper: HIFU pressure = 1MPa peak (a) simulated (b) measured. Lower: HIFU pressure = 6MPa peak. (c): simulated. (d): measured

The linear relation of time shift with HIFU pressure is consistent with Eq.(3), however the prediction of linear growth with distance was not observed. This was because the diffraction pattern of the HIFU beam meant that the interrogation pulse didn't maintain the same phase relationship with the HIFU beam throughout its propagation. The symmetry of the patterns of phases 180° apart is consistent with the argument that a pulse starting on the crest of the HIFU wave will be delayed an equal but opposite amount to a pulse which started at the trough of the HIFU wave. The diffraction peaks and nulls through which each pulse travels will be the same – only the phase will be inverted and therefore the nonlinearly induced phase speed and resulting temporal shifts will be opposite. All this suggests that the nonlinear-induced differences in pulse arrival time can be canceled out by averaging the arrival times of pulses with opposite phase relationships to the HIFU wave. This will be examined for the experiments carried out in tissue.

Extended 1D model

The plane wave progressive model was extended to account for the diffraction effects of the HIFU beam on the nonlinear time shift. The following assumptions were made: 1. The beam width of the interrogation pulse is narrow so that the pressure field it encounters is just the HIFU field on-axis 2. The timeshift is solely due to a translation of the pulse and the distortion of the pulse shape is negligible. Under these conditions an estimate for the timeshift at position x' due to the focused HIFU field can be derived from a modified version of the plane wave case, Eq. (2)

$$TS = \left(\frac{\beta}{\rho_0 c_0^3} \right) \int_0^{x'} p(x) dx \quad (6)$$

where $p(x)$ is the local HIFU pressure that the interrogation pulse encounters at distance x and can be obtained from

$$p(x) = Re\{e^{(ikx+i\phi)} P(x)\} \quad (7)$$

where $P(x)$ is the complex HIFU pressure on axis, $exp(ikx)$ accounts for the phase shift associated with the propagation of a plane wave to location x , and ϕ represents the phasing between the HIFU and interrogation source. Here the complex HIFU pressure is calculated using the O'Neil solution. Figure 6 shows the results for the four phases for HIFU pressures of 1 and 6 MPa., and bears similarity to the measured and KZK-simulated results in Figure 5.

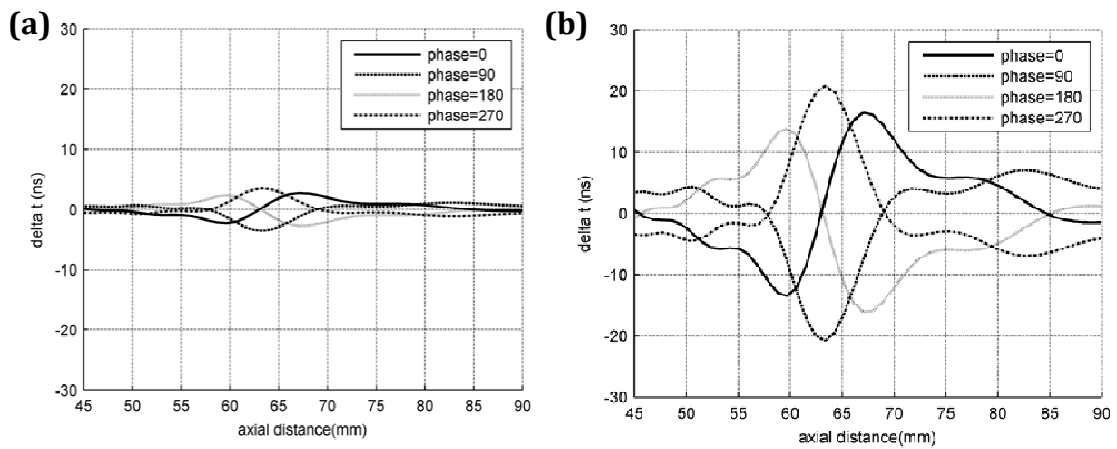


Figure 6. Predicted time shifts from the extended 1-d model (a) 1MPa, (b) 6MPa

Tissue data

Store-bought chicken breast (de-gassed for 30 minutes under vacuum in phosphate buffered saline (PBS) solution) was mounted in the tank in place of the hydrophone, with the mutual focus of the HIFU and interrogation transducers set at 15mm beneath the tissue surface. The difference in arrival time was determined as a function of position for the four phases. Since the phase could not be measured at the focal point in the tissue, the phases represent the temporal location of the excitation voltages of the interrogation pulse and the HIFU wave. Since each data run is unique due to changing tissue properties with time, it was desired to gather different phase data during the same run. The custom-made delay gate generator circuit was used to change the phase from the HP6118 pulser by 180° every pulse. In this way, two of the four phases were gathered at the PRF of the function generator 1.25kHz. The phase delay from the function generator was then altered by 90

degrees and another pair of A-lines acquired in order to get the other two phases.

Figure 7 shows the results from chicken breast. The HIFU peak pressure was 2MPa, and operated in CW for 200ms. A pair of baseline A-lines was taken 100ms before the start of the HIFU. A pair of A-lines was taken 1.6ms before the end of the HIFU burst which measured the response when the tissue was forced and another taken 1.6ms after the HIFU shut off in order to differentiate displacement due to temperature effects and radiation force effects. The data represent two separate runs, one for phase 0° and 180° , and another for phase 90° and 270° . We note that in this case, in addition to the nonlinear effect, the absorption of the HIFU results in heating, which also changes the sound speed and therefore induces apparent displacement of the tissue. Thus the data contains contributions from the nonlinear effect, the temperature effect, and the actual tissue displacement caused by acoustic forcing of the HIFU wave.

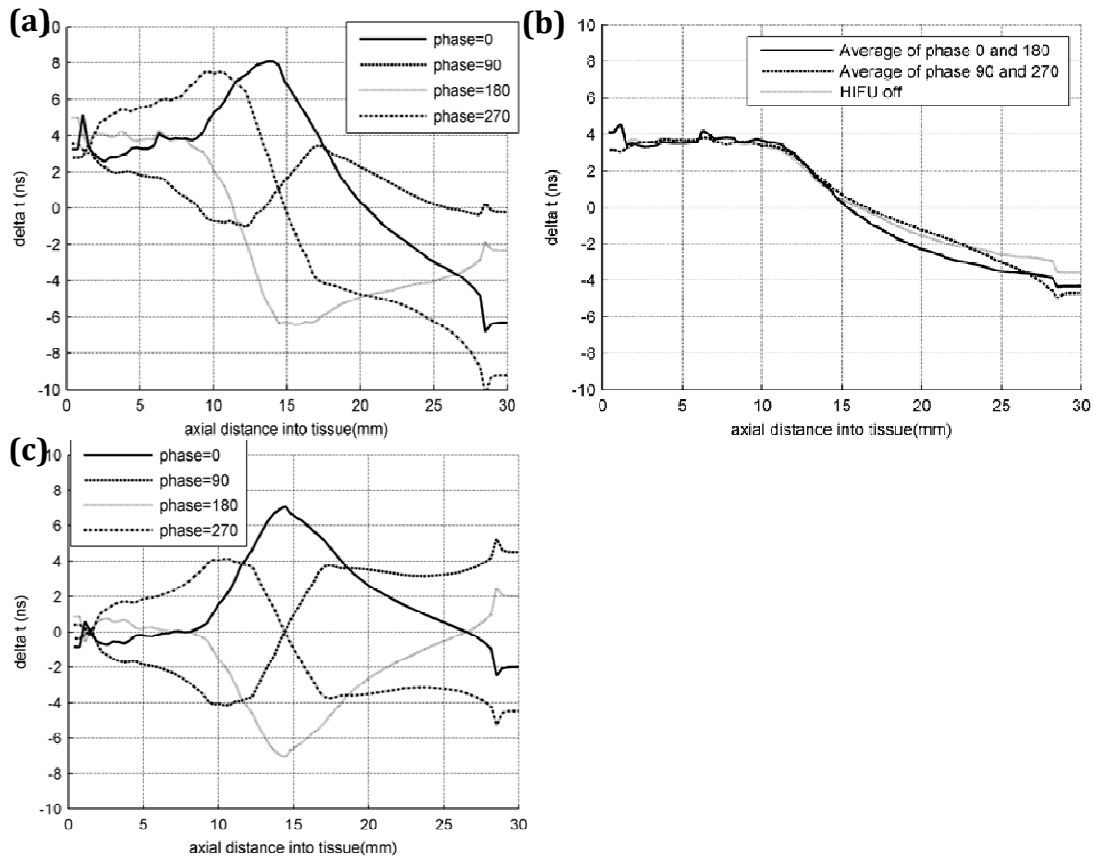


Figure 7. Change in pulse arrival time vs. depth in chicken breast for a 1.1MHz, 2MPa CW HIFU burst. (a): Data from the four phases. (b): Averages of the opposite phases 0°, 180°, and 90°, 270°, superimposed on data taken 1.6ms after HIFU turned off. (c): The four phases after the opposite phase averages were subtracted off.

Figure 7a shows the individual results for the four phases. In addition to the waveform structure it can be seen that all four curves show a large dip for distances beyond 10 mm. In order to remove the nonlinearly-induced apparent displacement we employed a signal processing scheme akin to pulse-inversion (Shen et al. 2005) where signals of opposite phase are subtracted in order to suppress linear effects and retain quadratic nonlinear effects. In this case we averaged the displacement data from the lines that were 180° out of phase—which should suppress the nonlinear effects and retain the linear effects. Recall the data shown in Fig. 4 where the displacement curves for the phase inversion did indeed display the opposite apparent displacement.

Figure 7b shows the results of averaging the displacement data from the lines that were 180° out of phase. It can be seen that the two curves for the 0°, 180° and 90°, 270° lie on top of each other

suggesting that this processing does indeed remove the nonlinear artifact and leaves the “motion” which will consist of the true motion and the apparent displacement due to the increased temperature at the focus. Also shown in Fig. 7b is the time difference curve for an A-line taken 1.6ms after the HIFU was turned off, that is, with no nonlinear distortion present. At this time the tissue has not had time to return to equilibrium position, nor has temperature elevation had time to dissipate. Thus, this line is expected to be close to the actual displacement (including temperature effects) at the end of the HIFU. It can be seen that this curve is in very good agreement with the two curves obtained from averaging the data from out-of-phase RF lines. The similarity of these three curves supports the proposition that averaging the opposite phases yields the true displacement for times when the HIFU is on.

Because the sound speed increases with temperature, at least for the range considered here, the temperature change results in a change in the gradient of the apparent displacement (Seip and Ebbini 1995, Maass-Moreno and Damianou 1996). The maximum change in temperature is expected to occur near the focus at 15mm, and that is indeed near where the slope is the greatest in Figure 7b. Also, since the time difference drops below zero starting at 15mm, one can assume the heating is making a significant contribution, since one would not expect negative displacement from the acoustic force of the HIFU wave. The 4ns time difference in the first 8 mm of the tissue corresponds to actual tissue displacement, with minimal heating artifact, which in this case is $4 \text{ ns} \times 0.75 \mu\text{m}/\text{ns} = 3 \mu\text{m}$. This value falls within the normal range observed in our work, as does the apparent drop due to temperature.

Figure 7c shows the same data in Figure 7a, except the average of the out-of-phase data has now been subtracted off. This should leave only the results of the nonlinear effect. It can be seen that the patterns resemble those of hydrophone data in Figure 5d, and there are no shifts due to forcing or temperature present. This is consistent with the previous data showing that nonlinearly-induced time shifts from data runs where the pulse-to-HIFU phase differed by 180° were symmetric and averaged to zero.

Figure 8 shows data from a similar experiment, using 3.3MHz HIFU instead of 1.1MHz. There is less difference between the displacement curves for the four phases. At this HIFU frequency, the interrogation pulse length is approximately the same as one period of the HIFU wave. Therefore the interrogation pulse as a whole will not be translated as the HIFU wave distorts but rather part of the interrogation pulse will be shifted forwards and part shifted backwards, resulting in little apparent displacement. That being said, the averaging of data from pulses that were 180° out of phase did show a reduction in variance of the displacement. In this case the averaged displacement data showed an initial increase with depth due to forcing, and the decrease beyond 12mm due to the temperature-induced effect.

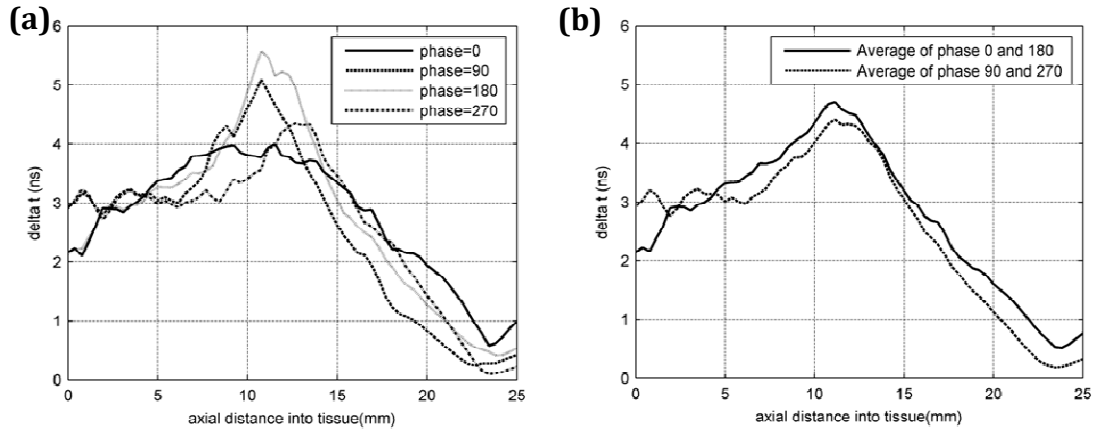


Figure 8. Change in interrogation pulse arrival time vs. depth in chicken breast for a 3.3MHz HIFU pushing wave. (a): timeshift of the four phases (b): average of the timeshifts for the phases that were 180° apart.

DISCUSSION AND CONCLUSIONS

For any application where a low-frequency pump beam and a high-frequency signal beam exist together in space and time (for example LHM imaging), acoustic nonlinearity can cause translation and/or distortion of the high frequency pulse. Here it was demonstrated that for a LHM application the time shifts induced by the nonlinearity resulted in an apparent displacement that was as on the order of the displacement to be measured.

The nonlinearly-induced apparent displacement (NIAD) was measured in water and simulated using the KZK equation for a 1.1MHz HIFU source and a 7.5 MHz interrogation pulse. It was observed that the NIAD was a function of source amplitude, propagation distance and initial phase and there was good agreement between the measurements and simulations. The variation with axial distance was dependent on diffraction pattern of the HIFU source. An approximate 1-D solution was developed using the on-axis linear solution for the HIFU source combined with nonlinear plane wave theory and the solution showed good agreement with the measurements and KZK simulations. Two key results were that the NIAD was of opposite sign when the phase relationship between the interrogation pulse and the HIFU wave was changed by 180° , and the second that the NIAD increased linearly with pressure.

Ex vivo measurements of acoustic radiation force on chicken breast indicated that the displacement obtained from the backscattered data had a NIAD that was consistent with the pressure measurements of distortion. In particular, the patterns of the NIAD vs. depth in the tissue for the four phases of the HIFU beam and interrogation pulse showed similar symmetry. The symmetry implied that by averaging data from pulses with 180° phase shift, the interrogation could be mitigated. Tissue data immediately after HIFU supported the strategy of averaging to remove the nonlinear distortion.

Experiments using a HIFU frequency of 3.3MHz suggested that the NIAD will be less as the forcing frequency approaches the center frequency of the interrogation pulse, as the interrogation pulse will extend over a larger fraction of the HIFU period. In this case the pulse will be distorted by the HIFU wave, but not necessarily shifted in arrival time.

The results suggest that for acoustic radiation force applications further mitigation of the NIAD might be obtained by increasing the HIFU pressure. Although this may seem counter-intuitive, the amplitude of the tissue displacement is proportional to the acoustic intensity, which is proportional to p^2 , whereas the NIAD is proportional to p . The ratio of the desired displacement to displacement artifact is therefore proportional to p , and thus higher pressure will diminish the relative effect of the NIAD.

In conclusion, it has been shown, through measurement and simulation, that the temporal shifts associated with nonlinear distortion result in apparent displacements of the same magnitude as might be expected from the displacements induced by acoustic forcing. The NIAD measured in the tissue experiments was in good agreement with the simulations. Finally, it was demonstrated that by sending out two interrogation pulses that are at different phases of the HIFU wave and averaging the results, the nonlinear artifact can be mitigated.

Acknowledgements – This work was supported in part by the Bernard M. Gordon Center for Subsurface Sensing and Imaging Systems (CENSSIS) under the Engineering Research Centers Program of the National Science Foundation (Award number EEC-9986821), and NSF grant 0835795.

REFERENCES:

- Beyer T. The parameter B/A. in *Nonlinear Acoustics*. Hamilton F. and Blackstock T. Eds. Academic Press, 1998, pp. 34
- Blackstock DT, Hamilton MF, Pierce AD. Progressive waves in lossless and lossy fluids. in *nonlinear acoustics*. Hamilton F. and Blackstock T. Eds. Academic Press, 1998, pp. 76-84
- Bush NL, Rivens I, TerHaar GR, Bamber JC. Acoustic properties generated with an ultrasound therapy system. *Ultrasound Med Biol* 1993; 19:789-801
- Fahey B, Nightingale K, Stutz D, Trahey G. Acoustic radiation force impulse imaging of thermally and chemically induced lesions in soft tissues: preliminary ex vivo results. *Ultrasound Med Biol* 2004;30:321-328
- Fatemi M, Greenleaf J. Ultrasound-stimulated vibro-acoustic spectrography. *Science* 1998; 280(3): 82 - 84
- Hamilton M. and Morfey C. Model equations in nonlinear acoustics. Hamilton F. and Blackstock T. Eds. Academic Press 1998. pp. 61.
- Kiss MZ, Varghese T, Hall TJ. Viscoelastic characterization of in-vitro canine tissue. *Phys. Med. Biol.* 2004; 49: 4207-4218
- Konofagou E, Thierman J, Hynynen K. The use of ultrasound-stimulated acoustic emission in the monitoring of modulus changes with temperature. *Ultrasonics* 2003;41(5):337-345.
- Lee Y and Hamilton MF. Time-domain modeling of pulsed finite-amplitude sound beams. *J Acoust Soc Am* 1995; 97:906-917
- Lizzi F, Muratore R, Deng C, Ketterling J, Alam K, Mikaelian S, Kalisz A. Radiation-force technique to monitor lesions during ultrasonic therapy. *Ultrasound Med. Biol* 2003; 29: 1593 - 1605
- Maleke C, Konofagou E. Harmonic motion imaging for focused ultrasound (hmifu): a fully integrated technique for sonication and monitoring of thermal ablation in tissues. *Phys Med Biol* 2008; 53:1773-1793
- Maass-Moreno R, Damianou C. Noninvasive temperature estimation in tissue via ultrasound echo-shifts. part I. analytical model. *J. Acoust. Soc. Am.* 1996; 100 (4): 2514-2521

- Nightingale K, Palmeri M, Nightingale R, Trahey G. On the feasibility of remote palpation using acoustic radiation force. *JAcoust Soc Am* 2001;110(1):625 - 634
- Nightingale K, Soo MS, Nightingale R, Trahey G. Acoustic radiation force impulse imaging: in vivo demonstration of clinical feasibility. *Ultrasound Med Biol* 2002;28(2):227-235
- O'Neil HT. Theory of focusing radiators. *JAcoust Soc Am* 1949;21(5): 516-526
- Palmeri ML, Wang MH, Dahl JJ, Frinkley KD, Nightingale KR. Quantifying hepatic shear modulus in vivo using acoustic radiation force. *Ultrasound Med Biol* 2008; 34(4): 546-558
- Sapin-de Brosses E, Gennisson JL, Pernot M, Fink M, Tanter M. Temperature dependence of the shear modulus of soft tissues assessed by ultrasound. *Phys. Med. Biol.* 55 (2010) 1701-1718
- Shen C, Chou Y, Li P. Pulse inversion techniques in ultrasonic nonlinear imaging. *J Med Ultrasound* 2005; 13(1):3-17
- Seip R, Ebbini E. Non-invasive estimation of tissue temperature response to heating fields using diagnostic ultrasound. *IEEE Trans. Biomed. Eng* 1995; 42(8) 828-839
- Walker W, Trahey G. A fundamental limit on the performance of correlation based phase correction and flow estimation techniques. *IEEE Trans Ultrason Ferroelectr Freq Control* 1994;41(5):644-654
- Wu T, Felmlee JP, Greenleaf JF, Riederer SJ, Ehman RL. Assessment of thermal tissue ablation with MR elastography. *Magnetic Resonance in Medicine* 2001; 45:80-87

Appendix F Additional Bubble Results

F.1 Agar-graphite phantom

This section will show the results of cavitation measurements on a phantom made with agar gel and graphite particles, to augment and compare to the results in chicken shown in section 4.3. The concentration of agar gel in the phantom was 28g/L and the concentration of graphite (325 mesh) was 35g/L. The acoustic attenuation was 5Np/m/MHz, and the stiffness was 200kPa. Figure F-1 shows the orientation of the phantom holder, which accommodated a phantom in the form of a 35mm film canister. The HIFU transducer provided the acoustic wave, and the scattered energy was measured by the central interrogation transducer and also a side-mounted passive transducer (15MHz center frequency, 0.75" focal length. Panametrics Inc., Waltham, MA). A B-mode imaging system (Terrason Inc, Burlington, MA) could also take images of the focal zone, and a PZT needle hydrophone (Dapco Inc., Oak Creek, WI) could measure the direct beam.

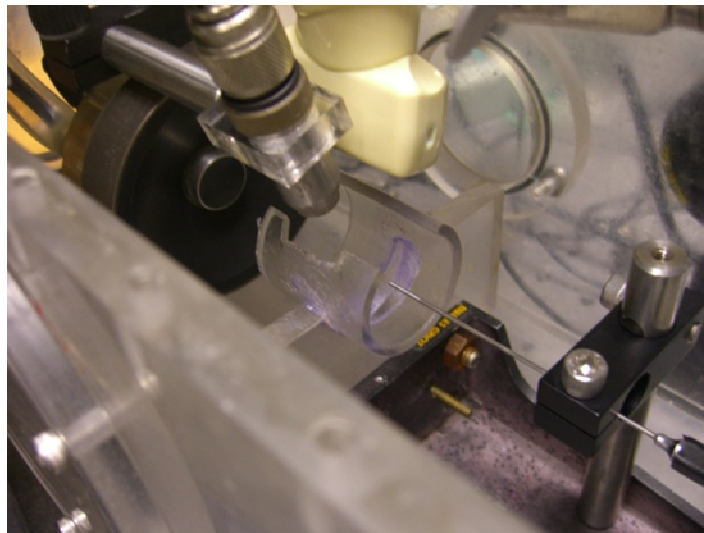


Figure F-1 Experimental setup for measuring scattering from bubbles in tissue samples or phantoms.

As with the chicken work, The HIFU focus was placed 15mm into the phantom. HIFU was delivered CW for 4s, with the pressure level starting at 0.9MPa and then ramping up by 0.77MPa every second after that. Figure F-2 shows the scattered energy received by the passive transducer during the insonation, which was digitized on the oscilloscope at a sample rate of 500 MHz. Plot (a) shows the spectrum of waveforms taken at 0.9 and 1.7 MPa. The 0.9MPa waveform has harmonics every multiple of $f_0/2$, where f_0 is the HIFU frequency (1.1MHz). It also shows a general broadband spectrum over the frequency ranges shown. The 1.7 MPa waveform has harmonics every $f_0/4$. Plots (c) and (e) show time traces of these waveforms, showing spikes every 2 and 4 HIFU periods, respectively. This reinforces the proposition put forth in section 4.3 that the presence of multiple HIFU harmonics and/or subharmonics in the scattered signal, outside of the frequency range expected from the nonlinear propagation of the HIFU wave through the media, are due to periodic inertial cavitation events. Note that the 1.7MPa curve in plot (a) drops after 6MHz. This results from the fact that the width of the 0.9MPa spikes are 0.066 μ s wide, and those of the 1.7MPa spikes are 0.11 μ s wide. When the HIFU wave reached the next level of pressure at 2.5MPa, the spikes disappeared, and the signal from the passive transducer dropped to the level of the electronic noise. It is possible that the bubbles were reduced in size to a point where inertial cavitation no longer took place. After this sequence, another CW HIFU exposure was initiated at the same spot on the phantom, at a constant pressure of 3.2MPa. Plots (b) and (d) show the frequency and time data. The shape of the spectrum looks similar to the 0.9 MPa curve, but the energy level is higher by 10dB under 5MHz. There are only three harmonics present, which is the approximate harmonic content of the HIFU wave. The time trace shows no periodic spikes, but does show an increase in overall energy from the 0.9 and 1.7MPa data, and possibly evidence of randomly occurring spikes from inertial cavitation. One possible scenario is that the 0.9 and 1.7MPa data came from one bubble or a group of bubbles close together, oscillating in unison. The 3.2MPa data may have been from many bubbles oscillating out of phase.

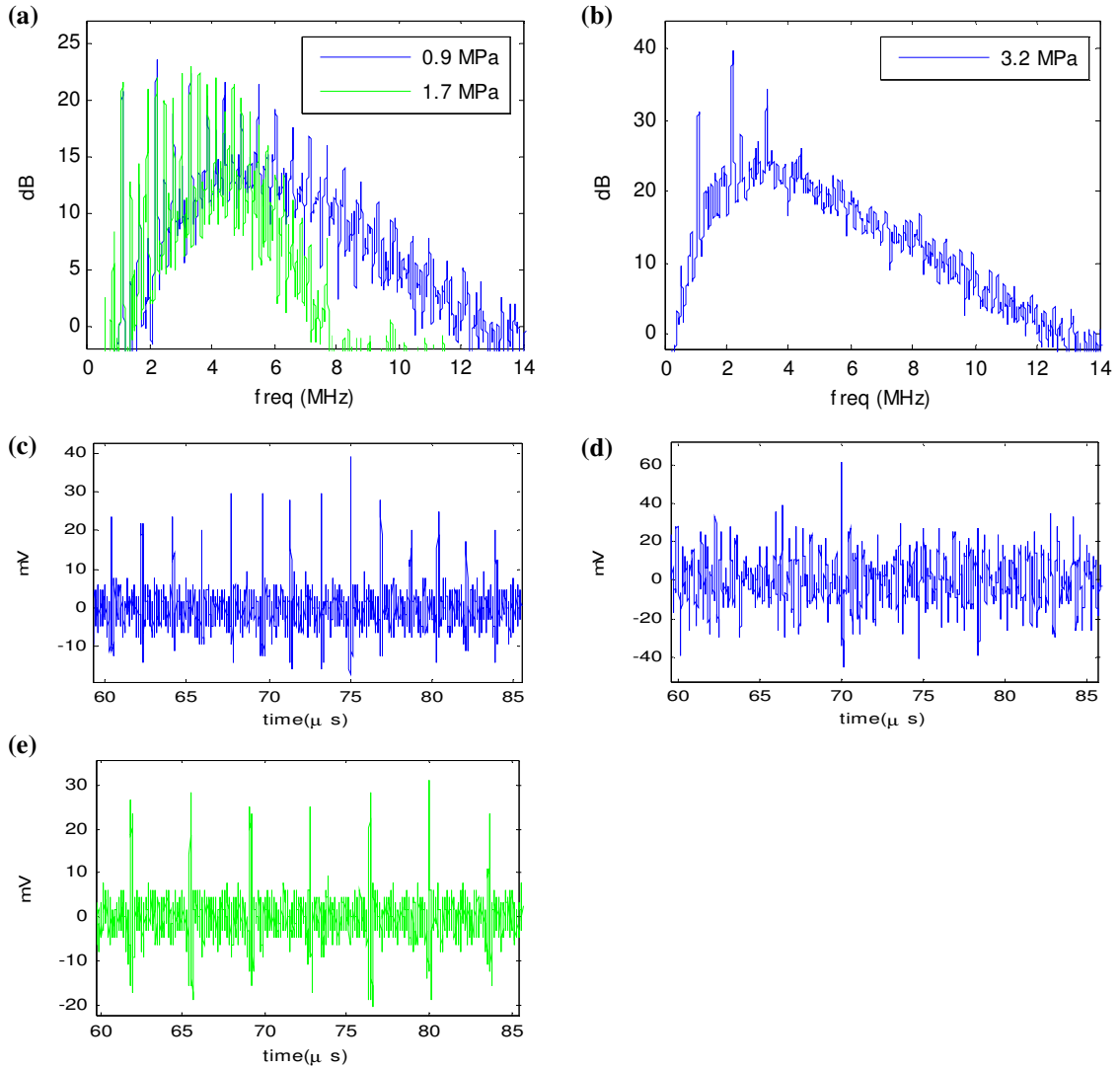


Figure F-2 Data from agar-graphite phantom exposed to 1.1MHz CW HIFU. (a), (c), and (e) were from one exposure in which the pressure was changed from 0.9MPa to 1.7MPa. (c) and (e) are time traces of the data in the spectra in(a). (b) and (d): same spot in phantom, exposed to constant 3.2MPa HIFU, 5 minutes after the previous exposure.

Figure F-3 shows data from the central interrogation transducer for the same 0.9 MPa exposure in Figure F-2. This data was taken in pulse-echo mode. Plot (a) shows a time waveform taken before the HIFU, showing the surface of the phantom, and backscattered energy from the graphite particles. Plots (b) and (c) are from data that was taken in the same 1 s window as the 0.9MPa curves in Figure

F-2. The spectra have a similar broadband shape, starting at 5MPa due to the hipass filter. No harmonics are seen. The time waveform in plot(c) shows no periodic spikes, however when the pre-HIFU data is subtracted off in plot(d), randomly occurring spikes can be seen (recall that each spike has a ringdown from the hipass filter). It is possible that the data was taken at a point within the 1s window in which the periodic cavitation seen in Figure F-2 had ended or had not started. The subtraction of the two waveforms is legitimate because there is little or no material motion or temperature-induced apparent displacement because the lines were taken close in time, and the material was too stiff to allow any detectable motion from HIFU forcing.

Finally, although not shown, the spectrum in (b) was similar to the spectrum from the time trace in (a), and the addition of the HIFU energy just added a uniform 5dB across the frequency range shown. This is useful information in the interpretation of the spectrograms of the HMI/lesion runs; inertial cavitation that is caused by the HIFU can thus manifest in two ways. If the cavitating bubbles collapse periodically and in unison, the spectrograms will show many harmonic lines across all time slices. If they are not in unison, or do not collapse periodically, the spectrogram will have a general increase in broadband energy uniformly across all time slices.

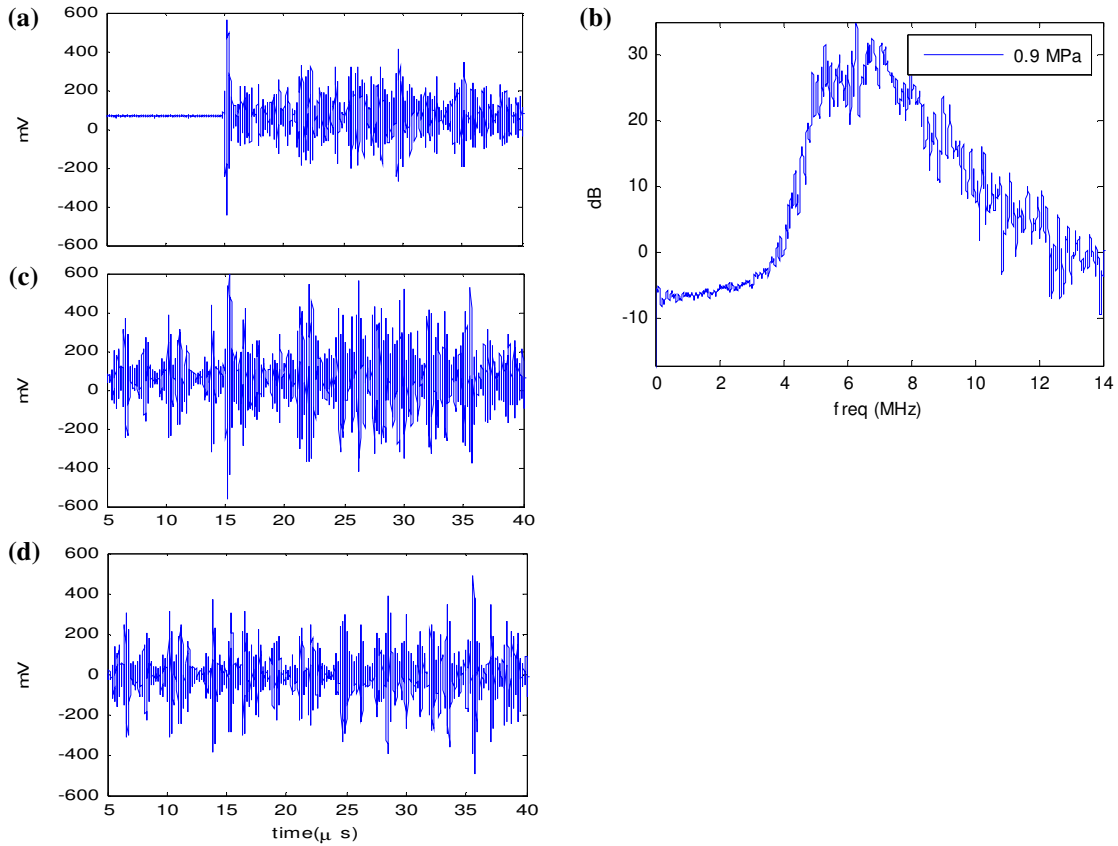


Figure F-3 Time and frequency data from central interrogation transducer, for the save experiment as shown in Figure F-2. (a): backscatter from the graphite particles, no HIFU. (b), (c): spectrum and time trace of data taken during the 0.9MPa portion of the HIFU exposure. (d): c-a

F.2 Miscellaneous Bubble Behavior

In this final section an interesting phenomenon is shown, which is a reminder of the complexity of bubble-related behavior. The data are from an HMI/lesion run of a 28s exposure at 7MPa, which made a lesion of average size (4mm x 13.5mm @ 7.5mm). The HMI data showed uniform displacement from 0 to 20mm in depth, with only small change when the lesion (presumably) started. Figure F-4 plots the A-lines, showing a typical increase in echogenicity somewhat before the focus. Figure F-5 shows the spectrograms of the first line, before HIFU, and the last line in which HIFU was on. There is an addition of broadband energy that is coincident with the region of

increased echogenicity seen in Figure F-4, and also a few harmonic lines due to scattering from the HIFU beam.

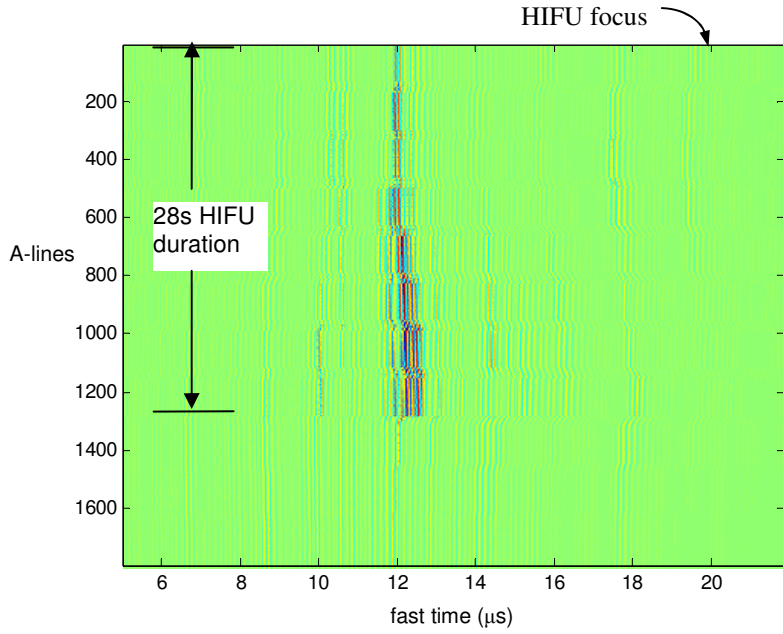


Figure F-4 A-lines from a 28s, 7MPa HIFU/HMI exposure in chicken.

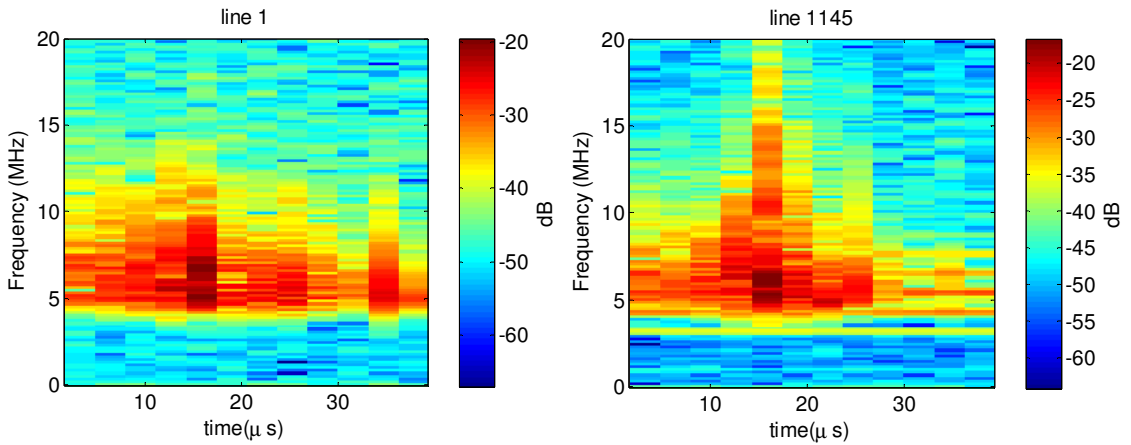


Figure F-5 Left: spectrogram of A-line #1 (pre-HIFU). Right: Last A-line taken with HIFU on.

Figure F-6 is a plot of the FFT of all the lines in which the HIFU was on, showing the spectrum of the entire line, rather than successive slices as done in the spectrograms. The special location of the source regions of the energy are lost, as is the ability to distinguish between the interrogation pulse and the HIFU wave as the source of the spectral information. However, there are more points in this

FFT and therefore finer frequency resolution. Note that these lines are a subset of the lines shown in Figure F-4, being only the lines fired during HIFU, and leaving out the HMI interrogation sequences. Increased broadband energy is seen starting about line #80 (25% of the way through the HIFU exposure). The demarcation of the start of this energy is clear, and no corresponding change is apparent in a plot of the A-lines (for example in the RMS level). Narrow frequency bands can be seen at the HIFU harmonics which end when the HIFU ends. There is a curve in the fine structure in the spectra, going downward in frequency, which curves back upward after HIFU. It was noted that the bubble shape instability threshold goes up with higher temperatures, thus allowing larger bubbles (Holt, 2011). The fine structure in the FFTs may be from many such bubbles growing and shrinking in average size. In this final data of HIFU heating and cavitation we are reminded of nature's complexity and intriguing unanswered questions.

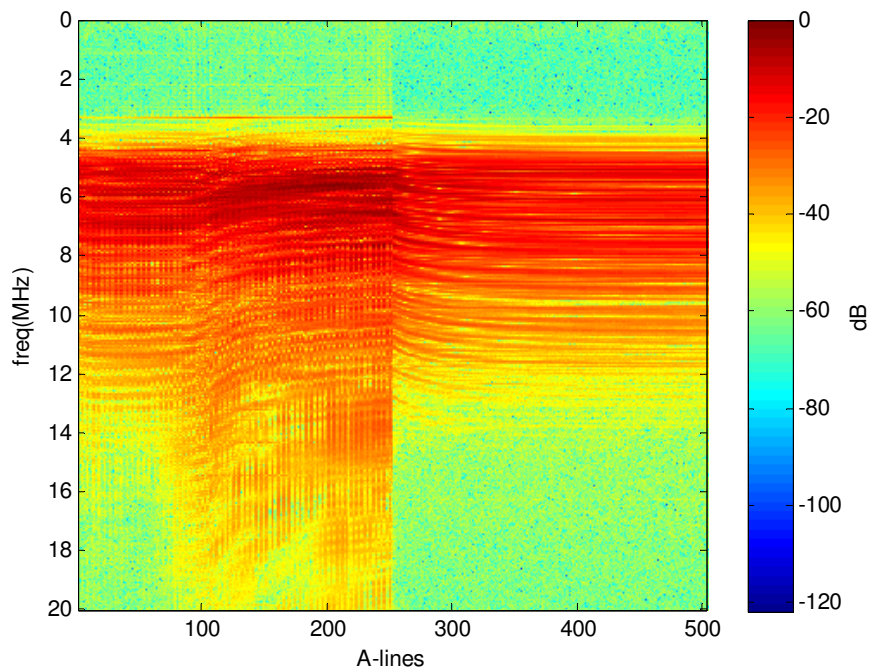


Figure F-6 FFT of each A-line during HIFU. HMI interrogation lines were omitted.

References

List of Journal Abbreviations

Adv. Drug Deliv. Rev	Advanced Drug Delivery Reviews
Ann Ophthalmol	Annals of Ophthalmology
Annu. Rev. Biomed. Eng	Annual Review of Biomedical Engineering
Appl. Sci. Res.	Applied Scientific Research
ARLO	Acoustic Research Letters Online
Curr. Urol. Rep.	Current Urology Reports
Eur. J. Radiol.	European Journal of Radiology
IEEE UFFC	IEEE Journal of Ultrasonics, Ferroelectrics, and Frequency Control
J. Acoust. Soc. Am.	Journal of the Acoustical Society of America
J Magn Reson Imaging	Journal of Magnetic Resonance Imaging
Laser Surg Med	Lasers in Surgery and Medicine
Phys. Med. Biol.	Physics in Medicine and Biology
Ultrasound Med. Biol.	Ultrasound in Medicine and Biology
Z. Phys. Chem.	Zeitschrift fur Physikalische Chemie

Alaniza A, Kallel F, Hungerford E, Ophir J. Variational Method For Estimating The Effects Of Continuously Varying Lenses In HIFU, Sonography, And Sonography-Based Cross-Correlation Methods J. Acoust. Soc. Am. 111, 468-474 (2002)

Anand A, Kaczkowski P. Monitoring Formation Of High Intensity Focused Ultrasound (HIFU) Induced Lesions Using Backscattered Ultrasound ARLO 5, 88-94 (2004)

Anand A And Kaczkowski P. Noninvasive Measurement Of Local Thermal Diffusivity Using Backscattered Ultrasound And Focused Ultrasound Heating. Ultrasound Med. Biol. 34, 1449-1464 (2008)

Arora D, Cooley D, Perry T, Skliar M, Roemer R. Direct Thermal Dose Control Of Constrained Focused Ultrasound Treatments: Phantom And In Vivo Evaluation. Phys Med Biol. 50, 1919-1935 (2005)

Bailey M, Couret L, Sapozhnikov OA, Khokhlova VA, Ter Haar G, Vaezy S, Shi X, Martin R, Crum LA. Use Of Overpressure To Assess The Role Of Bubbles In Focused Ultrasound Lesion Shape In Vitro. Ultrasound Med Biol. 27 695-708 (2001)

Bailey M, Khokhlova V, Sapozhnikov O, Kargl S, Crum L. Physical Mechanisms Of The Therapeutic Effect Of Ultrasound(A Review) Acoustical Physics. 49, 369-388. (2003)

Baker L, Bamber J. Performance Of Reflex Transmission Imaging (RTI) Using A Lineararray. IEEE Ultrasonics Symposium 2, 1551-1554 (2001)

- Bamber JC. "Ultrasonic Properties In Tissue" In *Ultrasound In Medicine*. Duck FA, Baker AC, Starritt HC Eds. Institute of Physics Publishing, Briston, UK 1998.
- Bamber J. Ultrasound Elasticity Imaging: Definition And Technology. *Eur. J. Radiol.* 9 327-330 (1999)
- Barannik E, Girnyk A, Tovstiyak V, Marusenko AI, Emelianov S, Sarvazyan A. Doppler Ultrasound Detection Of Shear Waves Remotely Induced In Tissue Phantoms And Tissue In Vitro. *Ultrasonics* 40 849-852 (2002)
- Barbone P, Bamber J. Quantitative Elasticity Imaging: What Can And Cannot Be Inferred From Strain Images *Phys. Med. Biol.* 47, 2147-2164 (2002)
- Ben-David M, Cantor R, Balbul N, Yehuda M, Gannot I. Measuring Tissue Heat Penetration By Scattered Light Measurements. *Lasers Surg Med.* 40, 494-499 (2008)
- Bercoff, J., Tanter, M., Fink, M. Supersonic Shear Imaging: A New Technique For Soft Tissues Elasticity Mapping *IEEE UFFC* 51, 374-409 (2004)
- Bevan P, Sherar M. B-Scan Ultrasound Imaging Of Thermal Coagulation In Bovine Liver: Frequency Shift Attenuation Mapping. *Ultrasound In Med. & Biol.* 27, 809-817 (2001)
- Beyer T. "The Parameter B/A" In *Nonlinear Acoustics*. Hamilton F. and Blackstock T. Eds. Academic Press, 1998. Pp. 34
- Blackstock DT, Hamilton MF, Pierce AD. "Progressive Waves In Lossless And Lossy Fluids" In *Nonlinear Acoustics*. Hamilton F. and Blackstock T. Eds. Academic Press, 1998. Pp.76-84
- Blonigen, F. J., A. Nieva, C. A. Dimarzio, S. Manneville, L. Sui, G. Maguluri, T. W. Murray, and R. A. Roy. Computations Of The Acoustically Induced Phase Shifts Of Optical Paths In Acoustophotonic Imaging With Photorefractive-Based Detection. *Applied Optics.* 44, 3735-3746 (2005)
- Bossy E, Funke A, Daoudi K, Boccara A, Tanter M, Fink M. Transient Optoelastography In Optically Diffusive Media. *Applied Physics Letters* 90, 174111 1-3 (2007)
- Boverman G, Miled M, And Miller E. Recent Work In Shape-Based Methods For Diffusive Inverse Problems. *Review of Scientific Instruments* 74, 2580-2582 (2003)
- Burgess SEP, Iwamoto T, Coleman DJ, Lizzi FL, Driller J, Rosado AL. Histological Changes In Porcine Eyes Treated With High Intensity Focused Ultrasound. *Ann Ophthalmol.* 19 133-138 (1987)
- Bush N, Rivens I, Ter Haar G, Bamber J. Acoustic Properties Of Lesions Generated With An Ultrasound Therapy. *Ultrasound Med Biol.* 19, 789-801 (1993)
- Chaussy C, Thuroff S. The Status Of High-Intensity Focused Ultrasound In The Treatment Of Localized Prostate Cancer And The Impact Of A Combined Resection. *Curr. Urol. Rep.* 4 248-252 (2003)
- Chen X, Phillips D, Schwarz K, Mottley J, Parker K. The Measurement Of Backscatter From A Broadband Pulse-Echo A New Formulation *IEEE UFFC* 44, 515-525 (1997)
- Cilesiz IF, Welch AJ. Light Dosimetry: Effects Of Dehydration And Thermal Damage On The Optical Properties Of The Human Aorta. *Applied Optics.* 32, 477-487 (1993)

- Clarke R, Ter Haar G. Temperature Rise Recorded During Lesion Formation By High-Intensity Focused Ultrasound. *Ultrasound In Med. & Biol.* 23, 299-306 (1997)
- Commander, K. W. and Prosperetti, A. Linear Pressure Waves In Bubbly Liquids – Comparison Between Theory And Experiments. *J. Acoust. Soc. Am.*, 85, 732–746 (1989)
- Coussios C, Farny C, Ter Haar G, Roy R. Role Of Acoustic Cavitation In The Delivery And Monitoring Of Cancer Treatment By High-Intensity Focused Ultrasound (HIFU) *International Journal Of Hyperthermia* 23, 105–120 (2007)
- Crum LA. . Nucleation And Stabilization Of Microbubbles In Liquids. *Appl. Sci. Res.* 38, 101–115 (1982)
- Curriel L, Huang Y, Vykhodtseva N, Hynynen K. Focused Ultrasound Treatment Of VX2 Tumors Controlled By Local Harmonic Motion. *Phys. Med. Biol.* 54 (2009)
- Curra FF, Mourad PD, Kholthlova VA, Cleveland RO, Crum LA. Numerical Simulations Of Heating Patterns And Tissue Temperature Response Due To High-Intensity Focused Ultrasound. *IEEE UFFC.* 4 (2000)
- Damianou C, Hynynen K. The Effect Of Various Physical Parameters On The Size And Shape Of Necrosed Tissue Volume During Ultrasound Surgery. *J Acoust Soc Am.* 95 1641–1649 (1994)
- Damianou C A, Sanghvi N. T. , Fry F. J. , Maass-Moreno R. , “Dependence Of Ultrasonic Attenuation And Absorption In Dog Soft Tissues On Temperature And Thermal Dose,” *J. Acoust. Soc. Am.* 102, 628–634 (1997)
- Delaye, P., L.A. Montmorillon, and G. Roosen. Transmission Of Time Modulated Optical Signals Through An Absorbing Photorefractive Crystal. *Optics Communications.* 118, 154-164 (1995)
- Dickinson R.J., Hill C.R., Measurement Of Soft Tissue Motion Using Correlation Between A Scans, *Ultrasound Med. Biol.* 8, 263-271 (1982)
- Dolfi D, Micheron F. Imaging Process And System For Transillumination With Photon Frequency Marking. *International Patent WO 89/00278*, (1989)
- Doyley M, Bamber J, Fuechsel F, Bush N. A Freehand Elastographic Imaging Approach For Clinical Breast Imaging: System Development And Performance Evaluation. *Ultrasound Med Biol.* 27 1347–1357 (2001)
- Draudt A, Lai P, Roy R, Murray T, Cleveland R. Detection Of HIFU Lesions In Excised Tissue Using Acousto-Optic Imaging. *Proceedings Of The 8th International Symposium On Therapeutic Ultrasound* (2008)
- Draudt AB and Cleveland RO. Impact Of Nonlinear Distortion On Acoustic Radiation Force Imaging. *Submitted To Ultrasound. Med. Biol.* (2011)
- Drewniak J, Frizzell L, Dunn F. Errors Resulting From Finite Beamwidth And Sample Dimensions In The Determination Of The Ultrasonic Absorption Coefficient. *J. Acoust. Soc. Am.* 88 967-977 (1990)
- Duck FA. *Physical properties of tissue: a comprehensive reference book.* Academic Press (1990)

- Eller A, Flynn HG. . Rectified Diffusion During Nonlinear Pulsations Of Cavitation Bubbles. *J. Acoust. Soc. Am.* 37, 493–503 (1965)
- Eller AI, Crum LA. . Instability Of Motion Of A Pulsating Bubble In A Sound field. *J. Acoust. Soc. Am.* 47, 762–67 (1970)
- Erpelding T, Hollman K, O'Donnell M. Bubble-Based Acoustic Radiation Force Elasticity Imaging *IEEE UFFC* 52, 971-979 (2005)
- Fahey B, Nightingale K, Stutz D, Trahey G. Acoustic Radiation Force Impulse Imaging Of Thermally And Chemically Induced Lesions In Soft Tissues: Preliminary Ex Vivo Results. *Ultrasound Med Biol.* 30, 321-328 (2004)
- Farny C. Identifying And Monitoring The Roles Of Cavitation In Heating From High-Intensity Focused Ultrasound Phd. Dissertation, Boston University (2007)
- Fatemi M, Greenleaf J. Ultrasound-Stimulated Vibro-Acoustic Spectrography. *Science* 280, 82 - 84 (1998)
- Findley WN, Lai JS, Onaran K. Creep And Relaxation Of Nonlinear Viscoelastic Materials With An Introduction To Linear Viscoelasticity. Amsterdam- New York-Oxford. North-Holland. 1976. P.67
- H. Frenzel And H. Schultes. Luminescenz Im Ultraschallbeschickten Wasser. *Z. Phys. Chem.* B27, 421-424 (1934)
- Fry W, Fry R. Determination Of Absolute Sound Levels And Acoustic Absorption Coefficients By Thermocouple Probes—Theory. *J. Acoust Soc. Am.* 26, 294-310 (1954)
- Fry W, Fry R. Determination Of Absolute Sound Levels And Acoustic Absorption Coefficients By Thermocouple Probes—Experiment. *J. Acoust Soc. Am.* 26, 310-317 (1954)
- Garra B, Shawker TH, Nassi M, Russell M. Ultrasound Attenuation Measurements Of The Liver In Vivo Using A Commercial Sector Scanner. *Ultrasonic Imaging* 6, 396–407 (1984)
- Garra B, Cespedes E, Ophir J, Spratt S, Zuurbier RA, Magnant CM, Pennanen MF. Elastography Of Breast Lesions: Initial Clinical Results. *Radiology* 202, 79–86 (1997)
- Gertner M, Wilson B, Sherar M. Ultrasound Properties Of Liver Tissue During Heating. *Ultrasound Med Biol.* 23, 1395–1403 (1997)
- Girault J, Ossant F, Ouahabi A, Patat F Time-Varying Autoregressive Spectral Estimation For Ultrasound Attenuation In Issue Characterization *IEEE UFFC* 45, 650 – 659 (1998)
- Goss S, Cobb W, Frizzell L. Effect Of Beam Width And Thermocouple Size On The Measurement Of Ultrasonic Absorption Using The Thermoelectric Technique. *Ultrasonic Symposium Proceedings, IEEE* 206-211 (1977)
- Green P, Arditi M. Ultrasonic Reflex Transmission Imaging. *Ultrasonic Imaging* 7, 201-214 (1985)
- Greenleaf J, Fatemi M, Insana .M Selected Methods For Imaging Elastic Properties Of Biological Tissues *Annu. Rev. Biomed. Eng.* 5, 57–78 (2003)

- Hamilton M. And Morfey C. Model Equations. In Nonlinear Acoustics. Hamilton F. And Blackstock T. Eds. Academic Press (1998). Pp. 61.
- Haw C. Using Ultrasound To Extract The Biomechanical Properties Of Soft Tissue. Phd Thesis, University Of Oxford, (2008)
- Haw C, Arora M, Coussious C, Noble A. The Effect Of Attenuation Coefficient On Radiation Force Impulse Monitoring Of Thermal Lesions. Proceedings Of The 9th International Symposium On Therapeutic Ultrasound (2009)
- Heikkila J, Hynynen K, Investigation Of Optimal Method For Inducing Harmonic Motion In Tissue Using A Linear Ultrasound Phased Array – A Simulation Study. Ultrasonic Imaging 28, 97-113 (2006)
- Heikkila J, Curiel L, Hynynen K. Local Harmonic Motion Monitoring Of Focused Ultrasound Surgery— A Simulation Model. IEEE Transactions on Biomedical Engineering, 57, (2010)
- Hilgenfeldt S, Lohse D, Zomack M. . Sound Scattering And Localized Heat Deposition Of Pulse-Driven Microbubbles. J. Acoust. Soc. Am. 107, 3530–3539 (2000)
- Hill, C.R., Bamber, J.C., Ter Haar, G.R. “Attenuation And Absorption” In: Physical Principles Of Medical Ultrasonics. John Wiley & Sons Ltd, Pp.93-166. (2004)
- Hindley J, Gedroyc W, Regan L, Stewart E, Tempany C, Hynynen K. MRI Guidance Of Focused Ultrasound Therapy Of Uterine fibroids: Early Results. American Roentgen Ray Society, 183, 1713. 2004
- Holt RG, Roy RA. Measurements Of Bubble-Enhanced Heating From Focused, Mhz-Frequency Ultrasound In A Tissue-Mimicking Material. Ultrasound Med. Biol. 27, 1399–412 (2001)
- Holt G, Roy R. “Bubble Dynamics” In Therapeutic Ultrasound Research Signpost 37/661 Tricandrum, Kerala, India Pp.184-229 (2005)
- Holt G. Private Conversation. 2011
- Huang J. Heating in Vascular Tissue and Flow-Through Tissue Phantoms Induced by Focused Ultrasound. PhD Thesis, Boston University (2002)
- Huang J, Holt R, Cleveland R, Roy R. Experimental Validation Of A Tractable Numerical Model For Focused Ultrasound Heating In Flow-Through Tissue Phantoms. J. Acoust. Soc. Am. 116, 2451-2458 (2004)
- Hynynen, K.. The Threshold For Thermally Significant Cavitation In Dog's Thigh Muscle In Vivo. Ultrasound Med Biol. 17, 157-169 (1991)
- Hynynen K, Pomeroy O, Smith DN, Huber PE, Mcdannold NJ, Kettenbach J, Et Al. MR Imaging-Guided Focused Ultrasound Surgery Of fibroadenomas In The Breast: A Feasibility Study. Radiology 219, 176–185 (2000)
- Illing R, Chapman A. The Clinical Applications Of High Intensity Focused Ultrasound In The Prostate. International Journal of Hyperthermia 23, 183-91 (2007)
- Incropera R. Fundamentals of Heat and Mass Transfer. 3rd ed. Wiley and Sons. New York. 1990

- Kaczkowski P, Anand A. Temperature Rise Measured Noninvasively During Thermal Therapy Using Backscattered Ultrasound. *Ultrasonics Symposium 1*, 720-723 (2004)
- Karbeyaz B. Modeling and Shaped Based Inversion for Frequency Domain Ultrasonic Monitoring of Cancer Treatment. Phd Thesis, Northeastern University (2005)
- Karbeyaz B, Miller E, Cleveland R, Roy R. Born Inversion For Broadband Ultrasonic Monitoring Of Cancer Treatment. 6th International Symposium on Therapeutic Ultrasound 166-170 (2006)
- Kempe, M., M. Larionov, D. Zaslavsky, And A. Z. Genack. Acousto-Optic Tomography With Multiply Scattered Light. *Journal Of The Optical Society Of America A*. 14, 1151-1158 (1997)
- Kennedy JE, Wu F, Ter Haar GR, Gleeson FV, Phillips RR, Middleton MR, And Cranston D, High-Intensity Focused Ultrasound For The Treatment Of Liver Tumours. *Ultrasonics*, 42, 931-5 (2004)
- Kiss MZ, Varghese T, Hall TJ. Viscoelastic Characterization Of In Vitro Canine Tissue. *Phys. Med. Biol.* 49, 4207-4218 (2004)
- Klibanov AL. Targeted Delivery Of Gas-filled Microspheres, Contrast Agents For Ultrasound Imaging. *Adv. Drug Deliv. Rev.* 37:139-57 1999
- Kobayashi Y, Onishi A, Watanabe H, Hoshi T, Kawamura K, Fujie MG. In Vitro Validation of Viscoelastic and Nonlinear Physical Model of Liver for Needle Insertion Simulation. *Proceedings of the 2nd Biennial IEEE/RAS-EMBS International Conference on Biomedical Robotics and Biomechatronics*. 469-476 (2008)
- Konofagou E, Thierman J, Hynynen K. A Focused Ultrasound Method For Synchronous Diagnostic And Therapeutic Applications—A Simulation Study. *Phys. Med. Biol.* 46, 2967-2984 (2001)
- Konofagou E, Thierman J, Karjalainen T, Hynynen K. The Temperature Dependence Of Ultrasound-Stimulated Acoustic Emission. *Ultrasound Med. Biol.* 28, 331 - 338 (2002)
- Konofagou E, Hynynen K. Localized Harmonic Motion Imaging: Theory, Simulations And Experiments. *Ultrasound Med. Biol* 29, 1405 -1413 (2003)
- Konofagou E, Thierman J, Hynynen K. The Use Of Ultrasound-Stimulated Acoustic Emission In The Monitoring Of Modulus Changes With Temperature. *Ultrasonics* 41,337-345 (2003)
- Korpel A. *Acousto-Optics*. Marcel Dekker, New York (1997)
- Krouskop TA, Vinson S, Goode B, Dougherty D. A Pulsed Doppler Ultrasonic System For Making Noninvasive Measurements Of The Mechanical Properties Of Soft Tissue. *Journal Of Rehabilitation Research And Development*. 24, 1 - 8 (1987)
- Krouskop TA, Wheeler TM, Kallel F, Garra BS, Hall T. Elastic Moduli Of Breast And Prostate Tissues Under Compression. *Ultrasonic Imaging* 20, 260-274 (1998)
- Kuc R, Schwartz M. Estimating The Acoustic Attenuation Coefficient Slope For Liver From Reflected Ultrasound Signals. *IEEE Transactions On Sonics And Ultrasonics*. Su-26, 353 - 362 (1979)
- Lai P, McLaughlan JR, Draudt AB, Murray TW, Cleveland RO, Roy R. Real-Time Monitoring Of High-Intensity Focused Ultrasound Lesion Formation Using Acousto-Optic Sensing. *Ultrasound Med. Biol.* 37, 239-252 (2011)

- Lai P. Photorefractive Crystal-Based Acousto-Optic Imaging In The Near-Infrared And Its Applications Phd Dissertation, Boston University. (2011)
- Lee Y and Hamilton MF. Time-Domain Modeling Of Pulsed Finite-Amplitude Sound Beams. *J Acoust Soc Am* 97, 906-917 (1995)
- Leighton, T.G. *The Acoustic Bubble*. London: Academic Press. (1994)
- Lev A, Kotler Z, Sfez B. Ultrasound Tagged Light Imaging In Turbid Media In A Reflectance Geometry. *Optics Letters*. 25, 378-380 (2000)
- Leveque S, Boccara A, Lebec M, Saint-Jalmes H. Ultrasonic Tagging Of Photon Paths In Scattering Media: Parallel Speckle Modulation Processing. *Optics Letters* 24, 181-183 (1999)
- Leutz, W., and G. Maret. Ultrasonic Modulation Of Multiply Scattered Light. *Physica B*. 204, 14-19 (1995)
- Li Y, Hemmer P, Kim C, Zhang H, Wang LV. Detection Of Ultrasound-Modulated Diffuse Photons Using Spectral-Hole Burning. *Optics Express* 16, 14862-14874 (2008)
- Li R, Song L, Elson DS, Tang M. Parallel Detection Of Amplitude-Modulated, Ultrasound-Modulated Optical Signals. *Optics Letters* 35, 2633 (2010)
- Lizzi F, Feleppa E, Astor M, Kalisz A. Statistics Of Ultrasonic Spectral Parameters For Prostate And Liver Examinations. *IEEE UFFC* 44, 935-942. (1997)
- Lizzi F, Muratore R, Deng C, Ketterling J, Alam K, Mikaelian S, Kalisz A. Radiation-Force Technique To Monitor Lesions During Ultrasonic Therapy. *Ultrasound Med. Biol.* 29, 1593 - 1605 (2003)
- Lighthill Sir J. Acoustic Streaming. *Journal Of Sound And Vibration* 61, 391-418 (1978)
- Lynn JG, Zwemer RL, Chick AJ, Miller AG. A New Method For The Generation And Use Of Focused Ultrasound In Experimental Biology. *Journal Of General Physiology* 26, 179 - 193 (1942)
- Lyons ME, Parker KJ. Absorption And Attenuation In Soft Tissues—Experimental Results. *IEEE UFFC* 35, 511-521 (1988)
- Maksimov AO, Leighton TG. . Transient Processes Near The Acoustic Threshold Of Parametrically-Driven Bubble Shape Oscillations. *Acustica* 87, 322-32 (2001)
- Mast TD, Raj S, Makin I, Faidi W, Runk M, Barthe PG, Slayton MH. Bulk Ablation Of Soft Tissue With Intense Ultrasound: Modeling And Experiments *J. Acoust. Soc. Am.* 118, 2715-2724 (2005)
- Maleke C, Konofagou E. Harmonic Motion Imaging For Focused Ultrasound (HMIFU): A Fully Integrated Technique For Sonication And Monitoring Of Thermal Ablation In Tissues. *Phys Med Biol* 53, 1773-1793 (2008)
- Marks, F. A., H. W. Tomlinson, and G. W. Brooksby. A Comprehensive Approach To Breast Cancer Detection Using Light: Photon Localization By Ultrasound Modulation And Tissue Characterization By Spectral Discrimination. *Proceedings of SPIE*, 1888, 500-510 (1993)
- Mcdannold N, Tempany CM, Fennessy FM, So MJ, Rybicki FJ, Stewart EA, Et Al. Uterine Leiomyomas: MR Imaging-Based Thermometry And Thermal Dosimetry During Focused Ultrasound Thermal Ablation. *Radiology* 240, 263-272 (2006)

- Meaney PM, Cahill MD, Terhaar GR. The Intensity Dependence Of Lesion Position Shift During Focused Ultrasound Surgery. *Ultrasound Med. Biol.* 26, 441–450 (2000)
- Meshorer A, Prionas S D, Fajardo L F, Meyer J L, Hahn G M And Martinez AA. The Effects Of Hyperthermia On Normal Mesenchymal Tissues. Application Of A Histologic Grading System. *Archives of Pathology and Laboratory Medicine* 107, 328–34 (1983)
- Miller N, Bamber J, Meaney P. Fundamental Limitations Of Noninvasive Temperature Imaging By Means Of Ultrasound Echo Strain Estimation. *Ultrasound Med. Biol.* 28, 1319–1333 (2002)
- Maass-Moreno R, Damianou C, Sanghvi N. Noninvasive Temperature Estimation In Tissue Via Ultrasound Echo-Shifts. Part II. In Vitro Study. *J Acoust Soc Am.* 100, 2522–2530 (1996)
- Malcolm AL, Ter Haar GR. Ablation Of Tissue Volumes Using High Intensity Focused Ultrasound. *Ultrasound Med Biol.* 22, 659–669 (1996)
- Maleke C, Konofagou E. An All-Ultrasound System For Sonication And Real-Time Monitoring Of Temperature And Ablation. *IEEE Ultrasonics Symposium* 204–207 (2006)
- Maleke C, Konofagou E. Harmonic Motion Imaging For Focused Ultrasound (HMIFU): A Fully Integrated Technique For Sonication And Monitoring Of Thermal Ablation In Tissues. *Phys. Med. Biol.* 53, 1773–1793 (2008)
- Maass-Moreno R, Damianou C A And Sanghvi N T Noninvasive Temperature Estimation In Tissue Via Ultrasound Echo-Shifts: Part II. In Vitro Study. *J. Acoust. Soc. Am.* 100, 2522–30 (1996)
- McDannold N, Hynynen K, Wolf D, Wolf G, Jolesz F. MRI Evaluation Of Thermal Ablation Of Tumors With Focused Ultrasound. *J Magn Reson Imaging* 8, 91–100 (1998)
- Miller N R, Bamber J C And Meaney P M Fundamental Limitations Of Noninvasive Temperature Imaging By Means Of Ultrasound Echo Strain Estimation. *Ultrasound Med. Biol.* 28, 1319–33 (2002)
- Miller E, Cheney M, Kilmer M, Boverman G, Ang L, Boas D. Feature-Enhancing Methods For Limited View Tomographic Imaging Problems. *Subsurface Sensing Technologies And Applications* 4, 327–353 (2003)
- Morse PM, Ingard KU. *Theoretical Acoustics.* Princeton University Press. (1968)
- Murray T, Sui L, Maguluri G, Roy R, Blonigen F, Nieva A, Dimarzio C. Detection Of Ultrasound Modulated Photons In Diffuse Media Using The Photorefractive Effect. *Optics Letters* 29, 2509–2511 (2004)
- Nyborg W. Solutions Of The Bio-Heat Transfer Equation. *Phys. Med. Biol.* 33, 785–792 (1988)
- Nightingale K, Palmeri M, Nightingale R, Trahey G. On The Feasibility Of Remote Palpation Using Acoustic Radiation Force. *J. Acoust. Soc. Am.* 110, 625–634 (2001)
- Nightingale K, Soo MS, Nightingale R, Trahey G. Acoustic Radiation Force Impulse Imaging: In Vivo Demonstration Of Clinical Feasibility. *Ultrasound Med Biol* 28, 227–235 (2002)
- Nightingale K, Palmeri M, And Trahey G, Analysis Of Contrast In Images Generated With Transient Acoustic Radiation Force. *Ultrasound Med Biol.* 32, 61–72 (2006)

- Nilsson AMK, Sturesson C, Liu DL, Andersson-Engels S. Changes In Spectral Shape Of Tissue Optical Properties In Conjunction With Laser-Induced Thermotherapy. *Applied Optics* 37, 1256–1267 (1998)
- Niu L, Wang Z, Zou W, Zhang L, Xiang L, Zhui H, Chen W, Bai J. Pathological Changes On Human Breast Cancer Specimens Ablated In Vitro With High-Intensity Focused Ultrasound. *Ultrasound Med. & Biol.* 36, 1437–1444 (2010)
- Nyborg WL. Solutions Of The Bio-Heat Transfer Equation. *Phys. Med. Biol.* 33, 785-792 (1988)
- O'Donnell M, Bauwens D, Mimbs J, Miller J. Broadband Integrated Backscatter: An Approach To Spatially Localized Tissue Characterization In Vivo. *Proceedings of IEEE Ultrasonics Symposium* 175–178 (1979)
- O'Donnell M, Skovoroda AR, Shapo BM, Emelianov SY. Internal Displacement And Strain Imaging Using Ultrasonic Speckle Tracking. *IEEE UFFC* 41, 1994
- O'Neil HT. Theory Of Focusing Radiators. *J Acoust Soc Am*, 21, 516-526 (1949)
- Ophir J, Shawker T, Maklad N. Attenuation Estimation In Reflection: Progress And Prospects. *Ultrasonic Imaging* 6, 349–395 (1984)
- Ophir J, Cespedes I, Ponnekanti H, Yazdi Y, Li X. Elastography: A Quantitative Method For Imaging The Elasticity Of Biological Tissues. *Ultrasonic Imaging* 13, 111–134 (1991)
- Orescanin M, Qayyum MA, Toohey KS, Insana MF. Complex Shear Modulus Of Thermally-Damaged Liver. *IEEE International Ultrasonics Symposium*, 127-130 (2009)
- Palmeri ML, Wang MH, Dahl JJ, Frinkley KD, Nightingale KR. Quantifying Hepatic Shear Modulus In Vivo Using Acoustic Radiation Force. *Ultrasound Med Biol.* 34, 546-558 (2008)
- Park SW. Analytical modeling of viscoelastic dampers for structural and vibration control. *International Journal of Solids and Structures.* 38, 8065-8092 (2001)
- Parker KJ. The thermal pulse decay technique for measuring ultrasonic absorption coefficients. *J. Acoust. Soc. Am.* 74, 1356-1361 (1983)
- Parker K. Effects Of Heat Conduction And Sample Size On Ultrasonic Absorption Measurements *J. Acoust.Soc. Am.* 77, 719-725 (1985)
- Parker K, Huang S, Musulin R, Lerner R. Tissue Response To Mechanical Vibrations For Sonoelasticity Imaging. *Ultrasound Med Biol.* 16, 241–246 (1990)
- Parker K, Fu D, Graceswki SM, Yeung F, Levinson SF, Vibrationsonoelastography And The Detectability Of Lesions. *Ultrasound Med Biol.* 24, 1437–47 (1998)
- Pierce A. *Acoustics: An Introduction to its Physical Principles and Applications.* American Institute of Physics, Melville (1989)
- Pennes H. Analysis Of Tissue And Arterial Blood Temperatures In The Resting Human Forearm. *Journal Of Applied Physics* 1, 93-122 (1948)
- Pernot M, Tanter M, Bercoff J, Waters K R And Fink M Temperature Estimation Using Ultrasonic Spatial Compound Imaging *IEEE UFFC* 51, 606–15 (2004)

- Rabkin B, Zderic V, Vaezy S. Hyperecho In Ultrasound Images Of HIFU Therapy: Involvement Of Cavitation. *Ultrasound Med Biol.* 31, 947–956 (2005)
- Rabkin B, Zderic V, Crum L, Vaezy S. Biological And Physical Mechanisms Of HIFU-Induced Hyperecho In Ultrasound Images. *Ultrasound In Medicine & Biology* 32, 1721-1729 (2006)
- Rademaker G, Jenne J, Rastert R, Roder D, Schad L-R. Comparison Of Noninvasive MRT-Procedures For The Temperature Measurement For The Application During Medical Thermal Therapies. *Zeitschrift fur Medizinische Physik* 13, 183–187 (2003)
- Raman CV and Nath NSN, The Diffraction Of Light By High Frequency Sound Waves. *Proceedings of the Indian Academy of Sciences* 2, 406, 413 (1935)
- Ramaz, F., B. C. Forget, M. Atlan, And A. C. Boccara. Photorefractive Detection Of Tagged Photons In Ultrasound Modulated Optical Tomography Of Thick Biological Tissues. *Optics Express.* 12, 5469-5474 (2004)
- Rayleigh, Lord (Strutt JW) On the Light From the Sky, its Polarization and Colour. *Scientific Papers Lord Rayleigh, Vol. 1.* Dover Publications, New York. (1964)
- Repacholi M, Grandolfo M, Rindi A. Eds., Effects Of Ultrasound On Solid Mammalian Tissue And Tumors In Vivo, Plenum, London, (1987)
- Ribault M, Chapelon JY, Cathignol D, Gelet A. Differential Attenuation Imaging For The Characterization Of High Intensity Focused Ultrasound Lesions. *Ultrasonic Imaging* 20, 160–177 (1998)
- Richards MS, Barbone PE, Oberai AA. Quantitative Three-Dimensional Elasticity Imaging From Quasi-Static Deformation: A Phantom Study. *Phys. Med. Biol.* 54, 757–779 (2009)
- Rivens I, Shaw A, Civale J, Morris H. Treatment Monitoring And Thermometry For Therapeutic Focused Ultrasound. *International Journal of Hyperthermia* 23, 121–139 (2007)
- Robinson TC and Lele PP. An Analysis of Lesion Development in the Brain and in Plastics by High-Intensity Focused Ultrasound at Low-Megahertz Frequencies. *J. Acoust. Soc. Am.* 51, 1333-1351 (1972)
- Robinson T and Lele P, An Analysis Of Lesion Development In The Brain And In Plastics By High-Intensity Focused Ultrasound At Low-Megahertz Frequencies, *J. Acoust. Soc. Am.* 51, (1976)
- Rosecan LR, Iwamoto T, Rosado AL, Lizzi FL, Coleman DJ. Therapeutic Ultrasound In The Treatment Of Retinal Detach-Ment: Clinical Observation And Light And Electron Microscopy. *Retina* 5, 115–122 (1985)
- Rousseau G, Blouin A, Monchalain J. Ultrasound-Modulated Optical Imaging Using A High-Power Pulsed Laser And A Double-Pass Confocal Fabry–Perot Interferometer. *Optics Letters* 34, 3445 (2009)
- Rudenko OV, Sarvazyan AP, Emelianov SY. Acoustic Radiation Force And Streaming Induced By Focused Nonlinear Ultrasound In A Dissipative Medium. *J Acoust Soc Am* 99, 2791–2798 (1996)
- Sachse W and Pao Y. On The Determination Of Phase And Group Velocities Of Dispersive Waves In Solids. *Journal of Applied Physics* 49, (1978)

- Sakadzic, S., And L. V. Wang, "Modulation Of Multiply Scattered Coherent Light By Ultrasound Pulses: An Analytical Model", *Physics Review E*. 72, 033620 (2005)
- Saleh And Teich, *Fundamentals Of Photonics*, 2nd Ed. Wiley And Sons. pp. 112 (2006)
- Sapareto S A And Dewey W C Thermal Dose Determination In Cancer Therapy. *International Journal of Radiation Oncology*Biology*Physics*. 10, 787–800 (1984)
- Sapin-De Broses E, Gennisson JL, Pernot M, Fink M, Tanter M. Temperature Dependence Of The Shear Modulus Of Soft Tissues Assessed By Ultrasound. *Phys. Med. Biol.* 55, 1701–1718 (2010)
- Sarvazyan AP, Rudenko OV, Swanson SD, Fowlkes JB, Emelianov SY. Shear Wave Elasticity Imaging: A New Ultrasonic Technology Of Medical Diagnostics. *Ultrasound Med Biol.* 24, 1419–1435 (1998)
- Seip R, Ebbini E. Noninvasive Estimation Of Tissue Temperature Response To Heating Fields Using Diagnostic Ultrasound. *IEEE Transactions on Biomedical Engineering*. 42, 828 – 839 (1995)
- Seo J, Tran B, Hall T, Fowlkes J, O'Donnell M, Cain C. Evaluation Of Ultrasound Tissue Damage Based On Changes In Image Echogenicity. *IEEE Ultrasonics Symposium* 2, 1431- 1434 (2002)
- Seo J, Tran B, Hall T, Fowlkes J, Abrams G, O'Donnell M, Cain C. Evaluation Of Ultrasound Tissue Damage Based On Changes In Image Echogenicity In Canine Kidney. *IEEE UFFC* 52, (2005)
- Sibille A, Prat F, Chapelon J, Abou El Fadil F, Henry L, Theilliere Y, Ponchon T, Cathignol D. Characterization Of Extracorporeal Ablation Of Normal And Tumor-Bearing Liver Tissue By High Intensity Focused Ultrasound. *Ultrasound Med. Biol.* 19, 803-813 (1993)
- Silverman RH, Vogelsang B, Rondeau MJ, Coleman DJ. Therapeutic Ultrasound For The Treatment Of Glaucoma. *American Journal of Ophthalmology* 111,327–337 (1991)
- Simon C, Vanbaren P, Ebbini E. Two-Dimensional Temperature Estimation Using Diagnostic Ultrasound *IEEE UFFC* 45, 1088 - 1099 (1998)
- Souchon R, Bouchoux G, Maciejko E, Lafon C, Cathignol D, Bertrand M, Chapelon J. Monitoring The Formation Of Thermal Lesions With Heat-Induced Echo-Strain Imaging: A Feasibility Study. *Ultrasound Med. Biol.* 31, 251–259 (2005)
- Sokka S, King R, Hynynen K. MRI-Guided Gas Bubble Enhanced Ultrasound Heating In In Vivo Rabbit Thigh. *Phys Med Biol.* 48, 223 – 241 (2003)
- Srinivasan S, Righetti R, Ophir J. An Experimental Characterization Of Elastographic Spatial Resolution: Analysis Of The Trade-Offs Between Spatial Resolution And Contrast-To-Noise Ratio. *Ultrasound Med Biol.* 30, 1269–1280 (2004)
- Stride EP, Coussios C. Cavitation And Contrast: The Use Of Bubbles In Ultrasound Imaging And Therapy. *Proceedings of the Institution of Mechanical Engineers* 224, Part H: J. Engineering In Medicine 171-191 (2003)
- Sui L, Murray T, Maguluri G, Nieva A, Blouin A, Dimarzio C, Roy R. Enhanced Detection Of Acousto-Photonic Scattering Using A Photorefractive Crystal. *Proceedings of SPIE*. 5320, 164-171 (2004)
- Sui L. Acousto-Optic Imaging In Diffuse Media Using Pulsed Ultrasound And The Photorefractive Effect . Phd. Dissertation, Boston University (2006)

- Suslick, K.S., Doktycz, S.J., Flint, E.B. On The Origin Of Sonoluminescence And Sonochemistry. *Ultrasonics* 28, 280-290 (1990)
- Szabo, T. *Diagnostic Ultrasound Imaging: Inside Out*. Elsevier (2004)
- Tay BK, Kim J, Srinivasan MA In Vivo Mechanical Behavior Of Intra-Abdominal Organs *IEEE Transactions on Biomedical Engineering*. 53, 2129 (2006)
- Taylor L S, Richards M S, Moskowitz A J, Lerner A L, Rubens D J And Parker K J. Viscoelastic Effects In Sonoelastography: Impact On Tumor Detectability. *IEEE Ultrasonics Symposium*. 1639–1642 (2001)
- Ter Haar G. *Ultrasound Focal Beam Surgery*. *Ultrasound In Medicine And Biology* 21, 1089-1100 (1995)
- Ter Haar G. "Ultrasonic Biophysics", Chap.3 In *Physical Principles Of Medical Ultrasonics*, Second Edition. Hill CR, Bamber JC, And Ter Haar GR Eds. John Wiley & Sons (2004)
- Ter Haar G. "Therapeutic And Surgical Applications", Chap. 13. In *Physical Principles Of Medical Ultrasonics*, Second Edition. Hill CR, Bamber JC, And Ter Haar GR Eds. John Wiley & Sons 2004 pp.427
- Ter Haar G, Coussios C. High Intensity Focused Ultrasound: Past, Present And Future. *International Journal of Hyperthermia* 23, 85–87 (2007)
- Thurston R, Mason W., Eds. *Physical Acoustics: Principles And Methods*. Academic Press (1976)
- Timoshenko S and Goodier J, *Theory Of Elasticity*. Mcgraw-Hill, New York, 1987
- Tiukinhoy-Laing SD, Buchanan K, Parikh D, Huang S, Macdonald RC, Mcpherson DD, Klegerman ME, Fibrin Targeting Of Tissue Plasminogen Activator-Loaded Echogenic Liposomes. *Journal of Drug Targeting*. 15, 109–114 (2007)
- Torr G. The Acoustic Radiation Force. *American Journal of Physics*. 52, 402-408 (1984)
- Tornberg E. Effects Of Heat On Meat Proteins—Implications On Structure And Quality Of Meat Products. *Meat Science*. 70, 493–508(2005)
- Trubestein G, Engel C, Etzel F, et al. Thrombolysis By Ultrasound. *Clinical Science and Molecular Medicine*. 3, 697-698 (1976)
- Tyreus P, Diederich C. Two-Dimensional Acoustic Attenuation Mapping Of High-Temperature Interstitial Ultrasound Lesions. *Phys. Med. Biol.* 49, 533 - 546 (2004)
- Van Dongen K, Wright W. A Forward Model And Conjugate Gradient Inversion Technique For Low-Frequency Ultrasonic Imaging. *J. Acoust. Soc. Am.* 120, 2086 – 2095 (2006)
- Vaezy S, Martin R, Schmiedl U, Caps M, Taylor S, Beach K, Carter S, Kaczkowski P, Keilman G, Helton S. Liver Hemostasis Using High-Intensity Focused Ultrasound. *Ultrasound Med. Biol.* 23, 1413–1420 (1997)
- Vaezy S, Shi X, Martin R, Chi E, Nelson P, Bailey M, Crum Real-Time Visualization Of High-Intensity Focused Ultrasound Treatment Using Ultrasound Imaging. *Ultrasound Med. Biol.* 27, 33–42 (2001)

- Vaezy S And Zderic V. Hemorrhage Control Using High Intensity Focused Ultrasound. *International Journal of Hyperthermia*. 23, 203–11 (2007)
- Vokurka, K. Amplitudes Of Free Bubble Oscillations In Liquids. *Journal of Sound and Vibration*. 141, 259–275 (1990)
- Vykhodtseva N, Mcdannold N, Martin H, Bronson RT, Hynynen K. Apoptosis In Ultrasound-Produced Threshold Lesions In The Rabbit Brain. *Ultrasound Med Biol*. 27, 111–117 (2001)
- Westervelt PJ, The Theory Of Steady Forces Caused By Sound Waves. *J. Acoust. Soc. Am*. 23, 312 (1951)
- Wilson LS, Robinson DE. Ultrasonic Measurement of Small Displacements And Deformations Of Tissues. *Ultrasonic Imaging* 4, 71-82 (1982)
- Worthington A, Trachtenberg J, Sherar M. Ultrasound Properties Of Human Prostate Tissue During Heating. *Ultrasound Med. Biol*. 28, 1311–1318 (2002)
- Wu T, Felmlee J, Greenleaf J, Riederer S, Ehman R. Assessment Of Thermal Tissue Ablation With MR Elastography. *Magnetic Resonance In Medicine* 45, 80-87 (2001)
- Xu X, Zhang H, Hemmer P, Qing D, Kim C, Wang L. Photorefractive Detection Of Tissue Mechanical Properties By Ultrasound Optical Tomography. *Optics Letters* 32, 656-658 (2007)
- Yang X. Investigation Of Bubble Dynamics And Heating During Focused Ultrasound Insonation In Tissue-Mimicking Materials. Phd Dissertation, Boston University (2003)
- Yang X, Roy R, Holt RG. Bubble Dynamics And Size Distributions During Focused Ultrasound Insonation. *J. Acoust. Soc. Am*. 116, 3421-3431 (2004)
- Yeh WC, Li PC, Jeng YM, Hsu HC, Kuo PL, Li ML, Yang PM, Lee PH. Elastic Modulus Measurements Of Human Liver And Correlation With Pathology. *Ultrasound Med Biol*. 28, 467–474 (2002)
- Yao H, Phulpattaranon P, Ebbini E. Detection And Mapping Of Thermal Lesions Using Dual-Mode Ultrasound Phased Arrays. *IEEE Ultrasonics Symposium*. 2 1431- 1434 (2002)
- Yaroslavsky AN, Schulze PC, Yaroslavsky IV, Schober R, Ulrich F, Schwartz H-J. Optical Properties Of Selected Native And Coagulated Human Brain Tissues In Vitro In The Visible And Near Infrared Spectral Range. *Phys Med Biol*. 47, 2059–2073 (2002)
- Zhang X, Lewis M, Johnson B. Influence Of Bubbles On Scattering Of Light In The Ocean. *Applied Optics* 37, 6525 (1998)
- Zhong H, Wan M, Jiang Y, Wang S. Monitoring Imaging Of Lesions Induced By High Intensity Focused Ultrasound Based On Differential Ultrasonic Attenuation And Integrated Backscatter Estimation *Ultrasound Med. Biol*. 33, 82–94 (2007)

Curriculum Vitae

Andrew Draudt

Dept. of Mechanical Engineering
Boston University
110 Cummington St. Boston, MA 02215
Email: andydraudt@gmail.com

Education

Cornell University	Applied and Engineering Physics	1985 (BS)
University Of Washington	Graduate study in Physics.	1987
Cornell University	PhD program in Electric Engineering (MEMS devices)	2004
Boston University	PhD program in Mechanical Engineering.	2012 (PhD)

Teaching

As a graduate student I've been a teaching assistant at the University of Washington, Cornell University, and Boston University in basic physics, electronic circuits lab, microelectronics, mechanical engineering lab, fluid dynamics.
In 2002 I taught a four week unit on harmonic oscillators to a high school physics class in Harvard, Massachusetts

Employment

Engineer, Vector Magnetics Inc. Ithaca, NY **2004, 2005**
Designed multi-axis magnetic dipole sources to fit inside oil well drill pipe.

Independent work **2002-2004**
Basic architectural acoustics consulting.
Apprenticed under a violin maker. Built a violin, using acoustic measurements and knowledge from research literature on violin acoustics.

Sr. Research Engineer, Bose Corporation. Framingham, MA. **1998 - 2002**
Lead acoustic engineer on a project to gain a theoretical and practical knowledge base for a new product direction for the company (compression drivers). Project encompassed solutions of the Helmholtz equation with source term for various compression driver "phase plug" designs, lumped element and finite element modeling of magnetic, electromechanical and acoustic systems. Designed prototypes. Measured acoustic fields, audio quality, and surface vibrations.

Design Engineer, Transonic Systems. Ithaca, NY. **1988 - 1998**
Research and design of a family of ultrasonic fluid flow sensors. As sole engineer, developed the product from infancy into a major company asset. Designed ultrasonic transducers to maximize efficiency and linearity of transfer function over many orders of magnitude of excitation voltage. Wrote computer models for acoustic fields and electro-mechanical transducers. Machining, CAD design, plastic molding, manufacturing engineering. Worked with major medical equipment manufacturers to design custom OEM products. Supervised and taught technicians.

Cornell High Energy Synchrotron Source.

1985 - 1986

Operator of a national accelerator x-ray lab. Trained and guided researchers. Designed, built, and repaired computerized x-ray optical hardware, safety systems, high-vacuum systems. Wrote documentation.

Professional Affiliations

Student member, Acoustical Society of America

Student Member, American Society of Mechanical Engineers

Member, CenSSIS (Gordon Center for Subsurface Sensing and Imaging Systems)

Awards

Award for best poster, NSF Site Visit, CenSSIS, April, 2008

Award for best poster, 39th Symposium of the Ultrasonic Industry Association, April, 2010

Publications

Refereed Journal Articles

A. Draudt, R. Cleveland. "Impact Of Nonlinear Distortion On Acoustic Radiation Force Elastography" *Ultrasound in Medicine and Biology* (2011)

P. Lai, J. R. McLaughlan, A. B. Draudt, T. W. Murray, R. O. Cleveland, and R. A. Roy, "Monitoring and guidance of high intensity focused ultrasound exposures in real time using acousto-optic imaging: feasibility and demonstration ex vivo", SPIE Photonics West, BIOS 2010

P. Lai, J. R. McLaughlan, A. B. Draudt, T. W. Murray, R. O. Cleveland, and R. A. Roy, "Real time monitoring of high intensity focused ultrasound lesion formation using acousto-optic imaging" in press, *Ultrasound in Medicine and Biology* Jan 2010

Articles in Conference Proceedings

A Draudt, P Lai, R A. Roy, T W. Murray, R O. Cleveland. "Detection of HIFU lesions in Excised Tissue Using Acousto-Optic Imaging" *Proc. of Second International Symposium on Therapeutic Ultrasound* (Minneapolis, MN 2008) pp 270-274.

A. Draudt and R. Cleveland, "Modeling HMI Measurement of HIFU Lesion Formation with Temperature-Dependent Tissue Properties" *Proc. of Second International Symposium on Therapeutic Ultrasound* (New York, NY 2011)

Oral Presentation Abstracts

A. Draudt. Numerical "Simulation of Harmonic Motion Imaging of HIFU Induced Lesion Formation" Meeting of the *International Symposium on Therapeutic Ultrasound* (New York, NY, April, 2011)

A. Draudt, R.O. Cleveland "Nonlinear distortion associated with high-intensity focused ultrasound (HIFU) creates apparent displacements in acoustic radiation force imaging (ARFI)" *Meeting of the Acoustical Society of America* (Baltimore, MD, May, 2010)

A Draudt, P Lai, R A. Roy, T W Murray, R O. Cleveland "Acousto-optic Detection Of High-intensity Focused Ultrasound Lesions In Real Time" Meeting of the *International Symposium on Therapeutic Ultrasound* (Minneapolis, MN 2008)

A Draudt, P Lai, R A. Roy, T W Murray, R O. Cleveland "A Multi-Modal Approach to Imaging and Monitoring HIFU Lesions" *Meeting of the American Society of Mechanical Engineers* (Boston, MA 2008)

Meeting Posters

A Draudt, P Lai, R A. Roy, T W Murray, R O. Cleveland “Detection Of HIFU Lesions In Excised Tissue Using Acousto-Optic Imaging” *Proc. of Second International Symposium on Therapeutic Ultrasound* (Minneapolis, MN 2008)

Real-time Monitoring of HIFU Lesion Formation with Combined Acoustic Force Elastography and Acousto-optic Imaging. 39th Symposium of the Ultrasonic Industry Association, (Boston, MA. April, 2010)

Characterizing the Dynamic Properties of HIFU Lesions. NSF/CenSSIS Site Visit, (Boston, MA, April, 2008)

Imaging HIFU Lesions Using Ultrasound. NSF/CenSSIS Site Visit, (Boston, MA, September, 2007)